10-25-2016 12:00 AM

Multiscale Wind Modelling for Sustainability and Resilience

Djordje Romanic
The University of Western Ontario

Supervisor
Dr. Horia Hangan
The University of Western Ontario

Graduate Program in Civil and Environmental Engineering
A thesis submitted in partial fulfillment of the requirements for the degree in Doctor of Philosophy

Recommended Citation

Romanic, Djordje, "Multiscale Wind Modelling for Sustainability and Resilience" (2016). *Electronic Thesis and Dissertation Repository*. 4210.
https://ir.lib.uwo.ca/etd/4210

Abstract

The research presented herein is a mix of meteorological and wind engineering disciplines. In many cases, there is a gap between these two fields and this thesis is an attempt to bridge that gap through multiscale wind modelling approaches. Data and methods used in this study cover a multitude of spatial and temporal scales. Applications are in the fields of sustainability and resilience. This relationship between multiscale wind modelling and sustainability and resilience is investigated examining several case studies of three different developments: urban, rural and coastal.

An urban wind modelling methodology is proposed and applied for a specific development in downtown Toronto, Canada. Micro-scale wind energy maps are created using computational fluid dynamics, analytical models, and the Canadian Wind Energy Atlas. It is demonstrated that urban wind energy projects are currently not feasible/sustainable due to decoupling between urban wind turbine power curves and wind speed histograms. Wind climatology for Toronto is calculated using the reanalysis data for the period 1948-2015. A trend analysis reveals statistically significant positive trends of the most frequent wind directions. Low-frequency wind spectra shows three distinguished peaks. The lowest frequency peak has the period of 11 year and it is linked to solar activity. The first methodology for microscale modelling of urban winds in changing climate is developed. Maximum wind speeds are more affected by climate change than the means.

A wind sustainability study is performed for a unique development in South Central Kansas, United States. The analyses are conducted on the wind data obtained from the closest weather station and for the period 1984-2015. The WAsP package is used to calculate the wind atlas and wind resources at the site. Five locations suitable for installation of wind turbines are determined.

A downburst that struck Livorno, Italy, on October 1, 2012 is analyzed from the wind resilience perspective. The analyses are conducted by gathering all available and relevant meteorological data. This research allowed for better understanding of downbursts, created a reference broad-band of information for the future calibration of analytical, physical and numerical models, and highlighted the potential of merging wind engineering and meteorology.

Keywords

Wind, sustainability, resilience, multiscale modelling, multidisciplinary approach, CFD, WAsP, wind energy, downbursts, meteorology.

Co-Authorship Statement

Chapter II is published in the Wind Engineering journal under the co-authorship of Djordje Romanic, Ashkan Rasouli and Horia Hangan.

Dr. Rasouli was responsible for generating CAD models of the Pan American Games Athletes' Village in downtown Toronto. Dr. Hangan supervised the research, helped in writing the manuscript and recommended literature review. Djordje Romanic conducted literature review, developed the new multiscale methodology for urban wind modelling, tested the methodology, ran numerical simulations, analyzed the results, plotted figures and wrote the manuscript.

Chapter III is submitted for publication in the Theoretical and Applied Climatology journal under the co-authorship of Djordje Romanic, Horia Hangan and Mladjen Ćurić.

Dr. Hangan supervised the research, helped in writing the manuscript and suggested some of the background literature. The trend analysis code used for this study was together developed by Djordje Romanic and Dr. Ćurić. Djordje Romanic conducted literature review, obtained and processed the reanalysis and solar activity data, conducted the whole trend, spectral and autocorrelation analyses, as well as the cross-correlation analysis between wind speed and solar activity records. Djordje Romanic also plotted all figures and wrote the manuscript.

Chapter IV is published in the Wind Engineering journal under the co-authorship of Djordje Romanic, Ashkan Rasouli and Horia Hangan.

Dr. Rasouli was responsible for generating CAD models of the Pan American Games Athletes' Village in downtown Toronto. Dr. Hangan supervised the research, helped in writing the manuscript and suggested literature review. The rest of the work was performed by Djordje Romanic, i.e., literature review, development of the new multiscale methodology for urban wind modelling in changing climate, testing the methodology for a specific urban development, running numerical simulations, analysis of results, figures, and writing the manuscript.

Chapter V is submitted for publication in the Renewable Energy journal under the co-authorship of Djordje Romanic, Dan Parvu, Maryam Refan and Horia Hangan.

This paper resulted from a series of technical (expert) reports prepared by Djordje Romanic in the framework of The Kansas Project. Mr. Parvu helped acquiring raw meteorological data from coded METER reports. Dr. Refan helped proofreading the final technical reports as well as improved the final version of the manuscript. Lastly, Dr. Hangan framed and supervised the research. Djordje Romanic was responsible for all meteorological/climatological analyses, WAsP numerical modelling including the preparation of orography and roughness maps, and uncertainty analysis. Djordje Romanic also prepared all figures, conducted literature review and wrote the manuscript.

Chapter VI is submitted for publication in the Monthly Weather Review journal under the co-authorship of Massimiliano Burlando, Djordje Romanic, Giovanni Solari, Horia Hangan and Shi Zhang.

The paper is part of collaboration between Windyn (University of Genoa) and WindEEE Research Institute (Western University) carried out as an interdisciplinary effort between two groups involving atmospheric scientists and wind engineers. Prof. Burlando supervised and organized the meteorological analysis conducted in this study. Prof. Solari supervised the signal analysis part of the study. Ms. Zhang helped in preparing some of the figures in the paper and extracted this downburst event from the large set of anemometric records. Dr. Hangan supervised this research, recommended literature and helped in writing the manuscript. Djordje Romanic wrote most of the manuscript, conducted literature review and performed most of the meteorological analyses. Djordje Romanic also created most of figures in this manuscript.

Acknowledgments

I would like to express my deepest gratitude to my research supervisor Dr. Horia Hangan for his enlightening guidance and continuous support throughout my doctoral studies at Western University. His immense knowledge stimulated my interest in the field of wind engineering.

I would like to thank my thesis examination committee: Dr. Girma Bitsuamlak (Western University), Dr. Chao Zhang (Western University), Dr. James Voogt (Western University), and Dr. Curran Crawford (University of Victoria) for reading my theses and suppling insightful comments and questions that improved the quality of the final version of this manuscript.

I would like to extend my thanks to co-authors on my publications – Dr. Mladjen Ćurić, Dr. Ashkan Rasouli, Dan Parvu, Dr. Maryam Refan, Dr. Massimiliano Burlando, Prof. Giovanni Solari and Shi Zhang. I would not be able to complete this journey without you! Thank you for the months of hard work you put into preparing the manuscripts, helping me in my research and fruitful discussions we have had over the past four years. Special thanks go to Dan Parvu and Dr. Maryam Refan for their friendship and support during my studies.

Many people helped me in different stages of my research. I owe a debt of gratitude especially to Dr. Slobodan P. Simonovic, who in 2012 recognized my Ph.D. potential in wind engineering and recommended me to my supervisor Dr. Horia Hangan. At that time, I was still a doctoral student in meteorology at the University of Belgrade, Serbia. Therefore, I also must send special thanks to Dr. Mladjen Ćurić, who was the research superivosr for my Ph.D. studies in meteorology and supported my decission to come here and pursue the second Ph.D. degree. These three people are the key persons for my academic carrear and I will always remember that! Thank you so much.

I would like to extend my thanks to Adrian Costache for his help regarding Matlab programming and huge support throughout the studies, as well as to Dr. Jubayer Chowdhury for the careful reading of the final version of the manuscript and many interesting discussions we had over the last several years. I thank Zoheb Nasir and Ziad Boutanios for their help regarding the CFD and WRF modelling, respectively. I thank Danica Trapara for proofreading some parts of the manuscript. I would like to thank Vladimir Nikolić for welcoming me at Western and for his support during my studies. In addition, I am gratefully to all my colleagues and friends at the Wind Engineering, Energy and Environment (WindEEE) Research Institute and Boundary Layer Wind Tunnel Laboratory (BLWTL): Mohammad Karami, Ryan Kilpatrick, Zeinab Samani, Julien LoTufo, Gerald Dafoe, and Karen Norman in particular. I also thank Chieh-Hsun Wu and Mahshid Nasiri for their support.

A special thanks go to all professors whose courses I attended at Western (Dr. Horia Hangna – Wind Engineering, Dr. Girma Bitsuamlak – Computational Wind Engineering, Dr. Greg Kopp – Bluff Body Aerodynamics, Dr. Eric Savory – Mechanism and Theory of Turbulent Flows, Dr. Kristy Tiampo and Dr. Gero Michel – Modelling Catastrophe Risk, and Prof. Giovanni Solari – Wind-Excited and Aeroelastic Response of Structures).

I would like to acknowledge the help of Mr. Travis Farncombe and The Kansas Project team who provided the information related to this project including the design and the site topography. The Kansas Project is funded by Another Design Experiment Inc. I would like to thank the Shared Hierarchical Academic Research Computing Network (SHARCNET: www.sharcnet.ca) and Compute/Calcul Canada for their facilities. Downburst anemometric data (Chapter VI) have been recorded by the wind monitoring network of the European Projects “Wind and Ports” and “Wind, Ports, and Sea”, funded by the Cross-border Cooperation Programme “Italy-France Maritime 2007-2013”. Satellite images in Chapter VI are based on Level 1 data recorded by SEVIRI satellite instruments (operated by EUMETSAT). LaMMA Consortium (http://www.lamma.rete.toscana.it/) is gratefully acknowledged for radar reflectivity data and measurements of their meteorological station in Livorno (Chapter VI).

I would also like to acknowledge the financial support from the generous donors of the Alan G. Davenport Memorial Scholarship, Victor Hangan Global Opportunities Award, Dr. Robert Addie Graduate Scholarship in Wind Engineering, The Ross and Jean Clark Scholarship, the C4 CatIQ 2015 conference and the WISE competition.

Last but not least, I am eternally grateful to my parents Dušanka and Nikola Romanić, my brother Jovan, my sister-in-law Aleksandra, my nieces Nikolina and Natalija, my grandparents and all my friends around the globe.

Dedication

I dedicate this doctoral thesis to my family in Serbia.

Ову докторску дисертацију посвећујем мојој породици у Србији.

“I was born not knowing and have had only a little

time to change that here and there”

-Richard Feynman

Table of Contents

List of Tables

List of Figures

List of Appendices

This page intentionally left blank

Chapter I

1 Introduction

This thesis is an attempt to address wind sustainability and wind resilience aspects from a multi-scale perspective while at the same time bridging the gap between atmospheric science and wind engineering approaches. The thesis is therefore structured as a collection of studies addressing multiscale aspects of urban wind sustainability (Chapter II, Chapter III and Chapter IV), mixed sustainability and resilience aspects related to new types of non-urban developments (Chapter V), as well as resilience (storm related) aspects of coastal urban areas (Chapter VI).

The Introduction of the thesis has been divided into five sections. General introduction in Section 1.1 familiarizes the reader with sustainability and resilience concepts, provides the main definitions, and describes how wind phenomena relates to these two concepts. Section 1.2 is dedicated to the literature review describing the studies that have investigated the connection between the sustainable development in urban environments and wind. Similarly, Section 1.3 discusses the latest advancements concerning the importance of wind-related research for the resilience of cities. Consequently, Section 1.4 establishes the main objectives and motivations behind this research.

1.1 General introduction

Wind can be defined as a horizontal movement of air. It is driven by the horizontal pressure gradients between two points above ground. These pressure gradients, on the other hand, are caused by the temperature differences between two areas; with warm air being light (low pressure) and cold air being heavy (high pressure). The other three forces that dictate the movement of air in a horizontal plane are the Coriolis force, which is an apparent force caused by the Earth's rotation, the centrifugal force and the friction force. The latter one is caused by the presence and roughness of Earth's surface and therefore the friction force diminishes as the air moves away from the surface. The region of atmosphere directly or indirectly influenced by the surface friction is called the atmospheric boundary layer (ABL) and its height is roughly the first 1000 m from the surface. For a more detailed description of wind dynamics the reader is referred to Zdunkowski and Bott (2003).

The wind, therefore, has kinetic energy (K); which can be expressed as:

$$K = \frac{1}{2} m U^2, \tag{1-1}$$

where m is the mass of air and U is the wind speed. Expressing the power in the wind as $P = dK/dt$ where t is time, and expanding the flow rate dm/dt in terms of air density (ρ), an area perpendicular to the wind (A), and wind speed (U), Eq. (1-1) reads:

$$P = \frac{1}{2} \rho A U^3. \tag{1-2}$$

The above equation shows that wind power is proportional to wind speed cubed, which is particularly important for the cost-effectiveness of wind energy projects. Wind energy is considered to be sustainable, where sustainability in this context is defined as meeting society's current needs without harming the next generations (United Nations 1987, Welch and Venkateswaran 2009). A similar definition is provided in Girardet (2008). Sustainable development requires a progressive transformation of both economy and society. This transformation has begun in the energy sector several decades ago. By the end of 2014, renewables (wind, solar, hydro) supplied approximately 23% of global electricity (REN21 2015), which is more than ever before in modern history. In an ideally sustainable world, the energy market should achieve a 100% penetration of renewables. This objective is not an easy task and the research presented in this doctoral dissertation will hopefully make a modest contribution towards this overarching goal.

Wind energy is sustainable because it generates neither emissions nor waste (although one could argue it takes energy and materials to build the turbines and associated infrastructure and these eventually generate waste when being upgraded/replaced) and for all practical purposes it is inexhaustible. Thanks to many technological advancements in the last several decades, wind energy efficiency is now comparable to traditional fossil fuels (Jacobson and Delucchi 2011, Delucchi and Jacobson 2011). For these reasons, wind is currently one of the fastest growing types of power in the world. The Global Wind Energy Council (GWEC) forecasts that the world wind energy production will almost double by 2020 (GWEC 2016). The leading country in 2015 was China, installing 30.8 GW of wind capacity, followed by Europe and the United States. It is expected that these countries will continue to be the leaders in wind energy. The on-going climate change will be the main factor to drive the growth of wind energy in the future. In accordance, representatives of 186 countries gathered in Paris in November and December of 2015 at the Paris Climate

Change Conference and called for a 100% carbon emissions free power sector by 2050 at the latest. This decision most certainly aims toward a more sustainable society, but at the same time requires large reductions in global emissions in order to achieve the above goal (United Nations 2016a). It is expected that wind and solar energy will be the most exploited renewables that meet this challenging objective.

Although wind energy itself is perfectly sustainable, the harvesting process and technology of extracting the energy from the wind is not. One of the biggest challenges of wind power is that the sites having higher wind resources are often located far from cities, which are the biggest energy consumers. In order to overcome this difficulty, transmission lines have to be built to bring the produced electricity from the wind turbines located in remote locations to the urban environments. Building transmission lines, however, increases the cost of a wind energy project. A more sustainable solution would be to have wind turbines located close to the cities or installed inside cities if possible. In this regard, the possibility of installing small-scale wind turbines in an urban environment is investigated in this study. A new development, the 2015 Pan American Games Athletes' Village in the city of Toronto is used as a base for this study that follows three main steps.

First, a new methodology for urban wind modelling is introduced. This methodology is a first attempt to couple the Canadian Wind Energy Atlas, computational fluid dynamics tool and analytical models in order to model urban winds. The proposed methodology is wind direction dependent and in this study it is tested for two wind directions (southwest winds and east winds). However, the method can be applied to any number of wind directions or wind sectors. Here, it is important to highlight that the proposed methodology has a wide range of applicability, such as in the fields of wind engineering and calculation of wind loads on buildings, dispersion of pollutants, investigation of urban heat islands, urban ventilation and channeling effects, and pedestrian comfort. In this study, feasibility of an urban wind energy project in the 2015 Pan American Games Athletes' Village is analyzed. Second, the proposed methodology is placed in the framework of the current climate change and the microscale urban wind modelling is performed taking into account the long-term wind trends on regional scales. For that reason, long-term wind speed trends (1948-2015) above Toronto are analyzed in great detail. The proposed methodology that couples urban wind modelling and long-term wind trends, however, does not take into account any changes in urban planning and urban topology during the same period of time. Third, some of the technological limitations and challenges for the use of vertical axes urban wind turbines in cities are discussed and new concepts are suggested.

One of the classifications of wind turbines is whether they are horizontal axis or vertical axis devices (HAWT and VAWT, respectively). Small wind turbines are typically considered to be those with capacities below 100 kW. In many cases, these turbines use the VAWT technology and usually they are off-grid and used to supply individual homes, buildings and farms. These small-scale wind turbines are difficult to connect to grid because when spinning at low rates, they only produce power that can charge a battery. Namely, due to the lack of a gearing system in small wind turbines, the generator shaft cannot be augmented to higher speed at the expense of torque, such as the possibility in large scale wind turbine technologies. Intermediate size wind turbines have generation capacity of 100 kW to 250 kW and they can power a small village or a group of houses, a complex of buildings, etc. They can be either off-grid or on-grid. Large wind turbines (capacity above approximately 0.5 MW) are typically grid-connected, HAWT technology and with rotor diameters of about 80 to 100 m. In this thesis, small-scale VAWT wind turbines are considered in urban environments, whereas the five locations suitable for installation of large wind turbines (HAVT) are analyzed in a rural environment. In remote locations, such as the rural development in Kansas, United States, that is analyzed in this study, stand-alone systems can be more cost-effective than extending a power line to the electricity grid. The cost of building a new transmission line can range from $US 15,000 to $US 50,000 per mile (Wind Energy Foundation, 2016). The cost effectiveness of small-scale wind turbines in many cases is second tier compared to large wind turbines. The main reasons are technological and some of them are discussed here (gearbox), while others are further addressed in Section 2.4.3. To conclude this paragraph on wind turbine technology, it is important to note that wind power is proportional to the wind speed cubed (Eq. (1-2)) and since urban environments are characterized with higher wind speeds than urban environments, wind energy in rural areas is overall more cost-effective than the urban wind energy projects. This study has confirmed the feasibility of rural wind power projects and current unfeasibility of wind power projects in cities.

The set of three studies (Chapter II, Chapter III, and Chapter IV) performed for Toronto at one of its blocks (i.e., 2015 Pan American Games Athletes’ Village) spans over several orders of spatial scale magnitudes. The wind speed and occurrence trends have been investigated using the NCEP/NCAR reanalysis 1 data (Kalnay et al. 1996), which are given on a grid representative for the meso-α scales (200-2000 km). Then, a methodology is proposed to zoom in from these regional scales (reanalysis data) to the level of wind flows around individual buildings in the downtown core (local scales). The transition from the largest scales to the smallest scales is achieved through the new approach described in Chapter II.

In climatology and meteorology, this concept is known as downscaling; a procedure developed to take information known at large scales and use it to make predictions at local scales. The two main approaches to downscaling are dynamical and statistical (e.g. Fowler et al. 2007, Flint and Flint 2012, Rockel 2015, Mandal et al. 2016). Dynamical downscaling is defined as running high-resolution meteorological models on mesoscales, using lower-resolution climate model output as boundary and initial conditions. These models use physical principles to reproduce local climates, hence the name dynamic downscaling. Statistical downscaling, on the other hand, relies on different statistical relationships between local micro-climate and large-scale climate. A combination of dynamical and statistical downscaling also exist (Mengelkamp et al. 1997). The approach applied to the Toronto case described in Chapter II falls into the one-way dynamic downscaling category. The proposed method has three major steps: (1) the input wind speeds obtained from the Canadian Wind Energy Atlas at three different heights and (far) upwind from the site of interest (2) evaluation of wind and turbulence intensity profiles (close) upwind from the site of interest using analytical relationships and surface roughness data, and (3) urban wind modelling using a computational fluid dynamics tool. The methodology relies on the so-called one-way coupling in which larger scale information are projected to smaller scales (i.e. the Canadian Wind Energy data to local scales), but not vice versa. One-way coupling is widely used in meteorological analysis and the differences between one-way and two-way coupling are discussed elsewhere (Harris and Durran 2010). The developed methodology is described in detail in Chapter II.

The reanalysis data used in this study (NCEP/NCAR reanalysis 1 dataset) represents the weather forecast model simulations of the past that include data assimilation of historical observations. That is, observations and a numerical model are combined objectively to generate a synthesized estimate of the recent weather and climate. To a limited extent, reanalysis data could be thought of as modified observations given on a rectangular grids. Reanalysis products are extensively used in climate research studies as well as in a number of commercial projects. Urban environments in reanalysis data are crudely represented using slab models in which urban environments are treated as surfaces with different roughness length, albedo and thermal characteristics compared to the surrounding regions. Complexity of three-dimensional urban geometry and multitude of meteorological processes typical for urban environments are neglected. Changing in urban development are therefore not accounted for accordingly.

Chapter V presents an example in which wind sustainability concepts are considered together with wind resilience aspects. The analyzed rural development is called the Kansas Project, which is a unique development in the design stage and located in remote, rural area of Central South Kansas, United States (The Kansas Project 2015). The purpose of the studies conducted as part of this project is to address the question: how can design foster a more symbiotic relationship between sustainability and resilience aspects and between people and weather? One of the goals of the project will be to compel the dweller to safely be able to see, hear, feel and experience the weather first-hand with clarity and intensity as never before while another goal is to find ways to harness wind in this rather harsh environment. Keeping in mind that the site is located at the global epicenter of extreme weather (i.e., “Tornado Alley”), the project will critically examine how to design a safe and resilient modern development (The Kansas Project 2015; see Figure 1-1).

The project objectives listed in Figure 1-1 can be regarded as a sustainability checklist for a modern development. In order to convert this innovative idea to realization, a number of numerical and physical simulations have been applied to connect the weather of Tornado Alley with human sensory experience. In accordance with that, a comprehensive meteorological analysis has been conducted in order to determine the climatology of the site including a wind resource assessment study. These studies are of key importance for designing sustainable and resilient development such as the Kansas Project site. The numerical wind resource assessment study is performed at several spatial scales. It starts at meso-β scales (20-200 km), downscales to meso-γ scales (2-20 km) and goes further to the wind resource assessment for several discrete points (local scales of few meters).

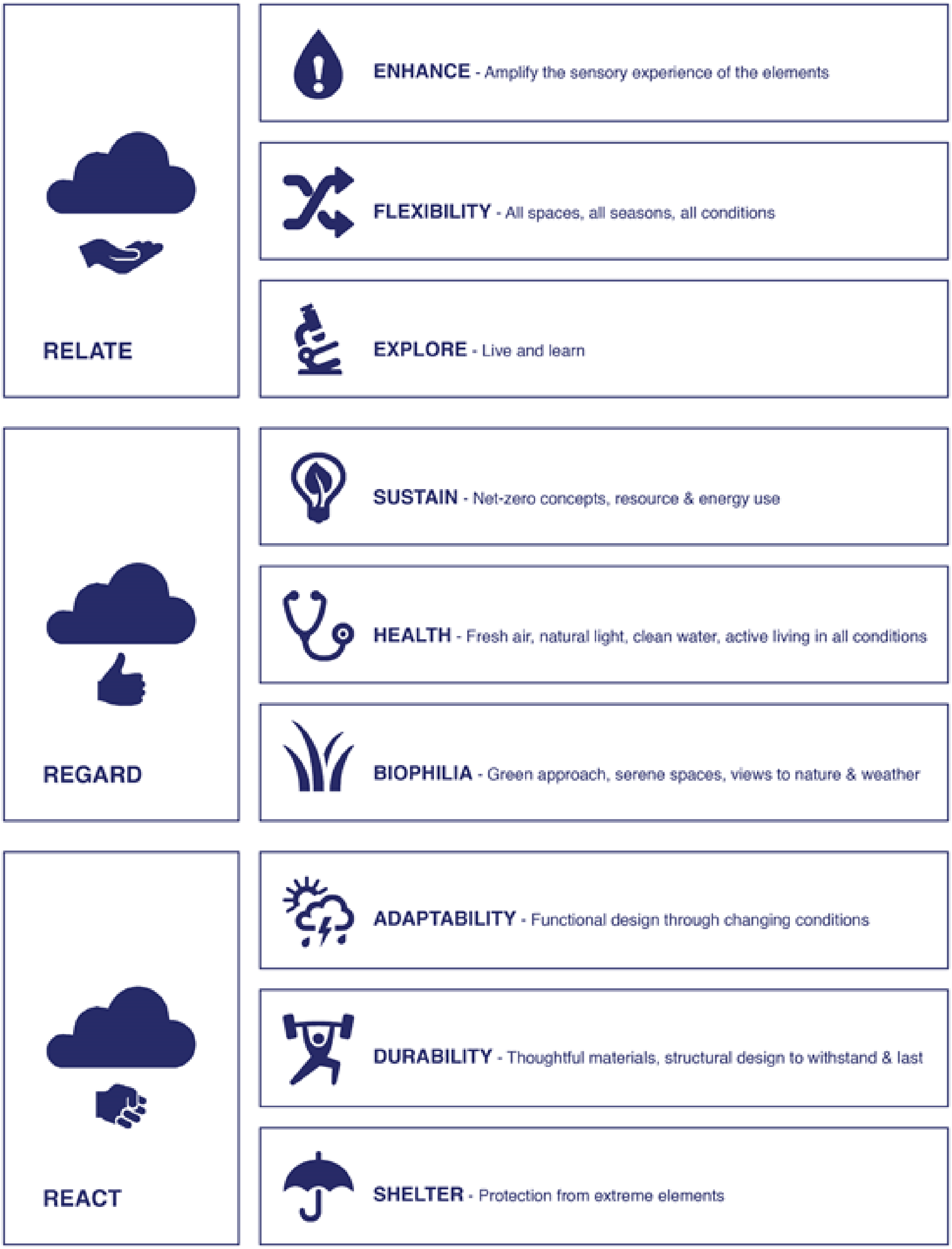

RELATE

ENHANCE - Amplify the sensory experience of the elements

FLEXIBILITY - All spaces, all seasons, all conditions

EXPLORE - Live and learn

REGARD

SUSTAIN - Net-zero concepts, resource & energy use

HEALTH - Fresh air, natural light, clean water, active living in all conditions

BIOPHILIA - Green approach, serene spaces, views to nature & weather

REACT

ADAPTABILITY - Functional design through changing conditions

DURABILITY - Thoughtful materials, structural design to withstand & last

SHELTER - Protection from extreme elements

Figure 1-1. Guiding objectives of the Kansas project. Source: The Kansas Project (2015).

Finally, Chapter VI presents a study primordially related to wind resilience aspects examining the meteorological and physical characteristics of one non-synoptic wind phenomena capable of creating extreme wind speeds – the phenomena of downburst.

As discussed by Solari et al. (2015), it seems there is a gap and a lack of communication between meteorology and its related fields, on one side, and wind engineering as well as other branches of wind-related engineering, on the other side. This lack of interaction is particularly noticeable in the research areas concerning non-synoptic winds. Research presented in this study, once again, tends to be multidisciplinary and multi-scale and therefore aims at connecting large meteorological scales and local field measurements of a downburst that struck the shore of Livorno, Italy, on October 1, 2012. This downburst is selected for several reasons. First, this is one of the very few downbursts that were recorded in the Mediterranean region approaching the land from the sea and therefore which is a rather unique downburst event. While the overall downburst footprint in wind measurements is evident, the anemometer records of this event seem to differ in certain parts from the downburst measurements conducted in the inland parts of United States (Goldman and Sloss 1969, Charba 1974, Wakimoto 1982, Gast and Schroeder 2004, Holmes et al. 2008). Therefore, it is interesting to analyze these differences. Second, this downburst was not coupled with strong background surface winds in the atmosphere, which simplifies the description of this event. Third, the investigation of this downburst is of particular importance for the safety and resilience of Mediterranean ports and cities along the Mediterranean shore (Solari et al. 2012, De Gaetano et al. 2014, Solari et al. 2015a). Thunderstorms in the Mediterranean (and Gulf of Genoa) are very frequent due to large number of cyclones that form in that geographical region. Since downburst are closely related to thunderstorms, these severe wind events are relatively common in the western Mediterranean.

All in all, this research presents a great mix of meteorology and wind engineering disciplines. In many cases, there is a gap between these two fields. In this thesis, an attempt is made to merge these two fields through the multiscale wind modelling approaches. Used data and applied methods cover a multitude of spatial and temporal scales. The applications are in the fields of sustainability and resilience. This relationship between multiscale wind modelling, on one hand, and sustainability and resilience, on the other hand, is investigated examining several specific case studies. In order to maximize the contributions to these fields, three different developments are considered: (1) urban, (2) rural and (3) coastal.

In order to address these subjects, the thesis has five results chapters. The first four chapters containing results are related to wind sustainability and they cover two subjects: (1) urban sustainability and winds (the city of Toronto, Canada) and (2) rural sustainability and winds (a unique development in remote regions of Kansas, United States). The last result chapter in the thesis analyzes the phenomena of downburst. This part is related to the resilience of a coastal city in Italy.

1.2 Urban wind sustainability – literature review

This sub-chapter addresses the overall literature review pertinent to Chapter II, Chapter III and Chapter IV. Specific literature review sections are part of each of these Chapters (papers).

Sustainable urban development is a wide subject that includes economics, social, cultural, environmental, health, and political sciences among others (Girardet 2008, Leon-Garcia et al. 2016). This literature review is limited to wind-related studies in urban environments. The review will include studies on urban wind resource assessment, urban wind climatology, flow dynamics around building-like obstacles, as well as a few applications of weather forecasting in urban environments. Although this doctoral dissertation is focused around urban wind resource assessment and urban climatology, all of the above-listed fields are of direct or indirect importance in urban wind sustainability. Furthermore, many recent studies are interdisciplinary and it is rather difficult to uniquely classify them under a single category.

1.2.1 Dynamics and complexity of flows in urban environments

Flows in urban environments have been historically investigated using field (in situ) measurements as well as multi-scale multi-disciplinary numerical modeling or physical, laboratory simulations.

The first scientifically documented temperature measurements in urban environments are conducted in London by Luke Howard, back in 1818 (Howard 1833). Yet another pioneering endeavored on urban measurements dates back to 1918 and the work of Taylor (1918), who measured the temperature profiles on the Eiffel Tower, Paris, France, in order to compare heat diffusivity between urban and rural environments. In 1946, a first set of measurements of urban turbulence was carried out in Tokyo, Japan (Shiotani and Yamamoto 1949). The goal was to measure the stream-wise velocity and its fluctuations using hot-wire anemometers. Similar measurements were also carried out in Uppsala, Sweden (Högström et al. 1982). Most of the studies from the 1950s to the 1970s investigated the mean properties of the urban boundary layer (Roth 2000). In the following years, the work has mainly been focused around the fluctuating components of wind velocity, urban turbulence, and the interaction between the atmosphere and surface (e.g. Davenport 1967, Sadeh et al. 1971, Raupach et al. 1980, Roth et al. 1989, Cheng and Castro 2002, Rotach et al. 2005, Hicks et al. 2011). An extensive review of urban wind studies with particular emphasis on urban turbulence before 2000 can be found in Roth (2000).

The overall conclusion is that cities strongly affect the upstream boundary layer and result in the development of urban boundary layer (Cermak et al. 2013). The influence is twofold: (1) an abrupt change in aerodynamic roughness and (2) emission of thermal heat. The portion of the urban boundary layer closest to the ground is known as the urban canopy layer. This layer exists between buildings and other obstacles inside urban environments. It directly depends on the geometry, shape and orientation of obstacles, and indirectly on the flow characteristics aloft. The layer is highly turbulent due to the flow separation from buildings and thermal convection. Boundary layer transition from open country to urban boundary layer is depicted in Figure 1-2.

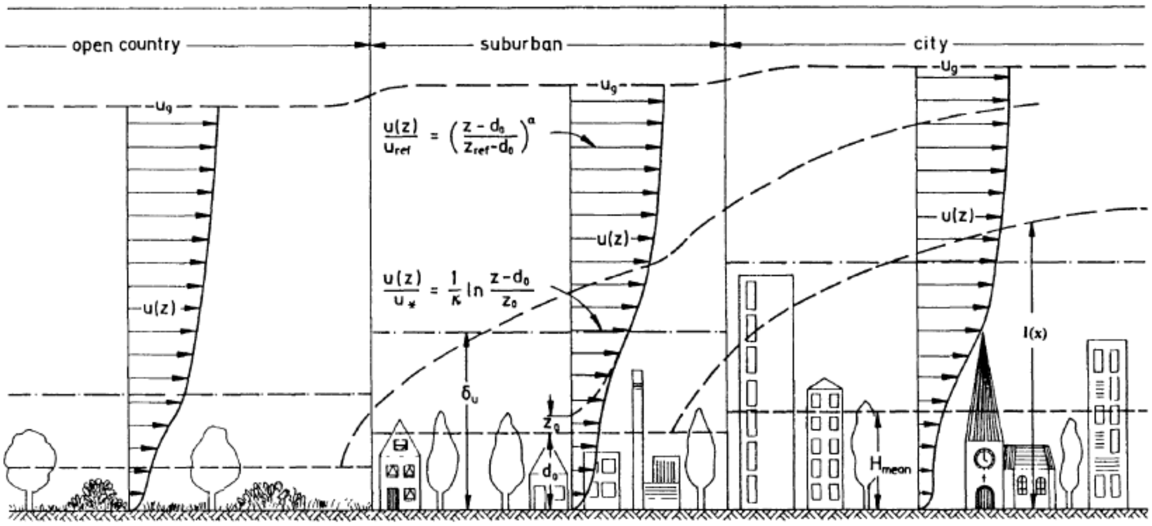

Figure 1-2. The urban boundary layer under neutral atmospheric stratification. Source: (Cermak et al. 2013).

It can be seen that the inner part of the boundary layer is characterized by a logarithmic wind profile, whereas the outer part is best described using the power law. In meteorology, the inner boundary layer is typically defined as the layer in which the wind direction does not change with height. In most wind engineering studies, wind direction dependency on height is not considered and the vertical wind profile is portrayed assuming the constant wind direction. Different models of the mean wind speed profiles over urban-like environments have been analyzed in many studies (Cionco 1965, Garratt 1990, Macdonald 2000, Sabatino et al. 2007, Xie et al. 2008, Zhang et al. 2016). In general, it has been found that an exponential wind profile inside the urban canopy layer is a good representation of the spatially averaged velocity profile in that layer. Similarly, the logarithmic profile is a good representation of the spatially averaged velocity profile in the roughness sublayer and above (Cheng and Castro 2002). Holmes (2007) argues that in strong wind conditions the logarithmic law is the most accurate representation of the wind profile in urban environments. However, this profile is sometimes difficult to implement due to the mathematical limitation of logarithm function (not defined for negative numbers) and therefore the power law is often preferred by wind engineers to avoid some of these problems (Lateb et al. 2016). Holmes (2007) concludes that the power law is quite adequate for engineering purposes. A more detailed description of the vertical structure of the urban boundary layer is provided in Sections 2.1 and 2.4.1 of this document and for a comprehensive discussion on this subject, the reader is referred to Cermak et al. (2013).

Most of these analytical models are developed assuming some kind of ideal form of urban environments (e.g. buildings represented as cubes, regular shapes, staggered, etc.). Urban environments are largely irregular. For that reason, in-situ measurements of urban boundary layer properties are of great importance. Some of the large full-scale measurement campaigns of urban boundary layer characteristics are, for instance, the Regional Air Pollution Study in St. Louis Missouri/Illinois Metropolitan area, United States, (Schiermeir 1978); METROMEX St. Louis, United States, (Auer Jr 1981); Roth and Oke (1995) in Vancouver, BC, Canada; URBAN 2000 and Joint URBAN 2000 in Salt Lake City, Utah, United States, (Allwine et al. 2002, Allwine et al. 2004); the UBL/CLU in Marseille, France (Mestayer et al. 2005); the BUBBLE in Basel City, Switzerland, (Rotach et al. 2005); 3D Wind in northern Indiana, United States, (Barthelmie et al. 2013); Wind and Ports project in several cities along the Mediterranean cost in Italy and France (Solari et al. 2012); and the 2015 Pan Am and Para-Pan Am Legacy Observational Data in Toronto, ON, Canada, (DMF 2016).

For example, the BUBBLE (The Basel UrBan Boundary Layer Experiment) was a year-long experiment that used a variety of measurement techniques (sonic anemometers, sodars, lidars, tethered balloons, etc.) at several locations (urban, suburban and rural sites) to investigate the structure of the urban boundary layer. They found that the mean wind speed profile in the canopy layer (up to the average building height) is rather constant and not exponential as previously documented in theoretical studies. Their values are point measurements (i.e., at few specific locations in city), whereas the theoretical profiles refer to the spatially averaged profile. Interestingly, they detected the exponential profile in a small layer above the average building height. The highest drag coefficient is observed to be around the average building height and the drag coefficient for the flow perpendicular to the canyon is found to be two times larger than for the flow parallel to the canyon. The BUBBLE campaign is interesting since the measurements were conducted not only in highly urban environment, but suburban and rural areas too. In this thesis, urban and rural environments are analyzed and differences in the obtained results are later discussed in the concluding chapter.

Computational studies have gained large popularity in the scientific community in the last several years (Richards and Hoxey 1993, Murakami 1997, Cermak et al. 2013, Rasouli et al. 2014a, Cai et al. 2014, Rasouli et al. 2014b, Aboshosha et al. 2015a, Abdi and Bitsuamlak 2016). Coceal et al. (2007) used highly computationally demanding direct numerical simulations (DNS) to analyze the turbulence statistics over regular arrays of building-like cubes. The spatial variability of the turbulence statistics are shown to be very significant in comparison with their spatial averages within the arrays. They also found that the flow immediately behind a building is considerably more heterogeneous than elsewhere in the canopy. Xie et al. (2008) performed large-eddy simulation (LES) of flow over uniform, but staggered cubes and analyzed the mean and turbulent characteristics of the flow. They noticed that there is a pronounced difference between turbulence characteristics inside the canopy layer and immediately above it. Aboshosha et al. (2015a) developed a new and robust method for modelling the surface roughness combining surface gradient drag and canopy models. They showed that the model is effective at simulating the mean and fluctuating velocity profiles in urban environments. In a very recent study, Liu and Niu (2016) compared performances of Reynolds Averaged Navier-Stokes (RANS), LES and Detached Eddy Simulation (DES) against wind tunnel tests for a case of the wind flow around an isolated building. They showed that the modelled mean velocity profile on the windward side in all three cases was in good agreement with the physical experiments. However, LES and DES performed much better than RANS in the leeward regions of the building.

1.2.2 Urban wind resource assessment

Much of the recent research on urban wind resource has been performed in the United Kingdom (Peacock et al. 2008, Sharpe and Proven 2010, Millward-Hopkins et al. 2012, Weekes and Tomlin 2013). For example, Millward-Hopkins et al. (2013a) mapped the wind speed potential over four major cities in the United Kingdom, which is an improved version of their previous study (Millward-Hopkins et al. 2013b). They concluded that there is a large wind energy potential above Edinburgh, Leeds, Manchester and Nottingham that is currently not exploited. Adam et al. (2016) used the logarithmic profile to predict long-term average wind speed above Leeds, United Kingdom. Surface parameters are derived from high-resolution three-dimensional building data. They identified 51 sites with promising wind potential and showed that at least 75% of the sites showed a positive net pre present value (the difference between the present value of cash inflows and the present value of cash outflows). Emejeamara and Tomlin (2016) introduce a concept of excess energy content in gusty urban winds based on measurements from 8 urban and suburban sites. They used the method to map turbulence intensities and the total kinetic energy available at different heights above Leeds.

In other parts of the world, Mithraratne (2009) evaluated the roof-top wind energy potential of urban houses in New Zealand. Their results show that the potential of wind farms in New Zealand using large turbines is more than 7 times the generating potential of roof-top turbines mounted on urban houses. However, they noticed that the roof-top turbines have a large potential to reduce the energy and carbon footprint of New Zealand electricity. A similar analysis in Singapore has been performed by Karthikeya et al. (2016). Walker (2011) made a review of several methods used for urban wind resource assessment and assessed their performances against full-scale measurements in urban Göteborg, Sweden, (Eliasson et al. 2006). Her findings are mostly negative as she noticed that methods which rely on simple extrapolation from existing large-scale datasets (e.g. Millward-Hopkins et al. (2013a)) are inaccurate. Furthermore, she reported low capacity factors for urban sites and highlighted the importance of accurate power curves of small urban turbines; a subject that has gained large research interest for large scale units, but has not been deeply investigated for urban wind turbines. Using a CFD tool developed particularly for urban wind resource assessment (UrbaWind software) and measure-correlate-predict (MCP) methodology, Kalmikov et al. (2010) analyzed the available wind resources for the Massachusetts Institute of Technology (MIT) campus. Estimated power densities at 20 m above ground for two sites on campus were under-predicted compared to the measurements. Simões and Estanqueiro (2016) performed wind resource assessment for an urban environment proposing a novel concept of urban digital terrain model. In essence, the model treats buildings as orography, hence the name urban digital terrain model. They tested the method for Estoril and São Domingos, Portugal, and found that the maximum discrepancy between their CFD simulations of wind power density and measurements is below 20%. A CFD model is combined with the Wind Atlas Analysis and Application Program (WAsP) in order to evaluate the available wind potential above a warehouse in an urban area of Port-Kennedy, Australia (Tabrizi et al. 2014). The WAsP is used to supply the inlet conditions for CFD. It is important to note here that due to the flow separation from buildings and other nonlinear flow phenomena, linear models (such as WAsP) cannot be used for accurate urban wind simulations (such as it was used in Alcoforado et al. 2009). A review discussion on urban wind resource assessment and related topics such as several proposed concepts for urban wind turbines can be found in Ishugah et al. (2014).

A possibility of coupling numerical weather prediction models with CFD in order to evaluate wind potential in urban environments was investigated by Zajaczkowski et al. (2011). It is difficult to evaluate the precision of their findings as they only made a comparison between the results obtained using coupled models against the mesoscale model. However, it can be said that such methodology is not dependent on the availability of local wind measurements and could easily be applied to any urban site around the world. The integration of Weather Research and Forecasting (WRF) model into urban environments is discussed in Chen et al. (2011). They integrated three urban models of different degrees of sophistication into WRF and tested their performance. Chen and his colleagues pointed out that one of the main goals of such a multiscale modelling approach is to analyze emerging environmental challenges in urban areas. Solazzo et al. (2010) coupled WRF with the urban model of Sabatino et al. (2007), in which the buildings are not explicitly modelled but implicitly introduced as a source of drag on airflow (the model is previously discussed in Section 1.2.1), to investigate the spatially averaged flow characteristics and heat island over Lisbon, Portugal. Their nested simulations were computationally efficient and provided fairly accurate wind and temperature profiles. An interesting approach to model urban areas is proposed by Lundquist et al. (2012). They implemented the immersed boundary algorithm into WRF model and compared their simulations with observations from the Joint URBAN campaign (Allwine et al. 2004; see Section 1.2.1). It is important to mention that they ran WRF in LES mode with one-way nesting in order to provide fully-developed inflow turbulence for the LES domain. The nested Oklahoma City domain had a horizontal resolution of 2 m and a time step of $1/60$ s. Unfortunately, WRF currently does not allow nesting in vertical direction, but the vertical resolution in the parent domain in their simulations was very high (1 m in the first 10 m and 3 m above 150 m above ground). Tewari et al. (2010) also investigated the possibility of coupling WRF and CFD to analyze transport of pollutants in Salt Lake City, Utah, United States. They validated their analysis against the URBAN 2000 measurements (see Section 1.2.1) and found quantifiably good agreement.

A novel approach for the investigation of urban winds is proposed by Romanic and Hangan (2015). Instead of coupling the mesoscale and CFD models, the mesoscale models could be coupled with physical simulators. A 3D physical model of an urban environment can be placed inside the new generation of large multi-fan wind tunnels or 3D and time-dependent testing chambers such as the Wind Engineering, Energy and Environment (WindEEE) Dome (Hangan 2010) at Western University. Then, the incidence wind and turbulence profiles (i.e., profiles at the edge of the urban environment) determined from mesoscale modelling can be physically modeled as inflow conditions. The advantage of the physical micro-scale modeling resides in their demonstrated capacity to simulate a large spectra of flow scales from the top of the urban layer to the level of the detailed flow patterns around buildings and structure. For instance, for wind engineering problems the physical (wind tunnel) simulators are preferred as they can model peak values of both flow and surface pressures which are essential for determining design loads. Furthermore, wind energy, pollution dispersion, pedestrian comfort and any other urban wind environment studies also benefit from the same capacity of reproducing a large spectra of scales. Similar coupling methodology has recently been proposed for the simulation of downbursts (Romanic et al. 2016; see Section 1.3).

Most certainly, the capacity of todays' supercomputers open new possibilities in performing a complete set of multiscale simulations from mesoscale (or even global scales) to the level of buildings in a short period of time. Today, there are many supercomputers installed in all large weather research centers (e.g. NOAA's Weather and Climate Operational Supercomputing System running on 3748 nodes with 84512 cores and 8.124

PB of storage (NCEP 2016)), as well as on university networks (e.g. SHARCNET: https://www.sharcnet.ca). The result of combining mesoscale and microscale simulations is the capacity of providing wind and other meteorological fields at the micro-level of buildings and their components in hours. This advancement opens the possibility of adaptation of cities both from a sustainability and resilience perspective.

1.2.3 Urban climatology

Although urban climatology in general terms and urban weather forecasting are not the main focus of this research, these topics are quintessential from the urban sustainability and resilience points of view and therefore they deserve a brief review in this dissertation.

A recent review of urban climatology studies can be found in Mills (2014). According to Mills (2014), approaches to study urban climate can be chronologically categorized into 6 groups (Figure 1-3).

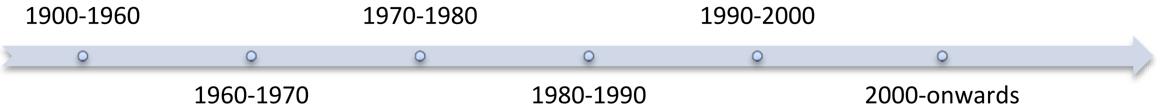

Figure 1-3. Timeline of phases characterized with different approaches to study urban climate; after Mills (2014).

Measurements of basic meteorological variables (e.g. temperature, wind, humidity) and their traditional interpretation had been the main approach used to represent urban climate in the period before the 1960s (see also Section 1.2.1). In the following approximately 10 years (1960-1970), there was a shift toward measurements of fluxes such as radiation, sensible and latent heat exchanges. Statistical methods were used to analyze and present data. Application of conventional micrometeorological theories to urban climates, such as the Monin-Obukhov similarity theory (Monin and Obukhov 1954), as well as use of energy budget concept is introduced in the period 1970-1980. This era is also important because of the first use of computer modelling techniques in urban studies. In the period 1980-1990, experimental studies of common urban features such as idealized urban canyons gained popularity. This decade is the time period when the wind tunnel scaled-physical models were used to investigate wind flows in urban environments. For example, Wind Tunnel II of the Boundary Layer Wind Tunnel Laboratory (BLWTL) at Western University (formerly the University of Western Ontario) was constructed in 1984 and used in a number of research and commercial projects. The last decade of the 20th century is the period when the real urban forms started to be tested in both computer models and wind tunnels. This period also saw a significant increase in the number of published research papers. After 2000, mesoscale numerical weather prediction models (e.g. WRF) are coupled with urban microscale models in order to investigate urban climatology at different scales. The emphasis is put on real urban areas and new observing technologies and techniques (e.g. Grimmond et al. 2010, Krayenhoff and Voogt 2010, Chen et al. 2012). This is also the time period when some of the new-generation of modern wind simulators were built with the goal to examine urban climate (e.g. WindEEE Dome, “Wall of Wind” at the Florida International University, etc.). The subject of urban climatology including a number of individual case studies and the background theory can be found in Hutchison (2010) and Ng and Ren (2015).

1.3 Urban resilience and downbursts – literature review

Downbursts are vigorous downdrafts of cold air originating from thunderstorms which upon reaching the ground create high-intensity diverging winds. A schematic drawing of an idealized downburst is depicted in Figure 1-4. Downbursts can come in various sizes, including very intense small ones called microbursts. Damaging winds in microbursts extend up to approximately 4 km in horizontal direction. Individual microbursts are a short-lived phenomenon, with a typical duration of less than 20 minutes.

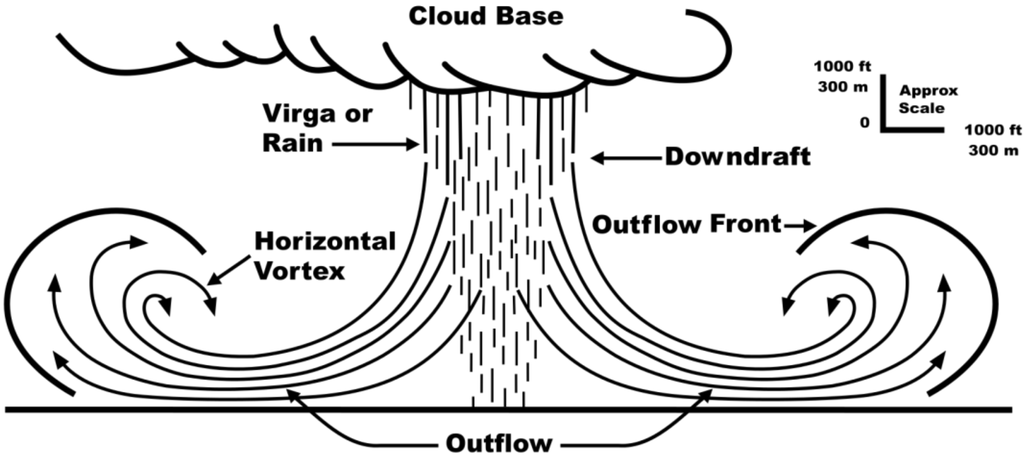

Figure 1-4. Schematic of a cross-section of a downburst. Source: Modified by the Federal Aviation Administration (ed. D. C. Beaudette) after Fujita (1985).

Microbursts are typically associated with very strong thunderstorms, i.e., cumulonimbus clouds. Wet microbursts occur in the portion of a thunderstorm containing the heaviest rain (Atkins and Wakimoto 1991). Dry microbursts, on the other hand, are not coupled with precipitation, they typically occur in high plains and desert areas, and are not necessarily produced in thunderstorms (Wakimoto 1985). Note that virga (Figure 1-4) is precipitation that evaporates before reaching the ground. Dry downbursts can appear together with virga.

Microbursts are dangerous because of their high intensities and difficulty in predicting them. The downdraft of a microburst is typically concentrated in an area of less than 1.5 km in diameter. Localized horizontal outbursts sometimes exceed 75 m s^{-1}. According to Wakimoto (1982), a downburst evolves through four main stages: (1) formative, (2) early mature, (3) late mature and (4) dissipative.

From a historical perspective, downbursts were first investigated after several commercial air plane crashes in the 1970s (Fujita 1976, Fujita 1981, Fujita 1985). Since then, the investigation of downbursts has been carried out through field measurements (e.g. Hjelmfelt 1988, Kareem and Fujita 1990, Solari et al. 2012, Gunter and Schroeder 2015), numerical simulations (e.g. Knupp 1989, Kim and Hangan 2007, Anabor et al. 2011, Orf et al. 2012, Sim et al. 2016) and wind tunnel experiments (e.g. Letchford et al. 2002, Xu and Hangan 2008). Analytical models of downbursts have also been developed (e.g. Oseguera and Bowles 1988, Vicroy 1991, Holmes and Oliver 2000). Although much progress has been made in understanding downbursts since the 1970s, there are still many aspects of the phenomena which are unknown at the present. Compared to the number of articles addressing other severe weather events associated with thunderstorm clouds, the body of literature on downbursts is most scarce. For example, in August of 2016, Google Scholar lists more than 300,000 articles on the subject of tornados, beyond 900,000 studies on lightning, and only 6,150 papers on downbursts. For sure, downbursts are not about 50 times less frequent or important than tornadoes, as literature might suggest. On the contrary, downbursts are more common than tornados. This discrepancy is most likely caused by the fact that tornadoes and lightning are easier to visually observe, when compared to downbursts which are usually “camouflaged” behind the storm front and do not have a pronounced visual appearance (at least to an untrained eye). Recall that downbursts were not even known as a meteorological phenomenon until the 1970s.

There are not many studies addressing the specific subject of urban resilience and downburst winds. For that reason, certain characteristics of downbursts which might be of importance for urban resilience will be discussed in this section. A brief historical retrospective of downburst-related research led by Prof. Theodore Fujita and the main feature of this non-synoptic phenomenon are given in Section 1.1. Urban resilience incorporates atmospheric science, engineering and socio and economic aspects. Meteorological and engineering studies on urban resilience will be reviewed herein.

Full-scale measurement campaigns of downburst winds in urban environments, such as the European project “Wind and Ports” (Solari et al. 2012), contributed largely to the understanding of potential effects of downbursts in urban areas. Keeping in mind that this measurement campaign is still on-going and the dataset of anemometric measurements is growing, many studies in the future will use these data to investigate downburst winds. Wind-excited response of structures are of particular importance for urban resilience. Recently, Solari et al. (2015b) and Solari (2016) developed a response spectrum technique to calculate the downburst-excited response of structures. A summary of the procedure is as follows. Firstly, the wind velocity of downburst record is decomposed into the sum of a slowly-varying mean part and a remaining fluctuation. The fluctuation represents a non-stationary random process. Secondly, the fluctuation is decomposed into slowly varying standard deviation and a reduced turbulence component, which is represented as a rapidly varying stationary Gaussian random process with a zero mean and a standard deviation of one. Solari et al. (2015b) demonstrated that downburst duration, turbulence intensity of surface winds, the power spectral density, and the integral length scale are relevant characteristics of downburst winds to the loading of structures.

There are few detailed full-scale observations of downburst winds (e.g. Holmes et al. 2008, Gunter and Schroeder 2015) reported wind profile measurements from three downbursts obtained using a novel dual-Doppler wind profile technique. A large complexity of outflow structure was noted. Namely, they observed large variations between outflows of different events. The differences are probably due to the highly transient nature of the phenomena, which makes it difficult to compare the outflows in the same development stage of the storm.

When it comes to numerical modelling of downbursts, three conceptually different numerical approaches are used in literature. First, cloud models use the set of dynamics and thermodynamics equations to resolve flow dynamics and microphysical processes within and outside the parent cloud (e.g. Knupp 1989, Proctor and Bowles 1992, Straka and Anderson 1993, Orf et al. 2012). Using this approach, Knupp (1989) demonstrated that commencement of the downdraft in the cloud is associated with the precipitation initiation and the advection. The environmental wind shear also plays an important role. Orf et al. (2012) showed that wind gusts in the starburst near the surface are short lived and as such, not likely to be captured by meteorological radars. However, the exact physical processes behind these pronounced wind speed fluctuations are still unknown. Although these models are the closest representation of real downburst, they are computationally expensive, have limited resolution near the surface, and thus unaffordable for many practical applications.

Sub-cloud models represent the second approach for the numerical investigation of downbursts. These models initiate the downburst as a negatively buoyant downdraft without explicitly modeling the parent cloud (e.g. Orf and Anderson 1999, Mason et al. 2009, Anabor et al. 2011). Instead of simulating many complex physical processes inside the cloud, the sub-cloud models typically use some kind of analytical function to represent the spatial and time characteristics of the negatively buoyant downburst source. This numerical approach significantly reduces the computational time in comparison to the cloud models since a large number of thermodynamic processes and the highly turbulent cloud environment are not modeled. Using this approach, Mason et al. (2010) investigated the influence of topography on the starburst winds and Orf et al. (1996) and Orf and Anderson (1999) analyzed the colliding and traveling downbursts, respectively. It has been noticed that due to inability to properly scale Froude number (Zhang et al. 2013, Orf et al. 2014), the results obtained using cloud and sub-cloud models are difficult to physically reproduce in test chambers (Alahyari and Longmire 1994). This issue might be resolved in the new generation of wind testing chambers, such as WindEEE Dome at Western University where downbursts can be physically generated at the sales of about 1:200.

The third class of models are the impinging jet downburst models (e.g. Nicholls et al. 1993, Letchford and Chay 2002, Kim and Hangan 2007, Aboshosha et al. 2015b, Sim et al. 2016). This concept was originally proposed by Fujita (1985). The downdraft in impinging jet models is initiated as a circular jet flowing downwards from a cylinder placed at some height above the ground. Kim and Hangan (2007) noticed that the maximum velocities are found in a zone that is less than 0.05 jet diameters from the surface immediately after the touchdown of the main ring-vortex. They related their numerical results to wind loading on structures which is of particular importance for urban resilience. A comparison of impinging jet methods using k-ε, k-ω and LES turbulence models and their performance against physical experiments are investigated by Sengupta and Sarkar (2008). They concluded that LES and realizable k-ε models provided the best match with experimental data. Aboshosha et al. (2015b) used LES to study turbulent characteristics of downburst winds above several land covers synthetically generated using the method of fractal surfaces (Aboshosha et al. 2015a). They found that vertical length scales are smaller than the circumferential length scales (which are 9 times the jet diameter), whereas the radial length scales are similar to the jet diameter. Turbulent characteristics of downburst winds are of particular importance for urban resilience and wind loading. According to full-scale measurements by Gunter and Schroeder (2015), the mean outflow profiles seem to go through a transition from being uniform to an impinging jet shape over the course of 1 minute.

A new approach for coupling an analytical model of downburst winds with a physical simulator capable of reproducing non-synoptic winds has recently been proposed by Romanic et al. (2016a). The main application of the methodology is the improvement of resilience of cities to sustain severe winds. A modified version of an analytical model of downburst winds is considered. The physical simulator considered in their study is the WindEEE Dome at Western University. In the first step, an existing analytical model (Chay et al. 2006) is adapted to reconstruct a downburst event and the main flow parameters are obtained (e.g. jet diameter, maximum radial velocity, the height of the maximum radial velocity and its distance from the jet center). In the second step, these parameters are used to set up the physical simulations of downburst in WindEEE Dome. Lastly, the scaled model of an urban environment can be placed inside the testing chamber and the downburst effects on the urban environment can be evaluated. Several applications of the proposed coupled method can be envisaged. The methodology can be used to investigate and provide improvements to the resistance of cities, city blocks and individual buildings and structures to severe thunderstorm winds. It could be used to investigate the propagation of surface downburst winds over various roughness of the underlying urban surfaces and therefore help define and improve numerical parametrization of surface thunderstorm wind fields.

1.4 Objectives and motivations

This thesis is an attempt to tackle some of the knowledge gaps related to wind sustainability and wind resilience. Most of these gaps are either at the interface between scales of motion or at the interface between traditional disciplines of atmospheric science and wind engineering. Therefore the thesis attempts to address from a multi-scale perspective aspects related to urban sustainability (Chapter II to Chapter IV), new non-urban development mixed sustainability and resilience aspects (Chapter V) as well as coastal-urban resilience aspects related to storm events (Chapter VI).

Cities are growing in size in all parts of the world. Percentage of urban dwellers is high in economically developed countries (80-90%), whereas the urbanization process is currently pronounced in the developing countries where people are increasingly migrating from rural areas into cities. The main motivation for this study is to conduct research that will contribute to urban sustainability and resilience. Being home for more than 50% of people, modern cities must strive to be more sustainable and resilient, especially in the framework of the on-going climate change. Sustainability and resilience are interdisciplinary fields. Meteorological analyses in this study are multiscale, spanning from the regional and mesoscales to the local scales. They rely on field measurements from weather stations and high-precision measurement masts, mesoscale meteorological simulations as well as reanalysis data. Even astrophysical measurements of solar activity (i.e., sunspots) are included retrieved and used. Engineering analysis relates mostly to the surface layer both in terms of resilience (wind engineering) and sustainability (wind energy) and relies on a different set of micro-scale simulations (CFD and WAsP), analytical models or physical simulations (wind tunnels) correlated with surface measurements such as meteorological towers and anemometers. A great motivation for this study was also to present high-quality research based on variety of input data. Moreover, the research is conducted using a variety of computational tools (e.g. CFD, WAsP, analytical models).

This thesis research work has also practical applications for sectors such as urban planning, wind energy, air quality, pedestrian comfort, sea transportation, to mention few. The imminent applications of this research are presented in Chapter II and Chapter V. The results can be used to assess sustainability of analyzed urban developments. Furthermore, there was a high motivation to conduct this research in such a way that can be directly implemented into commercial projects such as the Kansas Project (Chapter V). Distinct practical applications are discussed in the other three result chapters of this thesis.

Pioneering work on urban wind resource assessment in changing climate and a possible link between winds at regional scales and solar activity are expected to be further investigated by many researchers in these fields. The examination of downburst data collected in several Mediterranean cities ("Wind and Ports" project (Solari et al. 2012)) will continue in the future and the methodology for their analysis is presented in Chapter VI.

The specific objectives of this study are:

- Sustainability
    - To develop a new methodology for urban wind modelling combining wind atlas data and a CFD tool.
    - To analyze long-term trends of urban winds using globally available reanalysis data.
    - To develop the first methodology for urban wind modelling under changing climate.
    - To design a research framework and conduct a wind sustainability study of a modern self-sustainable development in a remote area.
- Resilience
    - To combine wind engineering practice and meteorological analysis in order to investigate the spatiotemporal characteristics of a severe downburst event.

1.5 Organization of the thesis

This thesis is written in the "integrated article" format as specified by the Faculty of Graduate Studies at Western University.

Chapter I provides a general introduction to the subject of wind sustainability and resilience. Comprehensive literature review on studies covering a wide range of sustainability- and resilience- related topics is given in Sections 1.2 and 1.3, respectively. These sections highlight the current progress in the wind sustainability and resilience topics. The introductory section also contains the main objectives and motivation for conducting this research. Chapter II presents a wind sustainability analysis of an urban block in downtown Toronto. The main features of urban boundary layer (e.g. flow separation, channeling effects) are also discussed. Chapter III contains detailed wind climatology of Toronto calculated based on a reanalysis dataset. Building up on the results from the previous two chapters, Chapter IV investigates the urban wind flows above Toronto in a changing climate. Chapter V is a wind sustainability analysis of a modern development situated in "Tornado Alley" (Central South Kansas, United States). Wind climatology and wind resource assessment studies are performed on the measurements obtained from the nearby automated weather station. Chapter VI describes the meteorological characteristics at different scales of a downburst event that struck Livorno, Italy, on October 1, 2012. Furthermore, the same chapter provides the main transient wind statistics of this downburst event that are of importance for wind-excited response of structures. This chapter, therefore, addresses the subject of wind resilience. At the end, conclusions, contributions and recommendations for future research are provided in Chapter VII

References

Abdi, D. S., and G. T. Bitsuamlak, 2016: Wind flow simulations in idealized and real built environments with models of various level of complexity. *Wind and Structures*, **22**, 503–524, doi:10.12989/was.2016.22.4.503.

Aboshosha, H., G. Bitsuamlak, and A. E. Damatty, 2015a: LES of ABL flow in the built-environment using roughness modeled by fractal surfaces. *Sustainable Cities and Society*, **19**, 46–60, doi:10.1016/j.scs.2015.07.003.

——, ——, and A. El Damatty, 2015b: Turbulence characterization of downbursts using LES. *Journal of Wind Engineering and Industrial Aerodynamics*, **136**, 44–61, doi:10.1016/j.jweia.2014.10.020.

——, A. Elawady, A. El Ansary, and A. El Damatty, 2016: Review on dynamic and quasi-static buffeting response of transmission lines under synoptic and non-synoptic winds. *Engineering Structures*, **112**, 23–46, doi:10.1016/j.engstruct.2016.01.003.

Adam, K., V. Hoolohan, J. Gooding, T. Knowland, C. S. E. Bale, and A. S. Tomlin, 2016: Methodologies for city-scale assessment of renewable energy generation potential to inform strategic energy infrastructure investment. *Cities*, **54**, 45–56, doi:10.1016/j.cities.2015.10.015.

Alahyari, A., and E. K. Longmire, 1994: Particle image velocimetry in a variable density flow: application to a dynamically evolving microburst. *Experiments in Fluids*, **17**, 434–440, doi:10.1007/BF01877047.

Alcoforado, M.-J., H. Andrade, A. Lopes, and J. Vasconcelos, 2009: Application of climatic guidelines to urban planning: The example of Lisbon (Portugal). *Landscape and Urban Planning*, **90**, 56–65, doi:10.1016/j.landurbplan.2008.10.006.

Allwine, K. J., J. H. Shinn, G. E. Streit, K. L. Clawson, and M. Brown, 2002: Overview of URBAN 2000: A multiscale field study of dispersion through an urban environment. *Bulletin of American Meteorological Society*, **83**, 521–536, doi:10.1175/1520-0477(2002)083<0521:OOUAMF>2.3.CO;2.

Allwine, K. J., M. J. Leach, L. W. Stockham, J. S. Shinn, R. P. Hosker, J. F. Bowers, and J. C. Pace, 2004: Joint urban 2003: study overview and instrument locations. *Symposium on Planning, Nowcasting, and Forecasting in the Urban Zone*, Seattle, Pacific Northwest National Laboratory Oak Ridge.

Anabor, V., U. Rizza, E. L. Nascimento, and G. A. Degrazia, 2011: Large-eddy simulation of a microburst. *Atmospheric Chemistry and Physics*, **11**, 9323–9331, doi:10.5194/acp-11-9323-2011.

Atkins, N. T., and R. M. Wakimoto, 1991: Wet microburst activity over the southeastern United States: Implications for forecasting. *Weather and Forecasting*, **6**, 470–482, doi:10.1175/1520-0434(1991)006<0470:WMAOTS>2.0.CO;2.

Auer Jr, A. H., 1981: Urban Boundary Layer. Metromex: A review and summary, S.A. Changnon, Ed., *Meteorological Monographs*, American Meteorological Society, 41–62 http://link.springer.com/chapter/10.1007/978-1-935704-29-4_3 (Accessed August 29, 2016).

Barthelmie, R. J., and Coauthors, 2013: 3D Wind and turbulence characteristics of the atmospheric boundary layer. *Bulletin of American Meteorological Society,* **95**, 743–756, doi:10.1175/BAMS-D-12-00111.1.

Cai, X., Q. Huo, L. Kang, and Y. Song, 2014: Equilibrium atmospheric boundary-layer flow: Computational fluid dynamics simulation with balanced forces. *Boundary-Layer Meteorology*, **152**, 349–366, doi:10.1007/s10546-014-9928-0.

Cermak, J. E., A. G. Davenport, E. J. Plate, and D. X. Viegas, 2013: *Wind climate in cities*. Springer Science & Business Media, 767 pp.

Charba, J., 1974: Application of gravity current model to analysis of squall-line gust front. *Monthly Weather Review*, **102**, 140–156, doi:10.1175/1520-0493(1974)102<0140:AOGCMT>2.0.CO;2.

Chay, M. T., F. Albermani, and R. Wilson, 2006: Numerical and analytical simulation of downburst wind loads. *Engineering Structures*, **28**, 240–254, doi:10.1016/j.engstruct.2005.07.007.

Chen, F., and Coauthors, 2011: The integrated WRF/urban modelling system: development, evaluation, and applications to urban environmental problems. *International Journal of Climatology,* **31**, 273–288, doi:10.1002/joc.2158.

——, and Coauthors, 2012: Research priorities in observing and modeling urban weather and climate. *Bulletin of American Meteorological Society*, **93**, 1725–1728, doi:10.1175/BAMS-D-11-00217.1.

Cheng, H., and I. P. Castro, 2002: Near wall flow over urban-like roughness. *Boundary-Layer Meteorology*, **104**, 229–259, doi:10.1023/A:1016060103448.

Cionco, R. M., 1965: A mathematical model for air flow in a vegetative canopy. Journal of Applied Meteorology, **4**, 517–522, doi:10.1175/1520-0450(1965)004<0517:AMMFAF>2.0.CO;2.

Coceal, O., T. G. Thomas, and S. E. Belcher, 2007: Spatial variability of flow statistics within regular building arrays. *Boundary-Layer Meteorology*, **125**, 537–552, doi:10.1007/s10546-007-9206-5.

Davenport, A., 1967: Instrumentation and measurements of wind speed spectra in a city. *Proceedings of the first Canadian conference on micrometeorology: Part 2, The first Canadian conference on micrometeorology*, Toronto, On, Canada, Meteorological Service of Canada, 361–386.

De Gaetano, P., M. P. Repetto, T. Repetto, and G. Solari, 2014: Separation and classification of extreme wind events from anemometric records. *Journal of Wind Engineering and Industrial Aerodynamics*, **126**, 132–143, doi:10.1016/j.jweia.2014.01.006.

Delucchi, M. A., and M. Z. Jacobson, 2011: Providing all global energy with wind, water, and solar power, Part II: Reliability, system and transmission costs, and policies. *Energy Policy*, **39**, 1170–1190, doi:10.1016/j.enpol.2010.11.045.

DMF, 2016: 2015 Pan Am and Para-Pan Am legacy observational data - product user guide. http://donnees.ec.gc.ca/data/weather/monitor/to2015-pan-and-parapan-american-games-atmospheric-monitoring-observations/Product_User_Guide/Product%20User%20Guide.pdf (Accessed August 29, 2016).

Eliasson, I., B. Offerle, C. S. B. Grimmond, and S. Lindqvist, 2006: Wind fields and turbulence statistics in an urban street canyon. *Atmospheric Environment*, **40**, 1–16, doi:10.1016/j.atmosenv.2005.03.031.

Emejeamara, F. C., and A. S. Tomlin, 2016: A method for mapping the turbulence intensity and excess energy available to building mounted wind turbines over a UK City. *Wind Energy*, **19**, 1423–1438, doi:10.1002/we.1928.

Flint, L. E., and A. L. Flint, 2012: Downscaling future climate scenarios to fine scales for hydrologic and ecological modeling and analysis. *Ecological Processes*, **1**, 2, doi:10.1186/2192-1709-1-2.

Fowler, H. J., S. Blenkinsop, and C. Tebaldi, 2007: Linking climate change modelling to impacts studies: recent advances in downscaling techniques for hydrological modelling. *International Journal of Climatology*, **27**, 1547–1578, doi:10.1002/joc.1556.

Fujita, T. T., 1976: *Spearhead echo and downburst near the approach end of a John F. Kennedy Airport runway, New York City*. Chicago University; Department of Geophysical Sciences, Chicago, IL, United States, http://ntrs.nasa.gov/search.jsp?R=19760014753 (Accessed January 7, 2016).

Fujita, T. T., 1981: Tornadoes and downbursts in the context of generalized planetary scales. *Journal of Atmospheric Science*, **38**, 1511–1534, doi:10.1175/1520-0469(1981)038<1511:TADITC>2.0.CO;2.

Fujita, T. T., 1985: *The downburst: microburst and macroburst*. *Satellite and Mesometeorology Research Project*, Department of the Geophysical Sciences, University of Chicago, Chicago, IL, United States, 136 pp.

Garratt, J. R., 1990: The internal boundary layer — A review. *Boundary-Layer Meteorology*, **50**, 171–203, doi:10.1007/BF00120524.

Gast, K. D., and S. Schroeder, 2004: Extreme wind events observed in the 2002 Thunderstorm Outflow Experiment. *22nd Conference on Severe Local Storms, 11th Conference on Aviation, Range, and Aerospace and the 22nd Conference on Severe Local Storms*, Boston, United States, American Meteorological Society https://ams.confex.com/ams/11aram22sls/webprogram/22SLS.html (Accessed July 30, 2016).

Girardet, H., 2008: *Cities people planet: urban development and climate change*. 2 edition. Wiley, Chichester ; New York, 328 pp.

Goldman, J. L., and P. Sloss, 1969: Structure of the leading edge of thunderstorm cold-air outflow. http://ntrs.nasa.gov/search.jsp?R=19700042459 (Accessed July 31, 2016).

Grimmond, C. S. B., and Coauthors, 2010: Climate and more sustainable cities: Climate information for improved planning and management of cities (producers/capabilities perspective). *Procedia Environmental Sciences*, **1**, 247–274, doi:10.1016/j.proenv.2010.09.016.

Gunter, W. S., and J. L. Schroeder, 2015: High-resolution full-scale measurements of thunderstorm outflow winds. *Journal of Wind Engineering and Industrial Aerodynamics*, **138**, 13–26, doi:10.1016/j.jweia.2014.12.005.

GWEC, 2016: Market forecasts | gwec. *Market forecast for 2016-2020*. http://www.gwec.net/global-figures/market-forecast-2012-2016/ (Accessed August 26, 2016).

Hangan, H., 2010: Current and future directions for wind research at Western: A new quantum leap in wind research through the Wind Engineering, Energy and Environment (WindEEE) Dome. *Wind Engineers, JAWE*, **35**, 277–281, doi:10.5359/jawe.35.277.

Harris, L. M., and D. R. Durran, 2010: An idealized comparison of one-way and two-way grid nesting. Monthly Weather Review., 138, 2174–2187, doi:10.1175/2010MWR3080.1.

Hathaway, D. H., R. M. Wilson, and E. J. Reichmann, 1994: The shape of the sunspot cycle. *Solar Physics*, **151**, 177–190, doi:10.1007/BF00654090.

Hicks, B. B., W. J. Callahan, W. R. Pendergrass, R. J. Dobosy, and E. Novakovskaia, 2011: Urban turbulence in space and in time. *Journal of Applied Meteorology and Climatology*, **51**, 205–218, doi:10.1175/JAMC-D-11-015.1.

Hjelmfelt, M. R., 1988: Structure and life cycle of microburst outflows observed in Colorado. *Journal of Applied Meteorology and Climatology*, **27**, 900–927, doi:10.1175/1520-0450(1988)027<0900:SALCOM>2.0.CO;2.

Högström, U., H. Bergström, and H. Alexandersson, 1982: Turbulence characteristics in a near neutrally stratified urban atmosphere. *Boundary-Layer Meteorology*, **23**, 449–472, doi:10.1007/BF00116272.

Holmes, J. D., 2007: *Wind Loading of Structures*. CRC Press, 444 pp.

Holmes, J. D., and S. E. Oliver, 2000: An empirical model of a downburst. *Engineering Structures*, **22**, 1167–1172, doi:10.1016/S0141-0296(99)00058-9.

Holmes, J. D., H. M. Hangan, J. L. Schroeder, C. W. Letchford, and K. D. Orwig, 2008: A forensic study of the Lubbock-Reese downdraft of 2002. *Wind and Structures,* **11**, 137–152, doi:10.12989/was.2008.11.2.137.

Howard, L., 1833: *The climate of London*. http://www.urban-climate.org/documents/LukeHoward_Climate-of-London-V1.pdf (Accessed November 4, 2016).

Hutchison, R., 2010: *Encyclopedia of urban studies*. SAGE Publications, Inc., 2455 Teller Road, Thousand Oaks California 91320 United States, http://sk.sagepub.com/reference/urbanstudies (Accessed August 30, 2016).

Ishugah, T. F., Y. Li, R. Z. Wang, and J. K. Kiplagat, 2014: Advances in wind energy resource exploitation in urban environment: A review. *Renewable and Sustainable Energy Reviews*, **37**, 613–626, doi:10.1016/j.rser.2014.05.053.

Jacobson, M. Z., and M. A. Delucchi, 2011: Providing all global energy with wind, water, and solar power, Part I: Technologies, energy resources, quantities and areas of infrastructure, and materials. *Energy Policy*, **39**, 1154–1169, doi:10.1016/j.enpol.2010.11.040.

Kalmikov, A., G. Dupont, K. Dykes, and C. Chan, 2010: Wind power resource assessment in complex urban environments: MIT campus case-study using CFD analysis. *AWEA 2010 WINDPOWER Conference*, Dallas, USA, 1–28 http://people.csail.mit.edu/cychan/papers/awea10-ra.pdf (Accessed August 29, 2016).

Kalnay, E., and Coauthors, 1996: The NCEP/NCAR 40-year reanalysis project. *Bulletin of the American Meteorological Society*, **77**, 437–471, doi:10.1175/1520-0477(1996)077<0437:TNYRP>2.0.CO;2.

Kareem, A., and T. Theodore Fujita, 1990: The Sixth U.S. National Conference on Wind Engineering Downbursts: meteorological features and wind field characteristics.

Journal of Wind Engineering and Industrial Aerodynamics, **36**, 75–86, doi:10.1016/0167-6105(90)90294-M.

Karthikeya, B. R., P. S. Negi, and N. Srikanth, 2016: Wind resource assessment for urban renewable energy application in Singapore. *Renewable Energy*, **87**, **Part 1**, 403–414, doi:10.1016/j.renene.2015.10.010.

Kim, J., and H. Hangan, 2007: Numerical simulations of impinging jets with application to downbursts. *Journal of Wind Engineering and Industrial Aerodynamics*, **95**, 279–298, doi:10.1016/j.jweia.2006.07.002.

Knupp, K. R., 1989: Numerical simulation of low-level downdraft initiation within precipitating cumulonimbi: some preliminary results. *Monthly Weather Review*, **117**, 1517–1529, doi:10.1175/1520-0493(1989)117<1517:NSOLLD>2.0.CO;2.

Krayenhoff, E. S., and J. A. Voogt, 2010: Impacts of urban albedo increase on local air temperature at daily–annual time scales: Model results and synthesis of previous work. *Journal of Applied Meteorology and Climatology*, **49**, 1634–1648, doi:10.1175/2010JAMC2356.1.

Lateb, M., R. N. Meroney, M. Yataghene, H. Fellouah, F. Saleh, and M. C. Boufadel, 2016: On the use of numerical modelling for near-field pollutant dispersion in urban environments − A review. *Environmental Pollution*, **208**, **Part A**, 271–283, doi:10.1016/j.envpol.2015.07.039.

Leon-Garcia, A., and Coauthors, 2016: Smart City 360°, *First EAI International Summit, Smart City 360°*, Bratislava, Slovakia and Toronto, Canada, October 13-16, 2015. Revised Selected Papers. Springer, 946 pp.

Letchford, C. W., and M. T. Chay, 2002: Pressure distributions on a cube in a simulated thunderstorm downburst. Part B: moving downburst observations. *Journal of Wind Engineering and Industrial Aerodynamics*, **90**, 733–753, doi:10.1016/S0167-6105(02)00163-0.

——, C. Mans, and M. T. Chay, 2002: Thunderstorms—their importance in wind engineering (a case for the next generation wind tunnel). *Journal of Wind Engineering and Industrial Aerodynamics*, **90**, 1415–1433, doi:10.1016/S0167-6105(02)00262-3.

Liu, J., and J. Niu, 2016: CFD simulation of the wind environment around an isolated high-rise building: An evaluation of SRANS, LES and DES models. *Building and Environment*, **96**, 91–106, doi:10.1016/j.buildenv.2015.11.007.

Lundquist, K. A., F. K. Chow, and J. K. Lundquist, 2012: An immersed boundary method enabling large-eddy simulations of flow over complex terrain in the WRF model. *Monthly Weather Review*, **140**, 3936–3955, doi:10.1175/MWR-D-11-00311.1.

Macdonald, R. W., 2000: Modelling the mean velocity profile in the urban canopy layer. *Boundary-Layer Meteorology*, **97**, 25–45, doi:10.1023/A:1002785830512.

Mandal, S., R. K. Srivastav, and S. P. Simonovic, 2016: Use of beta regression for statistical downscaling of precipitation in the Campbell River basin, British Columbia, Canada. *Journal of Hydrology*, **538**, 49–62, doi:10.1016/j.jhydrol.2016.04.009.

Mason, M. S., G. S. Wood, and D. F. Fletcher, 2009: Numerical simulation of downburst winds. *Journal of Wind Engineering and Industrial Aerodynamics*, **97**, 523–539, doi:10.1016/j.jweia.2009.07.010.

——, ——, and ——, 2010: Numerical investigation of the influence of topography on simulated downburst wind fields. *Journal of Wind Engineering and Industrial Aerodynamics*, **98**, 21–33, doi:10.1016/j.jweia.2009.08.011.

Mengelkamp, H.-T., H. Kapitza, and U. Pflüger, 1997: Statistical-dynamical downscaling of wind climatologies. *Journal of Wind Engineering and Industrial Aerodynamics*, **67**, 449–457, doi:10.1016/S0167-6105(97)00093-7.

Mestayer, P. G., and Coauthors, 2005: The urban boundary-layer field campaign in Marseille (ubl/clu-escompte): Set-up and first results. *Boundary-Layer Meteorology*, **114**, 315–365, doi:10.1007/s10546-004-9241-4.

Mills, G., 2014: Urban climatology: History, status and prospects. *Urban Climate*, **10**, **Part 3**, 479–489, doi:10.1016/j.uclim.2014.06.004.

Millward-Hopkins, J. T., A. S. Tomlin, L. Ma, D. Ingham, and M. Pourkashanian, 2012: The predictability of above roof wind resource in the urban roughness sublayer. *Wind Energy*, **15**, 225–243, doi:10.1002/we.463.

Millward-Hopkins, J. T., A. S. Tomlin, L. Ma, D. B. Ingham, and M. Pourkashanian, 2013a: Assessing the potential of urban wind energy in a major UK city using an analytical model. *Renewable Energy*, **60**, 701–710, doi:10.1016/j.renene.2013.06.020.

——, ——, ——, ——, and ——, 2013b: Mapping the wind resource over UK cities. *Renewable Energy*, **55**, 202–211, doi:10.1016/j.renene.2012.12.039.

Mithraratne, N., 2009: Roof-top wind turbines for microgeneration in urban houses in New Zealand. *Energy and Buildings*, **41**, 1013–1018, doi:10.1016/j.enbuild.2009.05.003.

Monin, A., and A. Obukhov, 1954: Basic laws of turbulent mixing in the surface layer of the atmosphere. *Trudy Geofizicheskogo Instituta, Akademiya Nauk SSSR*, **24**, 163–187.

Murakami, S., 1997: Computational wind engineering current status and future trends in computational wind engineering. *Journal of Wind Engineering and Industrial Aerodynamics*, **67**, 3–34, doi:10.1016/S0167-6105(97)00230-4.

NCEP, 2016: NCEP quarterly newsletter - January 2016. http://www.ncep.noaa.gov/newsletter/january2016/printable.shtml (Accessed August 30, 2016).

Ng, E., and C. Ren, 2015: *The urban climatic map: A methodology for sustainable urban planning*. Routledge, 543 pp.

Nicholls, M., R. Pielke, and R. Meroney, 1993: Large eddy simulation of microburst winds flowing around a building. *Journal of Wind Engineering and Industrial Aerodynamics*, **46**–**47**, 229–237, doi:10.1016/0167-6105(93)90288-Y.

Orf, L., E. Kantor, and E. Savory, 2012: Simulation of a downburst-producing thunderstorm using a very high-resolution three-dimensional cloud model. *Journal of Wind Engineering and Industrial Aerodynamics*, **104**–**106**, 547–557, doi:10.1016/j.jweia.2012.02.020.

Orf, L. G., and J. R. Anderson, 1999: A numerical study of traveling microbursts. *Monthly Weather Review*, **127**, 1244–1258, doi:10.1175/1520-0493(1999)127<1244:ANSOTM>2.0.CO;2.

——, ——, and J. M. Straka, 1996: A three-dimensional numerical analysis of colliding microburst outflow dynamics. *Journal of Atmospheric Science*, **53**, 2490–2511, doi:10.1175/1520-0469(1996)053<2490:ATDNAO>2.0.CO;2.

——, C. Oreskovic, E. Savory, and E. Kantor, 2014: Circumferential analysis of a simulated three-dimensional downburst-producing thunderstorm outflow. *Journal* *of Wind Engineering and Industrial Aerodynamics*, **135**, 182–190, doi:10.1016/j.jweia.2014.07.004.

Oseguera, R. M., and R. L. Bowles, 1988: *A simple, analytic 3-dimensional downburst model based on boundary layer stagnation flow*. National Aeronautics and Space Administration, Langley Research Center, Hampton, Va, 19 pp. http://iucat.iu.edu/iue/6640029.

Peacock, A. D., D. Jenkins, M. Ahadzi, A. Berry, and S. Turan, 2008: Micro wind turbines in the UK domestic sector. *Energy and Buildings*, **40**, 1324–1333, doi:10.1016/j.enbuild.2007.12.004.

Peck, A. M., E. A. Bowering, and S. P. Simonovic, 2014: A flood risk assessment to municipal infrastructure due to changing climate part II: case study. *Urban Water Journal*, **11**, 519–531, doi:10.1080/1573062X.2013.781760.

Proctor, F. H., and R. L. Bowles, 1992: Three-dimensional simulation of the Denver 11 July 1988 microburst-producing storm. *Meteorology and Atmospheric Physics*, **49**, 107–124, doi:10.1007/BF01025403.

Raupach, M. R., A. S. Thom, and I. Edwards, 1980: A wind-tunnel study of turbulent flow close to regularly arrayed rough surfaces. *Boundary-Layer Meteorology*, **18**, 373–397, doi:10.1007/BF00119495.

Richards, P. J., and R. P. Hoxey, 1993: Appropriate boundary conditions for computational wind engineering models using the k-ϵ turbulence model. *Journal of Wind*

Engineering and Industrial Aerodynamics, **46**, 145–153, doi:10.1016/0167-6105(93)90124-7.

Rockel, B., 2015: The regional downscaling approach: A brief history and recent advances. *Current Climate Change Reports*, **1**, 22–29, doi:10.1007/s40641-014-0001-3.

Romanic, D., and H. Hangan, 2015: Coupling of numerical weather prediction models and physical simulations for urban wind environment. *9th International Conference on Urban Climate (ICUC9)*, Toulouse, France, Meteo-France, 1–5 https://www.conftool.com/icuc9/index.php?page=browseSessions&form_session=27&presentations=hide (Accessed October 22, 2015).

——, D. Parvu, and H. Hangan, 2016: downburst reconstruction using physical simulation and analytical model with application to urban environments. *Proceedings of the First International Conference on Urban Physics (FICUP)*, Quito – Galápagos, Ecuador, 1–12.

Rotach, M. W., and Coauthors, 2005: BUBBLE – an Urban Boundary Layer Meteorology Project. *Theoretical and Applied Climatology*, **81**, 231–261, doi:10.1007/s00704-004-0117-9.

Roth, M., 2000: Review of atmospheric turbulence over cities. *Quarterly Journal of the Royal Meteorological Society*, **126**, 941–990, doi:10.1002/qj.49712656409.

——, and T. R. Oke, 1995: Relative efficiencies of turbulent transfer of heat, mass, and momentum over a patchy urban surface. *Journal of Atmospheric Science*, **52**, 1863–1874, doi:10.1175/1520-0469(1995)052<1863:REOTTO>2.0.CO;2.

——, ——, and D. G. Steyn, 1989: Velocity and temperature spectra and cospectra in an unstable suburban atmosphere. *Boundary-Layer Meteorology*, **47**, 309–320, doi:10.1007/BF00122336.

Sabatino, S. D., E. Solazzo, P. Paradisi, and R. Britter, 2007: A simple model for spatially-averaged wind profiles within and above an urban canopy. *Boundary-Layer Meteorology*, **127**, 131–151, doi:10.1007/s10546-007-9250-1.

Sadeh, W. Z., J. E. Cermak, and T. Kawatani, 1971: Flow over high roughness elements. *Boundary-Layer Meteorology*, **1**, 321–344, doi:10.1007/BF02186035.

Schiermeir, F., 1978: Air monitoring milestones, RAP's field measurements are in. *Environmental Science Technology*, **12**, 644–651, doi:10.1021/es60142a608.

Sengupta, A., and P. P. Sarkar, 2008: Experimental measurement and numerical simulation of an impinging jet with application to thunderstorm microburst winds. *Journal of Wind Engineering and Industrial Aerodynamics*, **96**, 345–365, doi:10.1016/j.jweia.2007.09.001.

Sharpe, T., and G. Proven, 2010: Crossflex: Concept and early development of a true building integrated wind turbine. *Energy and Buildings*, **42**, 2365–2375, doi:10.1016/j.enbuild.2010.07.032.

Shiotani, M., and G. Yamamoto, 1949: Atmospheric turbulence over the large city, 2nd report. *Journal of the Meteorological Society of Japan. Series II*, **27**, 67–73.

Sim, T. S., M. C. Ong, W. Y. Quek, Z. W. Sum, W. X. Lai, and M. Skote, 2016: A numerical study of microburst-like wind load acting on different block array configurations using an impinging jet model. *Journal of Fluids and Structures*, **61**, 184–204, doi:10.1016/j.jfluidstructs.2015.11.002.

Simões, T., and A. Estanqueiro, 2016: A new methodology for urban wind resource assessment. *Renewable Energy*, **89**, 598–605, doi:10.1016/j.renene.2015.12.008.

Simonovic, S. P., A. Schardong, D. Sandink, and R. Srivastav, 2016: A web-based tool for the development of Intensity Duration Frequency curves under changing climate. *Environmental Modelling & Software*, **81**, 136–153, doi:10.1016/j.envsoft.2016.03.016.

Solari, G., 2016: Thunderstorm response spectrum technique: Theory and applications. *Engineering Structures*, **108**, 28–46, doi:10.1016/j.engstruct.2015.11.012.

——, M. P. Repetto, M. Burlando, P. De Gaetano, M. Pizzo, M. Tizzi, and M. Parodi, 2012: The wind forecast for safety management of port areas. *Journal of Wind Engineering and Industrial Aerodynamics*, **104–106**, 266–277, doi:10.1016/j.jweia.2012.03.029.

——, M. Burlando, P. De Gaetano, and M. P. Repetto, 2015a: Characteristics of thunderstorms relevant to the wind loading of structures. *Wind and Structures*, **20**, 763–791, doi:10.12989/was.2015.20.6.763.

——, P. De Gaetano, and M. P. Repetto, 2015b: Thunderstorm response spectrum: Fundamentals and case study. *Journal of Wind Engineering and Industrial Aerodynamics*, **143**, 62–77, doi:10.1016/j.jweia.2015.04.009.

Solazzo, E., S. D. Sabatino, N. Aquilina, A. Dudek, and R. Britter, 2010: Coupling mesoscale modelling with a simple urban model: The Lisbon case study. *Boundary-Layer Meteorology*, **137**, 441–457, doi:10.1007/s10546-010-9536-6.

Statistics Canada, 2015: Census metropolitan areas. http://www.statcan.gc.ca/pub/91-214-x/2016000/section01-eng.htm (Accessed August 6, 2016).

Straka, J. M., and J. R. Anderson, 1993: Numerical simulations of microburst-producing storms: some results from storms observed during COHMEX. *Journal of Atmospheric Science*, **50**, 1329–1348, doi:10.1175/1520-0469(1993)050<1329:NSOMPS>2.0.CO;2.

Tabrizi, A. B., J. Whale, T. Lyons, and T. Urmee, 2014: Performance and safety of rooftop wind turbines: Use of CFD to gain insight into inflow conditions. *Renewable Energy*, **67**, 242–251, doi:10.1016/j.renene.2013.11.033.

Taylor, G. I., 1918: Phenomena connected with turbulence in the lower atmosphere. *Monthly Weather Review*, **46**, 211–211, doi:10.1175/1520-0493(1918)46<211b:PCWTIT>2.0.CO;2.

Tewari, M., H. Kusaka, F. Chen, W. J. Coirier, S. Kim, A. A. Wyszogrodzki, and T. T. Warner, 2010: Impact of coupling a microscale computational fluid dynamics model with a mesoscale model on urban scale contaminant transport and dispersion. *Atmospheric Research*, **96**, 656–664, doi:10.1016/j.atmosres.2010.01.006.

The Kansas Project, 2015: The Kansas Project | Architecture & Development Blog. *Highways and Hailstones*. http://highwaysandhailstones.com/the-kansas-project/ (Accessed March 7, 2016).

United Nations, 1987: *Report of the World Commission on Environment and Development: Our common future*. World Commission on Environment and Development, United Nations, http://www.un-documents.net/wced-ocf.htm (Accessed August 27, 2016).

United Nations, 2015: *World urbanization prospects: The 2015 revision*. United Nations, Department of Economic and Social Affairs, Population Division, New York, United States, https://esa.un.org/unpd/wpp/publications/files/key_findings_wpp_2015.pdf (Accessed August 27, 2016).

United Nations, 2016a: *Decisions adopted by the Conference of the Parties*. United Nations, Paris, France, http://unfccc.int/resource/docs/2015/cop21/eng/10a01.pdf (Accessed August 26, 2016).

United Nations, 2016b: *Urban population (% of total). World urbanization prospects.* United Nations, Paris, France, http://data.worldbank.org/indicator/SP.URB.TOTL.IN.ZS (Accessed August 27, 2016).

Vicroy, D. D., 1991: *A simple, analytical, axisymmetric microburst model for downdraft estimation*. NASA Langley Research Center, Hampton, VA, United States, http://ntrs.nasa.gov/search.jsp?R=19910011819 (Accessed January 7, 2016).

Wakimoto, R. M., 1982: The life cycle of thunderstorm gust fronts as viewed with Doppler radar and rawinsonde data. *Monthly Weather Review*, **110**, 1060–1082, doi:10.1175/1520-0493(1982)110<1060:TLCOTG>2.0.CO;2.

——, 1985: Forecasting dry microburst activity over the High Plains. *Monthly Weather Review*, **113**, 1131–1143, doi:10.1175/1520-0493(1985)113<1131:FDMAOT>2.0.CO;2.

Walker, S. L., 2011: Building mounted wind turbines and their suitability for the urban scale—a review of methods of estimating urban wind resource. *Energy and Buildings*, **43**, 1852–1862, doi:10.1016/j.enbuild.2011.03.032.

Weekes, S. M., and A. S. Tomlin, 2013: Evaluation of a semi-empirical model for predicting the wind energy resource relevant to small-scale wind turbines. *Renewable Energy*, **50**, 280–288, doi:10.1016/j.renene.2012.06.053.

Welch, J. B., and A. Venkateswaran, 2009: The dual sustainability of wind energy. *Renewable and Sustainable Energy Reviews*, **13**, 1121–1126, doi:10.1016/j.rser.2008.05.001.

Wind Energy Foundation, 2016: Wind energy foundation | Small wind energy. http://windenergyfoundation.org/about-wind-energy/small-wind/ (Accessed November 4, 2016).

Xie, Z.-T., O. Coceal, and I. P. Castro, 2008: Large-eddy simulation of flows over random urban-like obstacles. *Boundary-Layer Meteorology*, **129**, 1–23, doi:10.1007/s10546-008-9290-1.

Xu, Z., and H. Hangan, 2008: Scale, boundary and inlet condition effects on impinging jets. *Journal of Wind Engineering and Industrial Aerodynamics*, **96**, 2383–2402, doi:10.1016/j.jweia.2008.04.002.

Zajaczkowski, F. J., S. E. Haupt, and K. J. Schmehl, 2011: A preliminary study of assimilating numerical weather prediction data into computational fluid dynamics models for wind prediction. *Journal of Wind Engineering and Industrial Aerodynamics*, **99**, 320–329, doi:10.1016/j.jweia.2011.01.023.

Zdunkowski, W., and P. D. A. Bott, 2003: *Dynamics of the atmosphere: A course in theoretical meteorology*. 1 edition. Cambridge University Press, Cambridge, UK ; New York, 738 pp.

Zhang, N., Y. Du, S. Miao, and X. Fang, 2016: Evaluation of a micro-scale wind model's performance over realistic building clusters using wind tunnel experiments. *Advances in Atmospheric Sciences*, **33**, 969–978, doi:10.1007/s00376-016-5273-1.

Zhang, Y., H. Hu, and P. P. Sarkar, 2013: Modeling of microburst outflows using impinging jet and cooling source approaches and their comparison. *Engineering Structures*, **56**, 779–793, doi:10.1016/j.engstruct.2013.06.003.

Chapter II

2 Wind resource assessment in complex urban environment

2.1 Introduction

The urban community is a quintessential cell of the future society. Accommodating about 50% of the world's population, cities consume more than 65% of the world's energy and produce more than 60% of the total greenhouse gas emissions (Munich Re 2004). According to the World Demographics Profile 2013 report (Index Mundi 2013), 50.5% of the global population lived in cities. The percentage is even higher for the North American countries, where more than 80% of their population in 2010 inhabited urban areas. Moreover, the urbanization is only set to increase. In the context of climate and economic changes and new demographics, sustainable urbanization is one of the present and future global challenges that need to be addressed by adopting specific and innovative renewable energy solutions. The aim is to create future "Smart Cities" sustained by new forms of renewable energy: wind, solar, and geothermal. While solar and geothermal have gained some building and urban implementation grounds during the last years, wind energy production in urban environment seems to be termed as economically not viable given its intermittent availability and the lack of urban-specific wind devices capable to extract it.

City blocks generate complex and turbulent wind fields due to a large spatial heterogeneity of the urban morphology. The mean flow profiles, unsteadiness of the flow as well as the turbulence characteristics in urban environments have all been investigated in many wind tunnel experiments (e.g. Raupach et al. 1980, Cheng and Castro 2002), numerical simulations (e.g. Kanda et al. 2004, Xie et al. 2008), and full scale measurements (e.g. Allwine et al. 2004, Rotach et al. 2005). The research conducted so far indicates that the urban boundary layer (UBL) can be divided into several sub-layers (Oke 1988), as schematically indicated in Figure 2-1. The first layer from the top of the UBL is the mixed layer (ML). The lower base of this layer is at about 10% of the height of the UBL. Turbulence characteristics in ML are not directly influenced by the surface roughness, but turbulence is rather generated by the convective air motions (e.g. Rayleigh – Taylor instability). The near-surface layer can be subdivided into three sublayers, each with different flow and turbulence characteristics. At the top of the near-surface layer is the inertial sublayer (ISL, or constant – flux layer). In this layer, the mean velocity profiles, $U(z)$, tend to follow the semi-logarithmic law (log law) and the Monin-Obukhov theory applies, i.e.:

$$U(z) = \frac{u_*}{k} \ln\left(\frac{z-d}{z_0} + \Psi(z, z_0, L)\right), \tag{2-1}$$

where u_* is the friction velocity, d is the displacement height, z_0 is the roughness height, k is the von Kármán constant, and $\Psi(z, z_0, L)$ is a stability term that depends on height (z), z_0 and the Monin-Obukhov stability parameter L. Under neutral atmospheric conditions (which are assumed throughout this paper), $L \to \infty$, hence resulting in $\Psi(z, z_0, L)$ being equal to zero.

A common issue associated with the application of Eq. (2-1) in urban environments is how to determine the surface parameters (u_*, z_0, and d). This is not an easy task. Cheng and Castro (2002) showed that the most accurate method is to estimate u_* from drag measurements and then to use Eq. (2-1) to calculate d and z_0. However, the drag measurements are usually not readily available, and thus the surface parameters are often determined using the geometrical (morphological) characteristics of the surface (Macdonald et al. 1998).

The layer below the ISL is commonly known as the roughness sublayer (RSL, see Figure 2-1). The upper boundary of the RSL is still a matter of debate in the scientific community (Tennekes 1973, Garratt 1978, Raupach et al. 1980, Garratt 1980). This layer is particularly important in urban wind resource assessment studies because most of wind turbines mounted on the rooftops would be located within it. The RSL is a highly turbulent region. Christen et al. (2007) showed that turbulence at roof heights is characterized by fairly small length scales, but with the increase of distance from the roof (in any direction – up or down), the length scales increase. Although the spatial variations of turbulent fluxes are a function of z, z_0, L, lateral wind fluctuations, and time (Schmid et al. 1991), Cheng and Castro (2002) and Millward-Hopkins et al. (2012) demonstrated in their studies that if u_* is known and accurate, then the spatially averaged mean velocity profiles can be fairly well described by a single log law simultaneously applied for both RSL and ISL.

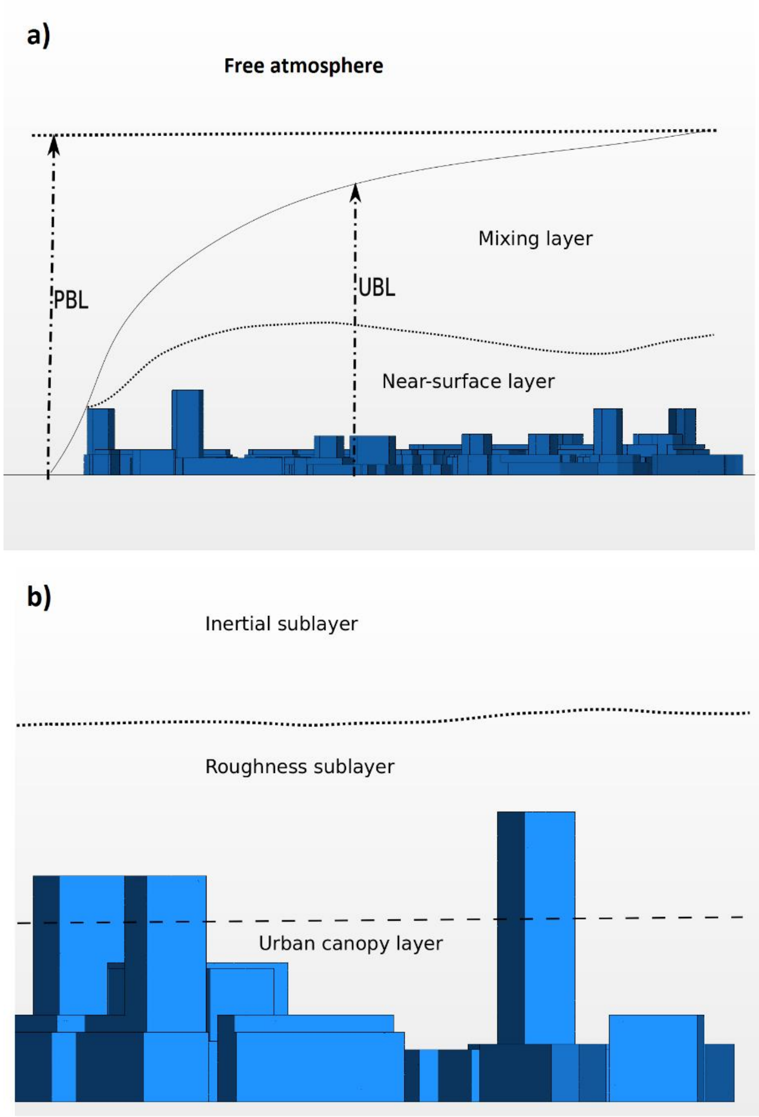

Figure 2-1. Sketch of the urban boundary layer structure: a) the mesoscale perspective, b) the near-surface layer. Modified after Oke (1988) and Rotach (1993). The geometry is a side cross-section of some of the buildings in the Pan American Games Athletes' Village block.

The lowest layer within the UBL is called the urban canopy layer (UCL, see Figure 2-1). This layer extends approximately up to approximately the mean building height (H). The morphological properties of the urban surface determine the flow characteristics inside the

UCL. Flows in this region are very complex. Conducting wind tunnel measurements on a simple array of obstacles, Cionco (1965, 1972) and Macdonald (2000) derived an equation for the wind profile inside the UCL, viz.

$$U(z) = U_H e^{a\left(\frac{z}{H}-1\right)}. \tag{2-2}$$

In the above equation, U_H is the mean wind speed at height H, as given by the log law (Eq. (2-1)), and a is a constant that depends on building geometry. For an array of cubes, $a \approx 9.6\lambda_f$, where λ_f is the frontal area index defined as:

$$\lambda_f = \frac{A_f}{A_d}, \tag{2-3}$$

where A_f is the frontal area of each obstacle exposed to the wind and A_d is the total area divided by the number of obstacles.

The complex structure of the UBL makes the wind resource assessment in urban environments very challenging. The most detailed way to assess the wind potential in cities is to perform long-term (several years long) measurement campaigns at the proposed location for the wind turbine(s) installations. The obvious drawbacks of this method are related to the complexity and the length of such campaigns. A popular option with the industry is to use a commercial software (e.g. WAsP, GH WindFarmer, WindSim) and wind resource assessment tools (μ-wind modeling (Bahaj et al. 2007), RETScreen, AWS Truepower, etc.). However, most of these software are developed and designed for the wind resource assessment in rural areas with smooth to mild complexity of the surface. Due to the non-linearity of the flows in cities, these methodologies are therefore not suitable for urban wind resource assessment. Millward-Hopkins et al. (2012) showed that if a simple wind resource assessment tool is used for wind resource assessment in urban environments, the uncertainties in the estimated wind resources are around 30%. An interesting option is to use wind atlas data to calculate the local wind speed at rooftop height (Mertens 2003, Heath et al. 2007). The edge of the urban area was treated as an abrupt change in the surface roughness in these studies. Mertens (2003) detected a region of accelerated flow with large vertical angles close to the leading edge of an isolated building. However, he noticed that the accelerated flow region is more attenuated if the building is located within urban areas. On the other hand, Heath et al. concluded that the accelerated region does not exist if the building is located in suburban areas. Millward-Hopkins et al. (2012) used numerical data by Xie et al. (2008) and wind tunnel data by Cheng and Castro (2002) to analyze the rooftop mean flow characteristics of an idealized urban environment made out of cubes with heterogeneous and uniform heights. They found that the accelerated region (Mertens 2003, Heath et al. 2007) is up to about 20% of the mean height of the blocks, and the region increases moving away downstream from the leading edge. Sunderland et al. (2013) used measurement from several sites located close to Dublin, Ireland to perform urban wind resource assessment study. Similar to Cheng and Castro (2002) and Millward-Hopkins et al. (2012), Sunderland et al. (2013) also concluded that the log law is suitable for characterization of the mean velocity profiles in urban environments under the assumption that the surface parameters are known and accurate.

The objective of the present work is to define a new resource assessment methodology for wind energy implementation in urban environments. Computational Fluid Dynamics (CFD) is used for the first time as microscale simulation in conjunction with the Canadian Wind Energy Atlas (Environment Canada 2003) to produce detailed wind energy assessment at the individual building level in the city of Toronto, Canada. The energy consumption of individual buildings is compared with maximum harvestable wind energy in the area. The actual energy production using generic wind turbines is estimated and the need of new wind turbines adapted to urban environment is discussed.

2.2 Inflow urban boundary layer

2.2.1 Site

The wind assessment study is performed on a city block covering approximately 14 hectares of land in the south of the city of Toronto, ON, Canada. The area is planned to serve as the 2015 Pan American Games Athletes' Village (PanAm Village, Figure 2-2).

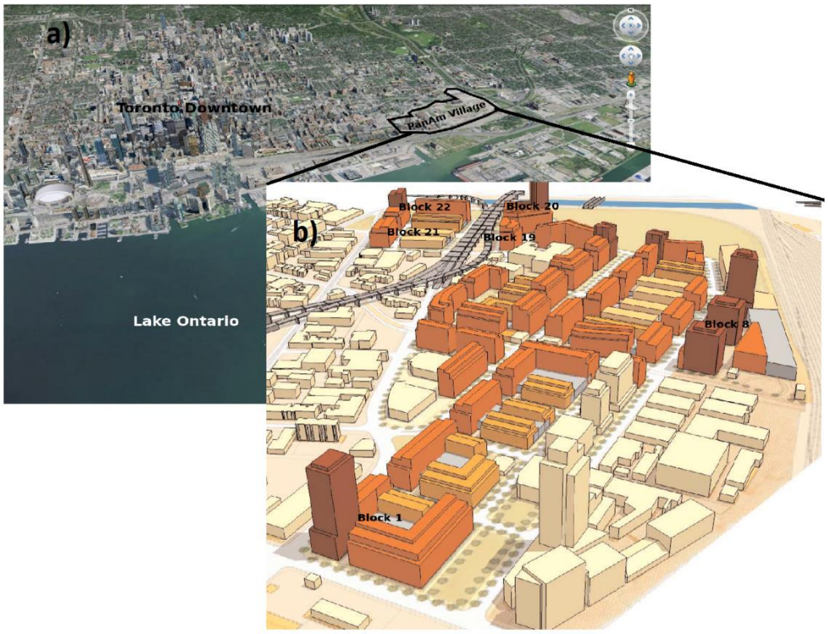

Figure 2-2. a) The 2015 Pan American Games Athletes' Village site location in Toronto, Canada (Google Earth$^{®}$ maps) b) A closer 3D view of the development blocks (source: (Urban Design Associates 2006)). The wind resource assessment study is performed for blocks 1, 8, 19, 20, 21 and 22.

The PanAm Village will contain 22 building blocks positioned along the existing streets. Blocks selected for the sustainability analysis in this study are marked in Figure 2-2. The main reasons for selecting these six blocks are: i) they have the highest wind energy potential (as demonstrated in Section 2.4.2), and ii) they will contain both commercial and residential building types, which presents an interesting combination from the resource planning point of view. The total areas of commercial and residential buildings for each of the selected blocks are given in Table 2-1.

Table 2-1. Areas of residential and commercial buildings for each of the selected blocks. Source: (Urban Design Associates 2006).

Block number	Area of the block (acres)	Residential area (m^2)	Non-residential area (m^2)	Total area (m^2)
1	2.01	47,200	3,280	50,480
8	4.20	60,000	5,000	65,000
19	0.46	10,400	0	10,400
20	1.18	31,380	0	31,380
21	1.98	10,500	1,430	11,930
22	2.34	38,800	1,600	40,400

2.2.2 Mean wind and turbulence intensity profiles

Annual wind data for the site location are obtained from the Canadian Wind Energy Atlas (Environment Canada 2003). The atlas was created following the statistical-dynamical downscaling methodology (Frey-Buness et al. 1995). In short, the method is based on mesoscale numerical modelling and an appropriate post-processing of the results. Table 2-2 shows the simulated wind conditions at a height of 80 m above ground level at the PanAm Village location (LAT: 43°39’06.82” N; LON: 79°21’26.63” W). The mean wind speed, power density and wind speed probability distribution function (PDF) are provided seasonally and annually. As expected, the wind speeds are highest in winter and lowest in summer. The wind speed PDF is expressed by the following relation:

$$p(U) = \left(\frac{k}{A}\right)\left(\frac{U}{A}\right)^{k-1} e^{-\left(\frac{U}{A}\right)^{k}}, \qquad (2\text{-}4)$$

where U is the mean wind speed, k and A are the Weibull shape and scale parameters, respectively. Figure 2-3a is a histogram of the annual average wind speeds while the annual average wind rose is depicted in Figure 2-3b. The present study is based on the annual average wind data. Figure 2-3b suggests that the winds blowing in from southwest (heading of 240° and coming in from Lake Ontario) have the highest probability of occurrence. Interesting to note is that the winds coming in from east (90°) have a similar percentage of occurrence as the northwest winds (coming in from 330° and 300°). The numerical simulations as well as the wind resource assessment for PanAm Village are performed for winds coming in from 240° and 90° directions.

Table 2-2. Wind data at a height of 80 m at the PanAm Village location. Source: (Environment Canada 2003).

Period	Mean wind speed ($m\ s^{-1}$)	Power density ($W\ m^{-2}$)	Weibull shape parameter	Weibull scale parameter($m\ s^{-1}$)
Annual	5.45	169.88	1.83	6.13
Winter (DJF)	6.41	248.25	2.02	7.23
Spring (MAM)	5.47	167.38	1.88	6.16
Summer (JJA)	4.34	78.69	1.98	4.89
Fall (SON)	5.61	177.38	1.91	6.33

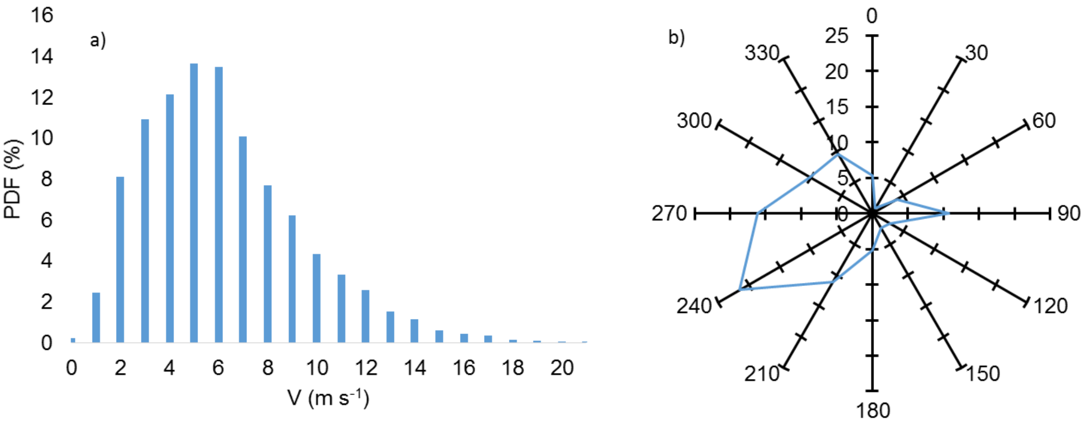

Figure 2-3. Annual averaged wind data at 80 m from the Canadian Wind Atlas: a) wind histogram, b) wind rose.

To modify the wind atlas data in order to account for the local effects (such as a step change in the surface roughness and consequential development of an internal boundary layer (IBL)), the upstream wind conditions, and not the wind profiles above the PanAm Village, are extracted from the Canadian Wind Energy Atlas. The modification of wind atlas data is performed in four steps, as schematically depicted in Figure 2-4.

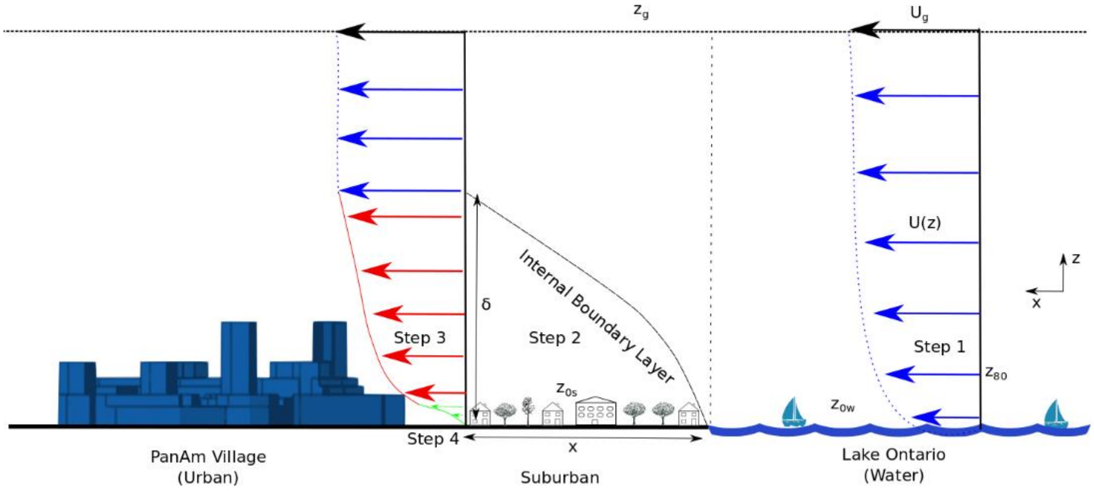

Figure 2-4. Schematic sketch of the internal boundary layer developed as a consequence of an abrupt change in surface roughness. See text for details.

In step one, the wind speed at a height of 80 m and upstream from the PanAm Village site is obtained from the Canadian Wind Energy Atlas. Then, the gradient wind speed has been calculated using the power law, i.e.:

$$U_g = U_z \left(\frac{z_g}{z}\right)^{\alpha}. \tag{2-5}$$

Here, U_g is the gradient wind speed at a height $z_g = 500$ m, U_z is the wind speed at a height z (in this step, $z = 80$ m), and α is the power law coefficient. In neutrally stable atmosphere, and above the water surfaces, α is approximately 0.1 (Kaltschmitt et al. 2007).

The second step is calculation of a height of the newly developed IBL. This layer develops as a response to an abrupt change in surface roughness. The calculations are based on Elliott's formula (Elliott 1958):

$$\delta = 0.75 z_{02} \left(\frac{x}{z_{02}}\right)^{0.8}. \tag{2-6}$$

In Eq. (2-6), δ is the height of the developed IBL at a distance x from the change in surface roughness, and z_{02} is the roughness length downwind from the roughness change.

The third and the fourth steps include calculations of wind profile at the PanAm Village site. Knowing the height of the IBL at the PanAm Village site (Step 2), it is possible to calculate the wind profile within the IBL. First, using Eq. (2-5), the wind speed at the height δ is calculated. Then, applying the same equation, but using the power law coefficient for the suburban area, the wind speed at the mean building height in suburban region of Toronto ($H_{sub} \cong 10$ m) is determined. Finally, utilizing Eq.'s (2-3) and (2-2), one can calculate the wind speed profile inside the suburban canopy layer (down to the height of 1 m above ground, U_{1m}). The results of these calculations are summarized in Table 2-3.

Table 2-3. Inlet velocity profile calculation. See text for further details.

Parameter	Unit	Reference	Wind direction 90°	Wind direction 240°
Longitude	deg min sec	Maps	79°18’00.85” W	79°23’28.40” W
Latitude	deg min sec	Maps	43°39’12.19” N	43°26’34.00” N
U_{80}	m s^{-1}	Wind atlas	5.67	6.25
α_w	-	Kaltschmitt et al. (2007)	0.1	0.1
z_g	m	Assumed	500	500
U_g	m s^{-1}	Eq. (2-5)	6.81	7.51
z_{0z}	m	ESDU (2002a)	0.7	0.7
x	m	Maps	2700	650
δ	m	Eq. (2-6)	388	124
U_δ	m s^{-1}	Eq. (2-5)	6.64	6.53
H_{sub}	m	Maps	10	10
α_s	-	Kaltschmitt et al. (2007)	0.34	0.34
$U_{H_{sub}}$	m s^{-1}	Eq. (2-5)	1.91	2.77
λ_F	-	Grimmond and Oke (1999) and maps	0.15	0.15
a	-	Eq. (2-3)	1.44	1.44
U_{1m}	m s^{-1}	Eq. (2-2)	0.52	0.76

The turbulence intensity (I_u) profiles have been calculated following the ESDU 83045 guidelines (ESDU 2002b), i.e.:

$$I_u = \frac{\sigma_u}{u_*}\frac{u_*}{U(z)}, \tag{2-7}$$

where σ_u is the standard deviation of the wind speed. The friction velocity, u_*, has been determined using the geostrophic drag law:

$$u_* = C_g U_g, \tag{2-8}$$

where

$$C_g = \frac{0.114}{R_o^{0.07}}, \tag{2-9}$$

$$R_o = \frac{U_g}{f z_0}. \tag{2-10}$$

Here, C_g is the geostrophic drag coefficient, R_o is the Rossby number, and f is the Coriolis parameter ($f = 2\Omega \sin \varphi$, Ω is the earth's angular velocity and φ is the latitude; for PanAm Village site, $f = 1.004 \times 10^{-4}\mathrm{s}^{-1}$). After u_* is obtained, parameters $\frac{\sigma_u}{u_*}$ and $\frac{u_*}{U(z)}$ can be calculated using the following equations:

$$K_{zx} = \frac{U(z)}{u_*} = 2.5\left(\ln\left(\frac{z}{z_0}\right) + 34.5\frac{fz}{u_*}\right), \tag{2-11}$$

$$\frac{\sigma_u}{u_*} = \frac{7.5\left(0.538 + 0.09\ln\left(\frac{z}{z_0}\right)\right)^{\eta^{16}}}{1 + 0.156\ln\left(\frac{u_*}{fz_0}\right)}, \tag{2-12}$$

where $\eta = 1 - \frac{6fz}{u_*}$.

Based on the methodology presented above, the inlet velocity and turbulence intensity profiles at the PanAm Village site were calculated and results are depicted in Figure 2-5.

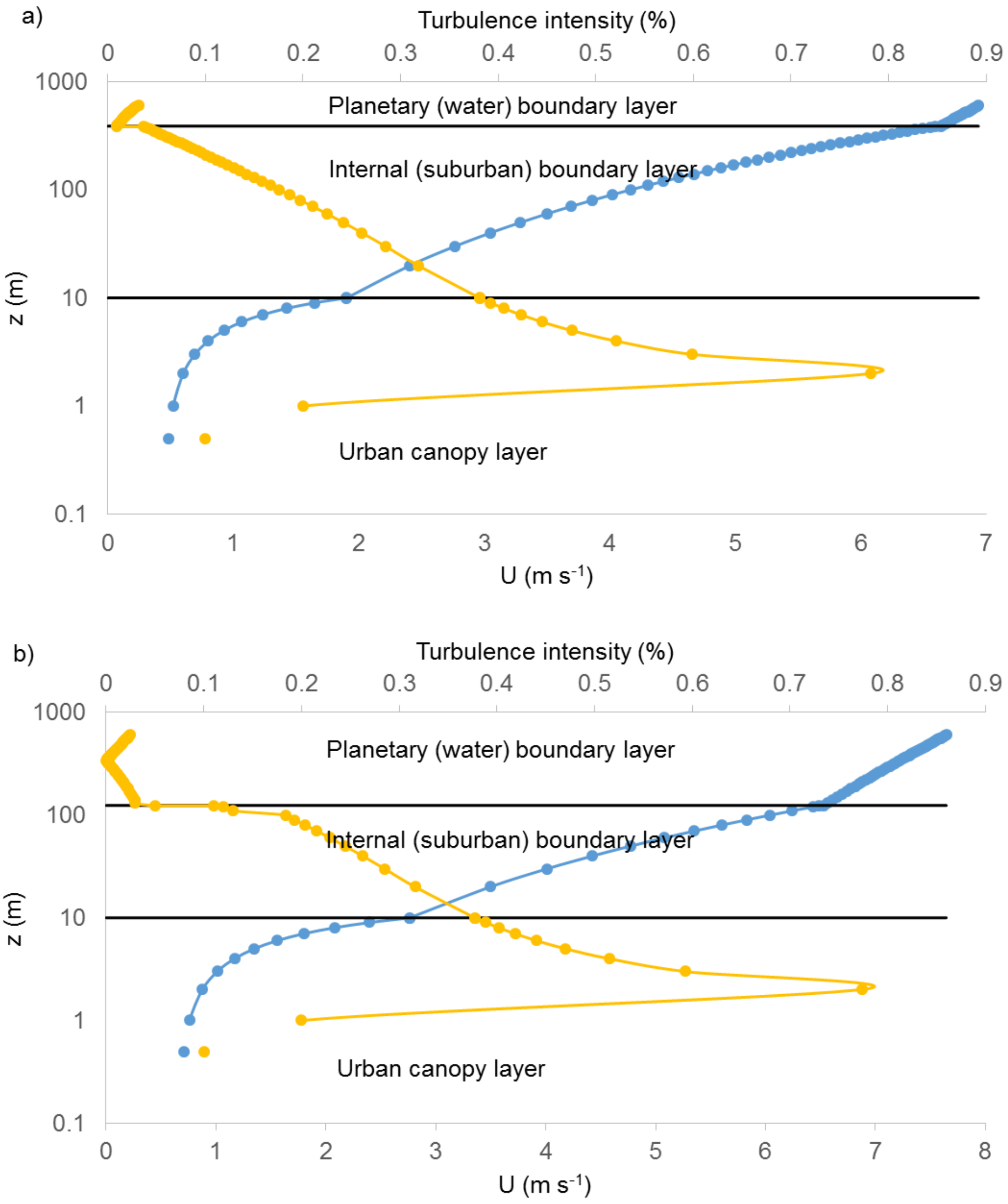

Figure 2-5. Inlet velocity (blue lines) and turbulence intensity (yellow lines) profiles: a) 90° wind direction, b) 240° wind direction.

2.3 Numerical setup

2.3.1 The solver

The CFD simulations are carried out using the STAR-CCM+ software developed by CD-Adapco. The use of a numerical code and the Reynolds-averaged Navier-Stokes (RANS) models are motivated by the interest to establish the methodology and provide fast calculations to be further integrated in a mesoscale-microscale cycle. The governing equations for this problem are three-dimensional steady incompressible RANS equations without heat transfer and Coriolis effect(CD-Adapco 2014) , viz.:

$$\oiint_{A} \rho\vec{v}\cdot d\vec{A} = 0, \tag{2-13}$$

$$\oiint_{A} \rho(\vec{v}\times\vec{v})\cdot d\vec{A} = -\oiint_{A}\left(\vec{T} - p\vec{I}\right)\cdot d\vec{A} + \iiint_{V} \rho\vec{g}dV\,. \tag{2-14}$$

In these equations, ρ is the air density (constant), $\vec{v}$ is the velocity vector, $d\vec{A}$ is the cell area vector ($d\vec{A} = \vec{n}dA$, where $\vec{n}$ the unit vector normal to the cell surface dA), $\vec{T}$ is the viscous stress tensor which includes the Reynolds stress tensor, p is the pressure, $\vec{I}$ the identity matrix, V is the total volume and $\vec{g}$ is the gravitational acceleration. Eq. (2-14) is discretized in the space domain with second-order accuracy and the pressure-velocity coupling is achieved using the segregated flow model with a predictor-corrector algorithm. The solution is updated according to the Semi-Implicit Method for Pressure-Linked Equations (SIMPLE) method (Pletcher et al. 1997). Shear stress transport (SST) k-ω turbulence model (Menter 1994) adjusted for a transitional flow is used. The turbulence model solves one equation for the turbulent kinetic energy (TKE) and one more equation for the specific dissipation (or turbulent frequency). The specific dissipation is a quantity that can be related to the time scale of turbulence. The solver employs the k-ω turbulence model in the inner region of the boundary layer (where most of the flow complexity occurs) and switches to the standard k-ε turbulence model in the free shear flow (see e.g. Menter 1994, Menter et al. 2003 and Versteeg and Malalasekera 2007). This approach has been adopted in many wind engineering studies (e.g. Yang and Luo 1996, Jubayer and Hangan 2014, Rocha et al. 2014).

The domain size is adjusted to meet the minimum size based on the COST guideline (Franke et al. 2011). Figure 2-6 shows a schematic sketch of the CFD model solution domain. The maximum height of the building is determined from the project documentation (*h*=100 m) and the domain is sized according to it.

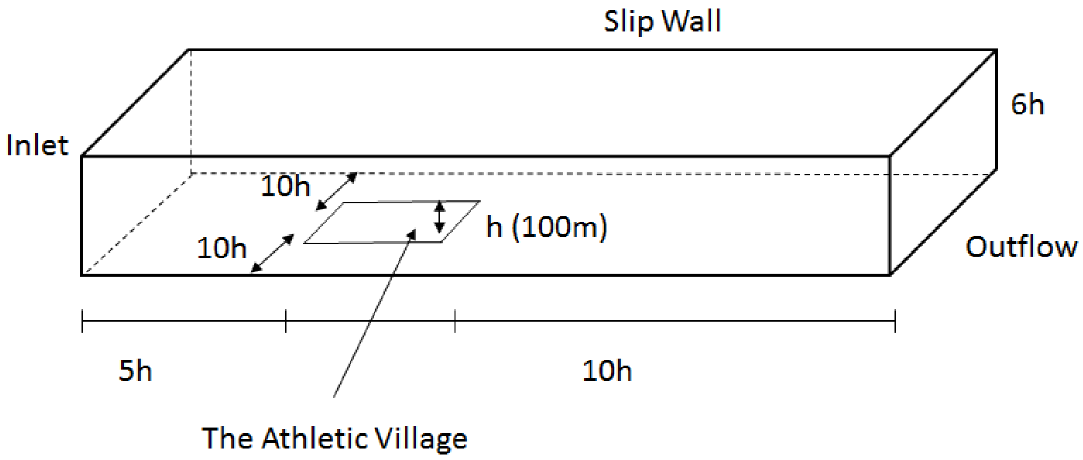

Figure 2-6. Solution domain and boundary conditions for the CFD model (sketch not to scale).

2.3.2 Boundary conditions

The boundary conditions for the simulation are as follows: the top wall and side walls are specified as the symmetry planes. Boundary condition for ground and building's surfaces is a no-slip wall without roughness. Minor details of buildings (windows, doors, etc.) were not taken into consideration. The inlet boundary is a velocity inlet with the velocity and turbulence intensity profiles as depicted in Figure 2-5. A pressure outlet boundary is used at 25h downstream from the inlet.

2.3.3 Grid independency analysis

The meshes for 90° and 240° directions have 4.75 (Figure 2-7) and 4.37 million polyhedral cells, respectively, with the prism layer mesh (orthogonal prismatic cells) close to the wall surfaces and boundaries. In order to improve the surface quality for meshing, the surfaces were retriangulated using the surface remesher tool (CD-Adapco 2014). The computational domain outside of PanAm Village is populated with cells that have a base size of 100 m and the domain has 4 prism layers close to the ground. The average cell size on faces of the buildings in PanAm Village is about 0.5 m while the average cell size inside the village is about 10 m; and 5 prism layers close to the ground. The fetch (the computational domain between the inlet and PanAm Village, see Figure 2-7) has a special high-resolution mesh close to the surface (average cell size of 20 m, and 8 prism layers).

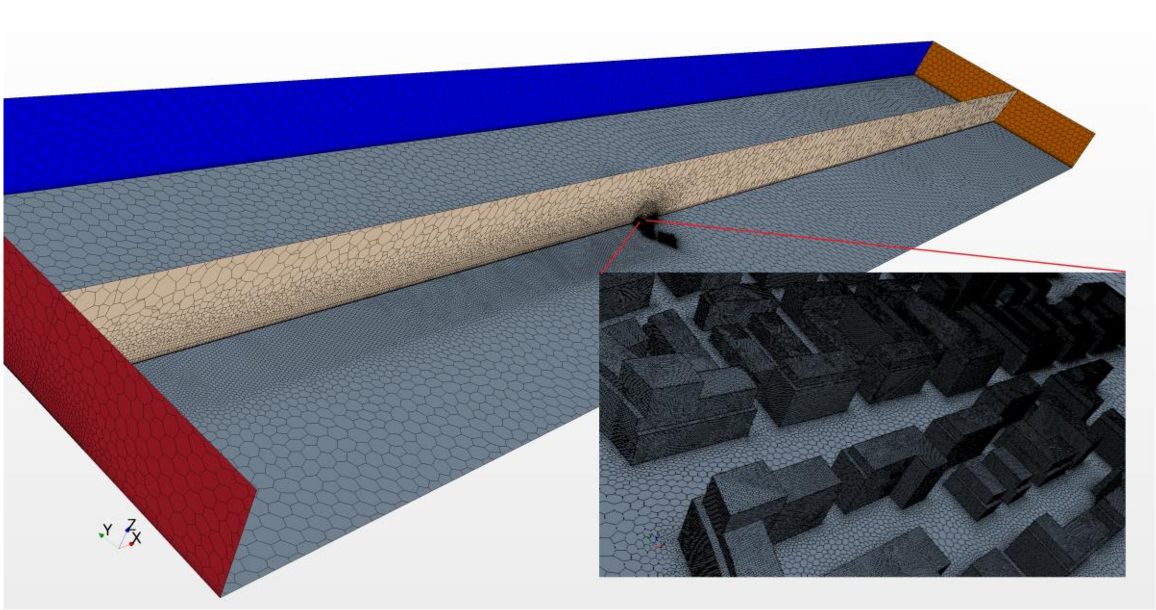

Figure 2-7. Overall view of the generated mesh and the mesh on faces of the buildings (lower right corner).

The grid independency analysis was performed for 90° direction, for which two additional meshes were created having 4.37 million cells and 5.74 million cells. The wind speed profiles at four different locations are presented in Figure 2-8. The percentage differences between the velocity profiles are calculated as:

$$PD_{ij} = \frac{1}{21}\sum_{k=1}^{21} \frac{2\left(V_{i,k} - V_{j,k}\right)}{V_{i,k} + V_{j,k}} \cdot 100 \ [\%], \tag{2-15}$$

where i and j are one of the grids (small (S), medium (M) or large (L); $i \neq j$), and V_k's are velocity values for a particular velocity profile (k = 1, 2, 3, …, 21). Results portrayed in Figure 2-8 demonstrate good matching between profiles among all of the three grids. *PD*'s in the fetch are well below 0.5%, indicating almost perfect matching between incoming wind profiles. Due to the complex geometry of PanAm Village site, PD's inside the village are somewhat higher, but are generally below 5%. This finding shows that the results are grid independent. Close inspection of Figure 2-8b and Figure 2-8c reveals that the smallest grid generally tends to overpredict the velocities in PanAm Village. However, the difference is very small.

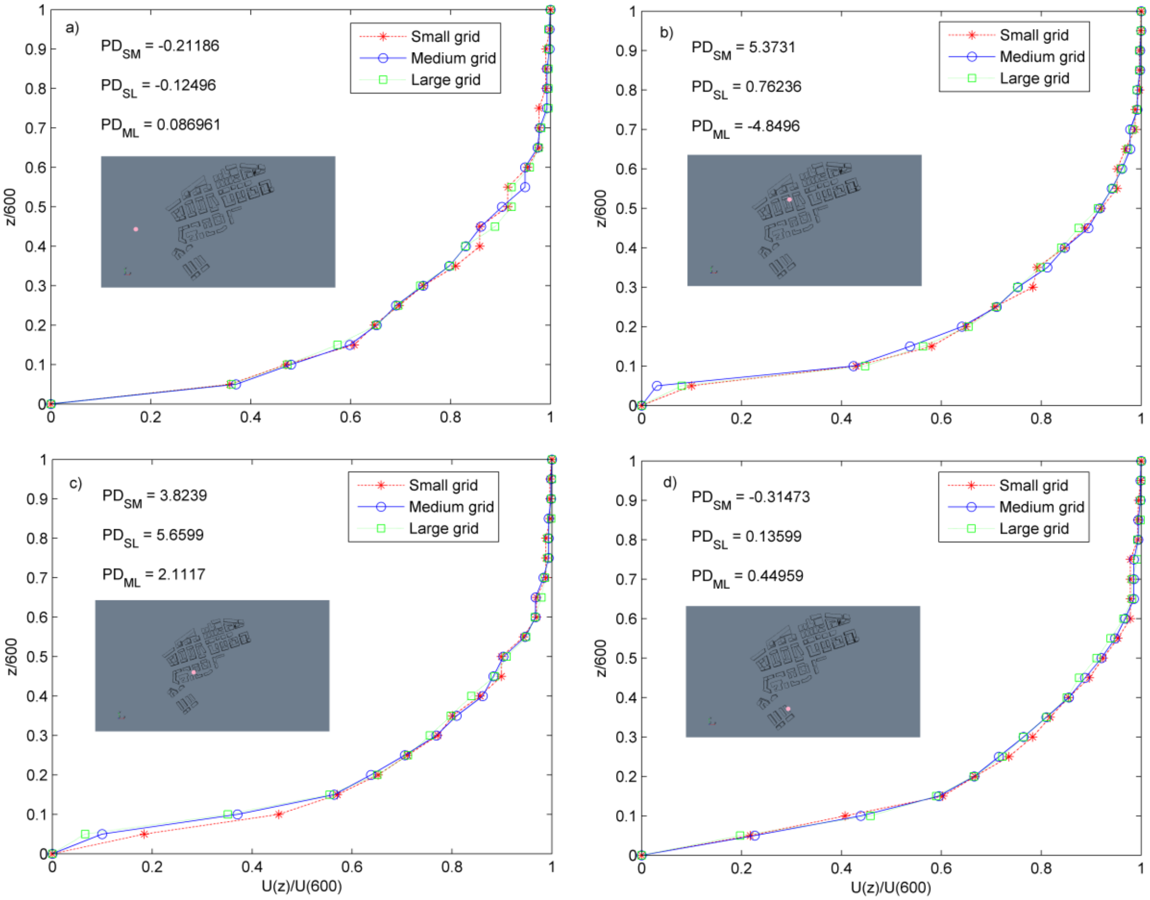

Figure 2-8. Grid independency analysis at four locations indicated with the pink dot. The dot locations in the *x*-*y* plane are: a) [-500,0], b) [0,200], c) [0,0], and d) [0,-200]. See text for further details.

2.4 Results

2.4.1 General characteristics of the urban boundary layer

A multitude of studies, both experimental and numerical, have characterized the flow around single and multiple bluff bodies (e.g. Castro and Robins 1977, Rodi 1997). Although most of these previous studies focused on generic uniform or staggered arrays of cubes, some of the flow patterns can still be observed in a real urban environments (such as the one analyzed herein). A vertical slice of velocity field around the buildings for southwest winds (240°) is shown in Figure 2-9. Recirculation zones develop at several locations; before the first building, across the building roofs and in the canyons between the buildings. These recirculation regions are formed due to low pressure wakes downstream of the buildings. The first recirculation zone before the building B1 is about 50 m long and 10 m tall (about 12% of the height of the building). This recirculation zone is always located below the stagnation point, but the characteristics of the flows and shape of the zone are mainly influenced by the approach wind characteristics. The region above the stagnation point (called upwash) occupies the upper one-quarter to one-third of the building face while the region below the stagnation point (lower one-half to two-thirds of the building face) is called the downwash (Parsons et al. 2005). The flow separation at the roof's leading edge of B1 is followed by the reattachment on the surface of the roof at approximately $0.18H_{B1}$ downstream of the leading edge (H_{B1}=78 m). The angle of the separation (the skew angle) is about 45° for B1, but the skewed angles at the edges of the buildings further downstream are considerably smaller. This finding confirms the observations made by Mertens et al. (2003) that the skew angle depends on the roughness of the upwind area in such a way that it decreases with the increase of the roughness.

Close to the separation point, and above the recirculation zone, the density of the streamlines increases creating the regions of high wind speeds. These regions are portrayed in Figure 2-9, and even more pronounced in Figure 2-10 (Figure 2-10b is the velocity field at the mean building height in PanAm Village (*H*=30 m)).

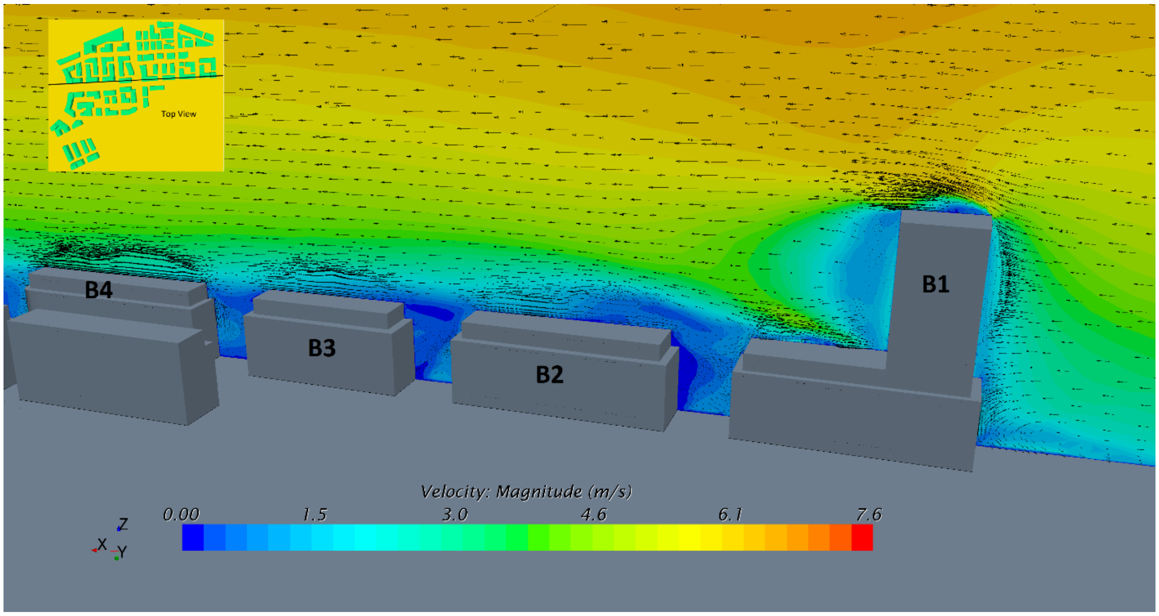

Figure 2-9. Velocity profile around the buildings. Wind from right to left.

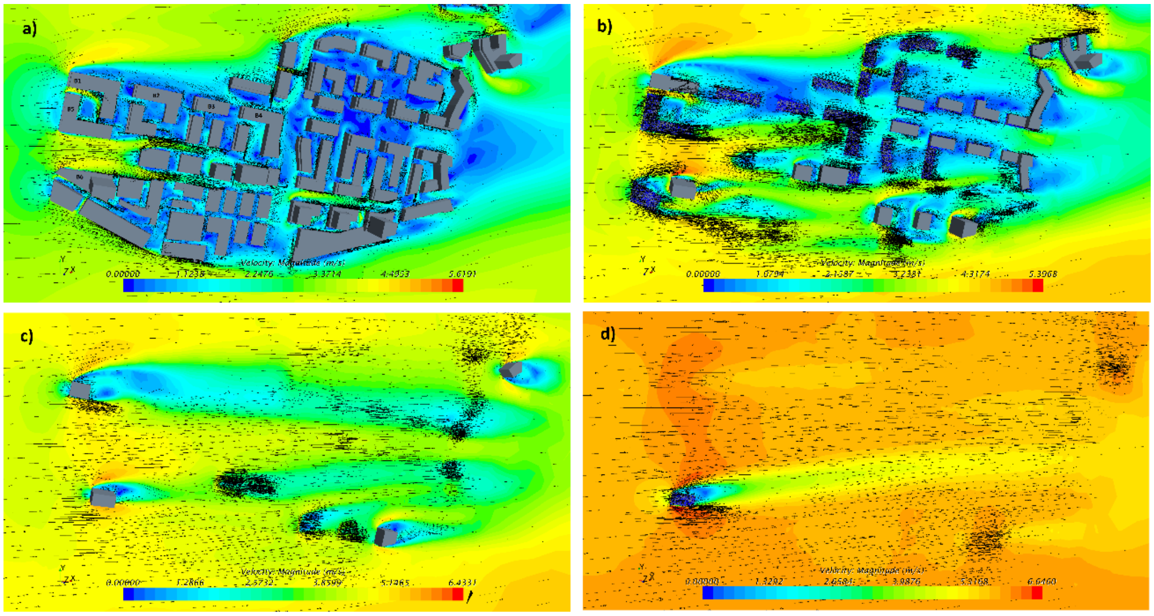

Figure 2-10. Velocity field on horizontal planes at: a) 10 m, b) 30 m, c) 50 m, and d) 100 m above ground. Wind direction is along the *x*-axis.

Figure 2-10 also depicts the flows inside canyons located between the buildings. Wind speeds within the canyons depend on the orientation of the canyon compared to the incoming wind direction. Namely, a canyon that is perpendicular to the incoming wind will have lower wind speeds. The buildings that are creating the canyon will at the same time elevate the flow above the canyon, and thus create a region of low wind speeds inside the canyon. The channeling of the flow occurred between the buildings B5 and B6 (especially evident in Figure 2-10b). Wind speeds in this canyon are about 2 m s^{-1} higher compared to the incoming wind. If close to ground, such phenomena can cause pedestrian discomfort, but may also be exploited by small street level wind turbines.

An interesting flow pattern can be observed in Block 1, as portrayed in Figure 2-11. Buildings B1 and B5 are L-shaped buildings that channel the flow into the rectangular zone

(Z) located in between the buildings. The flow channeling at the entrance (C) results in wind speeds that are about 2.5 m s^{-1} larger than the incoming wind speeds, and about 4 m s^{-1} higher than the wind speeds in Z (note that Z is only about 30 m away from C), where a strong vortex forms due to the unique buildings layout. Figure 2-11 at the same time gives a closer look at the channeling zone that was discussed in the previous paragraph.

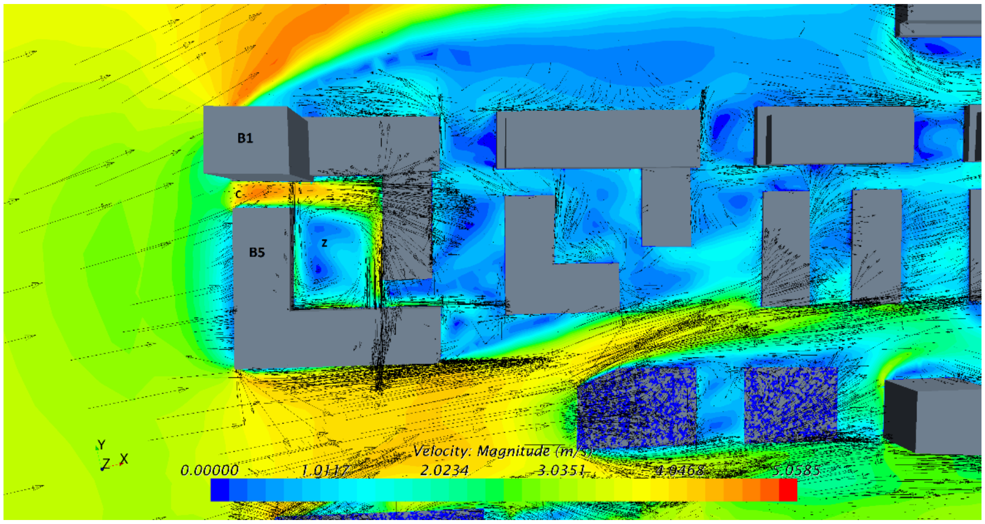

Figure 2-11. The circulation vortex in Block 1. Velocity contours and vector field are at 20 m above the ground.

Figure 2-9 and Figure 2-10 show that the wind speed increases moving away from the surface and/or moving closer to the windward side of PanAm Village. Both increasing trends have the same physical explanation – loss of the momentum (and energy) in wind due to the drag caused by the surface. Even though the underlying surfaces in cities are usually smooth (concrete, asphalt, etc.), the total drag on irregularly spaced obstacles is larger than the overall drag of the underlying surface, resulting in the loss of momentum from the overhead flow (Macdonald 2000). The spatial irregularity of buildings creates non-uniform velocity fields in both horizontal and vertical directions. Therefore, a generally accepted approach is to determine the area-averaged velocity profiles, rather than focus on single profiles at various locations. The area-averaged velocity profiles at PanAm Village in dimensional and non-dimensional forms, and for both wind directions, are presented in Figure 2-12. Figure 2-12b shows that quasi-exponential velocity profiles are present below the mean building height (H=30 m). However, some discrepancies from the exponential profile given by Eq. (2-2) are especially evident for 240° direction, where a slight increase in wind speed at the pedestrian level exists (1.75 m above the ground).

The logarithmic profiles that exist above H (up to a certain height) have different slopes and offsets indicating that the friction velocity and the roughness height are wind direction dependent. Many morphological methodologies for estimation of the surface parameters use λ_F (Eq.(2-3)) and/or the plan area density $\lambda_P = A_p/A_d$ (A_p is the plan area of an obstacle as viewed from above) to find d and z_0. With an estimate of one of these two parameters, Eq. (2-1) can further be used to calculate u_*. However, while λ_F is generally dependent on the wind direction, λ_P is not, and therefore d and z_0 estimates based on λ_P will be independent of the incoming wind direction as well. λ_P for PanAm Village is calculated to be equal to 0.59, indicating that the site is highly urban. Using equations $d = 0.7H$ (Grimmond and Oke 1999) or $\frac{d}{H} = 1 + \alpha^{-\lambda_P}(\lambda_P - 1)$ (Macdonald et al. 1998) ($\alpha = 4.42$, an empirical parameter) to calculate the displacement height at PanAm Village, it is found that d=21 m or d=25 m, respectively. Besides giving different results, the above two formulas show that the resulting values of d are independent of the incoming wind directions, and therefore the morphology of the surface. The result that the surface parameters are not a function of the incoming wind directions is not something that is necessarily fulfilled in reality, and hence this topic requires yet more research.

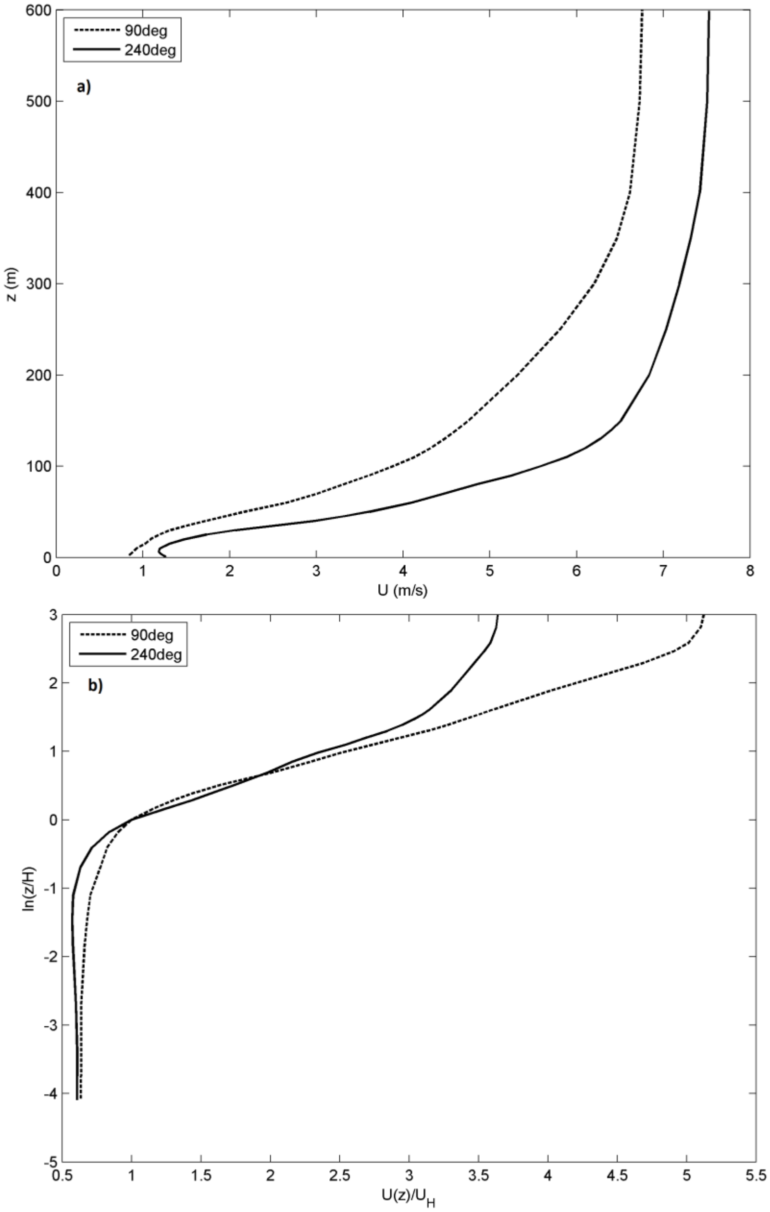

Figure 2-12. Area-averaged velocity profiles over the PanAm Village site for 90° winds (dashed line) and 240° winds (full line): a) dimensional profiles and b) non-dimensional profiles. Heights and velocities are scaled using the mean building height, *H*, and the area-averaged velocity at *H*, U_H, respectively.

2.4.2 Wind sustainability analysis

Numerical simulation results for wind sustainability analysis performed in this study are presented as the wind and power density maps at a height of 8 m above the ground and building surfaces (Figure 2-13). The height of 8 m is selected as an approximate effective height for the present type of urban wind turbines. The highest wind speeds are observed at the roof of the tallest buildings. The available annual average power in the wind per unit area (P_w) is calculated as (e.g. Romanić et al. 2014):

$$P_w = \frac{1}{2}\rho A^3 \Gamma\left(1 + \frac{3}{k}\right), \tag{2-16}$$

where Γ is the gamma function, ρ=1 kg/m^3 is the air density, k=1.83 is the Weibull shape parameter (see Table 2-2) and the Weibull scale parameter A is calculated as: $A = \frac{U}{\Gamma\left(1+\frac{1}{k}\right)}$; with U being the mean wind speed at the wind turbine height. P_w is directly proportional to the cube of wind speed, thus the areas with lower wind speeds in Figure 2-13c and Figure 2-13d have a significantly lower wind power compared to the areas with the higher wind speeds (Figure 2-13a and Figure 2-13b). The wind energy assessment is performed for the six blocks located in PanAm Village. The blocks 1, 8, 19, 20, 21 and 22 (see Figure 2-2) have the highest wind power density which makes them suitable for the present study.

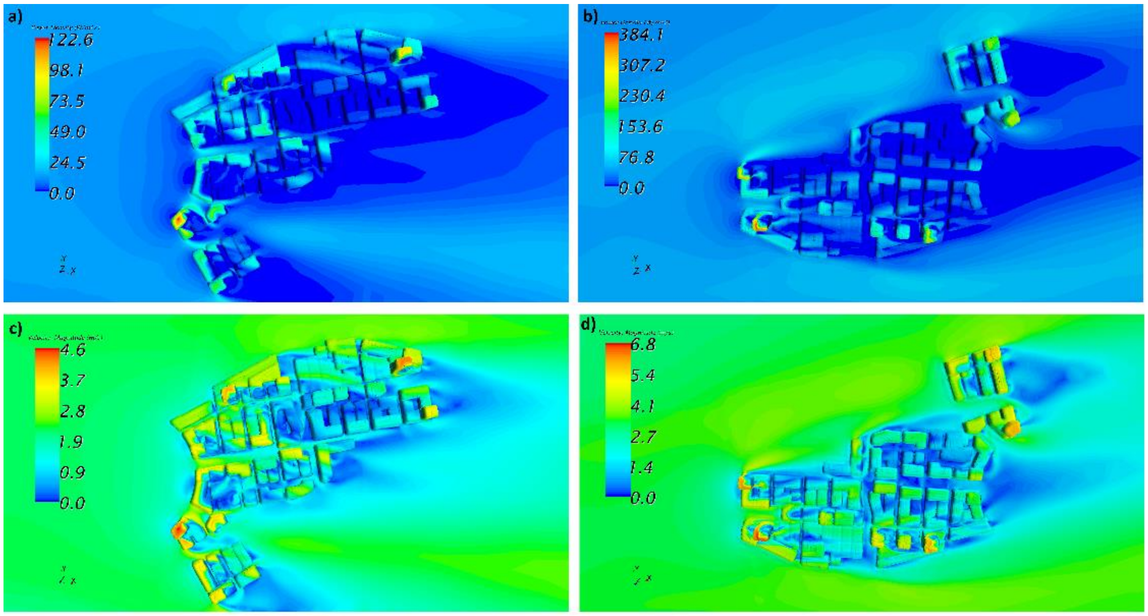

Figure 2-13. Mean power density (upper panels) and wind speed (lower panels) above the buildings and ground for 90° direction (left panels) and 240° direction (right panels). Flow direction is along the *x*-axis.

A generic 30 kW Darrieus type vertical axis wind turbine is selected for wind energy production analysis. Urban areas are highly turbulent regions and thus the horizontal axis wind turbines could not operate at their maximum efficiency in these environments. Table 2-4 shows the technical specifications for the wind turbines selected for this study. In Figure 2-14, the wind turbine power curve is plotted against the wind speed PDF for the windiest site in PanAm Village (roof of B1; the mean annual wind speed of 6.07 m s^{-1} for winds coming in from 240°). The wind speeds between 3 and 5 m s^{-1} have the highest probability of occurrence. The wind turbine, however, starts to generate energy at the speed of approximately 4 m s^{-1}. This de-coupling between the wind speed distribution and the wind turbine power curves is typical for present urban type wind turbines.

Table 2-4. 30 kW generic wind turbine specifications.

Nominal Power	30 kW	Nominal Speed	11.8 m s^{-1}
Rotor Diameter (*D*)	10 m	Cut-in Speed	4 m s^{-1}
Rotor Length (*L*)	8 m	Cut-out Speed	20 m s^{-1}
Hub height	8 m		

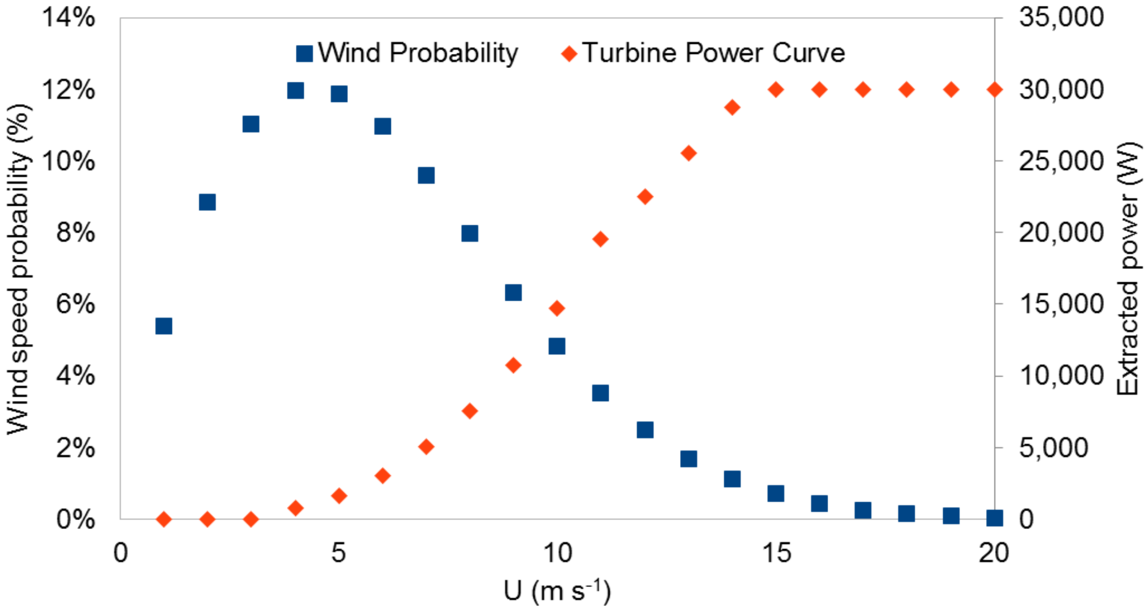

Figure 2-14. The wind probability distribution function and the power curve for the generic 30 kW wind turbine used in this study.

An optimal number of the wind turbines for each of the selected blocks is determined (Table 2-5) based on the windiness of roof tops (Figure 2-13a and Figure 2-13), the roof area of each block (extracted from the design documentation (Urban Design Associates 2006)), and the wind turbine dimensions (Table 2-4). The minimum separation distance between wind turbines is set to be 2 m. P_w over the swept area of all wind turbines in a given block (P_{wt}) is calculated as:

$$P_{wt,i} = L \cdot D \cdot n \cdot \left(\sum_{j=1}^{n} P_{w,i,j} \right), \quad (2\text{-}17)$$

where i is one of the two wind directions (90° or 240°), L is the rotor length of the wind turbine, *D* is the rotor diameter and *n* is the number of wind turbines in a given block. P_{wt} values represent the maximum extractable wind power contained within the swept area of all wind turbines. Considering only the two wind directions selected (90° and 240), it is possible to calculate the annual (maximum) wind energy (E_{am}) for each of the blocks, viz.:

$$E_{am} = \left(P_{wt,90^\circ} \cdot p(90^\circ) + P_{wt,240^\circ} \cdot p(240^\circ)\right) \cdot \frac{365 \cdot 24}{10^6} \quad \left[\frac{\text{MWh}}{\text{year}}\right], \tag{2-18}$$

with $p(90^\circ) = 0.107$ and $p(240^\circ) = 0.215$; $p(\theta)$ is the probability of occurrence of winds coming in from the direction θ. The estimated annual energy required for the selected blocks, E_r, is calculated based on annual averages of 57.05 kWh m^{-2} for residential spaces and 144.24 kWh m^{-2} for commercial (EIA, 2005; see Table 2-5). Areas allocated for the commercial and residential spaces are extracted from the design documentation (Table 2-1). The ratio

$$R_{mr} = \frac{E_{am}}{E_r} \cdot 100 \tag{2-19}$$

represents the theoretical maximum amount of energy at the wind turbine locations that these two wind directions could deliver to the selected blocks in PanAm Village over a 1 year period. Therefore, this ratio is dependent on the wind turbine locations and their size. For instance, R_{mr} would be larger for wind turbines with larger *D* and/or *L*. However, R_{mr} is independent of the power curve characteristics for a given wind turbine. The maximum extractable wind energy to the required power for PanAm Village ranges from about 3%-12% when only the two simulated wind directions 90° and 240° are considered.

Table 2-5. Results of the sustainability analysis for the selected blocks in PanAm Village based only on 90° and 240° wind directions. See text for details.

		Block 1	Block 8	Block 19	Block 20	Block 21	Block 22
Optimal number of wind turbines		4	13	4	4	8	9
P_{wt} (W)	90° wind direction	8547.60	27065.73	10483.60	19537.71	5143.06	30127.95
	240° wind direction	52156.27	93903.22	24899.35	44965.13	49806.53	83549.85
E_{am} (MWh/year)		106.24	202.23	56.72	103.00	98.63	185.60
E_r (MWh/year)		3159.6	4136.3	592.0	1786.1	803.9	2439.2
R_{mr} (%)		3.36	4.89	9.58	5.77	12.27	7.61
E_{ad} (MWh/year)		33.51	64.96	18.83	33.52	32.44	61.45
R_{dr} (%)		1.06	1.57	3.18	1.88	4.03	2.52
UCF		0.32	0.32	0.33	0.33	0.33	0.33

Taking into account the wind turbine power curve, the combined hourly mean power, P_h (kWh/year) is calculated using the following relation:

$$P_h = \sum_{U=U_{cutin}}^{U_{cutout}} P_T(U)\,p(U)\Delta U, \tag{2-20}$$

where, $p(U)$ is the wind speed PDF (Eq. (2-4)) associated only with the two analyzed wind directions, and $P_T(U)$ is the wind turbine power at a wind speed of U. The power curve of a wind turbine can be also estimated using the following equation:

$$P_T(U) = \frac{1}{2}\rho S U^3 C_P, \tag{2-21}$$

with S being the swept area of the wind turbine blades, and C_P is wind turbine power coefficient (it has a typical value of 0.3-0.4). In order to calculate the mean annual energy output for all wind turbines and for each wind direction analyzed in this study, it is necessary to account for the probability of the winds blowing in from these two wind directions. Thus, the mean annual energy production for the two analyzed wind directions (E_{ad}) is:

$$E_{ad} = \left(P_{h,90^\circ} \cdot p(90^\circ) + P_{h,240^\circ} \cdot p(240^\circ)\right) \cdot \frac{365 \cdot 24}{10^3} \quad \left[\frac{\mathrm{MWh}}{\mathrm{year}}\right]. \qquad (2\text{-}22)$$

The methodology described above can be generalized for any number of wind sectors (wind directions) and therefore an estimate of the total extractable wind energy can be obtained. Eq.'s (2-18) and (2-22) in general forms are:

$$E_{am} = \frac{365 \cdot 24}{10^6} \sum_{i=1}^{\theta_{max}} P_{wt,\theta_i} \cdot p(\theta_i) \quad \left[\frac{\mathrm{MWh}}{\mathrm{year}}\right], \qquad (2\text{-}23)$$

where θ_{max} is the total number of wind sectors (directions). Similarly, Eq. (2-22) is now

$$E_{ad} = \frac{365 \cdot 24}{10^3} \sum_{i=1}^{\theta_{max}} P_{h,\theta_i} \cdot p(\theta_i) \quad \left[\frac{\mathrm{MWh}}{\mathrm{year}}\right]. \qquad (2\text{-}24)$$

Values of E_{ad} for each block, but only taking into consideration the two analyzed wind directions, are given in Table 2-5. The ratio between delivered and required energy, R_{dr}, is now:

$$R_{dr} = \frac{E_{ad}}{E_r} \cdot 100. \qquad (2\text{-}25)$$

Note that $R_{dr} < R_{mr}$ because the delivered (or produced) energy from a wind turbine is always smaller than the maximum available energy in the wind. R_{dr} values are presented in Table 2-5. Comparing them with R_{mr}, one can realize the present wind turbines with conventional rooftop installations are able to generate only a fraction of the maximum extractable wind energy. The values of R_{dr} are in the range from 1.1 to 4.0% which is approximately 1/3 of R_{mr}.

The ratio of the maximum extractable wind energy, E_{am}, to the delivered wind energy, E_{ad}, can now be defined as an Urban Capacity Factor (UCF) for a block:

$$UCF = \frac{E_{ad}}{E_{am}}. \tag{2-26}$$

UCF in this study is defined on an annual basis, but it can be defined for any time period as well as for individual buildings or the whole city. The index is always less than unity. Note that $UCF = R_{dr}/R_{mr}$ also holds. UCF values for PanAm Village (Table 2-5) are calculated only for the two selected wind directions. The values are similar to the typical values of the Capacity Factors for wind farms in the rural and countryside regions.

2.4.3 Urban wind turbines limitations

Normally, the wind turbines are designed to start spinning and producing energy at wind speeds in the range of 3-5 m s^{-1} while their nominal speeds are typically 11-15 m s^{-1}. To solve this problem, a different wind turbine design must be used for wind energy production in urban areas. Vertical axis wind turbines (VAWT) have certain characteristics (e.g. wind direction independency) that make them the most suitable for the urban areas. Lift based VAWTs, such as Darrieus wind turbine, are not as sensitive to turbulence compared to the conventional horizontal axis wind turbines. They create less vibration and the frequent change in wind direction does not affect their efficiency. However, the cut-in wind speed for lift based turbines is still not sufficiently low to achieve maximum energy production in urban setups. Drag based VAWTs, e.g. Savonius wind turbine, create less noise and vibration, are less sensitive to turbulence and change in wind direction. They also have the lowest cut-in speeds among all the other wind turbine designs. On the other hand, the drag based VAWTs, become very inefficient in higher wind speeds (Table 2-6).

Table 2-6. Advantages and disadvantages of HAWTs, Lift VAWTs, Drag VAWTs. Source: Wineur (2006).

	HAWT	Lift VAWT	Drag VAWT
Advantages	Efficient. Proven product. Widely used. Most economic. Many products available.	Efficient. Wind direction immaterial. Less sensitive to turbulence than HAWT. Less vibration.	Proven product (globally). Silent. Reliable and robust. Wind direction immaterial. Can benefit from turbulent flows. Create fewer vibrations.
Disadvantages	Does not respond well to frequently changing wind direction. Does not cope well with buffeting.	Not yet proven. More sensitive to turbulence than drag VAWT.	Not efficient. Comparatively uneconomic.

In order to achieve the maximum efficiency in an urban set up, the wind turbine must operate at highest efficiency in both low and high wind speed ranges in the presence of wind turbulence. A solution would be to have a combination of a lift based and drag based VAWT i.e. a combined Savonius-Darrieus wind turbine. The inner part (Savonius turbine blades) would start to spin the main shaft in low wind speeds, while the outer blades (Darrieus turbine) would create torque in higher wind speeds. Such wind turbine concepts exist already (e.g. Sharma et al. (2013)). However, there is a major design problem in this approach. The power available in the wind is proportional to the cube of the wind speed; therefore, if a wind turbine is designed to operate in lower wind speeds, the blades have to sweep a significantly larger area to extract more power from wind. But in the combined Savonius-Darrieus wind turbines, the Savonius wind turbine has to be smaller than the Darrieus turbine in order to fit inside the assembly. Since the Savonius turbine is intended to extract the power of wind in lower speed, the available power is already less that the power available to the outer blades (Darrieus); the smaller size of the Savonius turbine will deteriorate the power output from it and therefore the combined turbine cannot effectively produce power in low wind speeds. Another downside to combined wind turbines are the losses created by the parts which passively disturb the flow and add mass when not operational.

The best solution will be designing a single wind turbine that operates as a drag based turbine in low wind speeds and changes into a lift based design in higher wind speeds. This can be done by using specially designed flexible blades that can shape into different profiles to create airfoils or drag sails. The swept area by the blades in low-speed and high-speed configuration stays nearly constant and the wind turbine can operate efficiently in both wind flow regimes (Gavaldà et al. 1990).

2.5 Concluding remarks

An urban boundary layer analysis and wind energy assessment is performed for the particular case of the Pan-American Games Athletic Village (PanAm Village) planned to be built in an area near the shore of Lake Ontario south of the city of Toronto. The PanAm Village is representative of a new urban development. Detailed wind energy maps are created using the available mesoscale wind simulations (herein Canadian Wind Atlas) as boundary conditions for a micro-scale CFD model.

The flow dynamics is analyzed at the scale of the entire village as well as at scales of individual buildings. Most of the flow characteristics typical for flows around bluff bodies are detected and qualitatively analyzed (flow separation, wake, and reattachment).

The numerical results are also used to calculate the maximum extractable wind energy within the PanAm Village. The annual power required for the buildings are estimated using statistical data available for residential and commercial spaces. Results based on only two wind directions show that the extractable wind power ratio to the required power ranges from 3%-12% depending on the building height, location in the village, wind flow pattern around the buildings, size of the building and the purpose it is designed for.

Annual energy production for some of the blocks of the PanAm Village are calculated using an optimal deposition of generic 30 kW wind turbines and compared to the maximum extractable wind energy. The approach is conservative as it only includes the probabilities associated with only two dominant wind directions. However, the method can be generalized to any number of wind sectors (directions). Based on this approach, the overall energy production is found to be three times smaller compared to the maximum extractable/potential wind energy. The nominal speed and power curve of the available wind turbines demonstrate an important gap between the required rated speed for urban wind energy production and the specifications of the current designs.

References

Allwine, K. J., M. J. Leach, L. W. Stockham, J. S. Shinn, R. P. Hosker, J. F. Bowers, and J. C. Pace, 2004: Joint Urban 2003: study overview and instrument locations. *Symposium on Planning, Nowcasting, and Forecasting in the Urban Zone*, Seattle, Pacific Northwest National Laboratory Oak Ridge http://www.eng.utah.edu/~pardyjak/documents/PNNL_JU03_SummaryReport.pdf (Accessed August 26, 2013).

Bahaj, A. S., L. Myers, and P. A. B. James, 2007: Urban energy generation: Influence of micro-wind turbine output on electricity consumption in buildings. *Energy and Buildings*, **39**, 154–165, doi:10.1016/j.enbuild.2006.06.001.

Castro, I. P., and A. G. Robins, 1977: The flow around a surface-mounted cube in uniform and turbulent streams. *Journal of Fluid Mechanics*, **79**, 307–335, doi:10.1017/S0022112077000172.

CD-Adapco, 2014: STAR-CCM+ User Guide Version 9.02. CD-Adapco, Melville, New York, Computer file (Accessed September 23, 2014).

Cheng, H., and I. P. Castro, 2002: Near wall flow over urban-like roughness. *Boundary-Layer Meteorology*, **104**, 229–259, doi:10.1023/A:1016060103448.

Christen, A., E. van Gorsel, and R. Vogt, 2007: Coherent structures in urban roughness sublayer turbulence. *International Journal of Climatology*, **27**, 1955–1968, doi:10.1002/joc.1625.

Cionco, R. M., 1965: A Mathematical Model for Air Flow in a Vegetative Canopy. *Journal of Applied Meteorology*, **4**, 517–522, doi:10.1175/1520-0450(1965)004<0517:AMMFAF>2.0.CO;2.

——, 1972: A wind-profile index for canopy flow. *Boundary-Layer Meteorology,* **3**, 255–263, doi:10.1007/BF02033923.

Elliott, W. P., 1958: The growth of the atmospheric internal boundary layer. Transactions, *American Geophysical Union*, **39**, 1048–1054, doi:10.1029/TR039i006p01048.

ESDU, 2002a: *Strong winds in the atmospheric boundary layer. Part 1: Hourly mean wind speeds*. ESDU International PLC, London.

ESDU, 2002b: *Strong winds in the atmospheric boundary layer: Part 2: Discrete gust speeds*. 83045. ESDU International PLC, London.

Franke, J., A. Hellsten, K. H. Schlunzen, and B. Carissimo, 2011: The COST 732 Best Practice Guideline for CFD simulation of flows in the urban environment: a summary. *International Journal of Environment and Pollution*, **44**, 419, doi:10.1504/IJEP.2011.038443.

Frey-Buness, F., D. Heimann, and R. Sausen, 1995: A statistical-dynamical downscaling procedure for global climate simulations. *Theoretical and Applied Climatology*, **50**, 117–131, doi:10.1007/BF00866111.

Garratt, J. R., 1978: Flux profile relations above tall vegetation. *Quarterly Journal of the Royal Meteorological Society*, **104**, 199–211, doi:10.1002/qj.49710443915.

——, 1980: Surface influence upon vertical profiles in the atmospheric near-surface layer. *Quarterly Journal of the Royal Meteorological Society*, **106**, 803–819, doi:10.1002/qj.49710645011.

Environment Canada, 2003: *Canadian Wind Energy Atlas [computer file]*. http://www.windatlas.ca/en/index.php (Accessed November 10, 2013).

Gavaldà, J., J. Massons, and F. Díaz, 1990: Experimental study on a self-adapting Darrieus—Savonius wind machine. *Solar & Wind Technology*, **7**, 457–461, doi:10.1016/0741-983X(90)90030-6.

Grimmond, C. S. B., and T. R. Oke, 1999: Heat storage in urban areas: Local-scale observations and evaluation of a simple model. *Journal of Applied Meteorology*, **38**, 922–940, doi:10.1175/1520-0450(1999)038<0922:HSIUAL>2.0.CO;2.

Heath, M. A., J. D. Walshe, and S. J. Watson, 2007: Estimating the potential yield of small building-mounted wind turbines. *Wind Energy*, **10**, 271–287, doi:10.1002/we.222.

Index Mundi, 2013: World Demographics Profile 2013. http://www.indexmundi.com/world/demographics_profile.html (Accessed November 7, 2013).

Jubayer, C. M., and H. Hangan, 2014: Numerical simulation of wind effects on a stand-alone ground mounted photovoltaic (PV) system. *Journal of Wind Engineering and Industrial Aerodynamics*, **134**, 56–64, doi:10.1016/j.jweia.2014.08.008.

Kaltschmitt, M., W. Streicher, and A. Wiese, 2007: *Renewable Energy - Technology, Economics and Environment*. XXXII. Springer, Berlin Heidelberg New York, 564 pp. http://download.springer.com/static/pdf/160/bok%253A978-3-540-70949-7.pdf?auth66=1410992253_4984dee130c697ec5c4907beb05bf5d1&ext=.pdf (Accessed September 15, 2014).

Kanda, M., R. Moriwaki, and F. Kasamatsu, 2004: Large-eddy simulation of turbulent organized structures within and above explicitly resolved cube arrays. *Boundary-Layer Meteorology*, **112**, 343–368, doi:10.1023/B:BOUN.0000027909.40439.7c.

Macdonald, R. W., 2000: Modelling the mean velocity profile in the urban canopy layer. *Boundary-Layer Meteorology*, **97**, 25–45, doi:10.1023/A:1002785830512.

Macdonald, R. W., R. F. Griffiths, and D. J. Hall, 1998: An improved method for the estimation of surface roughness of obstacle arrays. *Atmospheric Environment*, **32**, 1857–1864, doi:10.1016/S1352-2310(97)00403-2.

Menter, F. R., 1994: Two-equation eddy-viscosity turbulence models for engineering applications. *AIAA Journal*, **32**, 1598–1605, doi:10.2514/3.12149.

Menter, F. R., M. Kuntz, and R. Langtry, 2003: Ten years of industrial experience with the SST turbulence model. *The fourth international symposium on turbulence, heat and mass transfer, turbulence heat and mass transfer series,* Vol. Turbulence, heat and mass transfer 4, Begell House, Antalya, 625–632 http://cfd.mace.manchester.ac.uk/flomania/pds_papers/file_pds-1068134610Menter-SST-paper.pdf (Accessed September 23, 2014).

Mertens, S., 2003: The energy yield of roof mounted wind turbines. *Wind Engineering*, **27**, 507–518, doi:10.1260/030952403773617472.

Mertens, S., G. van Kuik, and G. van Bussel, 2003: Performance of an H-Darrieus in the skewed flow on a roof. *Journal of Solar Energy Engineering*, **125**, 433–440, doi:10.1115/1.1629309.

Millward-Hopkins, J. t., A. s. Tomlin, L. Ma, D. Ingham, and M. Pourkashanian, 2012: The predictability of above roof wind resource in the urban roughness sublayer. *Wind Energy*, **15**, 225–243, doi:10.1002/we.463.

Munich Reinsurance Company (Munich Re), 2004: *Megacities - Megarisks: trends and challenges for insurance and risk management*. Munich Reinsurance Company (Munich Re), Munich, Germany, http://www.preventionweb.net/english/professional/contacts/v.php?id=1107 (Accessed December 17, 2013).

Oke, T. R., 1988: The urban energy balance. *Progress in Physical geography*, **12**, 471–508.

Parsons, R., T. H. Kuehn, R. J. Couvillion, J. W. Coleman, N. Suryanarayana, and Z. Ayub, 2005: 2005 *ASHRAE Handbook : Fundamentals : Inch-Pound Edition*. American Society of Heating, Atlanta, GA.

Pletcher, R. H., J. C. Tannehill, and D. Anderson, 1997: *Computational Fluid Mechanics and Heat Transfer*, Second Edition. CRC Press, 828 pp.

Raupach, M. R., A. S. Thom, and I. Edwards, 1980: A wind-tunnel study of turbulent flow close to regularly arrayed rough surfaces. *Boundary-Layer Meteorology*, **18**, 373–397, doi:10.1007/BF00119495.

Rocha, P. A. C., H. H. B. Rocha, F. O. M. Carneiro, M. E. Vieira da Silva, and A. V. Bueno, 2014: k–ω SST (shear stress transport) turbulence model calibration: A case study on a small scale horizontal axis wind turbine. *Energy*, **65**, 412–418, doi:10.1016/j.energy.2013.11.050.

Rodi, W., 1997: Comparison of LES and RANS calculations of the flow around bluff bodies. *Journal of Wind Engineering and Industrial Aerodynamics,* **69–71**, 55–75, doi:10.1016/S0167-6105(97)00147-5.

Romanić, D., M. Ćurić, I. Jovičić, and M. Lompar, 2014: Long-term trends of the "Koshava" wind during the period 1949–2010. *International Journal of Climatology*, **35**, 288-302, doi:10.1002/joc.3981.

Rotach, M. W., 1993: Turbulence close to a rough urban surface part I: Reynolds stress. *Boundary-Layer Meteorology*, **65**, 1–28, doi:10.1007/BF00708816.

——, and Coauthors, 2005: BUBBLE – an Urban Boundary Layer Meteorology Project. *Theoretical and Applied Climatology*, **81**, 231–261, doi:10.1007/s00704-004-0117-9.

Schmid, H. P., H. A. Cleugh, C. S. B. Grimmond, and T. R. Oke, 1991: Spatial variability of energy fluxes in suburban terrain. *Boundary-Layer Meteorology*, **54**, 249–276, doi:10.1007/BF00183956.

Sharma, K. K., A. Biswas, and R. Gupta, 2013: Performance measurement of a three-bladed combined Darrieus - Savonius rotor. *International Journal of Renewable Energy Research (IJRER)*, **3**, 885–891.

Sunderland, K. M., G. Mills, and M. F. Conlon, 2013: Estimating the wind resource in an urban area: A case study of micro-wind generation potential in Dublin, Ireland. *Journal of Wind Engineering and Industrial Aerodynamics*, **118**, 44–53, doi:10.1016/j.jweia.2013.04.002.

Tennekes, H., 1973: The logarithmic wind profile. *Journal of the Atmospheric Sciences*, **30**, 234–238, doi:10.1175/1520-0469(1973)030<0234:TLWP>2.0.CO;2.

Urban Design Associates, 2006: *West Don Lands Block Plan and Design Guidelines*. [computer files and paper documentation].

Versteeg, H., and W. Malalasekera, 2007: *An introduction to computational fluid dynamics: The finite volume method*. 2 edition. Prentice Hall, Harlow, England ; New York, 520 pp.

Wineur, 2006: *Urban wind turbines technology review*. European Commission under the Intelligent Energy - Europe Programme.

Xie, Z.-T., O. Coceal, and I. P. Castro, 2008: Large-eddy simulation of flows over random urban-like obstacles. *Boundary-Layer Meteorology*, **129**, 1–23, doi:10.1007/s10546-008-9290-1.

Yang, R.-J., and W.-J. Luo, 1996: Turbine blade heat transfer prediction in flow transition using k-omega two-equation model. *Journal of Thermophysics and Heat Transfer*, **10**, 613–620, doi:10.2514/3.837.

EIA, 2005: *Annual energy outlook 2005*. U.S. Energy Information Administration, http://www.eia.gov/forecasts/archive/aeo05/ (Accessed December 17, 2013).

Chapter III

3 Wind climatology of Toronto based on the NCEP/NCAR reanalysis 1 data and its potential relation to solar activity

3.1 Introduction

Rapid urbanization is a global phenomenon. In 2014, 54% of the world's population inhabited urban areas (United Nations 2014). The same study reported that the percentage has been even higher in Canada, where 82% of Canadians in 2014 were urban dwellers. In 2015, the Toronto, Montréal and Vancouver regions were home to more than one in three Canadians (Statistics Canada 2015a). Therefore, urban climatology studies are of great public interest worldwide. From dynamic and thermodynamic points of view, urban environments represent rough surfaces that contain many sources and sinks of heat and aerosols. Cities have a large influence on climate conditions at different meteorological scales. For example, the process of urbanization is changing the albedo of Earth's surface and thus the reflectivity of the whole Earth-atmosphere system (IPCC 2013), in addition to the albedo change due to conversion of natural areas to agriculture in rural areas. One of the results of this process is the formation of heat islands above cities (Niino et al. 2006; He et al. 2007; McCarthy et al. 2010). Air flows in urban environments are very complex.

This complexity is due large number of irregularly located, shaped, and spaced objects (Cheng and Castro 2002; Rotach et al. 2005) that act as obstacles to the incoming wind. For that reason, compared to rural areas, winds in cities are generally characterized by higher values of turbulence intensity and smaller mean speeds.

From a practical point of view, urban wind studies are important in urban planning and design (Grimmond et al. 2010). As described by Katzschner (1998), urban climate studies covering different spatial scales have different applications in urban planning. Local- and micro-scale wind studies, for example, are important in analysis of urban climate diversity, quality of living inside and outside, pedestrian comfort, wind loads on buildings as well as urban wind resource assessment. Most of the studies of this type are wind engineering analyses based either on computational fluid dynamics (Clifford et al. 1997; Araújo et al. 2012; Gagliano et al. 2013; Romanić et al. 2015b) or wind tunnel tests (Kozmar 2009; Cheng and Castro 2002; Klein et al. 2010). On the other side, urban wind studies focusing at the regional scales have their practical application in the municipality and city planning (VDI 1997; Baumüller et al. 2012), as well as in the urban development planning (Katzschner 1998; Ren et al. 2011). These studies are typically carried out utilizing mesoscale numerical models (Best 2005) and in-situ and remote sensing meteorological measurements (Grimmond 2005). There are also urban wind studies which cover a broad range of spatial scales simultaneously, i.e. from large scales all the way down to micro-scales (Rotach et al. 2005; Zajaczkowski et al. 2011). A comprehensive overview of urban climate studies can be found in Ren et al. (2011) and Mills (2014).

The body of literature on urban climatology and wind trends is vast (Best 2005; McVicar et al. 2012; Hebbert and Mackillop 2013; Mills 2014). Most studies show that the near-surface winds are slowing down across the globe (McVicar et al. 2012). Vautard et al. (2010) reported that wind speeds in the northern middle latitudes declined between 5% and 15% in the period 1979-2008. They concluded that 25-60% of these negative trends were due to the increase of surface roughness, which in turn is a consequence of the intense urbanization in the last several decades. When it comes to wind climatology studies of Canada, Wan et al. (2010) performed a trend analysis over homogenized wind data obtained from 117 weather stations located across Canada. They reported a negative annual trend of the surface wind speeds in the province of Ontario (-0.058 m s-1 over 10 years). Holt and Wang (2012), however, showed that the winter westerlies at 80 m level in the Great Lake region had large and positive trends in the period from 1979 to 2009 (approximately 0.15 m s-1 over 10 years). A similar trend has also been noticed for southerly winds and it was particularly pronounced in the winter and spring seasons. Potential reasons for the large differences between the results obtained in these two studies are: (1) geographical regions covered in these studies were similar, but not the same, (2) Holt and Wang (2012) analyzed winds at 80 m above ground, whereas Wan et al. (2010) investigated surface data, (3) Wan et al. (2010) used homogenized measurements and Holt and Wang (2012) based their study on the reanalysis data, and (4) the studies did not cover the same time period. Interestingly, an absence of pronounced wind speed trend in the Lake Ontario region is reported by Li et al. (2010). Their analysis is based on a 30-year period of data (1979-2008). A nice overview of wind trend studies can be found in McVicar et al. (2012). The wind trend analysis performed in this paper is based on the National Center for Environmental Prediction/National Center for Atmospheric Research (NCEP/NCAR) reanalysis 1 dataset (Kalnay et al. 1996). The analyzed data cover the period from 1948 to 2014 (67 years).

An additional objective of this study is to analyze the low-frequency spectrum of the wind speed over Toronto. Figure 3-1 is a schematic plot of the wind spectra. The peaks in the spectra correspond to a significant wind speed changes or, more precisely, they represent the time periods at which most of the energy that drives wind is produced. The energy is afterwards transferred to other scales through the process of energy cascade. An important feature in the spectrum is the spectral gap. Its existence enables independent analysis of high-frequency wind fluctuations from the low-frequency wind variability (Jensen 1999). Low-frequency variations are associated with the climatology of the site, while the high-frequency fluctuations are due to localized turbulence (Van der Hoven 1957; Harris 2008). The largest peak in spectra, with an approximate period of 4 days, is caused by the passage of the large-scale pressure systems over the measuring site. Namely, it can be seen investigating synoptic charts that the typical period of cyclone passages in mid-latitudes is 2-4 days (Trigo et al. 1999). The 12-hour peak is associated with the diurnal temperature pattern. However, this local maximum is not always present as it is largely site-specific (Harris 2008). The lowest frequency peak with the period of 1 year had not been originally detected in the paper published by Van der Hoven (1957) since it was unobtainable from his data that covered 1 year of wind measurements. Instead, the existence of the peak is noticed for the first time in the study by Gomes and Vickery (1977). This annual pattern is due to the change of seasons thorough the year and, as such, it usually ceases to exist in the tropical regions and close to the equator. The present study focuses on investigation of the macrometeorological wind spectrum with periods larger than 1 day.

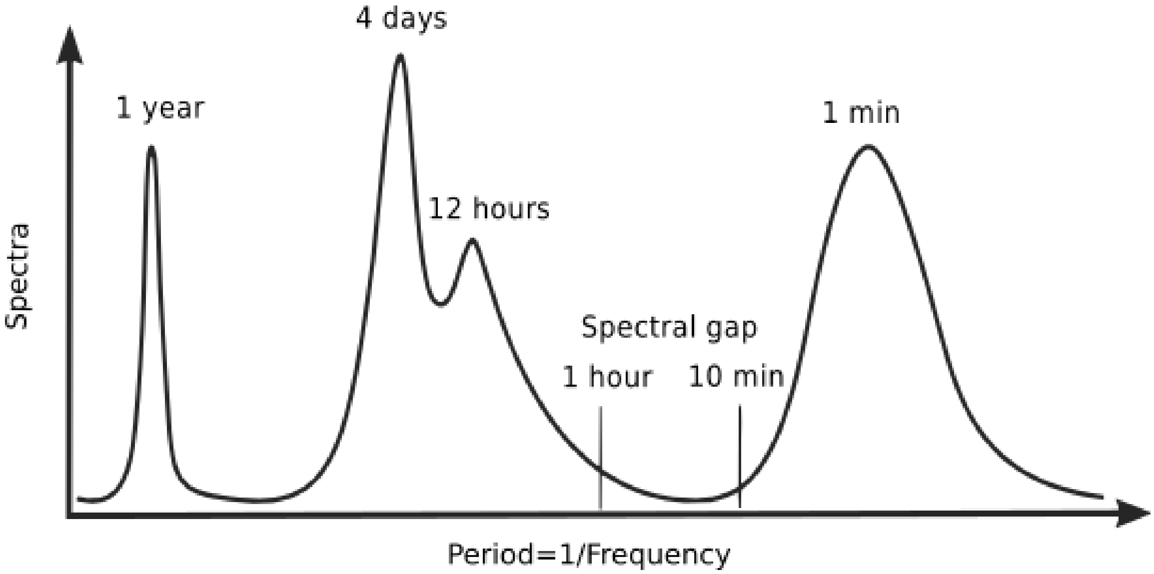

Figure 3-1. A schematic sketch of the wind energy spectrum. Modified after Van der Hoven (1957) and Harris (2008).

The goal of this paper is to investigate the wind climatology of the city of Toronto, Ontario, Canada from the regional scale perspective. To be more specific, the study is focused on the following topics: (1) wind speed and wind direction climatology, (2) wind power analysis, (3) wind speed and wind occurrence trends (4) spectral analysis of wind speed time series in low-frequency domain, and (5) wind speed autocorrelation analysis. The results could have practical implications in various areas of urban sustainability and resilience of Toronto. First, a straightforward application of the first two research goals is in the field of the urban wind resource assessment. In a recent study, Romanić et al. (2015b) analyzed the wind energy potential for the 2015 Pan American Games Athletes' Village, located in downtown Toronto. Defining the Urban Capacity Factor as the ratio of the maximum extractable wind energy to the delivered wind energy for a city block, they concluded that two wind directions (240° and 90°) can supply up to 5% of the total required energy of this urban development. Second, wind trend analyses have important applications in wind power sector not only on a city scale, but on the larger scales too (Romanić et al. 2015a). Lastly, the results presented in this study can be used to improve planning and design of the City of Toronto. For instance, wind direction analysis contributes to better understanding of the ventilation and pollutant dispersion patterns in Toronto (Sabaliauskas et al. 2015).

3.2 Data and methodology

3.2.1 Study area

Toronto, the provincial capital of Ontario, Canada, is located on the northwest shore of Lake Ontario. The city had a population of 2,826,498 people in July of 2015 (Statistics Canada 2015b). This figure makes Toronto the fourth most populous city in North America and the largest city in Canada. The City of Toronto stretches over an area of 630 km2. From the socio-economic point of view, Toronto represents a global center for business and it is one of the most multicultural cities around the world.

Based on the Köppen-Geiger climate classification, Toronto sits in a Dfa climate zone (Peel et al. 2007). This continental type of climate is characterized by hot and humid summers accompanied with cold winters that are consequence of the large influence of the continental surface. However, the presence of Lake Ontario brings generally mild winters compare to other continental cities in Canada.

3.2.2 Data

The wind data used in this study are obtained from the NCEP/NCAR reanalysis 1 dataset (Kalnay et al. 1996). These data are the product of an advanced analysis and forecast system which performs data assimilation starting from 1948 to the present. The data cover the whole globe with a 2.5° latitude by 2.5° longitude spatial resolution and with 4 times a day, daily, and monthly temporal availabilities. This study is conducted using the mean daily values for two wind components (zonal, u, and meridional, v) above Toronto for the time period from January 1, 1948 to December 31, 2014.

The NCEP/NCAR reanalysis have been used in a large number of meteorological studies (over 20,000 peer-reviewed articles) and the number of wind-related studies based on this dataset is large (e.g. Troccoli et al. 2012; Dadaser-Celik and Cengiz 2014; Romanić et al. 2015a). Inhomogeneities in the dataset are small and constant over time in the Northern Hemisphere (Sterl, 2004). The constant inhomogeneities, if any, therefore do not influence intensities of calculated trends. The high-quality of the reanalysis dataset in the Northern Hemisphere is due to high density of the meteorological observational network in these parts of the world. Although this dataset has been used in numerous trend analysis studies around the globe, it has not yet been used for wind trend analysis in the Toronto area. Figure 3-2 shows the locations of weather stations in the wide region around Toronto obtained from Environment and Climate Change Canada (2014) for Canada and NOAA (2015) for the United States. The weather station network around Toronto is very dense with the total of 51 weather stations in the reanalysis cell in which Toronto is located. There are around 10 urban weather station in the Greater Toronto area. The weather stations in

Buffalo and Rochester in the United States are also representatives of urban climate in the area. The largest part of Lake Ontario and a part of Lake Erie are situated in the considered reanalysis cell. This diversity of land cover is important since the climate of Toronto is highly influenced by the presence of the surrounding lakes. It is important to note here that reanalysis data are created using an unchanged data assimilation scheme and numerical models which incorporate all available observations every 6 to 12 hours over the analyzed period. The unchanging methodology ensures that the climatological outputs are dynamically consistent at each time step. Over the time, however, more data from new sources are added in assimilation.

The main reasons behind using the NCEP/NCAR reanalysis 1 dataset in this study instead of observations or some other reanalysis data are the following. First, some aspects of wind climatology based on surface measurements and observations have already been investigated by other researchers, such as Wan et al. 2010, and there is no need to repeat these comprehensive analyses. Second, the NCEP/NCAR reanalysis 2 and the North American Regional Reanalysis (NARR) datasets go back to the 1970s, while reanalysis 1 data are from 1948. A longer dataset is more suitable for a long-term trend analysis. Furthermore, a trend analysis using NARR data has already been performed by Li et al. (2010). Lastly, it will be insightful to compare the results of this study with the findings reported by other researchers who used different datasets to conduct their studies. Therefore, this paper nicely fills the gap in the literature providing a comprehensive Toronto wind climatology analysis based on reanalysis 1 data.

3.2.3 Methodology

3.2.3.1Data processing and statistical analyses

Wind characteristics above Toronto are calculated from the four nearest reanalysis grid points applying the bilinear interpolation as shown in Figure 3-2 and mathematically represented as:

$$f(x,y) = f_{P(1,1)}(1-dx)(1-dy) + f_{P(1,2)}dx(1-dy) + f_{P(2,1)}dy(1-dx) + f_{P(2,2)}dxdy. \qquad (3\text{-}1)$$

Here f is any variable calculated at the point (x, y) in Cartesian coordinates (see Figure 3-2 for further details). Nearest neighbor method was also used to obtain the wind data above Toronto. Although the results are not shown, they are briefly discussed in Section 3.4.1 in relation to the wind trend results presented in this study. Nearest neighbor interpolation method assigns the value from the nearest grid point and therefore it is more appropriate for categorical data (e.g. land use categories). For that reason this study relies on the bilinear method of spatial interpolation. More complex interpolation methods also exist, such as the cubic spline. One of the advantages of bilinear method is that it interpolates the data in a predictable way. That is, the interpolated value is always within the range of the values in the four neighboring points. Keeping in mind that the goal of this paper is to investigate winds above an urban environment, it is not reasonable to expect that the interpolated urban wind speeds should exceed wind speeds in the reanalysis grid points that are positioned in rural areas or above water surfaces (Figure 3-2). Such outcome, however, would be possible using higher-order interpolation methods. Bilinear interpolation has been used in many climatological and downscaling studies (e.g. Bergant and Kajfež-Bogataj 2006; Benestad 2010; Kumar et al. 2015; Haan et al. 2015).

Furthermore, the bilinear method is computationally more efficient than the cubic spline. This factor can play an important role in the studies that use large sets of data, such as this study.

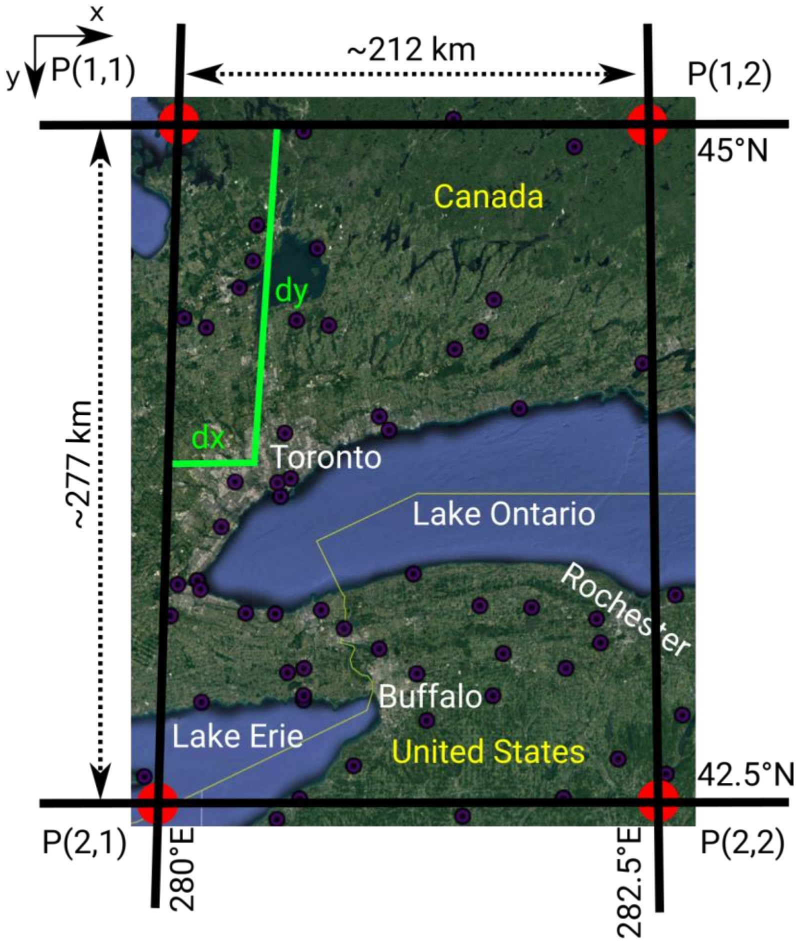

Figure 3-2. Schematics of bilinear interpolation method used in this study with geographic coordinates of Toronto: LON 280.545°E, LAT 43.653°N. The four nearest reanalysis grid points to Toronto are indicated with the red circles: P(1,1), P(1,2), P(2,1), P(2,2). The distances from the meridional and zonal grid lines are dx and dy, respectively. The nearest reanalysis grid point to Toronto is P(2,1) with the distance of about 140 km. The purple dots depict the positions of weather stations in the considered area.

The extracted wind data are at the sigma-995 level (σ_{995}). Sigma is a vertical pressure-based coordinate frequently employed in meteorology. It is defined as a ratio of the pressure at a given point in the atmosphere to the surface pressure beneath; thus $\sigma = 1$ at the surface and $\sigma = 0$ at the top of the atmosphere. It follows that $\sigma = 0.995$ represents a level in the atmosphere where the pressure is 99.5% of the surface pressure. The mean daily wind speed at σ_{995} level is calculated from the two wind components as:

$$V_{\sigma 995}(u_{\sigma 995}, v_{\sigma 995}) = \sqrt{u_{\sigma 995}^2 + v_{\sigma 995}^2}. \tag{3-2}$$

The mean daily wind direction at σ_{995} is also obtained through $u_{\sigma .995}$ and $v_{\sigma .995}$ components i.e.:

$$D_{\sigma 995}(u_{\sigma 995}, v_{\sigma 995}) = \frac{180}{\pi}\left(2\tan^{-1}\frac{\sqrt{u_{\sigma 995}^2 + v_{\sigma 995}^2} - v_{\sigma 995}}{u_{\sigma 995}} + \pi\right). \tag{3-3}$$

The height of the σ_{995} level ($z_{\sigma 995}$) is calculated using the barometric equation:

$$z_{\sigma 995} = \frac{R^* \bar{T}}{Mg} \ln\left(\frac{p_s}{p_{\sigma 995}}\right), \tag{3-4}$$

where, $R^* = 8.314$ J (mol K)$^{-1}$ is the universal gas constant, $M = 0.029$ kg mol^{-1} is the molar mass of air, g = 9.81 m s^{-2} is the gravitational acceleration, $p_{\sigma 995} = 0.995 \cdot p_s$ is the pressure at the σ_{995} level, p_s is the surface pressure and $\bar{T} = 0.5(T_{2m} + T_{\sigma 995})$ is the average temperature in the layer between the surface and the σ_{995} level. In order to calculate $z_{\sigma 995}$ using Eq. (3-4), the following variables have also been obtained from the reanalysis dataset: p_s, T_{2m}, and $T_{\sigma 995}$. The air density ($\rho_{\sigma 995}$) is afterwards calculated from the ideal gas law.

Weibull distribution is used to describe the observed wind speed distribution. It has the probability density function (f_{WD}) defined as:

$$f_{WD}(V_{\sigma 995}) = \left(\frac{k}{A}\right)\left(\frac{V_{\sigma 995}}{A}\right)^{k-1} e^{-\left(\frac{V_{\sigma 995}}{A}\right)^{k}}, \tag{3-5}$$

where parameters k and A are the Weibull shape and scale parameters, respectively. The parameters are estimated from wind data using the maximum likelihood method (Harris and Stöcker 1998).

Wind power density ($P_{\sigma .995}$) is then calculated as (Troen and Petersen 1989):

$$P_{\sigma 995} = \frac{1}{2}\rho_{\sigma 995} A^{3}\Gamma\left(1+\frac{3}{k}\right), \tag{3-6}$$

where Γ is the gamma function which represents a generalization of the factorial function. The mean wind speed, Weibull parameters and wind power density are calculated for 12 wind directions as well as on the seasonal and annual bases.

The Mann-Kendall non-parametric test for trend (Mann 1945; Kendall 1970) and Sen’s slope technique (Sen 1968) are used to detect and estimate trends in data. These two methods are widely used in climatological studies (e.g. Liuzzo et al. 2014; Romanić et al. 2015a; Romanic et al. 2016). The two-tailed Mann-Kendall test inspects the null hypothesis of the absence of trend in the time series at an s significance level. Rejection of the null hypothesis at the significance level of $s = 0.1$, 0.05, 0.01, and 0.001 is indicated as $H = 1$, 2, 3 and 4 in this study, respectively. For instance, if $s = 0.001$ there is only a 0.1% chance that the observed trend is random and therefore the existence of a monotonic and statistically significant trend is very likely. The acceptance of the null hypothesis and the absence of trend is indicated as $H = 0$. Sen’s slope method applies the median slope (Q)

among all the slopes determined by all pairs of data points. The trend analyses in this study are performed over 12 wind directions and they are also conducted on seasonal and annual bases. The trend analysis is performed over 12 wind directions and the study is conducted on seasonal and annual bases.

Lastly, this study also uses a moving average method to inspecting the variability of data series as well as a cross-correlation analysis to quantify the statistical similarity between two sets of data. For a time series a_i (i *=1, 2, ..., N*), an *n*-moving average, s_i, is defined as:

$$s_i = \frac{1}{n}\sum_{j=1}^{i+n-1} a_j. \tag{3-7}$$

The cross-correlation of two functions $f(t)$ and $g(t)$, where t is time, is defined as:

$$f \star g = \bar{f}(-t) * g(t), \tag{3-8}$$

where $*$ represents the convolution operation and $\bar{f}(t)$ is the complex conjugate of $f(t)$. If the time series are real, such as the one used in this paper, the cross-correlation analysis Eq. (3-8) can be written as:

$$f \star g = \int_{-\infty}^{\infty} f(\tau)g(t+\tau)d\tau, \tag{3-9}$$

where τ is the time lag. For two finite time series and in the discrete domain Eq. (3-9) reads:

$$f \star g = \sum_{n=0}^{N-m-1} f_n g_{n+m}. \tag{3-10}$$

Here, N is the lengths of the time series (i.e. number of elements) and m is the time lag in the discrete domain. In this paper, Eq. (3-10) is normalized so that the autocorrelations at zero lag equal 1 (Stoica and Moses, 2005):

$$c(m) = \frac{1}{\sqrt{R_{ff}(0)R_{gg}(0)}} f \star g, \tag{3-11}$$

where R_{ff} and R_{gg} represent the autocorrelation functions of f and g, respectively, and $c(m)$ is the cross-correlation coefficient at time lag m. Note that the autocorrelation is nothing more but cross-correlating a function with itself; that is: $f \star f$ or $g \star g$ in Eq. (3-9). A value of $c(m) = 1$ would indicate that at time lag m the two time series have identical shape, however the magnitudes might differ. On the other hand, $c(m) = -1$ depicts two time series that have the same shape, but opposite signs. Lastly, $c(m) = 0$ indicates the complete lack of correlation, i.e. time series are uncorrelated. Cross-correlation coefficients above approximately 0.75 indicate a strong correlation between the two records.

3.2.3.2 Spectral analysis

Spectral analysis of wind signal describe the distribution of harmonic content in wind over the range of frequencies. This paper uses the non-parametric Welch method (Welch 1967) to calculate the power spectral density. The method is widely used in engineering and signal processing studies as it reduces the noise in estimated power spectra compared to the standard methods of averaged periodograms. Namely, the Welch method partitions a time series (X) into K batches ($X_k,\ k = 1, 2, \dots, K$), each of length L, and calculates a modified periodogram for these segments through the finite Fourier transforms $A_k(n)$:

$$A_k(n) = \frac{1}{L} \sum_{j=0}^{L-1} X_k(j)\, W(j) e^{-\frac{2kijn}{L}}. \tag{3-12}$$

Here, $n = 0, 1, \dots, L/2$, $i = \sqrt{-1}$ is the imaginary unit $W(j)$, $(j = 0, 1, \dots, L-1)$ is the Hamming window used to multiply the periodograms in order to produce a clearer spectra;

hence the name modified pereiodograms. Repeating this procedure for each segment, one obtains K modified periodograms:

$$I_k(f_n) = \frac{L}{U}|A_k(n)|^2, \tag{3-13}$$

where $f_n = n/L$ and the noise gain, U:

$$U = \frac{1}{L}\sum_{j=0}^{L-1} W^2(j). \tag{3-14}$$

Lastly, an average of modified periodograms produces the estimate of the power spectral density:

$$S(f_n) = \frac{1}{K}\sum_{k=1}^{K} I_k(f_n). \tag{3-15}$$

Due to the underlying assumption that the process is stationary and Welch's method uses power spectral density estimates of different segments of the time series, the modified periodograms represent approximately uncorrelated estimates of the true power spectral density and therefore averaging reduces the variability. The Hamming window in Eq. (3-12) is defined as:

$$W(j) = 0.54 - 0.46\cos\left(2\pi\frac{j}{N}\right). \tag{3-16}$$

The data is divided into 8 segments with 50% overlap between them. The described methodology is applied to generate the macrometeorological wind speed power spectra.

3.3 Results

3.3.1 Wind climatology

Seasonal and annual wind climatology for Toronto based on the NCEP/NCAR reanalysis 1 data (Kalnay et al., 1996) at the σ_{995} level is presented in Figure 3-3. It can be observed that winds coming in from the third quadrant are the most frequent in summer, fall and winter and thus on the overall annual basis. Together they occur about 45% of the time in year. Dominant wind direction in these seasons is 240° ($V_{\sigma 995}^{240°}$). In fall, the frequency of occurrence of the $V_{\sigma 995}^{240°}$ winds is very similar to the occurrence of the $V_{\sigma 995}^{210°}$ winds. The occurrence of the $V_{\sigma 995}^{240°}$ winds on annual basis is approximately 18% of the time. The most frequent winds in spring are the $V_{\sigma 995}^{270°}$ winds (18% of the time), closely followed by the $V_{\sigma .995}^{240°}$ and $V_{\sigma 995}^{300°}$° winds (each present in 17% of the time). Winds coming in from the first and the fourth quadrants were rare. For example, the $V_{\sigma 995}^{90°}$ winds were present only 4% of the time in year. It can be observed that wind rose in spring is more omnidirectional compared to the other seasons and the annual case. Figure 3-3 also shows the distribution of wind speeds for each of 12 wind directions. The strongest winds are observed in winter ($\bar{V}_{\sigma 995}$=5.61 m s^{-1}) and the strongest winds are coming in from 240° direction. Interestingly, the winter $V_{\sigma 995}^{240°}$ winds in the 8-10 m s^{-1} interval have the similar occurrence as the winds in 6-8 m s^{-1} range; each wind speed bin being present in approximately 5% of the time in winter. The weakest winds are observed in summer with speeds rarely exceeding 8 m s^{-1}, i.e. in only about 2% of the time.

The mean annual wind speed over Toronto at the σ_{995} level is 4.83 m s^{-1}. Inter-annual variability of wind speed is such that the spring and summer seasons have lower wind speeds compared to the fall and winter seasons. Standard deviation of the inter-annual wind speed oscillation is 0.63 m s^{-1}, which in relative terms is equal to 13% of the mean annual wind speed. This value of variation is typical for the extra-tropical latitudes. The same values of *k*, but different values of *A* Weibull parameters are observed in spring and fall seasons. A larger value of *A* in fall results in the probability density function (PDF) being more stretched out compared to the PDF in spring. Consequentially, the peak of the PDF for the fall season is smaller. The mean power density over Toronto at the σ_{995} level is equal to 123.2 W m^{-2}. The inter-annual standard deviation is 48.4 W m^{-2} (38.6% of the mean value). Difference between wind power density in winter (190.7 W m^{-2}) and summer (56.3 W m^{-2}) is very pronounced (134.4 W m^{-2}). Detailed wind statistics per direction and for each season, as well as on the annual basis, are given in Table 3-1.

The strongest winds in all seasons are from the 240° direction. The overall largest mean wind speed is observed in winter for the $V_{\sigma995}^{240°}$ winds (6.62 m s^{-1}). The smallest wind speeds are reserved for the 90° direction in summer (2.82 m s^{-1}). The second windiest directions are the two adjacent directions to the 240° direction. From the wind energy point of view, these three wind directions alone contribute to 60% of the overall annual power density presented in Figure 3-3. The smallest variability of the Weibull *k* parameter is observed in spring and the largest in winter season. This variability of *k* parameter indicates that wind speeds in spring are more uniformly distributed among all wind directions, whereas winds in winter are mostly associated with a few wind directions. This pattern is also evident examining Figure 3-3.

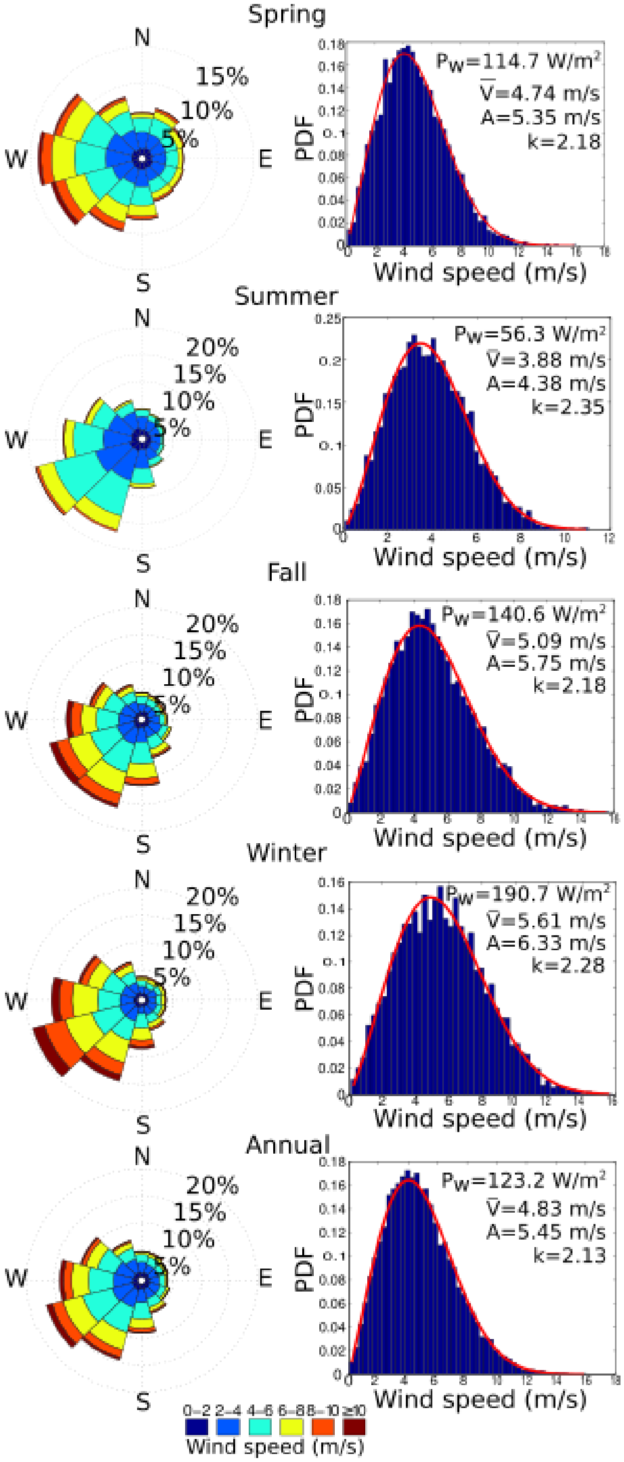

Figure 3-3. Seasonal and annual wind climatology for Toronto at the σ_{995} level. $\bar{V}$ - mean wind speed, A and k – Weibull scale and shape parameters, respectively, and P_w- mean wind power density

Table 3-1. Sector-wise wind statistics for Toronto for each season and on an annual basis. All values are given at the σ_{995} level.

Wind direction (°)	Spring				Summer				Fall				Winter				Annual			
	$\bar{V}$ (m s^{-1})	A (m s^{-1})	k	P_w (W m^{-2})	$\bar{V}$ (m s^{-1})	A (m s^{-1})	k	P_w (W m^{-2})	$\bar{V}$ (m s^{-1})	A (m s^{-1})	k	P_w (W m^{-2})	$\bar{V}$ (m s^{-1})	A (m s^{-1})	k	P_w (W m^{-2})	$\bar{V}$ (m s^{-1})	A m s^{-1})	k	P_w (W m^{-2})
0	3.97	4.49	2.32	64.93	3.28	3.70	2.22	35.85	4.08	4.58	1.96	79.54	4.25	4.79	2.11	89.48	3.87	4.36	2.10	64.44
30	4.37	4.92	2.12	92.09	3.26	3.68	2.21	35.50	4.06	4.58	1.88	83.31	4.39	4.95	2.01	103.68	4.05	4.57	1.99	78.40
60	4.18	4.72	2.10	81.42	3.22	3.64	2.24	34.00	4.04	4.56	2.01	76.52	4.16	4.68	1.99	88.91	3.94	4.45	2.03	70.93
90	3.97	4.48	2.17	67.48	2.82	3.19	2.32	22.02	3.59	4.05	2.07	51.92	4.15	4.69	2.08	84.71	3.69	4.17	2.05	57.43
120	4.00	4.52	2.09	71.11	2.84	3.20	2.20	23.34	3.70	4.17	2.17	54.06	4.02	4.53	2.01	78.37	3.69	4.17	2.03	57.68
150	4.32	4.88	2.07	89.57	3.11	3.51	2.06	32.44	4.64	5.25	2.25	103.38	4.66	5.26	2.26	108.89	4.24	4.78	2.06	85.25
180	4.52	5.11	2.23	96.18	3.73	4.20	2.42	48.58	5.20	5.85	2.55	130.84	5.79	6.51	2.61	185.61	4.84	5.46	2.29	115.22
210	5.23	5.90	2.33	142.34	4.35	4.89	2.72	71.04	5.60	6.31	2.54	163.75	6.09	6.85	2.61	217.94	5.29	5.97	2.41	144.38
240	5.47	6.16	2.27	167.99	4.42	4.97	2.66	75.43	5.96	6.72	2.35	210.85	6.62	7.44	2.63	280.27	5.61	6.33	2.30	180.27
270	5.26	5.93	2.34	147.49	4.22	4.74	2.64	66.22	5.80	6.54	2.36	195.69	6.26	7.04	2.50	246.46	5.40	6.09	2.29	162.78
300	4.92	5.56	2.34	123.24	3.89	4.39	2.37	56.66	5.03	5.69	2.25	134.05	5.53	6.23	2.54	170.98	4.85	5.48	2.27	120.19
330	4.62	5.22	2.24	105.40	3.39	3.83	2.12	41.46	4.42	4.99	2.25	90.42	4.75	5.36	2.26	118.90	4.31	4.86	2.13	88.67

3.3.2 Wind trends

3.3.2.1 Wind speed trends

Figure 3-4 shows the direction-wise wind speed trends over Toronto at the σ_{995} level and the quantitative details of the observed trends are given in Table 3-2. Only winds coming in from the 90°, 150°, 180°, and 330° directions had negative trends. However, these trends are not statistically significant, as indicated by the zero values of H and near-zero Z statistics. The strongest positive trends with Sen's slope equal to 0.021 m s^{-1} $year^{-1}$ and 0.015 m s^{-1} $year^{-1}$ are detected for the $V_{\sigma 995}^{30°}$ and $V_{\sigma 995}^{60°}$ winds, respectively. Therefore, the $V_{\sigma 995}^{30°}$ winds have increased their speed for 1.41 m s^{-1} in the period from 1948 to 2014 (0.21 m s^{-1} per decade).The windiest directions, $V_{\sigma 995}^{240°}$ and $V_{\sigma 995}^{270°}$, have also experienced statistically significant upward trends. Sen's slope of the trend for these two winds is the same and equal to 0.008 m s^{-1} $year^{-1}$. Therefore, the $V_{\sigma 995}^{240°}$ winds have increased for 0.54 m s^{-1} in the analyzed 67-year period. It is important to note that the positive trends of the $V_{\sigma 995}^{240°}$ and $V_{\sigma 995}^{270°}$ winds are significant at the 99% confidence level, as indicated by H=3 values in Table 3-2. The positive trend of northern winds is also fairly significant (H=1). The moving averages in Figure 3-4, however, seem to indicate that the windiest directions (210°, 240° and 270°) were fairly trendless after about year 2000. The strong upward trends for $V_{\sigma 995}^{0°}$, $V_{\sigma 995}^{30°}$ and $V_{\sigma 995}^{60°}$ are also noticeable in the moving average trend.

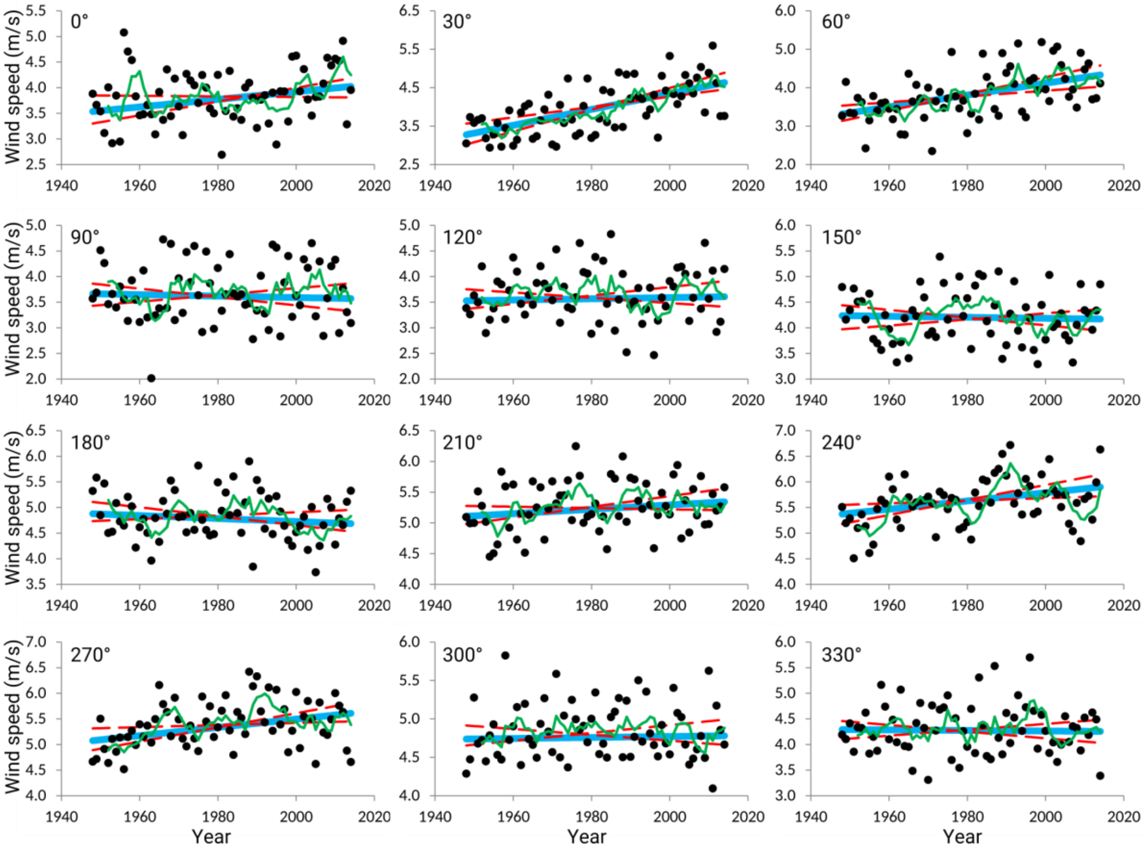

Figure 3-4. Mean annual wind speeds for each wind direction. The blue lines are Sen's slope (m s^{-1} $year^{-1}$) and the red dashed lines are trends at the 95% confidence intervals and the green lines are a 5-year moving average. See Table 3-2 for additional details.

The trend analysis of the omnidirectional mean annual wind speed series is presented in Figure 3-5 and in the last row in Table 3-2. A positive and statistically significant trend at the 95% confidence level ($H = 2$) is observed. Sen's slope is equal to 0.003 m s^{-1} $year^{-1}$. This trend reflects as a wind speed increase of 0.2 m s^{-1} in the period 1948-2014. The most important contributors to this small wind speed increase are positive trends of the $V_{\sigma 995}^{30^\circ}$, $V_{\sigma 995}^{60^\circ}$, $V_{\sigma 995}^{240^\circ}$ and $V_{\sigma 995}^{270^\circ}$ winds, as described in the previous paragraph. Note, however, that the trend of the mean annual wind speed at the lower 99% confidence level is trendless

(Q_{min99} = 0). The 5-year moving average series in Figure 3-5 has an increasing trend until the 1990s and is relatively trendless afterwards. A periodicity in the moving average line can be observed. The first six peaks (in years 1952, 1961, 1969, 1977, 1985 and 1991) have the period between 7 and 9 years, whereas the periodicity of the last three peaks is 11 years (years 1991, 2003 and 2014). This result shows the presence of the interdecadal variability of the mean annual wind speeds above Toronto. Figure 3-4 further depicts that the strongest winds above Toronto were present in the early 1990s and the late 1980s.

Table 3-2. Trend analysis of the mean seasonal wind speeds and the mean annual wind speeds for each wind direction and overall (last row). Subscripts denote different significance level, B is the offset of the linear trend line (m s^{-1}), Q is the slope of the trend (m s^{-1} $year^{-1}$) and the meaning of other symbols is given in the text. All values are given at the σ_{995} level. Graphical representations of these trends are shown in Figure 3-4, Figure 3-5 and Figure 3-6.

Wind speed series	Z	H	Q	Q_{min99}	Q_{max99}	Q_{min95}	Q_{max95}	B	B_{min99}	B_{max99}	B_{min95}	B_{max95}
0°	1.83	1	0.007	-0.003	0.016	-0.001	0.013	3.54	3.91	3.27	3.85	3.30
30°	5.26	4	0.021	0.011	0.031	0.014	0.028	3.28	3.66	2.91	3.57	3.02
60°	4.05	4	0.015	0.006	0.025	0.007	0.022	3.32	3.59	3.05	3.53	3.14
90°	-0.34	0	-0.001	-0.011	0.010	-0.008	0.007	3.67	4.01	3.34	3.86	3.43
120°	0.32	0	0.001	-0.007	0.010	-0.005	0.008	3.53	3.83	3.31	3.75	3.37
150°	-0.23	0	-0.001	-0.010	0.008	-0.008	0.006	4.24	4.53	3.88	4.44	3.97
180°	-0.80	0	-0.003	-0.011	0.005	-0.009	0.003	4.88	5.15	4.69	5.11	4.73
210°	1.50	0	0.004	-0.003	0.010	-0.001	0.009	5.11	5.36	4.95	5.28	4.98
240°	2.74	3	0.008	0.001	0.017	0.003	0.015	5.37	5.59	5.12	5.55	5.18
270°	2.59	3	0.008	0.000	0.015	0.002	0.014	5.08	5.37	4.87	5.31	4.89
300°	0.36	0	0.001	-0.005	0.007	-0.004	0.005	4.74	4.97	4.60	4.91	4.65
330°	-0.14	0	-0.001	-0.009	0.008	-0.006	0.006	4.29	4.53	4.03	4.46	4.10
Spring	-0.95	0	-0.002	-0.006	0.003	-0.005	0.002	4.77	4.89	4.68	4.87	4.71
Summer	-0.52	0	-0.001	-0.005	0.004	-0.004	0.003	3.91	4.09	3.77	4.05	3.79
Fall	4.21	4	0.012	0.006	0.019	0.007	0.017	4.65	4.89	4.46	4.81	4.51
Winter	1.67	1	0.004	-0.002	0.011	-0.001	0.009	5.46	5.66	5.21	5.61	5.28
Annual	2.45	2	0.003	0.000	0.007	0.001	0.006	4.71	4.86	4.59	4.83	4.61

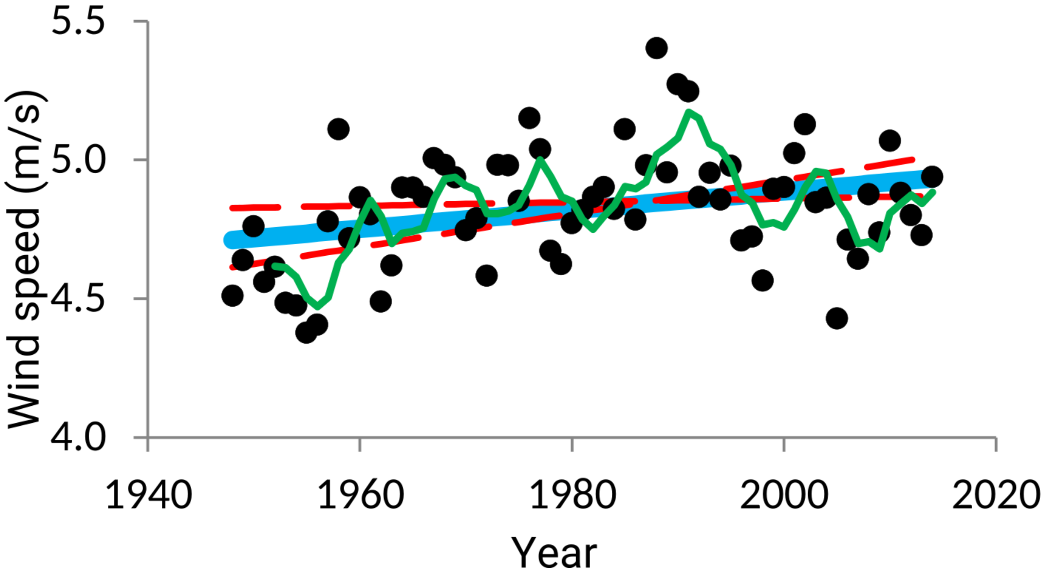

Figure 3-5. Mean annual wind speeds for all wind directions and the associated trends. See Figure 3-4 and Table 3-2 for nomenclature and further details.

Further analysis is conducted in order to determine the seasonal wind speed trends. The results presented in Figure 3-6 and Table 3-2 highlight some interesting findings. Namely, wind speeds in the warm half of the year (spring and summer) have almost negligible and statistically not significant trends with slightly negative Sen's slopes. On the other hand, wind speeds in the cold part of the year (fall and winter) have experienced a strong and positive trend of 0.08 m s^{-1} per decade on average (0.54 m s^{-1} over the whole analyzed period). The positive trend in fall season is significant at the 99.9% confidence level (H = 4) while the winter wind speed trend is significant with the 95% statistical confidence. It can also be seen that the trend of mean annual wind speed is similar to the trend of winter winds. Furthermore, trend in the annual winds is half of the average of the winter and fall trends. This result is somewhat expected, since an average of the seasonal trends should approximately, but not necessarily identically, result in the observed trend of the annual wind. The observed positive trends of the winter and fall winds, as well as the positive trends of the windiest directions, are for example important in wind energy. Namely, these positive trends might contribute to long-term stability and sustainability of urban wind energy projects in the Toronto and nearby regions as the future positive trends in surface wind speeds in this region are predicted by climate change models (McInnes et al. 2011). Similar to the moving average trend in Figure 3-4, there seem to be an absence of moving average trends in the summer, fall and winter seasons after approximately the year 2000. On the contrary, a negative trends in the last about 15 years is noticed in the spring season.

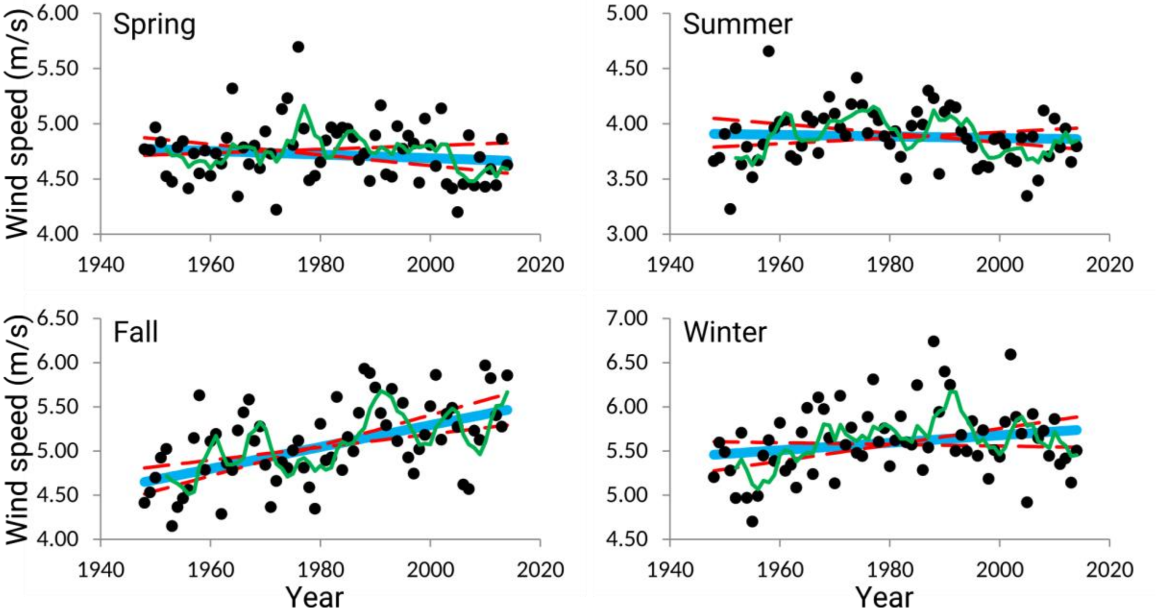

Figure 3-6. Mean annual wind speeds per season. See Figure 3-4 and Table 3-2 for nomenclature and further details.

3.3.2.2 Wind occurrence trends

Overall windiness of the Toronto area has not changed over time as shown in Figure 3-7 and Table 3-3. The same figure, however, indicates that a redistribution of wind directions has occurred in the analyzed 67-year period. It can be seen that the occurrence of winds in the first quadrant has increased, while the winds in the other three quadrants have experienced downward trends of their occurrence.

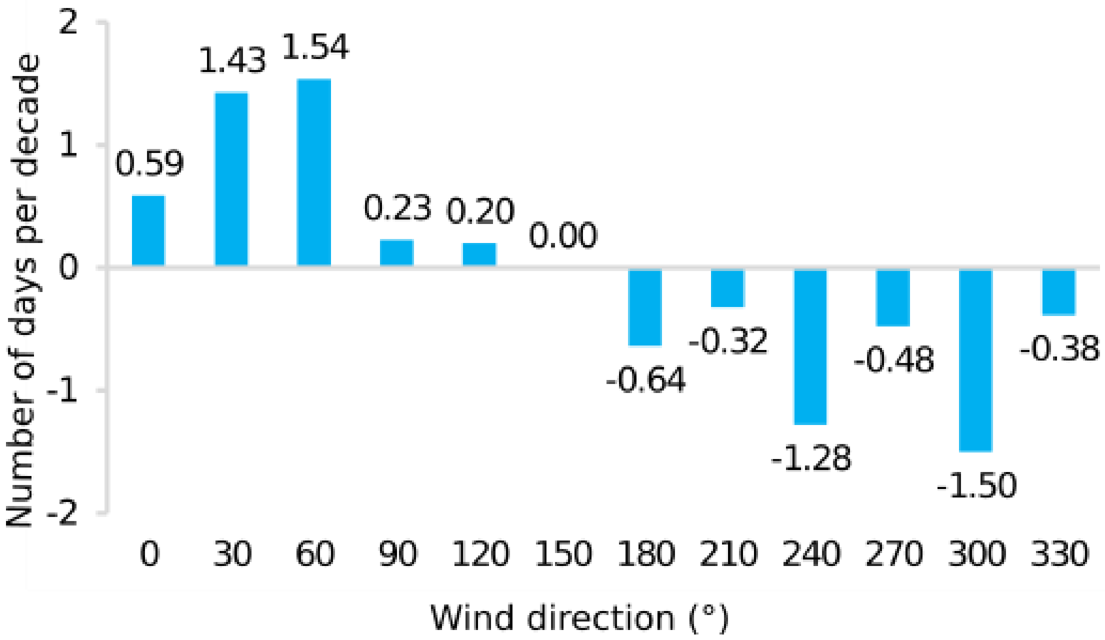

Figure 3-7. Trends of the annual number of days per decade for each wind direction.

The strongest upward trends have been detected for the frequency of occurrence of the $V_{\sigma 995}^{60°}$ and $V_{\sigma 995}^{30°}$ winds. In these two cases, their incidence has increased for 1.54 days per decade and 1.43 days per decade, respectively. Statistically significant, but negative trends are observed for the 300° and 240° wind directions. The number of days with the $V_{\sigma 995}^{300°}$ winds has declined by 1.5 days per decade, whereas the occurrence of the $V_{\sigma 995}^{240°}$ winds is reduced for 1.28 days per decade. The occurrence trends for other wind directions are not statistically significant.

Table 3-3. Trend analysis of the annual number of days with winds coming in from different directions. All values are given at the σ_{995} level. See Figure 3-7 for more details. Explanation of symbols is given in the text and Table 3-2.

Wind direction (°)	Z	H	Q	Q_{min99}	Q_{max99}	Q_{min95}	Q_{max95}	B	B_{min99}	B_{max99}	B_{min95}	B_{max95}
0	1.88	1	0.059	0.000	0.133	0.000	0.115	14.82	17.00	12.47	17.00	12.81
30	3.76	4	0.143	0.047	0.233	0.074	0.214	12.14	14.73	9.50	13.89	9.93
60	4.43	4	0.154	0.071	0.239	0.091	0.222	10.38	13.21	7.46	12.36	7.78
90	0.99	0	0.023	-0.038	0.095	-0.021	0.079	13.98	15.85	11.71	15.42	11.97
120	0.78	0	0.020	-0.055	0.102	-0.036	0.083	14.76	17.62	12.16	17.11	12.75
150	0.37	0	0.000	-0.077	0.102	-0.053	0.077	20.00	22.62	16.57	21.68	17.08
180	-1.26	0	-0.064	-0.188	0.058	-0.154	0.029	34.68	38.88	29.54	38.39	30.39
210	-0.59	0	-0.032	-0.188	0.118	-0.143	0.077	55.29	57.88	51.00	57.29	51.54
240	-2.03	2	-0.128	-0.291	0.036	-0.250	0.000	65.09	72.26	61.21	70.50	62.00
270	-0.97	0	-0.048	-0.171	0.086	-0.143	0.055	52.33	56.81	48.60	55.86	49.47
300	-3.26	3	-0.150	-0.263	-0.033	-0.239	-0.067	42.50	46.53	38.86	45.57	39.73
330	-1.55	0	-0.038	-0.115	0.025	-0.098	0.000	26.50	28.92	24.60	28.21	25.00

3.3.3 Low-frequency wind spectrum

Figure 3-8 shows the wind speed spectrum in the low-frequency domain at the σ_{995} level over Toronto. Three pronounced peaks are noticeable. The peak associated with the highest frequency has a period of 2 to 4.5 days. This local maximum in the spectrum has previously been reported in a number of wind studies (see discussion in Introduction and Figure 3-1). The passage of large scale pressure systems, such as depressions and cyclones, is associated with the energy production with the period of 3-4 days (Estoque 1955; Van der Hoven 1957). The Great Lake region is an area where two major North American cyclonic tracks merge (Zishka and Smith 1980) and afterwards take northeasterly trajectories. The same study reported that these cyclones are most frequent in winter, which has been later confirmed in the study by Zhang et al. (2004). Their findings are in a good agreement with the presented results that winter is the windiest month in Toronto.

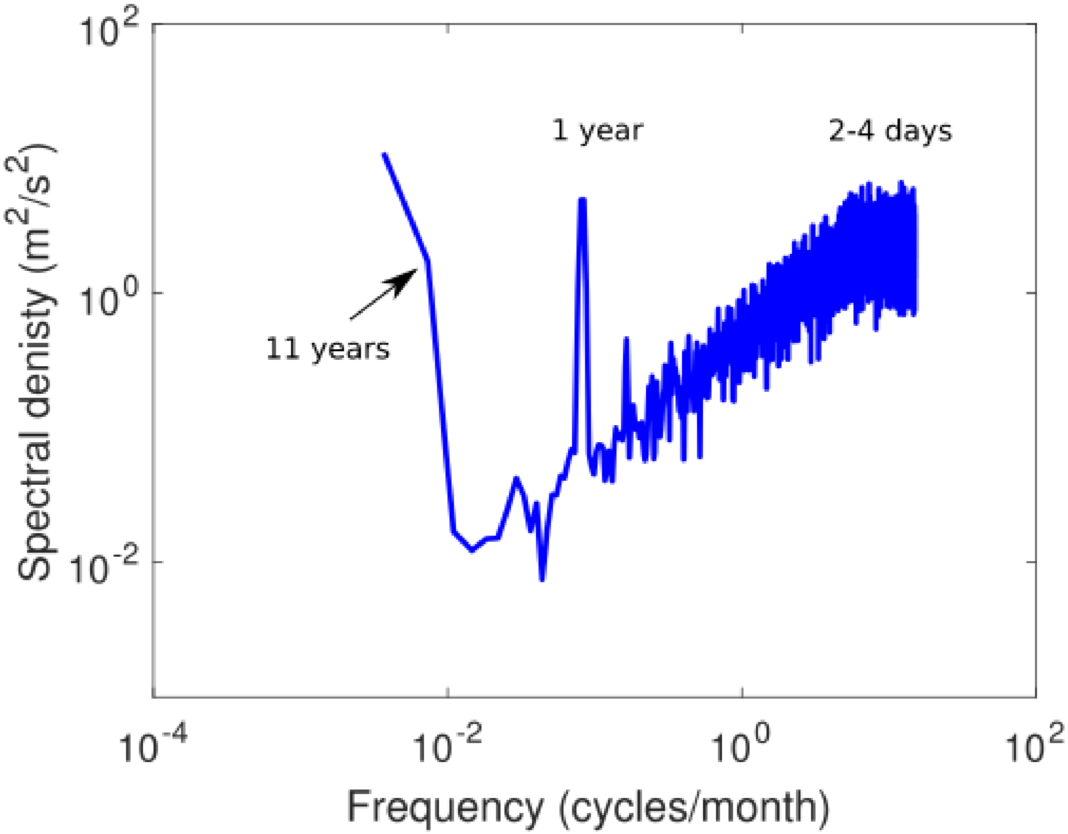

Figure 3-8. Low-frequency wind speed spectrum for Toronto based on the mean daily wind speeds.

The second pronounced peak in the spectra possesses a period of 1 year. This peak is associated with alternation of seasons throughout the year. As already demonstrated, winds over Toronto are the strongest in winter and weakest in summer. The existence of a 1-year peak is reported by many researchers (Gomes and Vickery 1977; Harris 2008; Belu and Koracin 2013). The autocorrelation function of the wind speed series also resembles the 1-year periodicity, as shown in Figure 3-9.

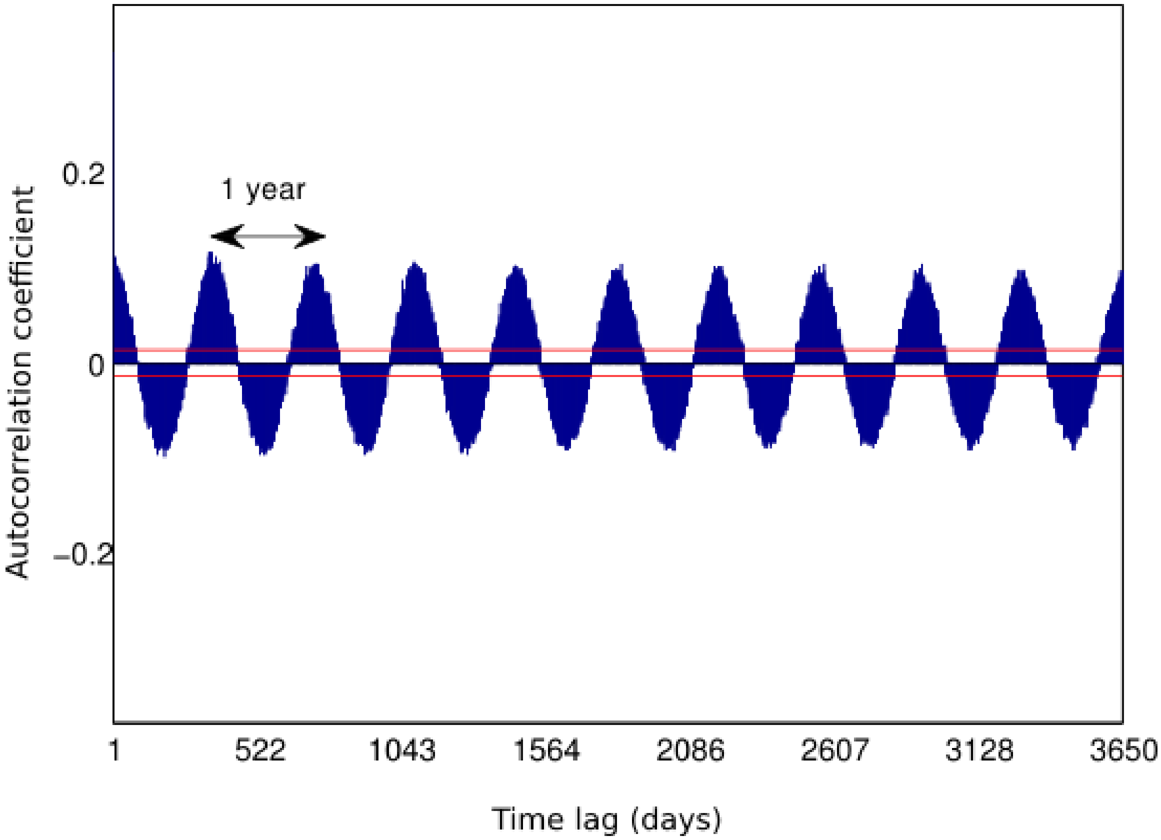

Figure 3-9. Autocorrelation of the mean daily wind speed. The horizontal red lines represent the 95% confidence intervals. Note that the *x*-axis starts at the time lag of 1.

A striking feature in the spectrum, however, is the presence of the third peak corresponding to the 11-year period. This finding required further investigation. To begin with, it should be noticed that very low frequencies correspond to very long time periods, which consequentially means that the lowest frequency oscillations often lack statistical significance. For example, the left end of the spectrum in Figure 3-7 corresponds to a period of approximately 22 years. Knowing that the input data cover only 67 years, such a (hypothetical) process could not occur more than three times in the timespan of the dataset. Thus, the presence of this last peak is not yet conclusive. Nevertheless, an astronomical process that possesses an 11-year period is the solar activity (Hathaway et al. 1994).

Since the observed 11-year peak in wind spectrum has the same period as the maximum of solar activity, combining these two time series seems to be a logical step. Data representing the monthly mean total sunspot number are obtained from the World Data Center SILSO at the Royal Observatory of Belgium, Brussels, Belgium (SILSO World Data Center, 1948), at: http://sidc.be/silso/. As we are not concerned with the inter-annual oscillations of the number of sunspots, the mean monthly wind speed as well as the total monthly number of sunspots were smoothed by applying a moving average with a 13-month low-pass filter (n), as described by Eq. (3-7).

The results of the moving average procedure are depicted in Figure 3-10. It can be observed that there were seven solar cycles in the analyzed period. The wind speed time series, although noisier, also contains some major peaks in 1958, 1977, 1989, as well as lower peaks in 1981 and 2002. An absolute wind speed minimum in 2005 is also evident. The same peaks, but not that pronounced, have been observed in the mean annual wind speed data series presented in Figure 3-5. The overlaps between the solar activity, on one side, and wind speed peaks, on the other side, can easily be observed in the years 1958, 1981, 1989 and 2002. It seems, however, that the absolute maximum in the wind speed series, recorded in 1977, does not directly coincide with a solar maximum. A peak in solar activity rather occurred some 8 years prior to the 1977 wind speed peak.

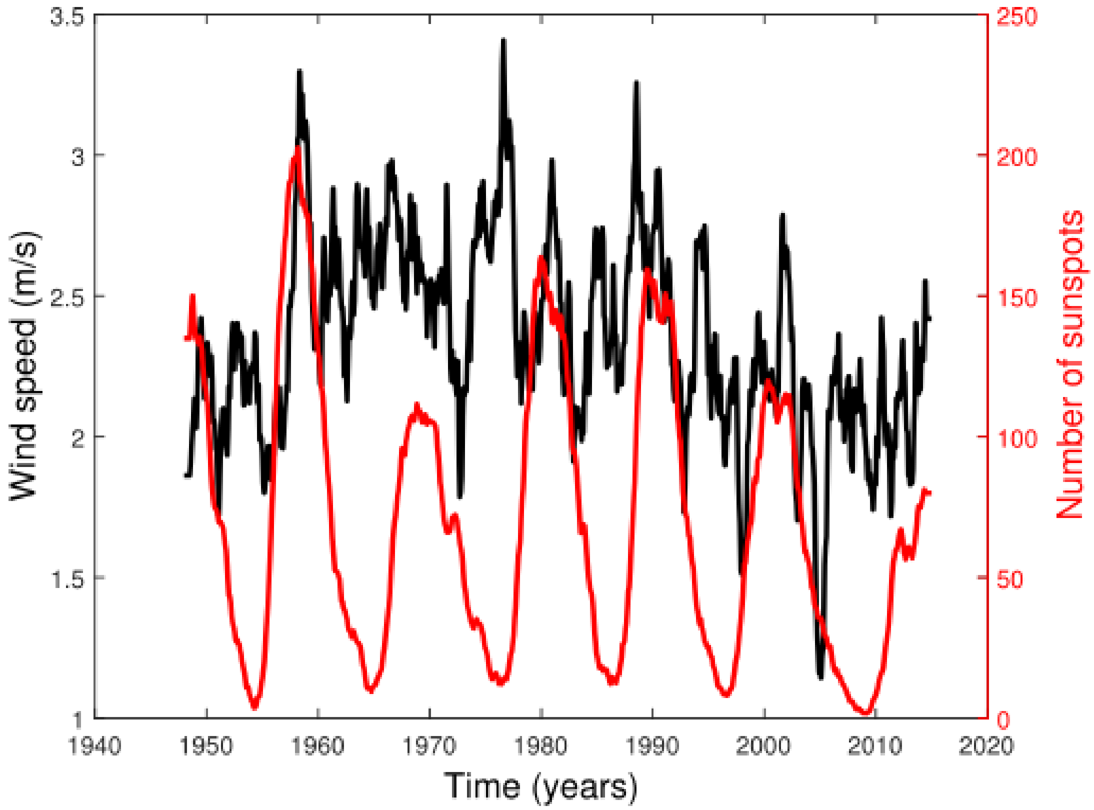

Figure 3-10. 13-month moving average of the mean monthly wind speeds above Toronto (black line) and the total monthly number of sunspots (red line)

An interesting occurrence is that this solar maximum has been the weakest maximum in the 1949 to 2002 period. In order to statistically quantify the strength of the observed relationship between the mean annual wind speed and the solar activity, a cross-correlation analysis between the two data sets is carried out. The results are portrayed in Figure 3-11.

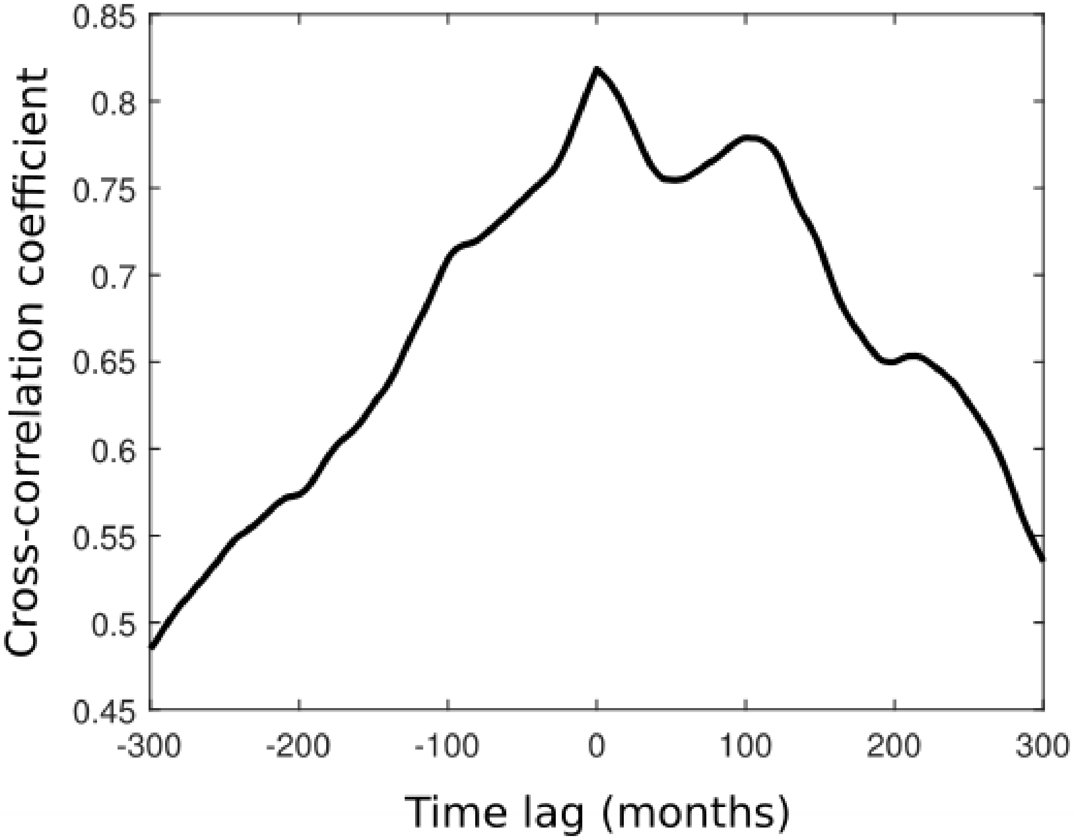

Figure 3-11. Cross-correlation between the 13-month moving averages of the mean monthly wind speed above Toronto and total monthly number of sunspots

The cross-correlation analysis confirms that there is a significant similarity between the two time series. The highest correlation is observed at zero time lag and reaches 0.82. A second and less pronounced peak in the correlation curve is located around 8.5 years in the direction of the positive lags; at the time lag equal 100 months. This may indicate that the response in wind speed maximum is considerably delayed after the period of the maximum solar activity. Examining Figure 3-10 again, it can be seen that the time lag between the peaks in the monthly number of sunspots in 1969 and the wind speed peak in 1977 occurred with the 8-year time shift in between them. Another example is the solar minimum that took place in 1997 and the most pronounced wind speed minimum recorded in 2005. The 8-year periodicity is also noticeable in the 5-year moving average series of mean annual wind speeds in Figure 3-4. However, the last three peaks in the moving average series in Figure 3-4 are 11 years apart. The above results seem to indicate that the solar activity either has instantaneous or time-delayed impact on the monthly wind speed over Toronto area.

3.4 Discussion

3.4.1 Wind trends

A trend analysis of several meteorological variables at the $\sigma995$ level is performed and the results are given in Table 3-4. Local variables that could have a direct or indirect implication on the observed wind trends are: (1) height of the $\sigma995$ level ($z_{\sigma995}$), (2) air density at the $\sigma995$ level ($\rho_{\sigma995}$), and (3) temperature at $\sigma995$ level ($T_{\sigma995}$).

Table 3-4. Trend analysis of the height of the mean annual height of σ_{995} level ($z_{\sigma995}$), mean annual air density at σ_{995} level ($\rho_{\sigma995}$) and mean annual temperature at the σ_{995} level ($T_{\sigma995}$). Slopes are given in units of m year^{-1}, kg m^{-3} year^{-1} and K year^{-1}, respectively. Explanation of symbols is given in the text and Table 3-2.

Time series	Z	H	Q	Q_{min99}	Q_{max99}	Q_{min95}	Q_{max95}	B	B_{min99}	B_{max99}	B_{min95}	B_{max95}
$z_{\sigma.995}$	-0.41	0	0.000	-0.002	0.002	-0.002	0.001	41.13	41.18	41.09	41.17	41.10
$\rho_{\sigma.995}$	-0.41	0	0.000	0.000	0.000	0.000	0.000	1.22	1.22	1.22	1.22	1.22
$T_{\sigma.995}$	0.29	0	0.001	-0.011	0.015	-0.009	0.012	280.36	280.77	279.99	280.69	280.08

It seems that local conditions at Toronto were not contributing to the observed wind trends. Namely, a possible trend in $z_{\sigma995}$ could have a pronounced impact on the observed wind trends as a negative trend of $z_{\sigma995}$ would result in the negative wind speed trends, whereas an upward trend of $z_{\sigma 995}$ would cause an increase of wind speeds. However, the value of $Q = 0$ as well as negligible values of Q even at the 99% confidence intervals remove this possibility. The average height of the σ_{995} level above Toronto is 41.1 m above ground. A trend in $T_{\sigma 995}$ could also impact wind speeds at the σ_{995} level (Dai and Deser 1999; Pirazzoli and Tomasin 2003; Dadaser-Celik and Cengiz 2014). However, a statistically significant temperature trend at the $\sigma_{.995}$ level is not detected in this study. Air density above Toronto was trendless too and the mean air density is 1.22 kg m^{-3}. The trend analysis has also been performed on the wind data obtained using the nearest-neighbor interpolation from the closest NCEP/NCAR reanalysis grid point (see Figure 3-2) and the outcomes were similar to the presented results (not shown).

Temperature in all regions of Canada rose in the period from 1948 to 2014 (Environment and Climate Change Canada, 2015). This resulted in a temperature increase for the country as a whole by 1.6 K in the same period. The average annual temperature in the northern region of Ontario has increased for 0.8 K in the analyzed 67-year period. In the same period, the temperature increased by only 0.6 K in the most southeastern region of Ontario. These uneven temperature increases across Ontario may result in an augmentation of the pressure gradients between these two geographical regions, which in turn would result in the positive wind speed trends. The Canadian Centre for Climate Modelling and Analysis reported a non-uniform increase of the surface temperature across the whole Canada (Vincent et al. 2012; Vincent et al. 2015). The strongest positive trends in the minimum and maximum temperatures occurred in winter season, in which the west coast experienced stronger positive trends than the east coast of Canada. The largest non-uniformity of temperature trends across Canada, however, is detected in the fall season. Interestingly, Table 3-2 shows that the strongest positive wind speed trends above Toronto were detected in the fall season. It should be mentioned that the same non-uniformity of temperature trends across Ontario and surrounding provinces could, if in the right direction, diminish the pressure gradients and result in downward wind speed trends. However, such negative wind speed trends were not detected in this study. Many climate change models indicate an increase in surface wind speeds in the Toronto region in coming decades (IPCC 2007; McInnes et al. 2011), but different results have also been reported (Yao et al. 2012).

Results in this paper are similar, in certain aspects, to the results reported by Holt and Wang (2012). Namely, they found considerably stronger positive wind speed trends at 80-m level above ground and smaller, but nevertheless positive, trends at 10 m above ground. It seems that the intensity of wind speed trends increases with the height. They concluded that the increase of the westerly winds is due to the strengthening of the mid-latitude jet stream. Our results, however, are not in accordance with the findings reported by Wan et al. (2010). We observed upward trends of the mean annual wind speed, while they reported negative wind speed trends. The downward wind speed trends found in this study (wind speeds in the spring season as well as a few wind directions in the fourth quadrant) are negligible and statistically not significant (Table 3-2). The discrepancies between the two studies could be due to different input data. Wan et al. (2010) used station data and homogenized wind series. However, it is not likely that the homogenization process that they performed on the raw data is the reason behind the discrepancy, since their trend analysis on raw dataset also resulted in the negative wind speed trends. It should also be mentioned that they used different statistical method to estimate trends. Last but not least, data used in our study are given at the σ_{995} level (≈ 41 m above ground), while they used weather station data at 10 m above ground. As demonstrated by Holt and Wang (2012), trend intensities tend to increase with height. Therefore, the difference between the Wan et al. (2010) findings and the results of this study could most likely be due to the differences in height at which the wind speed trends were analyzed. Interestingly, there seem to be one similarity between the Wan et al. (2010) and our study in the wind data after the 1990s. Namely, both studies suggest that the mean annual wind speeds after the 1990s are trendless. Li et al. (2010) in their study on wind climatology of the Great Lakes, on the other hand, did not find any significant trend of the 80-m mean annual wind speeds in the period 1979-2008. Their study was based on the NARR dataset. The trends captured from the reanalysis data usually differ from the trends calculated using the observations alone (Pryor et al. 2009) and therefore the results should be interpolated and compared with caution (Li et al. 2010). It is important to mention that the research in this paper is the first wind trend study based on the NCEP/NCAR reanalysis 1 dataset for the Toronto area.

3.4.2 Solar activity and climate

The solar constant as measured by satellites since the 1980s has a value of approximately 1366 W m^{-2} with an absolute uncertainty of ±2 W m^{-2}. The measurements further show that the solar output is increased for about 1.1 W m^{-2} during the solar maximum periods (Barry and Chorley 2009). The solar activity has the largest influences on the high frequency spectrum of solar radiation with wavelengths below 300 nm (Lean and Rind 1998). These alterations in shortwave spectrum primarily affect the stratosphere, where the ozone layer absorbs UV light (Hood et al. 1993). Directly, and indirectly through the thermal-wind relation, this thermodynamic change in stratosphere can alter the temperature gradients and winds at both higher and lower altitudes.

So far there is no satisfactory analytical relationship found between solar activity and climatological variables. For that reason, most studies report statistical relations between the solar activity and the earth's climate. Landsberg (1975) found a strong statistical relationship between the annual number of sunspots and rainfall in Dakar, Senegal, during the Sahel drought from 1970 to 1972. One of the best known connections between solar activity and a hydro-meteorological phenomenon is the oscillation of the water level in the lakes in Central Africa in the period from 1902 to 1921 (Henry 1924). The correlation coefficient between the water level in the lakes and the number of sunspots was 0.87. In our study, the cross-correlation coefficient between smoothed wind speed and solar activity series is 0.82. Hansen and Lacis (1990) demonstrated that a decrease in the Sun's output of 0.1% in the period 1980-1986 was accompanied by a 0.2 K global temperature decrease. The same study further argues that on time scales less than a decade, solar activity can match the influence of greenhouse gasses on the global climate. An overview of literature on solar variability and its relation to the weather and climate can be found in Haigh (2007) and Gray et al. (2010).

After the works of Van der Hoven (1957) and Davenport (1965), the existence of the 11-year peak in wind spectrum was speculated by Houghton and Carruthers (1976). A connection between solar activity and winds was reported for the quasi-biennial oscillation of equatorial wind (Salby and Callaghan 2000). They found the 11-year peak in the frequency spectrum of the equatorial zonal winds at 45 hPa level. Using the European Center for Medium range Weather Forecasting (ECMWF) reanalysis data, Crooks and Gray (2005) demonstrated that broadening of the Hadley cell follows the 11-year solar activity pattern. They found that one of the consequences of this broadening is the increased strength of the mid-latitude winds in the northern hemisphere between 40°N and 70°N. Our study also found a positive correlation between wind speed and solar activity in the same geographical region (43.653°N). Shindell et al. (2001) hypothesized how the solar activity influences the surface winds and pressure gradients. They argue that a modulation of the meridional temperature gradients, caused by the different absorption of the solar UV radiation in the meridional direction, is affecting the planetary (Rossby) wave activity, as well as the stratospheric thermal structure. These modifications influence the stratospheric winds, which in turn affects the wind shear. The upward propagating planetary waves are refracted equatorward in the zone of increased wind shear. This equatorward refraction of the planetary waves is balanced by a transfer of angular momentum towards the North Pole, which consequentially augments the westerlies. Furthermore, Shindell et al. (2001) detected the positive wind speed trends of the surface westerlies over the North Atlantic (approximately 0.19 m s^{-1} in the period 1951-1997). They attributed these positive wind speed trend to the positive trend of Arctic Oscillation, which, in turn, is altered by combining effects of global warming and the solar activity. Our study showed that the near-surface westerlies above Toronto increased for 0.4 m s^{-1} in the period 1951-1997, as shown in Table 3-2. Several solar influences on tropospheric winds and mid-latitude jet stream locations obtained from the NCEP/NCAR reanalysis data have been reported in the works by Haigh (2003), Haigh et al. (2005) and Haight and Blackburn (2006). Several mostly qualitative mechanisms proposed to explain the relationship between solar activity and earth's climate are discussed in Gray et al. (2010), but the future work in this field needs to be concentrated around the development of physical-mathematical models that would describe these mechanisms in a rigorous way. Such a work, however, is beyond the scope of this study in which the relationship is statistically described.

3.5 Conclusions

This study represents a comprehensive analysis of the wind climatology above Toronto based on the NCEP/NCAR reanalysis 1 data acquired for the period from 1948 to 2014. The mean daily wind speed and direction are given at the sigma-995 level, which is calculated to be positioned at 41.1 m above ground. The paper is focused on the three aspects of the wind climatology: (1) wind speed and direction distributions, (2) long-term wind trends, and (3) low-frequency wind spectrum. In addition, a possible relationship between solar activity and wind characteristics at Toronto is also discussed.

Winds coming in from 240°, 270° and 210° were the most frequent. On an annual basis, these three wind directions were present in about 50% of the time. The windiest season is winter with an average wind speed of 5.61 m s^{-1} and the wind power density of 190.7 W m^{-2}. The mean annual wind speed above Toronto is found to be 4.83 m s^{-1}. Besides being the most frequent, the 240° wind direction is also associated with the strongest winds. The windiest season after winter is fall, followed by spring and summer, respectively.

Mean annual wind speeds above Toronto increased for 0.2 m s^{-1} in the period 1948-2014. The positive trend is statistically significant at the 95% confidence level. The strongest positive trends are observed in the fall and winter seasons. The fall winds increased their speed for 0.8 m s^{-1} in the 67-year-long period. Negative wind speed trends in the summer and spring seasons are statistically not significant with very small values of Sen's slope. The windiest directions, 240° and 270°, have also experienced statistically significant upward wind speed trends. The positive wind speed trends are potentially beneficial for urban wind power projects as well as ventilation of the city and removal of pollutants. Our results are in a good agreement with the findings published by Holt and Wang (2012) and present some discrepancies with the results obtained by Wan et al. (2010). These similarities and discrepancies are discussed in Section 3.4.1. Lastly, it is important to note that a redistribution between different wind directions took place in such a way that winds in the first quadrant increased their frequency of occurrence, while the winds in the other three quadrants have been less frequent.

Spectral analysis of wind speed series in the low-frequency domain reveals three distinguished peaks. One of the peaks corresponds to the passage of the low pressure systems (cyclones and depressions) with a period of 2 to 4.5 days. The second peak has a period of 1 year and corresponds to the annual cycle of seasons. This peak is also evident in the autocorrelation analysis which resembles 1-year statistically significant periodicity. The striking feature, however, is the existence of the third peak with the period of 11 years. Cross-correlation analysis between smoothed wind speed series and the total monthly number of sunspots indicates that the 11-year peak in wind spectrum might be due to the solar activity that manifest as the famous 11-year solar cycle. The highest correlation between these two time series is observed at zero time lag and reaches 0.82. It should be noted that our analysis between wind speed and solar activity is purely statistical and without an attempt to develop analytical theory of it. Comprehensive literature review confirms that solar activity can have a profound influence on earth’s climate; directly in the stratosphere and indirectly in the troposphere.

References

Araújo AM, Valença DA de A, Asibor AI, Rosas PAC (2012) An approach to simulate wind fields around an urban environment for wind energy application. Environ Fluid Mech 13:33–50. doi: 10.1007/s10652-012-9258-z

Barry RG, Chorley RJ (2009) Atmosphere, weather and climate, 9th edn. Routledge, London ; New York

Baumüller J, Hoffmann U, Ulrich R (2012) Climate booklet for urban development. Ministry of Transport and Infrastructure of Baden-Württemberg, Stuttgart, Germany

Benestad RE (2010) Downscaling precipitation extremes. Theor Appl Climatol 100:1–21. doi: 10.1007/s00704-009-0158-1

Bergant K, Kajfež-Bogataj L (2005) N–PLS regression as empirical downscaling tool in climate change studies. Theor Appl Climatol 81:11–23. doi: 10.1007/s00704-004-0083-2

Belu R, Koracin D (2013) Statistical and spectral analysis of wind characteristics relevant to wind energy assessment using tower measurements in complex terrain. J Wind Energy 2013:e739162. doi: 10.1155/2013/739162

Best MJ (2005) Progress towards better weather forecasts for city dwellers: from short range to climate change. Theor Appl Climatol 84:47–55. doi: 10.1007/s00704-005-0143-2

Cheng H, Castro IP (2002) Near wall flow over urban-like roughness. Bound-Layer Meteorol 104:229–259. doi: 10.1023/A:1016060103448

Clifford MJ, Everitt PJ, Clarke R, Riffat SB (1997) Using computational fluid dynamics as a design tool for naturally ventilated buildings. Build Environ 32:305–312. doi: 10.1016/S0360-1323(97)00002-4

Crooks SA, Gray LJ (2005) Characterization of the 11-year solar signal using a multiple regression analysis of the ERA-40 dataset. J Clim 18:996–1015. doi: 10.1175/JCLI-3308.1

Dadaser-Celik F, Cengiz E (2014) Wind speed trends over Turkey from 1975 to 2006. Int J Climatol 34:1913–1927. doi: 10.1002/joc.3810

Dai A, Deser C (1999) Diurnal and semidiurnal variations in global surface wind and divergence fields. J Geophys Res Atmospheres 104:31109–31125. doi: 10.1029/1999JD900927

Davenport AG (1965) The relationship of wind structure to wind loading. In: Proceedings of the Conference on Wind Effects on Structures. ICWE-1, HMSO, Teddington, UK, p 53

Environment and Climate Change Canada (2014) Meteorological station catalogue - open government portal. Government of Canada. http://open.canada.ca/data/en/dataset/9764d6c6-3044-450c-ac5a-383cedbfef17. Accessed 11 Nov 2016

Environment and Climate Change Canada (2015) Climate trends and variations bulletin. Government of Canada. https://www.ec.gc.ca/sc-cs/default.asp?lang=En&n=A3837393-1. Accessed 18 May 2015

Estoque MA (1955) The spectrum of large-scale turbulent transfer of momentum and heat. Tellus 7:177–185. doi: 10.1111/j.2153-3490.1955.tb01150.x

Gagliano A, Nocera F, Patania F, Capizzi A (2013) Assessment of micro-wind turbines performance in the urban environments: an aided methodology through geographical information systems. Int J Energy Environ Eng 4:43. doi: 10.1186/2251-6832-4-43

Gomes L, Vickery BJ (1977) On the prediction of extreme wind speeds from the parent distribution. J Wind Eng Ind Aerodyn 2:21–36. doi: 10.1016/0167-6105(77)90003-4

Gray LJ, Beer J, Geller M, et al (2010) Solar influences on climate. Rev Geophys 48:RG4001. doi: 10.1029/2009RG000282

Grimmond CSB (2005) Progress in measuring and observing the urban atmosphere. Theor Appl Climatol 84:3–22. doi: 10.1007/s00704-005-0140-5

Grimmond CSB, Roth M, Oke TR, et al (2010) Climate and more sustainable cities: climate information for improved planning and management of cities (producers/capabilities perspective). Procedia Environ Sci 1:247–274. doi: 10.1016/j.proenv.2010.09.016

Haan LLD, Kanamitsu M, Sales FD, Sun L (2015) An evaluation of the seasonal added value of downscaling over the United States using new verification measures. Theor Appl Climatol 122:47–57. doi: 10.1007/s00704-014-1278-9

Haigh JD (2003) The effects of solar variability on the Earth’s climate. Philos Trans A Math Phys Eng Sci 361:95–111. doi: 10.1098/rsta.2002.1111

Haigh JD (2007) The Sun and the Earth’s climate. Living Rev Sol Phys 4:2. doi: 10.12942/lrsp-2007-2

Haigh JD, Blackburn M, Day R (2005) The response of tropospheric circulation to perturbations in lower-stratospheric temperature. J Climate 18:3672–3685. doi: 10.1175/JCLI3472.1

Haigh JD, Blackburn M (2006) Solar influences on dynamical coupling between the stratosphere and troposphere. Space Sci Rev 125:331–344. doi: 10.1007/s11214-006-9067-0

Hansen JE, Lacis AA (1990) Sun and dust versus greenhouse gases: an assessment of their relative roles in global climate change. Nature 346:713–719. doi: 10.1038/346713a0

Harris JW, Stöcker H (1998) Handbook of mathematics and computational science, 1998 edn. Springer, New York

Harris RI (2008) The macrometeorological spectrum—a preliminary study. J Wind Eng Ind Aerodyn 96:2294–2307. doi: 10.1016/j.jweia.2008.03.008

Hathaway DH, Wilson RM, Reichmann EJ (1994) The shape of the sunspot cycle. Sol Phys 151:177–190. doi: 10.1007/BF00654090

He JF, Liu JY, Zhuang DF, et al (2007) Assessing the effect of land use/land cover change on the change of urban heat island intensity. Theor Appl Climatol 90:217–226. doi: 10.1007/s00704-006-0273-1

Hebbert M, Mackillop F (2013) Urban climatology applied to urban planning: a postwar knowledge circulation failure. Int J Urban Reg Res 37:1542–1558. doi: 10.1111/1468-2427.12046

Henry AJ (1924) C. e. p. brooks on variations in the level of the central African Lakes, Victoria and Albert. Mon Weather Rev 52:148–152. doi: 10.1175/1520-0493(1924)52<148:CEPBOV>2.0.CO;2

Hood LL, Jirikowic JL, McCormack JP (1993) Quasi-decadal variability of the stratosphere: influence of long-term solar ultraviolet variations. J Atmos Sci 50:3941–3958. doi: 10.1175/1520-0469(1993)050<3941:QDVOTS>2.0.CO;2

Holt E, Wang J (2012) Trends in wind speed at wind turbine height of 80 m over the contiguous United States using the North American Regional Reanalysis (NARR). J Appl Meteorol Climatol 51:2188–2202. doi: 10.1175/JAMC-D-11-0205.1

Houghton EL, Carruthers NB (1976) Wind forces on buildings and structures: an introduction. John Wiley & Sons Inc, New York

IPCC (2007) Contribution of working group i to the fourth assessment report of the Intergovernmental Panel on Climate Change, 2007. Intergovernmental Panel on Climate Change, Cambridge University Press, Cambridge, United Kingdom and New York, United States

IPCC (2013) Climate Change 2013: The physical science basis. Intergovernmental Panel on Climate Change, Cambridge University Press, Cambridge, United Kingdom and New York, United States

Jensen NO (1999) Atmospheric boundary layers and turbulence. Wind Eng 21 Century 1:29–42.

Kalnay E, Kanamitsu M, Kistler R, et al (1996) The NCEP/NCAR 40-year reanalysis project. Bull Am Meteorol Soc 77:437–471. doi: 10.1175/1520-0477(1996)077<0437:TNYRP>2.0.CO;2

Katzschner L (1998) Designation of urban climate qualities and their implementation in the planning process. In: Proceedings of PLEA’98. James & James Scientific Publishers Ltd., Lisbon, Portugal, pp 75–78

Kendall MG (1970) Rank correlation methods. Griffin, London

Klein P, Leitl B, Schatzmann M (2010) Concentration fluctuations in a downtown urban area. Part II: analysis of Joint Urban 2003 wind-tunnel measurements. Environ Fluid Mech 11:43–60. doi: 10.1007/s10652-010-9195-7

Kozmar H (2009) Scale effects in wind tunnel modeling of an urban atmospheric boundary layer. Theor Appl Climatol 100:153–162. doi: 10.1007/s00704-009-0156-3

Kumar P, Kishtawal CM, Pal PK (2015) Impact of ECMWF, NCEP, and NCMRWF global model analysis on the WRF model forecast over Indian Region. Theor Appl Climatol 1–9. doi: 10.1007/s00704-015-1629-1

Landsberg PDHE (1975) Sahel drought: change of climate or part of climate? Arch Für Meteorol Geophys Bioklimatol Ser B 23:193–200. doi: 10.1007/BF02246775

Lean J, Rind D (1998) Climate forcing by changing solar radiation. J Clim 11:3069–3094. doi: 10.1175/1520-0442(1998)011<3069:CFBCSR>2.0.CO;2

Li X, Zhong S, Bian X, Heilman WE (2010) Climate and climate variability of the wind power resources in the Great Lakes region of the United States. J Geophys Res Atmospheres 115:D18107. doi: 10.1029/2009JD013415

Liuzzo L, Viola F, Noto LV (2014) Wind speed and temperature trends impacts on reference evapotranspiration in Southern Italy. Theor Appl Climatol 123:43–62. doi: 10.1007/s00704-014-1342-5

Mann HB (1945) Nonparametric tests against trend. Econometrica 13:245–259. doi: 10.2307/1907187

McCarthy MP, Best MJ, Betts RA (2010) Climate change in cities due to global warming and urban effects. Geophys Res Lett 37:L09705. doi: 10.1029/2010GL042845

McInnes KL, Erwin TA, Bathols JM (2011) Global Climate Model projected changes in 10 m wind speed and direction due to anthropogenic climate change. Atmosph Sci Lett 12:325–333. doi: 10.1002/asl.341

McVicar TR, Roderick ML, Donohue RJ, et al (2012) Global review and synthesis of trends in observed terrestrial near-surface wind speeds: implications for evaporation. J Hydrol 416–417:182–205. doi: 10.1016/j.jhydrol.2011.10.024

Mills G (2014) Urban climatology: History, status and prospects. Urban Clim 10, Part 3:479–489. doi: 10.1016/j.uclim.2014.06.004

Niino H, Mori A, Satomura T, Akiba S (2006) Flow regimes of nonlinear heat island circulation. J Atmospheric Sci 63:1538–1547. doi: 10.1175/JAS3700.1

NOAA (2015) Land-based station data | National Centers for Environmental Information (NCEI) formerly known as National Climatic Data Center (NCDC). In: National Centers for Environmental Information (NCEI), National Oceanic and Atmospheric Administration. https://www.ncdc.noaa.gov/data-access/land-based-station-data. Accessed 11 Nov 2016

Peel MC, Finlayson BL, McMahon TA (2007) Updated world map of the Köppen-Geiger climate classification. Hydrol Earth Syst Sci 11:1633–1644. doi: 10.5194/hess-11-1633-2007

Pirazzoli PA, Tomasin A (2003) Recent near-surface wind changes in the central Mediterranean and Adriatic areas. Int J Climatol 23:963–973. doi: 10.1002/joc.925

Pryor SC, Barthelmie RJ, Young DT, et al (2009) Wind speed trends over the contiguous United States. J Geophys Res Atmospheres 114:D14105. doi: 10.1029/2008JD011416

Ren C, Ng EY, Katzschner L (2011) Urban climatic map studies: a review. Int J Climatol 31:2213–2233. doi: 10.1002/joc.2237

Romanić D, Ćurić M, Jovičić I, Lompar M (2015a) Long-term trends of the "Koshava" wind during the period 1949–2010. Int J Climatol 35:288–302. doi: 10.1002/joc.3981

Romanić D, Rasouli A, Hangan H (2015b) Wind resource assessment in complex urban environment. Wind Eng 39:193–212. doi: 10.1260/0309-524X.39.2.193

Romanic D, Refan M, Wu C-H, Michel G (2016) Oklahoma tornado risk and variability: a statistical model. International Journal of Disaster Risk Reduction 16:19–32. doi: 10.1016/j.ijdrr.2016.01.011

Rotach MW, Vogt R, Bernhofer C, et al (2005) BUBBLE – an urban boundary layer meteorology project. Theor Appl Climatol 81:231–261. doi: 10.1007/s00704-004-0117-9

Sabaliauskas K, Jeong C-H, Yao X, et al (2015) Development of a land-use regression model for ultrafine particles in Toronto, Canada. Atmos Environ 110:84–92. doi: 10.1016/j.atmosenv.2015.02.018

Salby M, Callaghan P (2000) Connection between the solar cycle and the QBO: the missing link*. J Clim 13:2652–2662. doi: 10.1175/1520-0442(1999)012<2652:CBTSCA>2.0.CO;2

Salmi T, Määttä A, Anttila P, et al (2002) Detecting trends of annual values of atmospheric pollutants by the Mann-Kendall test and Sen's slope estimates –the Excel template application MAKESENS. Finnish Meteorological Institute, Helsinki, Finland

Sen PK (1968) Estimates of the regression coefficient based on Kendall's Tau. J Am Stat Assoc 63:1379–1389. doi: 10.2307/2285891

Shindell DT, Schmidt GA, Miller RL, Rind D (2001) Northern hemisphere winter climate response to greenhouse gas, ozone, solar, and volcanic forcing. J Geophys Res Atmospheres 106:7193–7210. doi: 10.1029/2000JD900547

Statistics Canada (2015a) Census metropolitan areas. Government of Canada. http://www.statcan.gc.ca/pub/91-214-x/2016000/section01-eng.htm. Accessed 6 Aug 2016

Statistics Canada (2015b) Population and demographic factors of growth by census division, provinces and territories. Government of Canada. http://www.statcan.gc.ca/pub/91-214-x/2016000/tbl/tbl3.5-eng.htm. Accessed 6 Aug 2016

Stoica P, Moses RL (2005) Spectral analysis of signals, 1st edn. Prentice Hall, Upper Saddle River, N.J

Trigo IF, Davies TD, Bigg GR (1999) Objective climatology of cyclones in the Mediterranean region. J Clim 12:1685–1696. doi: 10.1175/1520-0442(1999)012<1685:OCOCIT>2.0.CO;2

Troccoli A, Muller K, Coppin P, et al (2012) Long-term wind speed trends over Australia. J Clim 25:170–183. doi: 10.1175/2011JCLI4198.1

Troen I, Petersen EL (1989) European wind atlas. RISØ National Laboratory, Roskilde, Denmark

United Nations (2014) World urbanization prospects: the 2014 revision. United Nations, Department of Economic and Social Affairs, Population Division, New Orleans, United States

Van der Hoven I (1957) Power spectrum of horizontal wind speed in the frequency range from 0.0007 to 900 cycles per hour. J Meteorol 14:160–164. doi: 10.1175/1520-0469(1957)014<0160:PSOHWS>2.0.CO;2

Vautard R, Cattiaux J, Yiou P, et al (2010) Northern Hemisphere atmospheric stilling partly attributed to an increase in surface roughness. Nat Geosci 3:756–761. doi: 10.1038/ngeo979

VDI (2015) VDI 3787 Blatt 1: environmental meteorology - climate and air pollution maps for cities and regions. http://www.vdi.eu/uploads/tx_vdirili/pdf/2308604.pdf. Accessed 5 Aug 2015

Vincent LA, Wang XL, Milewska EJ, et al (2012) A second generation of homogenized Canadian monthly surface air temperature for climate trend analysis. J Geophys Res Atmospheres 117:D18110. doi: 10.1029/2012JD017859

Vincent LA, Zhang X, Brown RD, et al (2015) Observed trends in Canada’s climate and influence of low-frequency variability modes. J Climate 28:4545–4560. doi: 10.1175/JCLI-D-14-00697.1

Wan H, Wang XL, Swail VR (2010) Homogenization and trend analysis of Canadian near-surface wind speeds. J Clim 23:1209–1225. doi: 10.1175/2009JCLI3200.1

Welch PD (1967) The use of fast Fourier transform for the estimation of power spectra: A method based on time averaging over short, modified periodograms. IEEE Trans Audio Electroacoustics 15:70–73. doi: 10.1109/TAU.1967.1161901

Yao Y, Huang GH, Lin Q (2012) Climate change impacts on Ontario wind power resource. Environmental Systems Research 1:2. doi: 10.1186/2193-2697-1-2

Zajaczkowski FJ, Haupt SE, Schmehl KJ (2011) A preliminary study of assimilating numerical weather prediction data into computational fluid dynamics models for wind prediction. J Wind Eng Ind Aerodyn 99:320–329. doi: 10.1016/j.jweia.2011.01.023

Zhang X, Walsh JE, Zhang J, et al (2004) Climatology and interannual variability of Arctic cyclone activity: 1948–2002. J Clim 17:2300–2317. doi: 10.1175/1520-0442(2004)017<2300:CAIVOA>2.0.CO;2

Zishka KM, Smith PJ (1980) The climatology of cyclones and anticyclones over North America and surrounding ocean environs for January and July, 1950–77. Mon Weather Rev 108:387–401. doi: 10.1175/1520-0493(1980)108<0387:TCOCAA>2.0.CO;2

Chapter IV

4 Urban wind resource assessment in changing climate: Case study

4.1 Introduction

An accurate, and rather simple definition of climate is that it represents the average of weather over time and space. The Earth's climate has always been changing. Although defining climate is easy, understanding the causes as well as the effects of climate changes is challenging indeed. This difficulty is caused by variety of terrestrial and extra-terrestrial climate factors that constantly interact among each other. As over 99% of the Earth's energy comes from solar radiation (Black and Flarend 2010), the astronomical climate factors, such as the shape of Earth's orbit around the Sun, tilt of Earth's axis, and precession are the main drivers of the Earth's climate, as described in 1920 by Milanković's theory of ice age cycles (Milanković 1920; 1930). These astronomical factors influence the amount of the Sun's energy reaching the Earth. However, these factors have large return periods and hence can be considered as being constant over the time periods of several hundreds of years or so (for example, the period for precession of Earth's orbit is around 23,000 years while the other two factors have even larger periods).

Changes in the concentration of greenhouse gases and the reflectivity of Earth’s atmosphere and surface are the most important terrestrial factors which can disrupt the Earth’s energy balance. Changes in concentration of the greenhouse gasses (water vapor (H_2O), carbon dioxide (CO_2), methane (CH_4), and chlorofluorocarbons (CFCs)) affect the amount of heat retained by Earth’s atmosphere. Numerous studies (e.g. Trenberth 2009; Hansen et al. 2011; Cook et al. 2013) suggest that human activities have altered the concentration of CO_2 in the atmosphere and thus resulted in the on-going climate change. Reflectivity of Earth’s atmosphere and surface has also been changing due to changes in land use and land cover such as deforestation, desertification, and urbanization.

Rapid urbanization is a global phenomenon. In 2014, 54% of the world’s population inhabited urban areas (United Nations 2014). The same study reported that the percentages have been even higher in economically developed countries. Therefore, estimating the effects of climate change in urban environments is of great interest.

From mechanics and thermodynamics points of view, urban environments represent rough surfaces with a variety of sources and sinks of heat. Air flows in urban environments are very complex due to a large number of irregularly located and spaced obstacles. Compared to rural areas, the winds in cities are characterized by larger values of turbulence intensity and smaller mean wind speed. Climate change analysis in urban environments are very challenging mainly due to three factors. First, complicated climate change feedback loops and mechanisms, as well as the relationship between different feedbacks, are not very well understood. For example, the role of clouds in different climate change scenarios is not fully know. However, this difficulty concerning the representation of clouds in climate models is not restricted only to urban environments, but to the climate change modelling in general. The second factor has already been mentioned and it is the complexity of wind fields in cities. Namely, it is difficult to perform any wind resource assessment study in urban environments due to large number of buildings and other objects which act as obstacles to the incoming wind. For that reason, the urban boundary layers are very complex and highly turbulent close to the surface. Lastly, an additional factor which complicates climate change analysis in cities is the change in the city landscape as well as the fact that cities are growing in size, population and built-up surface. What is a park or a field today might be a built-up area in the future. We, here, presume to only consider the climate change aspects and not the changes in the city landscape.

Wind is one of the meteorological variables mostly influenced by climate change. A number of studies has shown that the near-surface winds are slowing down across the globe (McVicar et al. 2012; Romanić et al. 2015). Vautard et al. (2010) reported that wind speeds in the northern mid-latitudes declined between 5% and 15% in the period 1979-2008. They further concluded that 25% to 60% of these negative trends are caused by the increase of surface roughness, which is mostly due to increased urbanization in the last several decades. Holt and Wang (2012), however, showed that the westerly winds at 80 m level in the Great Lake region had pronounced positive trends in the period from 1979 to 2009 (~0.24 m s^{-1} over 10 years).

The present study investigates a potential influence of climate change on wind resources in an urban environment. To the authors' knowledge, this is the first study that aims to relate the urban wind resource assessment with the long-term wind speed trends. The proposed method is based on combining microscale Computational Fluid Dynamics (CFD) simulations with the long-term wind speed trends calculated from the National Centers for Environmental Prediction/National Center for Atmospheric Research (NCEP/NCAR) Reanalysis 1 data (Kalnay et al. 1996).

The detailed description of data, test site and methodology used to relate long-term wind speed trends to available wind resources is presented in Section 4.2. The results and critical discussion are given in Section 4.3. The concluding remarks follow in the last section of this chapter.

4.2 Data, methodology and numerical setup

4.2.1 Site

The analysis of urban wind resource assessment in changing climate is conducted on a city block located in Toronto, Ontario, Canada. The site had been used as the 2015 Pan American Games Athletes' Village (PanAm Village, Figure 4-1). The construction work on the site were finished in the first half of 2015. PanAm Village is located between Bayview Avenue and Cherry Street and from north of Front Street to a rail corridor north of the shores of Lake Ontario (Lat 43°39′12″ N, Lon 79°21′16″ W). The PanAmVillage is bounded by the urban area from the north and east sides while the southern and western sides are mostly exposed to land with low terrain roughness neighboring the lake. The athletic village is composed of 22 building blocks positioned along the existing streets.

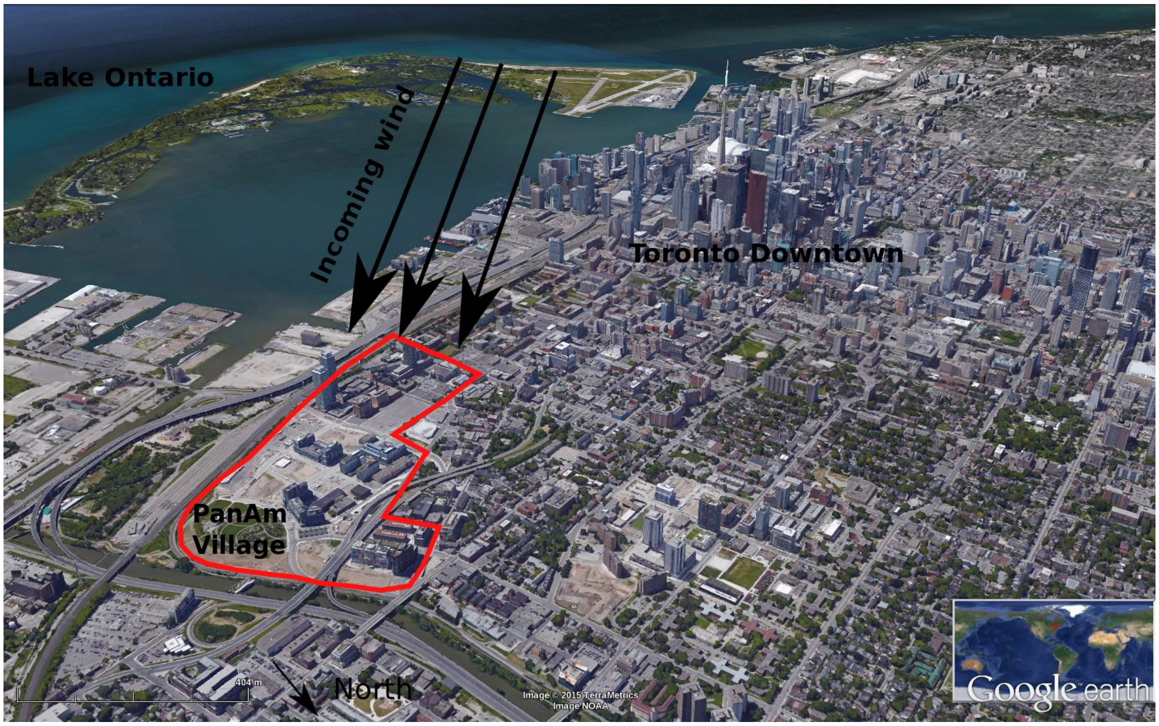

Figure 4-1. Location of PanAm Village in Toronto. Winds coming in from southwest direction (240°) are shown. The arrow in the lower-left corner indicates the North direction.

4.2.2 Data

The wind data used in this study are extracted from the global NCEP/NCAR Reanalysis 1 dataset (Kalnay et al. 1996). The reanalysis data are the result of an advanced analysis/forecast system that performs data assimilation using past data from 1948 to the present. The data have 2.5° latitude by 2.5° longitude spatial resolution over the whole globe and are available at three different temporal resolutions (4 times a day, daily and monthly). The mean daily values for the two wind components (zonal, *u*, and meridional, *v*) are extracted for the PanAm Village site from the entire global database. The extracted data cover the time period from January 1, 1948 to January 1, 2015 (67 years of data which corresponds to 24,473 data records).

The wind data are given at the sigma-.995 level (also known as the near-surface level, $\sigma_{.995}$). Sigma, σ, is a vertical coordinate used in many meteorological weather forecast models. The coordinate is defined as a ratio of the pressure at a given point in the atmosphere to the surface pressure underneath it. Thus, σ = 1 at the surface and σ = 0 at the top of the atmosphere. A level where σ is equal to 0.995 therefore represents the level in the atmosphere where the pressure is 0.995 times the surface pressure. Wind speed at $\sigma_{.995}$ level is calculated from the wind components as $V_{\sigma.995} = \sqrt{u^2 + v^2}$. Note that $\sigma_{.995}$ actually represents $\sigma_{0.995}$ level, but the zero in the symbol is omitted for simplicity. Wind direction at the $\sigma_{.995}$ level ($D_{\sigma.995}$) is obtained from the two wind components using the four-quadrant inverse tangent, viz.:

$$D_{\sigma.995}(u, v) = \frac{180}{\pi}\left(2\tan^{-1}\frac{\sqrt{u^2 + v^2} - v}{u} + \pi\right), \tag{4-1}$$

where the factor 180/π is used to convert radians to degrees.

Wind rose of direction and intensity, as well as histograms of the wind probability density function (PDF) for the PanAm Village site are shown in Figure 4-2. It can be observed that winds coming in from the third quadrant are the most frequent. These winds were active more than 50% of the time. Southwest winds (240° direction, $V_{\sigma.995}^{240°}$) were blowing approximately 18% of the time. The orientation of this wind direction with respect to the PanAm Village is portrayed in Figure 4-1. It can be seen that the southwest winds are coming in to the PanAm Village from Lake Ontario. Winds blowing from the first and fourth quadrant were rare. Besides being the most frequent winds, Figure 4-2a and histograms in Figure 4-2b,c show that the $V_{\sigma.995}^{240^\circ}$ winds were also the strongest winds (50% of the time $V_{\sigma.995}^{240^\circ} > 6.04$ m s^{-1}).

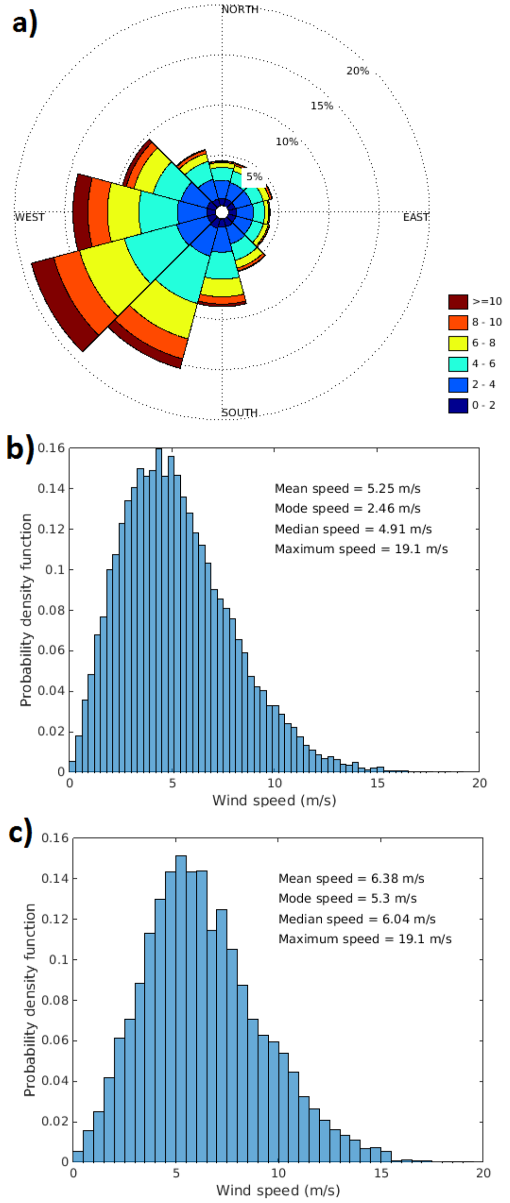

Figure 4-2. a) Wind rose with speed distribution, b) Wind histogram for all wind directions, c) Wind histogram for southwest winds ($V_{\sigma.995}^{240^\circ}$). All data are for the PanAm Village and at the the $\sigma_{.995}$ level.

Due to the dominance of the $V_{\sigma.995}^{240°}$ winds over the PanAm Village site, we chose to perform the wind resource assessment analysis for this wind direction. The methodology described in this paper, however, can be extended and applied to any number of wind directions.

Hereafter the following notation will be used. $X_{\sigma.995}^{240°}$ will represent any variable X given at $\sigma_{.995}$ level when $V_{\sigma.995}^{240°}$ winds were observed. Geometric height of the $\sigma_{.995}$ level ($z_{\sigma.995}$) is computed utilizing the barometric formula rearranged to be solved for the height, i.e.:

$$z_{\sigma.995} = \frac{R^{*}\bar{T}}{Mg} \ln\left(\frac{p_s}{p_{\sigma.995}}\right). \tag{4-2}$$

Here, R^{*} = 8.3145 J mol^{-1} K^{-1} is the universal gas constant, M = 0.029 kg mol^{-1} is the molar mass of air, g = 9.81 m s^{-2} is the gravitational acceleration, $p_{\sigma.995}=0.995 \cdot p_s$ is the pressure at the $\sigma_{.995}$ level (in Pa), p_s is the surface pressure (in Pa), and $\bar{T} = \frac{T_{2m}+T_{\sigma.995}}{2}$ (in K) is the average temperature in the layer between the surface and $\sigma_{.995}$ level. In order to calculate $z_{\sigma.995}$ from Eq. (4-2), the following variables have also been obtained from the reanalysis dataset: p_s, T_{2m}, and $T_{\sigma.995}$. All downloaded data are stored in the self-describing NetCDF files and the total size of the downloaded data is 13.5 MB

Lastly, the air density ($\rho_{\sigma.995}$) is calculated from the ideal gas law as:

$$\rho_{\sigma.995} = \frac{p_{\sigma.995}}{RT_{\sigma.995}}, \tag{4-3}$$

where R = 286.9 J kg^{-1} K^{-1} is the gas constant for dry air.

4.2.3 Methodology and numerical setup

The methodology to estimate the climate change influences on available wind resources in PanAm Village is based on the magnitude and sign of the linear trend of the $V_{\sigma.995}^{240°}$ winds

(Figure 4-3a). Recall, however, that wind speeds are given at the $\sigma_{.995}$ level, which has a variable geometric height (see Section 4.2.2) that depends on the surface pressure. For that reason, the trend of $z_{\sigma.995}^{240°}$ had to be calculated as well (Figure 4-3b) in order to properly interpret the observed trend of $V_{\sigma.995}^{240°}$. The trend in air density, $\rho_{\sigma.995}^{240°}$, is shown in Figure 4-3c.

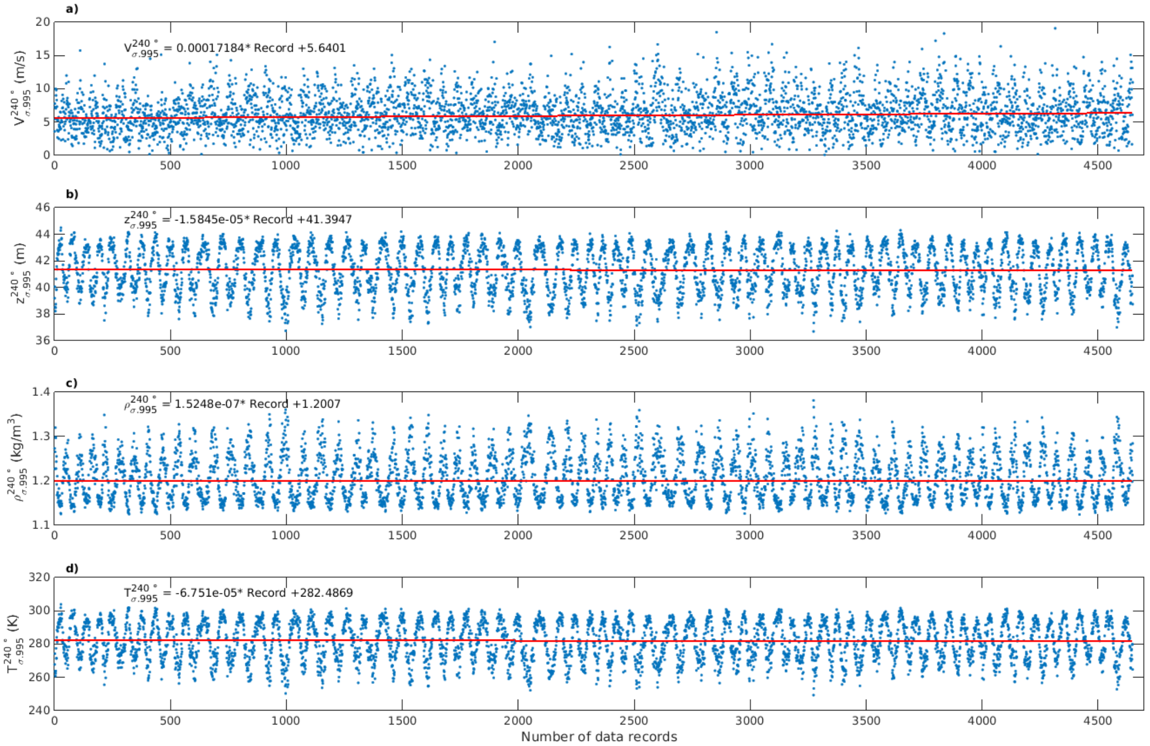

Figure 4-3. Time series and calculated trend lines of: a) $V_{\sigma.995}^{240°}$, b) $z_{\sigma.995}^{240°}$, c) $\rho_{\sigma.995}^{240°}$, and d) $T_{\sigma.995}^{240°}$.

The Mann-Kendall non-parametric test for trend (Mann 1945; Kendall 1970) and Sen's slope estimator (Sen 1968) are used to detect and estimate strength of trends in the time series. These two methods are widely used in many meteorological, climatological as well as wind trend analysis studies (e.g. Tyrlis and Lelieveld 2013; Romanić et al. 2015). The two-tailed Mann-Kendall test inspects the null hypothesis of the absence of trend in the time series at the s significance level (in this study, s = 0.05). Sen's slope estimator calculates and applies the median slope among all the slopes determined by all pairs of data points. The linear equations of the trend lines are given in figures in which trends are analyzed.

The trend lines are used as the inputs for the CFD analysis. Namely, one CFD analysis of wind resources in PanAm Village is performed using the values of $V_{\sigma.995}^{240°}$, $z_{\sigma.995}^{240°}$, and $\rho_{\sigma.995}^{240°}$ at the beginning of each of these three trend lines. In other words, the offset values on the trend lines are used as inputs for the first CFD simulation. The values at the end points on the trend lines are used as the numerical inputs for the second CFD analysis. Difference in the computed wind resources between the first and the second CFD simulation is an estimate of the climate change influence on the wind resources over the PanAm Village. The employed methodology therefore links the long-term wind speed changes over the PanAm Village site with the complexity of flows in that urban environment without taking into consideration the changes in urban planning during the same period of time.

The numerical simulations of wind resources in PanAm Village are performed using a CFD software STAR-CCM+$^{®}$ (Version 9.04), developed by CD-adapco. The numerical setup of the model used in this study is described in Romanić et al. (2015). Namely, the steady-state Reynolds-averaged Navier-Stokes (RANS) equations with the k-ω SST (shear stress transport) turbulence model (Menter et al. 2003) are used to simulate turbulent flow over PanAm Village. The k-ω SST turbulence model has been used in many wind engineering studies (e.g. Jubayer and Hangan 2014; Romanić et al. 2015). The domain is set to be thermally homogeneous with constant air density and the Coriolis effect is neglected. The discretization of the RANS equations is achieved applying second-order accuracy with pressure-velocity coupling through the segregated flow model. The SIMPLE method (Semi-Implicit Method for Pressure-Linked Equations) (Pletcher et al. 2011) is utilized to update the solution between successive iterations.

The inflow velocity profiles are calculated applying the power law on $V_{\sigma.995}^{240°}$ values at the $\sigma_{.995}$ level, viz.:

$$V_{gr}^{240°} = V_{\sigma.995}^{240°}\left(\frac{z_g}{z_{\sigma.995}^{240°}}\right)^{\alpha_s}. \tag{4-4}$$

Here, $V_{gr}^{240°}$ is the gradient wind speed for the 240° wind direction. Boundary layer height of z_g = 500 m is selected. The power law exponent, α_s, for suburban environment is set to be 0.34 (Kaltschmitt et al. 2007). Turbulence intensity profiles are calculated following the ESDU 83045 guidelines (ESDU 2002), as implemented in Romanić et al. (2015). The inflow velocity and turbulence intensity profiles are presented in Figure 4-4.

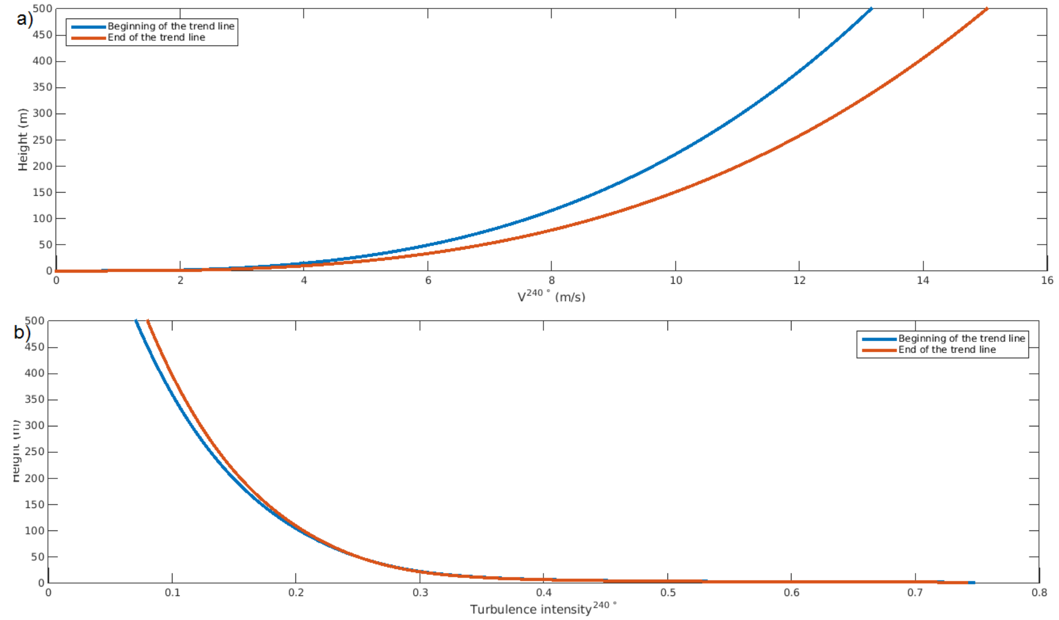

Figure 4-4. a) Inlet velocity profiles and b) inlet turbulence intensity profiles.

The generated polyhedral mesh contains 4.37 million cells in the computational domain sized according to the COST guideline (Franke et al. 2004) (see Figure 4-5). The computational domain is sized in respect to the height of the tallest building in PanAm Village (h = 100 m). Detailed description of the mesh as well as the grid independency analysis are given in Romanić et al. (2015).

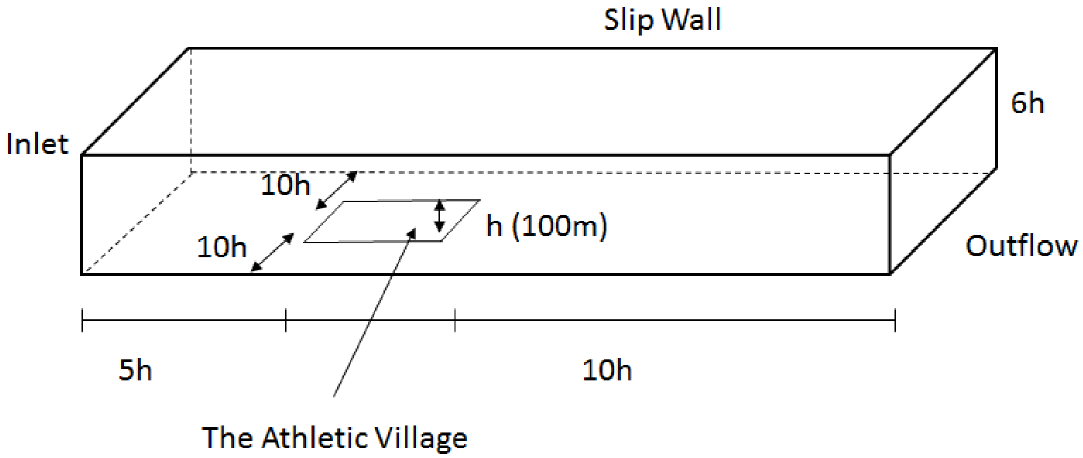

Figure 4-5. Extension of the computational domain with boundary conditions (Romanić et al. 2015).

4.3 Results and discussion

4.3.1 Observed trends

Figure 4-3 shows that $V_{\sigma.995}^{240°}$ winds at the PanAm Village site increased by 0.8 m s^{-1} in the period from 1948 to 2015. This speed-up corresponds to a 14.2 % increase of the offset wind speed. The observed trend is statistically significant with the *p*-value bellow 10^{-4} (see Table 4-1). Important to note is that Sen's slopes of $V_{\sigma.995}^{240°}$ are statistically significant even at the 95% confidence level. $z_{\sigma.995}^{240°}$, $\rho_{\sigma.995}^{240°}$, and $T_{\sigma.995}^{240°}$, on the other hand, were all trendless during the same time period.

Table 4-1. Evaluation statistics of the trend analysis study.

Variable	Mann-Kendall coefficient	Hypothesis test	p-value	Sen's slope (m s^{-1} per record)	Sen's slope with 95 % confidence intervals (m s^{-1} per record)	
					Lower	Upper
$V_{\sigma.995}^{240°}$	0.0533	1	$<10^{-4}$	$1.7\cdot10^{-4}$	$1.1\cdot10^{-4}$	$2.3\cdot10^{-4}$
$z_{\sigma.995}^{240°}$	-0.0091	0	0.3536	$-1.6\cdot10^{-5}$	$-5.0\cdot10^{-5}$	$1.8\cdot10^{-5}$
$\rho_{\sigma.995}^{240°}$	0.0029	0	0.7634	$1.5\cdot10^{-7}$	$-8.4\cdot10^{-7}$	$1.1\cdot10^{-6}$
$T_{\sigma.995}^{240°}$	-0.0056	0	0.5670	$-6.8\cdot10^{-5}$	$-3.0\cdot10^{-4}$	$-1.6\cdot10^{-4}$
$u_{\sigma.995}^{240°}$	0.0492	1	$<10^{-4}$	$1.4\cdot10^{-4}$	$8.4\cdot10^{-5}$	$1.9\cdot10^{-4}$
$v_{\sigma.995}^{240°}$	0.0487	1	$<10^{-4}$	$8.6\cdot10^{-5}$	$5.2\cdot10^{-5}$	$8.6\cdot10^{-4}$
Meridional $\Delta T_{\sigma.995}^{240°}$	0.0415	1	$<10^{-4}$	$1.1\cdot10^{-4}$	$5.7\cdot10^{-5}$	$1.6\cdot10^{-4}$
Zonal $\Delta T_{\sigma.995}^{240°}$	0.0319	1	0.0011	$1.0\cdot10^{-4}$	$4.1\cdot10^{-5}$	$1.6\cdot10^{-4}$

Trend analysis of the wind speed components (zonal, $u_{\sigma.995}^{240°}$), and meridional, $v_{\sigma.995}^{240°}$) is further performed in order to better understand the observed trend of the $V_{\sigma.995}^{240°}$ winds. The results are depicted in Figure 4-6 and Table 4-1. Both wind components have statistically significant positive trends. The positive trend in zonal wind speeds (1.4×10^{-4} m s^{-1} per record) is considerably stronger than the trend in meridional wind speeds (8.6×10^{-5} m s^{-1} per record). Holt and Wang (2012) concluded that the increase of zonal wind speed components in the Great Lake region is due to the positive trend of the westerly winds. They also noticed that the strength of mid-latitude jet stream increased over the last several decades. The westerly belt and the mid-latitude jet stream are the key elements of the general circulation of the atmosphere.

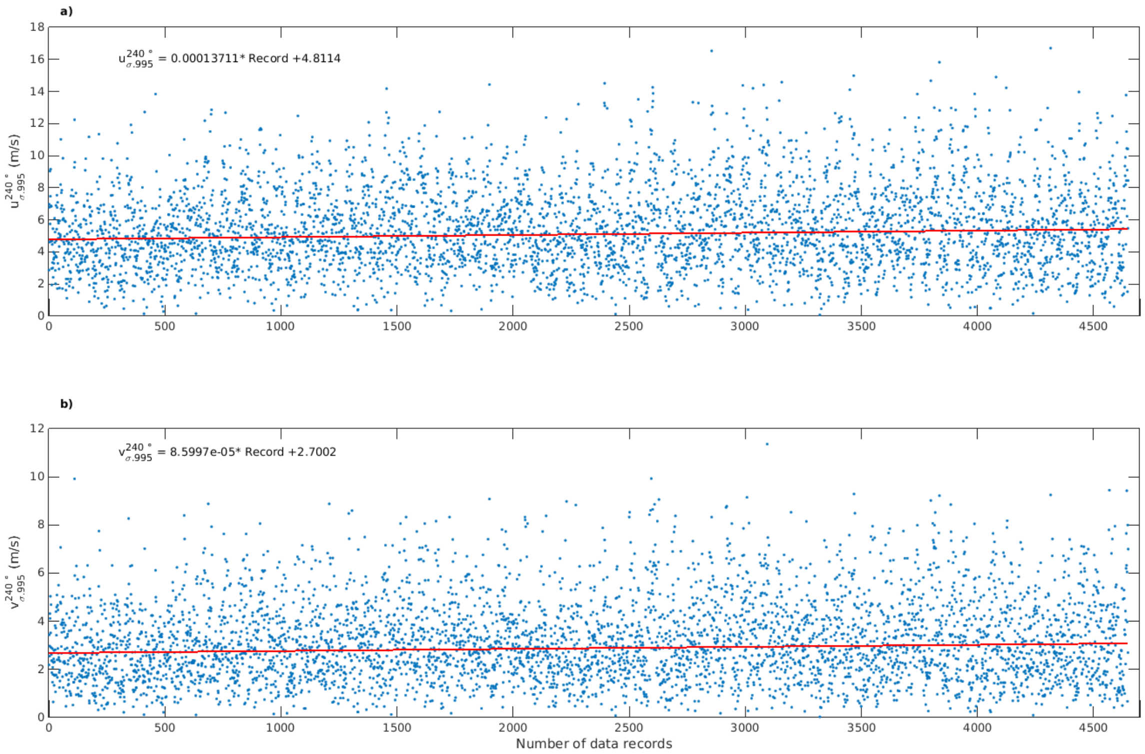

Figure 4-6. Trend analysis of a) zonal and b) meridional components of the $V^{240°}_{\sigma.995}$ winds.

The long-term trends of wind speeds could also be caused or altered by the trends of the horizontal temperature gradients. The relationship between trends of wind speed and trends of temperature is relatively straightforward. Namely, winds are caused by differences in temperature which in turn result in pressure differences (i.e. pressure gradients). A long-term trend of temperature gradients would therefore be accompanied with the corresponding wind speed changes. For that reason, the meridional and zonal temperature gradients over 5° latitude and 5° longitude are calculated at the PanAm Village site (Figure 4-7 and Table 4-1). The positive trend in the period 1949-2015 is statistically significant for both meridional and zonal temperature gradients. The meridional temperature gradient, however, is more pronounced than the zonal temperature gradient. This result is in accordance with the previous finding that the zonal wind component ($u_{\sigma.995}^{240°}$) has experienced stronger positive trend in the analyzed 67-year long period.

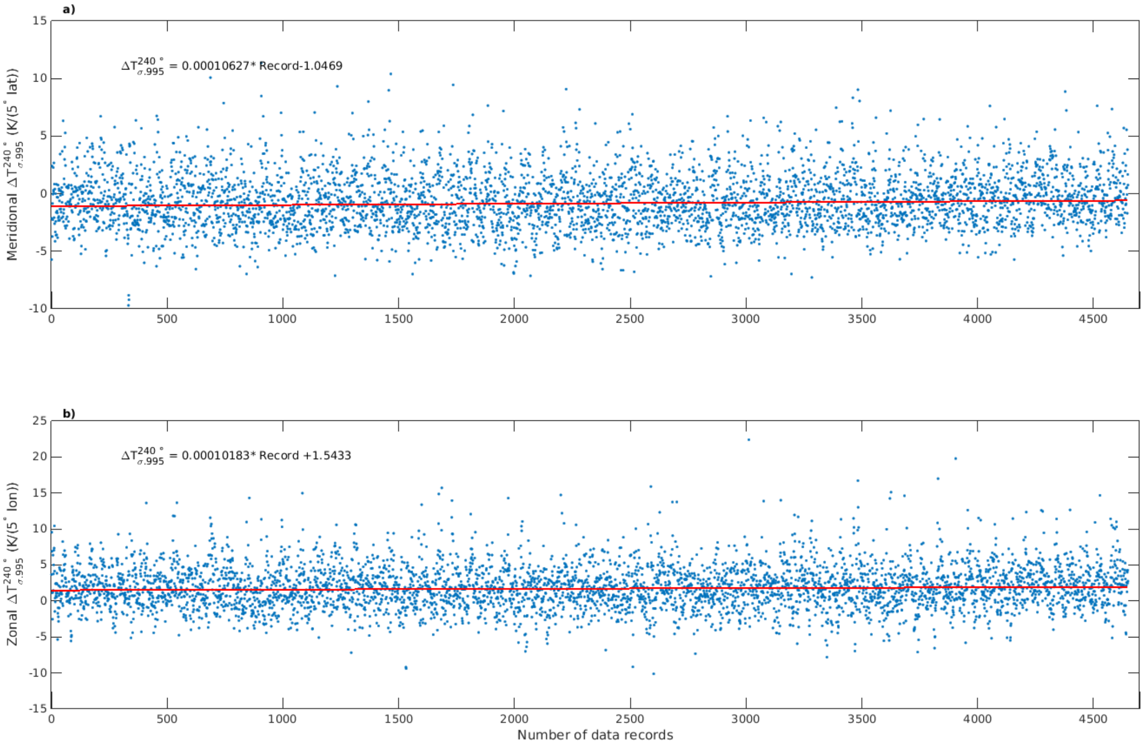

Figure 4-7. Trend analysis of a) meridional and b) zonal temperature gradients.

4.3.2 Wind resource assessment study

The results of the wind resource assessment analysis at the PanAm Village site are shown in Figure 4-8. As previously explained in Section 4.2.2, flow fields in Figure 4-8a,b are based on the $V_{\sigma.995}^{240°}$ values from the first and the last point on the trend line in Figure 4-3a, respectively. Wind speeds in Figure 4-8 are given at 5 m above all surfaces (roads, roofs, and walls) in PanAm Village. The height of 5 m is chosen for the reason that most urban wind turbines are either Vertical Axes Wind Turbines (VAWT) or Horizontal Axis Wind

Turbines (HAWT) with low hub heights which are typically below 10 m above the roof surface.

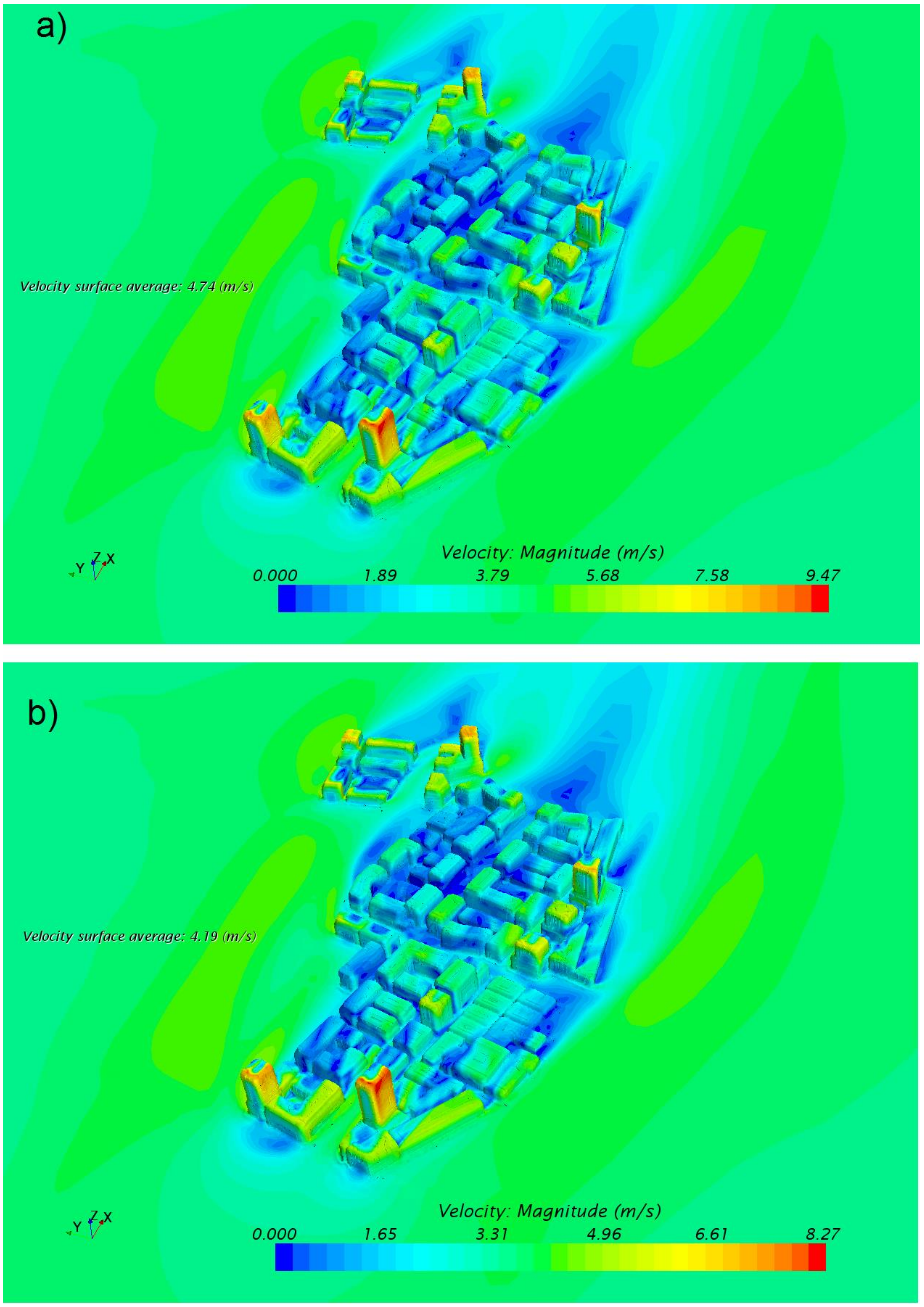

Figure 4-8. Velocity field at 5 m above building and ground surfaces calculated using the trend line in Figure 3a). Wind fields based on a) the first (i.e. the offset) value of the $V_{\sigma.995}^{240^\circ}$ trend line and b) the last points on the trend line. Flow is along *x*-axis.

The resulting wind field portrayed in Figure 4-8 can be compared with the long-term wind speed trend in Figure 4-3a. It can be seen that the difference between the area-averaged speeds on the isosurface positioned at 5 m above all surfaces is 0.25 m s^{-1} smaller than the corresponding long-term increase of the $V_{\sigma.995}^{240°}$ winds (see Figure 4-3a and Table 4-1). The spatial average of velocities is the standard method to address the problem of horizontal inhomogeneity of flows in urban environments (Cheng and Castro 2002; Kastner-Klein and Rotach 2004; Romanić et al. 2015). These results lead to the conclusion that the long-term increase of the $V_{\sigma.995}^{240°}$ winds above PanAm Village is a function of complexity of the urban environment. The influence of urban environment on the flow is incorporated twofold. First, the nonlinearity of the power law (Eq. (4-4)) and the adequate values of the power law exponent for urban or sub-urban environments are necessary to vertically extrapolate velocities from one height to another. Due to the non-linearity of the power law and the requirement of no-slip condition at the surface, the calculated wind speed trends will be a function of the height above ground. Second, small scale features of urban environments (e.g. buildings, trees, cars) are not directly accounted for in the reanalysis data. The presented CFD analysis, on the other hand, is capable of capturing some of these features and therefore their non-linear effects on the flow field in the analysed urban block. The above discussion and the presented results indicate that an accurate modelling of the complex nature of urban winds is an important prerequisite for adequate urban wind resource assessment in changing climate.

The difference between surface averaged velocities between the two model runs is 0.55 m s^{-1}, as indicated in Figure 4-8a,b. The maximum (peak) velocities, on the other hand, differ by 1.2 m s^{-1}. This observation is in accordance with literature. Namely, Cheng et al. (2012) investigated a possible impact of climate change on wind gusts in Ontario, Canada. They concluded that the hourly wind gusts above 28 m s^{-1} in the period 2081-2100 are expected to be 10% to 15% greater than the observed gusts for the period 1994-2007. It seems that the peak velocities are more influenced by climate change than the mean velocities.

The observed long-term increase of the mean wind speed could be beneficial for the urban wind energy utilization. Wind turbines employed in urban environments are typically vertical axis wind turbines (Romanić et al. 2015). For this reason, the observed increase in the peak wind speed and hence turbulence intensity should not considerably affect their performances.

Increased ventilation effect due to higher wind speeds results in better air quality in cities. Namely, higher wind speeds carry away the pollutants from their origin faster and more efficient. The increase of the turbulence intensity contributes in diluting pollutants. The observed increase in peak winds, however, could have negative effects on the wind turbine performance and building design from a structural point of view. Higher peak speeds and increased turbulence intensity lead to more pronounced wind loadings and wind-induced dynamic responses.

Lastly, it should be noted here that the presented analysis takes into account only one wind direction and no changes in urban coverage. For the complete picture of the connection between climate change and urban winds, actual and planned changes to the urban surface with time as well as all wind directions should be considered. These factors shall be investigated in the next step of this research. Furthermore, future work should include the thermal effects, atmospheric stability and increased vertical air flow due to local heating.

4.4 Concluding remarks

This study analysed the long-term wind speed trend above the 2015 Pan American Games Athletes' Village (PanAm Village), located in Toronto, Ontario, Canada. Based on the NCEP/NCAR Reanalysis 1 data (Kalnay et al. 1996), it is shown that the speed of the predominant winds at PanAm Village, the southwest winds, increased by 0.8 m s^{-1} in the period from 1948 to 2015.

The increase of the zonal wind component was larger than the increase of the meridional wind component. Air temperature and air density, on the other hand, were trendless. An additional analysis showed that both zonal and meridional temperature gradients above the PanAm Village had positive trends during the same period. This finding indicates that the observed positive trends of wind speeds might be caused by the positive trends of the temperature gradients.

A wind resource assessment analysis based on the velocity data obtained from the trend analysis is performed using the CFD tool. The results show that the long-term wind speed changes do not affect the mean velocity field at PanAm Village as much as they influence the peak values. It has been demonstrated that randomly spaced and located objects in urban environments are factors which have to be accounted for in urban wind resource studies in changing climate.

References

Black B and Flarend R (2010) *Alternative Energy*. 1 edition. Santa Barbara, Calif: Greenwood.

Cheng CS, Li G, Li Q, et al. (2012) Possible impacts of climate change on wind gusts under downscaled future climate conditions over Ontario, Canada. *Journal of Climate* **25** (9): 3390–3408.

Cheng H and Castro IP (2002) Near wall flow over urban-like roughness. *Boundary-Layer Meteorology* **104** (2): 229–259.

Cook J, Nuccitelli D, Green SA, et al. (2013) Quantifying the consensus on anthropogenic global warming in the scientific literature. *Environmental Research Letters* **8** (2): 24024.

ESDU (2002) *Strong winds in the atmospheric boundary layer: Part 2: Discrete gust speeds*. 83045. London: ESDU International PLC.

Franke J, Hirsch C, Jensen AG, et al. (2004) Recommendations on the use of CFD in wind engineering. *Cost action C* **14**: C1.

Hansen J, Sato M, Kharecha P, et al. (2011) Earth's energy imbalance and implications. *Atmospheric Chemistry and Physics* **11**(24): 13421–13449.

Holt E and Wang J (2012) Trends in Wind Speed at Wind Turbine Height of 80 m over the Contiguous United States Using the North American Regional Reanalysis (NARR). *Journal of Applied Meteorology and Climatology* **51**(12): 2188–2202.

Jubayer CM and Hangan H (2014) Numerical simulation of wind effects on a stand-alone ground mounted photovoltaic (PV) system. *Journal of Wind Engineering and Industrial Aerodynamics* **134**: 56–64.

Kalnay E, Kanamitsu M, Kistler R, et al. (1996) The NCEP/NCAR 40-Year Reanalysis Project. *Bulletin of the American Meteorological Society* **77**(3): 437–471.

Kaltschmitt M, Streicher W and Wiese A (2007) *Renewable Energy - Technology, Economics and Environment*. XXXII. Berlin Heidelberg New York: Springer. Available from: http://download.springer.com/static/pdf/160/bok%253A978-3-540-70949-7.pdf?auth66=1410992253_4984dee130c697ec5c4907beb05bf5d1&ext=.pdf (accessed 15 September 2014).

Kastner-Klein P and Rotach MW (2004) Mean Flow and Turbulence Characteristics in an Urban Roughness Sublayer. *Boundary-Layer Meteorology* **111**(1): 55–84.

Kendall MG (1970) *Rank correlation methods*. London: Griffin.

Mann HB (1945) Nonparametric Tests Against Trend. *Econometrica* **13**(3): 245–259.

McVicar TR, Roderick ML, Donohue RJ, et al. (2012) Global review and synthesis of trends in observed terrestrial near-surface wind speeds: Implications for evaporation. *Journal of Hydrology* **416–417**: 182–205.

Menter FR, Kuntz M and Langtry R (2003) Ten Years of Industrial Experience with the SST Turbulence Model. In: *The fourth international symposium on turbulence, heat and mass transfer, turbulence heat and mass transfer series*, Begell House, Antalya, pp. 625–632. Available from: http://cfd.mace.manchester.ac.uk/flomania/pds_papers/file_pds-1068134610Menter-SST-paper.pdf (accessed 23 September 2014).

Milanković M (1920) *Théorie mathématique des phénomènes thermiques produits par la radiation solaire*. Paris: Gauthier-Villars et Cie.

Milanković M (1930) *Mathematische Klimalehre und astronomische Theorie der Klimaschwankungen*. Berlin: Gebrüder Borntraeger.

Pletcher RH, Tannehill JC and Anderson D (2011) *Computational Fluid Mechanics and Heat Transfer*, 3rd edition. Boca Raton: CRC Press.

Romanić D, Ćurić M, Jovičić I, et al. (2015) Long-term trends of the 'Koshava' wind during the period 1949–2010. *International Journal of Climatology* **35**(2): 288–302.

Romanić D, Rasouli A and Hangan H (2015) Wind resource assessment in complex urban environment. *Wind Engineering* **39**(2): 193–212.

Sen PK (1968) Estimates of the Regression Coefficient Based on Kendall's Tau. *Journal of the American Statistical Association* **63**(324): 1379–1389.

Trenberth KE (2009) An imperative for climate change planning: Tracking Earth's global energy. *Current Opinion in Environmental Sustainability* (1): 19–27.

Tyrlis E and Lelieveld J (2013) Climatology and dynamics of the summer etesian winds over the Eastern Mediterranean. *Journal of the Atmospheric Sciences* **70**(11): 3374–3396.

United Nations (2014) *World Urbanization Prospects The 2014 Revision*. New York: United Nations. Available from: http://esa.un.org/unpd/wup/Highlights/WUP2014-Highlights.pdf (accessed 20 January 2015).

Vautard R, Cattiaux J, Yiou P, et al. (2010) Northern Hemisphere atmospheric stilling partly attributed to an increase in surface roughness. *Nature Geoscience* **3**(11): 756–761.

Chapter V

5 Wind climatology and wind resource modelling for a modern development situated in “Tornado Alley”

5.1 Introduction

Environmental sustainability is one of the main goals of a modern society. Meteorology, being the science that investigates the atmosphere and its phenomena, is therefore a key factor in the field of environmental sustainability. Most of the current research dealing with the meteorological applications in sustainability is focused on wind and solar resource assessments (Welch and Venkateswaran 2009, Jacobson and Delucchi 2011, Delucchi and Jacobson 2011). In fact, these two renewable sources of energy are the main combatants against the on-going climate changes.

This paper presents a comprehensive wind climatology analysis, as well as a wind resource assessment study with applications to sustainability and resilience of a modern development, called the Kansas Project (KP; Figure 1; http://kansasproject.com/), located in the heart of Tornado Alley; South Central Kansas, United States (US). This one-of-a-kind project investigates puzzling questions such as how to design a resilient building(s) that will realistically evoke relationship between people and weather in a safe environment, as well as how can a design foster a more symbiotic relationship between people and weather? In essence, these are the quintessential questions behind the concept of sustainable developments. Answering these questions, however, requires a number of engineering and meteorological analysis to be performed. A series of numerical and experimental simulations are designed and executed by the Wind Engineering, Energy and Environment (WindEEE) Research Institute (Hangan 2010) at Western University to develop a place that is equal parts laboratory, house, theatre, playground and shelter. Herein, we present a part of the research that focuses only on wind-related aspects which are of practical importance for sustainability of the KP. In an accompanying study, tornado climatology along with aerodynamic wind loads experienced by this development under atmospheric boundary layer and tornadic flows will be studied. This project, for the first time, links the weather of Tornado Alley with human sensory experience through a multidisciplinary approach and therefore, can act as a guide for future attempts of this kind.

A number of recent case studies have investigated the feasibility and benefits of wind power projects in rural (Weekes et al. 2015, Sharma and Ahmed 2016, Watts et al. 2016), offshore (Oh et al. 2012, Castro-Santos et al. 2016a, Castro-Santos et al. 2016b), and urban (Romanić et al. 2015b, Weekes et al. 2015, Sharma and Ahmed 2016, Romanic et al. 2016a) environments. Furthermore, the growth of renewable energy share in the overall production is set only to increase in the next several decades (Johansson et al. 1993). For all practical purposes, wind energy is inexhaustible and presents a clean source of electricity with zero emissions. Potentially harmful ecological effects of wind energy are discussed in Saidur et al. (2011) and Mann and Teilmann (2013). According to the 2015

Global Wind Report (GWEC 2016), the US installed more than 74 GW of wind power capacity in 2015. As of 2016, the installed wind capacity in the US increased by an additional 65 GW (AWEA 2016). Moreover, the same study shows that 23.9% of the overall electricity consumed in 2015 in Kansas was generated from the wind. Interestingly, Kansas could annually yield an amount of wind generated electricity that is more than 75% of the total electricity produced in the US in 2011 (Lopez et al. 2012).

The Kansas wind resource at 50 m height shows a large spatial variability (NREL 2009). The western and central regions are characterized by the highest wind energy potential, which typically lies between 400 and 600 W m^{-2}. The lowest wind energy potential is found in the eastern parts of the state, where it generally falls below 300 W m^{-2}. These values are more conservative than the one previously reported in the Wind Energy Resource Atlas of the US (Elliott et al. 1986). Although the large-scale wind potential maps, such as NREL (2009) and Elliott et al. (1986), are valuable materials to locate potential regions suitable for wind farms, they have limited precision due to the interpolation of data with low spatial resolution. For that reason, results obtained using wind resource assessment software packages, such as the Wind Atlas Analysis and Application Program (WAsP), are more reliable for estimating the wind potential of a particular site due to the higher resolution of orography and roughness used in these simulations.

Herein, WAsP is employed to assess the wind potential of the KP site. In addition, this study provides wind climatology analysis for the region around the site. The climatological analysis is conducted with the goal of understanding the overall wind conditions around the project site. The KP site is located in “Tornado Alley”; an area well-known for extreme weather conditions such as tornados and droughts. Hence, an additional goal of the project is to design a safe environment for inhabitants.

The shape of the KP site roughly resembles a backwards C (Figure 5-1). The project site is 680 acres (2.75 km^2) of pasture, meadows and buttes, nestled in the rugged Gypsum Hills of South Central Kansas (Figure 5-1). It is approximately 130 km southwest of Wichita and about 20 km west of the town of Medicine Lodge. In the other direction, Dodge City is located approximately 117 km to northwest of the site.

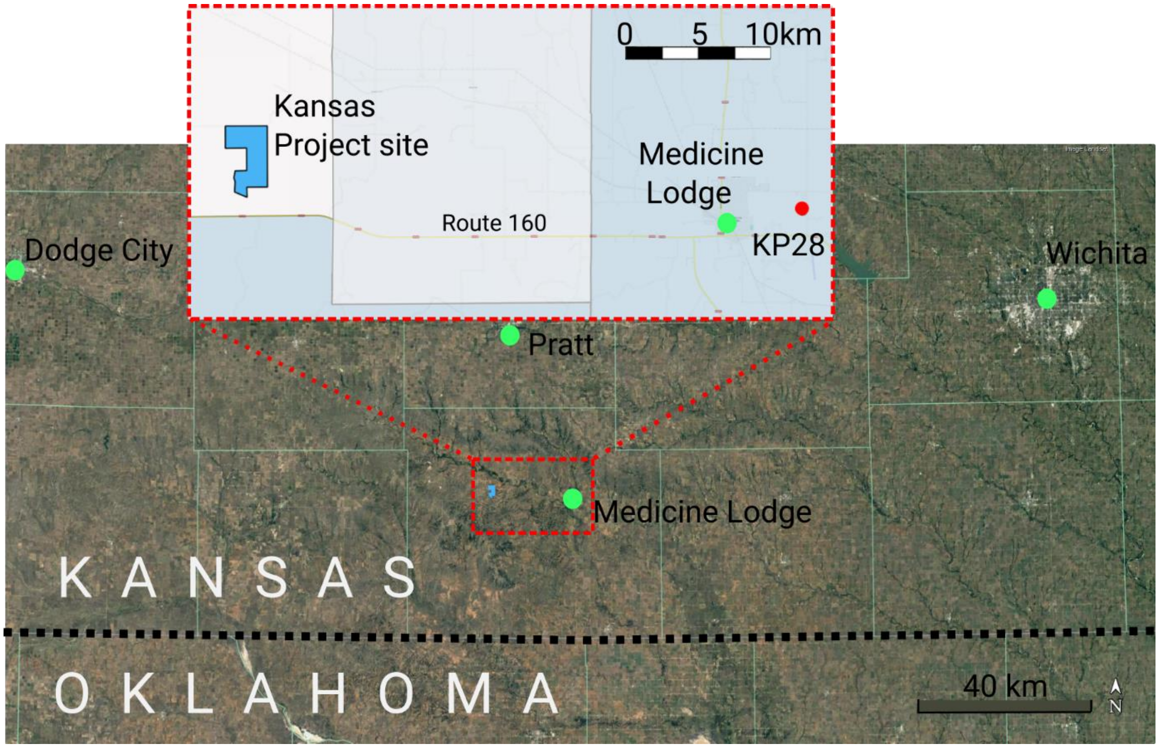

Figure 5-1. The Kansas Project site (blue polygon) and the town of Medicine Lodge (location of the weather station KP28 indicated with the red circle).

5.2 Methods and data

5.2.1 WAsP methodology

The numerical model used to assess the wind resource at the KP site is WAsP. This software package was developed at the Department of Wind Energy, the Risø National Laboratory, Technical University of Denmark, in order to create the European Wind Atlas (Troen and Petersen 1989). WAsP is a linear model composed of several individual modules that based on the well-established physical principles of atmospheric flows perform horizontal and vertical extrapolation of wind. The inputs for the WAsP flow model are: (1) elevation of terrain, (2) terrain roughness and (3) sheltering obstacles.

The WAsP modelling concept is known as the wind atlas methodology. The wind atlas represents a hypothetical wind climate for an ideally smooth, featureless terrain with a uniform land cover assuming that the whole computational domain is under the same weather regime (Troen and Petersen 1989). In order to determine the wind atlas of the region from measurements in actual terrain, the WAsP flow model is used to remove the local terrain effects such as terrain elevation, roughness and sheltering obstacles. On the other side, in order to determine the local wind climate at the location of interest using the wind atlas created in the previous step, the WAsP flow model is used to incorporate the effects of terrain features, i.e. elevation, roughness and sheltering obstacles. This study uses the latest version of the WAsP software package: WAsP 11 (Version 11.05.0002), WAsP Map Editor 11 and WAsP Climate Analyst (Versions 2 and 3).

5.2.2 Wind data

Raw wind data used for the wind resource assessment study are acquired from the nearest weather station situated in Medicine Lodge, Kansas (lat: 37° 17' 2"N, lon: 98° 33' 10" W, altitude: 468 m above sea level, Figure 5-1). This weather station is located approximately 20 km east of the project site. Hereafter, the station will be referred to as KP28, which is the International Civil Aviation Organization (ICAO) Call Sign of this weather station. KP28 belongs to the Automated Surface Observations System (ASOS) network of stations. As such, data are collected and transmitted automatically and the site is not manned.

ASOS continuously measures wind direction and speed once every second and then 5-second wind direction and wind speed averages are computed from the 1-second measurements. These 5-second averages are rounded to the nearest degree and nearest knot and are retained for 2 minutes. The 5-second averages are the fundamental units used to compute reportable wind values in ASOS system. The ASOS algorithm uses a 2-minute period to obtain the current average wind direction from 24 5-second segments. The 2-minute average is therefore updated every 5 s. Once each minute, the current 2-minute average wind is stored in memory for 12 hours and made available for hourly reports. The full description of the ASOS weather data is provided in NOAA (1998) and NCDC (2003). Table 5-1 lists the main specification of the anemometer and wind vane installed at KP28.

Table 5-1. Specification of the anemometer installed at the KP28 weather station. The units in this table are the one used in calibration of the instruments, whereas the units in the rest of this chapter are SI units.

Element name	Units	Range	Resolution	Time average (min)	Start date	End date
Wind speed	knots	0 to 125	1	2	1-Jan-1984	31-Dec-2015
Wind direction	°	0 to 359	1	2	1-Jan-1984	31-Dec-2015

There are three noticeable gaps in wind measurements from KP28. The first gap without data is between 25-Sep-1986 (07:00 UTC) and 03-Feb-1987 (15:00 UTC), with only few data points in between. The second period with missing data is from 26-Jul-1996 (06:48 UTC) to 23-Aug-1996 (16:48 UTC). The third and last time interval without data is from 02-Feb-2000 (15:56 UTC) to 03-May-2000 (00:56 UTC).

Table 5-2 provides the statistical information of raw wind data, such as data coverage, number of recordings in the time series and calm threshold used during the pre-processing of raw wind data from KP28. Wind speeds below 0.5 m s^{-1} were flagged as calms. Namely, anemometer and wind vane readings for these small wind speeds are unreliable and, moreover, these small wind speeds have no practical importance in wind energy projects (Romanić et al. 2015a). These small velocities are below the cut-in wind speed of any wind turbine on the market. Recovery percentage (87.84%) is a figure which represents the number of successfully imported records as a percentage of the total number of records in the file.

Table 5-2. The import statistics of raw wind data from KP28 weather station used in wind resource assessment study.

Name	Wind speed	Wind direction
Recordings count	265899	265899
Start time	1-Jan-1984	1-Jan-1984
End time	29-Dec-2015	29-Dec-2015
Lower limit	0 m s^{-1}	1°
Readings below lower limit	None	19551 (7.35%)
Upper limit for wind speed	64.3 m s^{-1}	360°
Reading above upper limit	None	None
Calms threshold	0.5 m s^{-1}	0.5 m s^{-1}
Calms	19248 (7.24%)	3234 (1.31%)
Valid readings accepted	265899 (100%)	246348 (92.65%)
Accepted values range	0-28 m s^{-1}	0-350°
Expected recording count:	280465	
Count of records in raw data	265889 (94.81%)	
Recordings in invalid values in one or more fields	19551 (7.35%)	
Entirely valid recordings accepted	246348 (92.65%)	
Recovery percentage (vs. expected)	87.84%	

A Weibull distribution is often a good approximation for the wind speed distribution. This distribution is used in WAsP to represent the wind characteristics of each directional sector. The Probability Density Function (PDF) of a Weibull distribution is given by the following expression:

$$\mathrm{PDF}(U) = \frac{k}{A}\left(\frac{U}{A}\right)^{k-1} e^{-\left(\frac{U}{A}\right)^{k}}. \tag{5-1}$$

Where, A is the scale parameter (m s^{-1}), k is the shape parameter, and U is the mean wind speed (m s^{-1}). Note that A is proportional to the mean wind speed. Weibull-k parameter takes values between 1 and 3, where small values of k represent very variable winds and large k values correspond to rather constant winds. The omnidirectional wind statistics of the processed data is given in Table 5-3.

Table 5-3. All-sectors wind statistics of the processed raw data from the KP28 weather station used in the wind resource assessment study.

Wind statistics	Weibull-A (m s^{-1})	Weibull-k	Mean speed (m s^{-1})	Power density (W m^{-2})
Source data	-	-	4.16	102
Fitted	4.8	1.69	4.31	108
Emergent	-	-	4.38	108
Combined	4.9	1.74	4.38	108

In Table 5-3, the “Fitted” parameters are representative of a Weibull distribution that is fitted to an all-sector wind speed histogram. This distribution is used only in connection with the observed wind climate and is not further used for wind resource calculations. In WAsP, wind resources are calculated using the Emergent distribution (Mortensen et al. 2014). The “Emergent” distribution represents the weighted sum of the Weibull distributions from all the directional sectors. In principle, this distribution does not have to be Weibull. Lastly, the “Combined” parameters are representative of a Weibull distribution matching the mean speed and power density with the weighted sum of the sector-wise mean speeds and power densities, respectively (Mortensen et al. 2014). For that reason, the Combined Weibull distribution has the same mean speed and power density as the Emergent distribution. The discrepancy between the source and Emergent mean wind speeds is 5.3%, whereas the discrepancy between the source and Emergent mean power densities is 5.2%.

The omnidirectional Weibull distribution and wind rose are shown in Figure 5-2. The most frequent winds at the KP28 weather station are blowing from (in decreasing order) south, south-southeast and north directions. These winds were present about 50% of the time in a year. Bi-directionality of the site is very pronounced. There is a small discrepancy between

Emergent and Fitted Weibull distributions, which, however, is not further projected to the power densities.

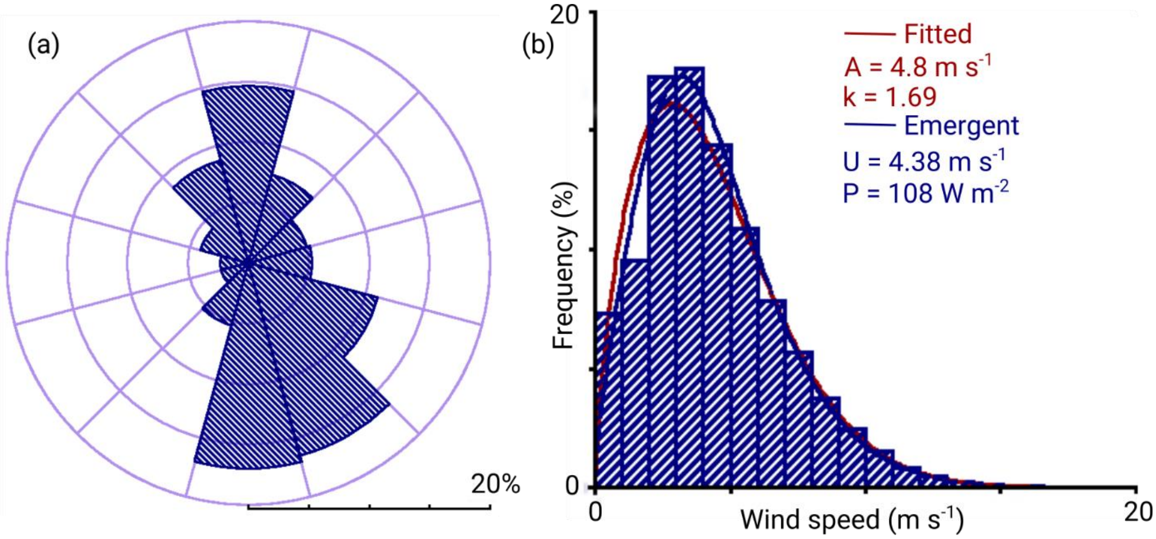

Figure 5-2. Wind rose and all-sector Weibull distribution based on the wind data from the KP28 weather station.

Sector-wise mean wind speed, Weibull parameters and mean power density are given in Table 5-4. It can be seen that the strongest winds are associated with the 180° sector, for which the mean wind speed is 5.14 m s^{-1} and the power density is equal to 140 W m^{-2}. The second and third windiest directions are 0° and 30°, with mean wind speeds of 5.08 m s^{-1} and 5.00 m s^{-1}, respectively. Interestingly, the 210° direction is characterized with strong winds (4.99 m s^{-1}), but small windiness (only 5.3% of the time in a year). The least frequent wind directions are 240° and 270°.

Table 5-4. Sectors-wise wind statistics of the processed raw data from the KP28 weather station. A – Weibull-A parameter (m s^{-1}); k – Weibull-k parameter; U – mean wind speed (m s^{-1}); P – mean power density (W m^{-2}), f – frequency of occurrence of winds from a given sector (%).

	0°	30°	60°	90°	120°	150°	180°	210°	240°	270°	300°	330°
A	5.7	5.6	4.4	3.8	3.6	4.7	5.8	5.6	3.7	3.0	3.6	5.3
k	1.70	1.96	1.89	2.06	2.50	2.27	2.16	1.99	1.36	1.28	1.28	1.57
U	5.08	5.00	3.87	3.37	3.22	4.14	5.14	4.99	3.41	2.83	3.36	4.74
P	174	141	68	41	31	70	140	138	73	47	77	157
f	14.6	7.6	5.0	5.3	11.1	16.5	17.0	5.3	2.4	2.4	4.1	8.7

5.2.3 Elevation and roughness maps

The elevation map of the area around the project site and the weather station in Medicine Lodge (anemometer symbol) are shown in Figure 5-3. The map projection is Universal Transverse Mercator (UTM), Zone 14 and the datum is WGS-1984. The elevation map is obtained from the US Geological Survey (USGS) products at: http://eros.usgs.gov/elevation-products. The map is a Digital Elevation Model (DEM), developed under the 3D Elevation Program (3DEP) which uses light detection and ranging (Lidar) as the primary source of elevation data. The obtained elevation map has a grid spacing at 1/3 arc-second, which is approximately 10 m. The elevation contours are afterwards interpolated using the System for Automated Geoscientific Analyses (SAGA) software to meet the resolution of 5 m.

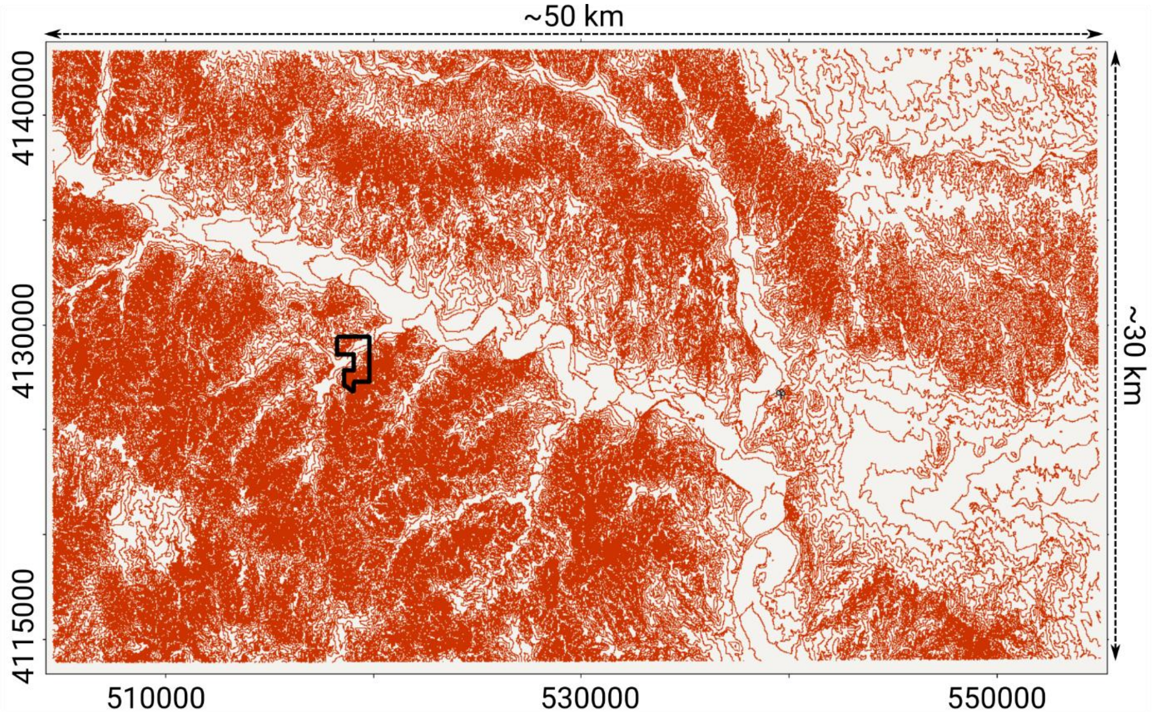

Figure 5-3. Elevation map of the area around the project site and KP28 weather station in Medicine Lodge.

In order to represent elevation and roughness changes around the project site and the reference weather station, the elevation (Figure 5-3) and roughness (Figure 5-4) maps are extended approximately 15 km from each site. The distance between the project site and the weather station is about 20 km in the west-east direction. The whole region is fairly smooth with the elevation ranging between 420 m and 625 m above sea level. In total, there are 4153 elevation contours in Figure 5-3.

The roughness map is presented in Figure 5-4. This map is created combining the available information from the National Land Cover Database 2011 (NLCD 2011, Homer et al. 2015) obtained at: http://www.mrlc.gov/nlcd2011.php and Google Earth®. NLCD 2011 is the most recent US national land cover product created by the Multi-Resolution Land

Characteristics (MRLC) Consortium. NLCD 2011 has a 16-class land cover classification scheme that has been applied consistently across the US at a spatial resolution of 30 m.

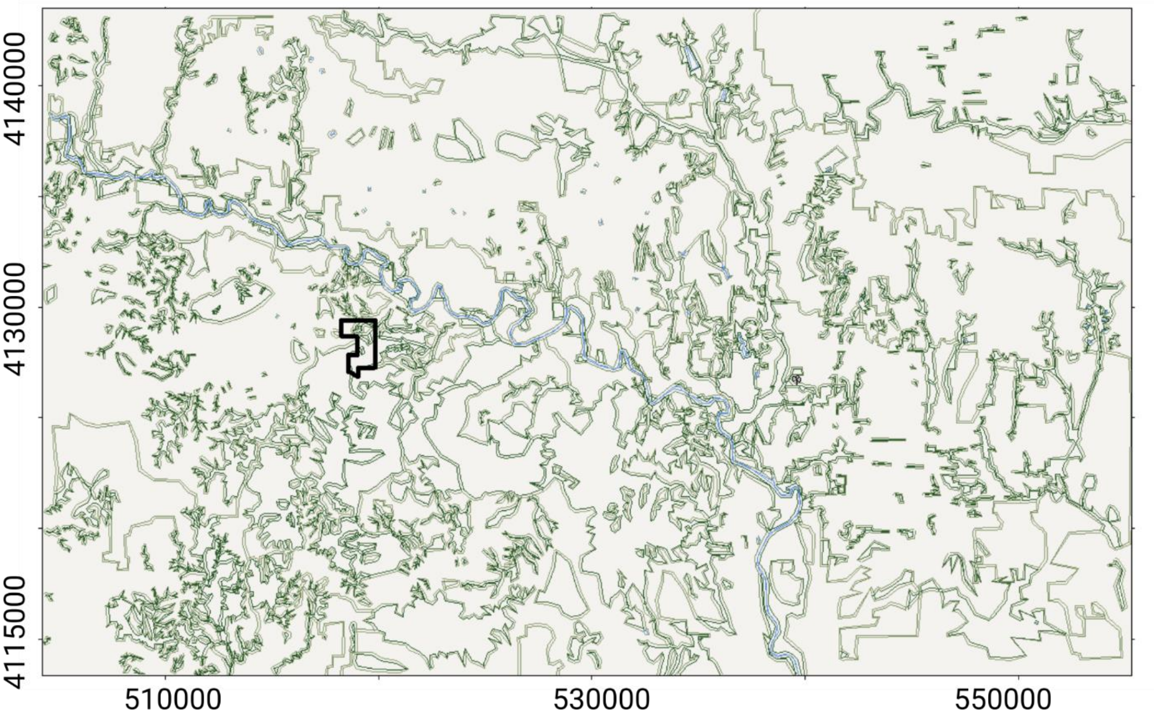

Figure 5-4. Roughness map of the area around the project site and KP28 weather station. Contour lines form closed areas with a constant value of roughness length inside.

The land coverage categories are transformed into roughness lengths following the recommendations by the US Environmental Protection Agency (EPA 2013). In accordance with that study (EPA 2013) and after the detailed inspection of the Google Earth® maps, the following relationships between different land cover categories and roughness lengths have been established (Table 5-5).

Table 5-5. Values of surface length for the NCLD 2011 land use categories.

Category number	Category name	Roughness length (m)
11	Water	0
71	Grasslands/Herbaceous	0.05
82	Cultivated crops	0.09
41/22	Deciduous forest/suburban	0.5
42	Evergreen forest	0.9
23	Urban (medium intensity)	1

The whole region of interest is characterized with 6 different roughness lengths. Water surfaces have a roughness lengths of 0 m (although WAsP internally uses the value of 0.0002 m), open terrain areas are given a roughness length of 0.05 m or 0.09 m (depending on exposure), small forest areas and some suburban zones are assigned a roughness length of 0.5 m, larger forests are characterized by a roughness length of 0.9 m and, finally, the urban parts of Medicine Lodge are given a roughness length of 1 m. In total, there are 1007 roughness lines in Figure 5-4. There are no sheltering obstacles around the KP28 weather station and the KP site.

5.2.4 Trend and extreme value analysis

In this paper, the Mann-Kendall test for trend (Mann 1945, Kendall 1970) and Sen's slope estimates (Sen 1968) are employed in the trend analysis of mean annual wind speeds. Both methods are well-examined and used in numerous climatological studies (Romanić et al. 2015a, Romanic et al. 2016b). A two-tailed Mann-Kendall test inspects the null hypothesis of trend absence in the time series, against the alternative of the trend. In this case, the result of the test is returned as H_1 = 1, 2, 3 or 4 indicating a rejection of the null hypothesis at the α significance level, where $\alpha = 0.1, 0.05, 0.01$ and 0.001, respectively. $H_1 = 0$ means that the null hypothesis is not rejected at $\alpha = 0.1$.

The extreme value analysis on the annual basis is performed using the Gumbel method (Palutikof et al. 1999). The ordered annual maxima are first plotted against the estimated cumulative distribution function of the Gumbel distribution. Then, a line is fitted using the least squares method to obtain the regression line. The intercept and slope of the straight line correspond to the location and scale parameters of the Gumbel distribution. The plotting position of the fitted line relies on the Gringorten estimation of probability (Gringorten 1963).

5.3 Results and discussion

5.3.1 Wind climatology

The climatological study is performed on the raw set of data without excluding calms from the wind measurements. The mean annual wind speed at the KP28 weather station is 4.45 m s^{-1} (Figure 5-5b). The highest mean annual velocity is observed in 1998 and it was equal to 4.84 m s^{-1}. Note, however, that the data coverage in this year is below 85%, which introduces an uncertainty to this value. The second maximum is recorded in 2002 and is equal to 4.77 m s^{-1}. The lowest mean annual speed occurred in 1995 (3.88 m s^{-1}). Wind speeds were below 4.5 m s^{-1} in 50% of the time during the period 1984-2015. The mode speed is equal to 3.88 m s^{-1}, which together with the above mean and median values indicate the right-skewedness in the underlying distribution of the mean annual wind speeds. The yearly oscillations of the mean annual wind speeds are small. Namely, the standard deviation of the time series in Figure 5-5b is 0.25 m s^{-1}. Small variability of mean annual wind speed is beneficial from the wind resource point of view, as it tends to decrease the uncertainty in the estimated annual wind resources at the site.

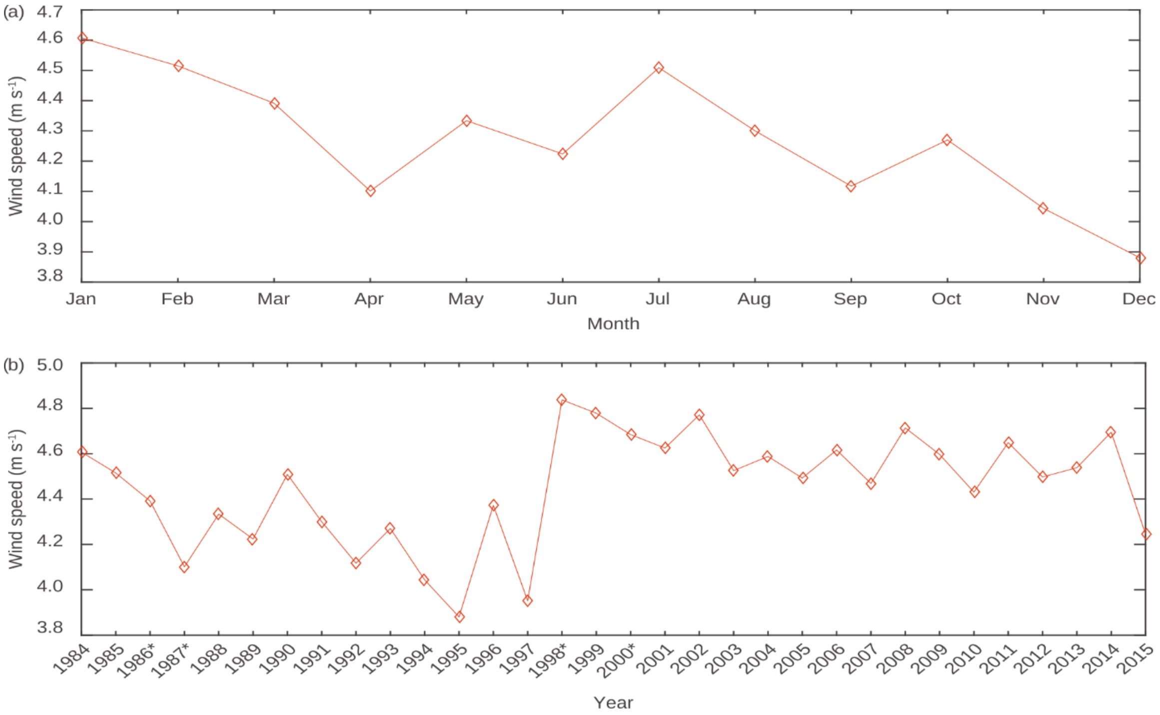

Figure 5-5. Mean monthly (a) and annual (b) wind speeds at KP28. Asterisks denote years with data coverage below 85%.

Mean monthly wind speeds are shown in Figure 5-5a. The highest wind speeds are observed in January, February and July with mean values of 4.61 m s^{-1}, 4.52 m s^{-1} and 4.51 m s^{-1}, respectively. The lowest mean wind speed (3.88 m s^{-1}) is recorded in December. Figure 5-5a further indicates that the mean monthly wind speeds are characterized with an overall decreasing trend throughout the year, i.e. from January to December. January and July are the windiest months in the year, while the lowest wind speeds are observed in the transitional seasons (spring and fall).

A 16-direction wind rose with the associated directional wind speed distribution is shown in Figure 5-6.

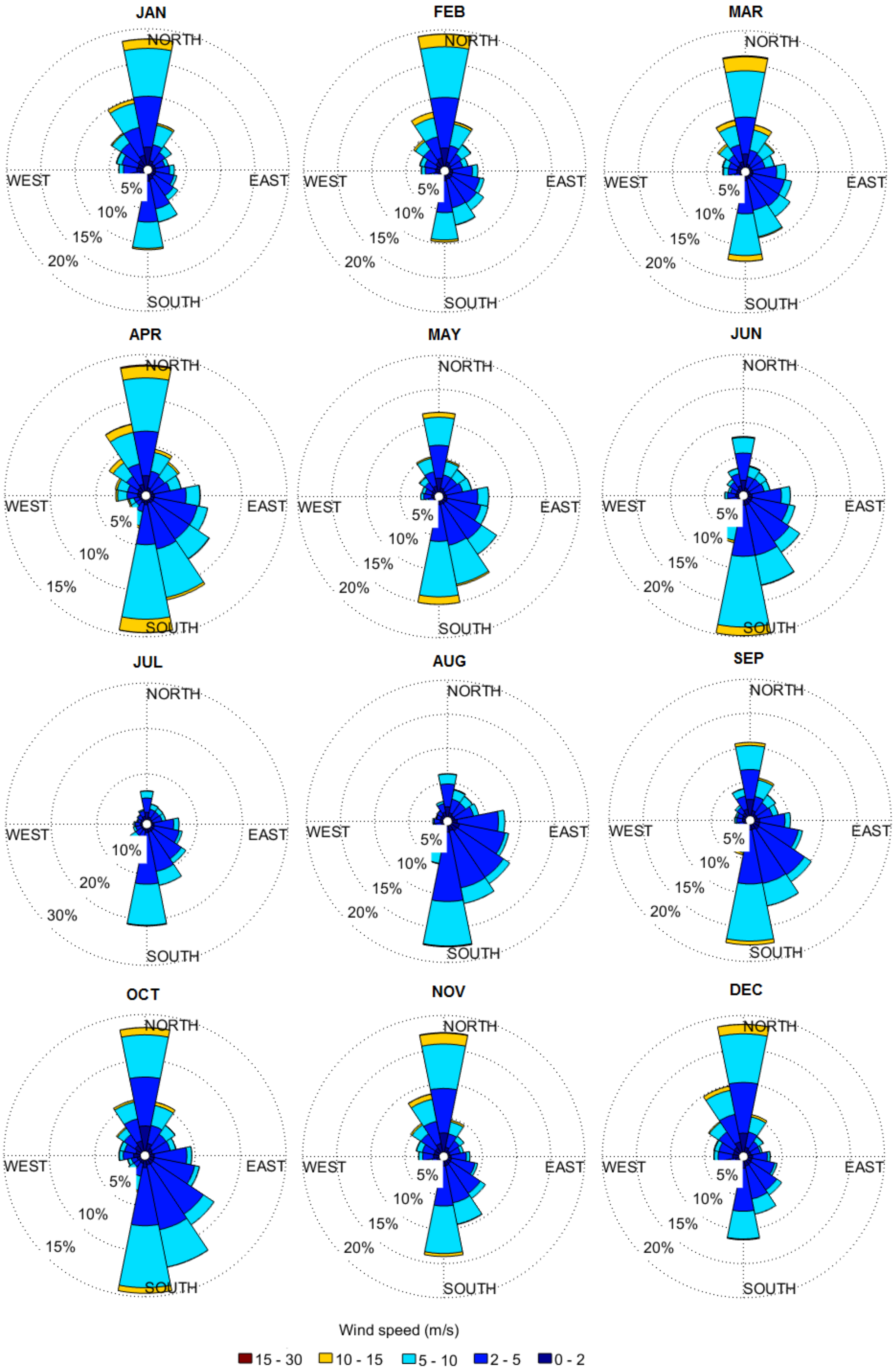

Figure 5-6. Wind rose with wind speed distribution for each month at KP28.

It can be seen that northerly and southerly winds are the most dominant wind directions at the site. North winds were present in about 13% of the time in year, whereas the south winds were observed in approximately 15% of the time. Winds from the fourth quadrant were also common, whereas the winds from the southwest and northeast directions were rare. It is important to note that the prevailing wind directions are also associated with the strongest winds, and the northerlies seem to be stronger than the southerlies. Weakest northerlies occur during the summer months, when they almost cease. The southerly winds, on the other hand, are present during the whole year, with a small decrease in their occurrence in December and January. Interestingly, northerlies in winter are approximately two times more frequent than southerlies.

The fact that the most dominant winds are blowing from opposite directions (i.e. northerly and southerly) is advantageous from the wind resource point of view. Namely, the optimal layout of wind turbines highly depends on the prevailing wind directions at the site. If the prevailing wind directions are along the same line-of-sight, as it is in the analyzed case, the optimal layout of wind turbines for southerly winds is the same as the optimal layout for the northerly winds. That is, displacing the turbines in the west-east direction eliminates wake interference between them when either north or south winds are present.

Figure 5-7 shows the diurnal wind cycle at the KP28 weather station. The strongest winds are observed in the afternoon, around 15:00 h. The mean hourly wind speeds above 5 m s^{-1} are present between 10:00 h and 18:00 h. The lowest wind speeds, on the other hand, are recorded in the early morning, from 04:00 h to 07:00 h. These diurnal changes are part of the daily cycle driven by the sun. That is, during the afternoon, the sun's heating is at peak, which results in destabilization of the atmosphere. The subsequent mixing of hot air close to the ground with cold air aloft results in bringing down stronger winds that are otherwise blowing at higher levels in the atmosphere. During the night, however, a temperature inversion creates a stable layer of air close to the surface. This stable layer of cool air prevents the winds higher up in the atmosphere from being mixing down to the surface. As the sun heats the ground in the morning, this inversion begins to break down and turbulence develops – all resulting in a well-mixed atmospheric boundary layer

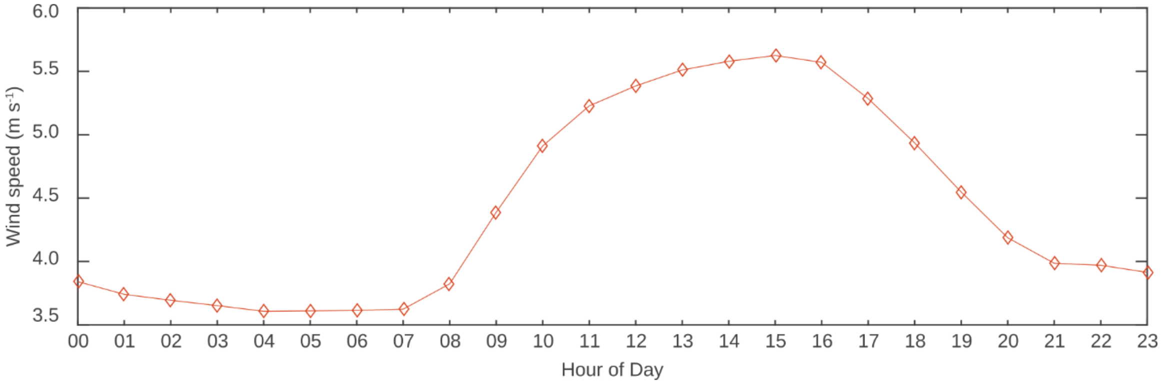

Figure 5-7. Diurnal wind speed variability at KP28.

Figure 5-8 shows the trends in the mean annual wind speeds. The positive trends are statistically not significant (~0.008 m s^{-1} $year^{-1}$). The exclusion of the four years with data coverage below 85% (1986, 1987, 1998 and 2000) has a negligible influence on the magnitude of these trends. In both cases, the estimated wind speed increase over the analyzed time period is below 0.2 m s^{-1}. Although the observed trends are not statistically significant, more important, they are not negative. This finding contributes to the long-term stability of wind power projects in that region. Namely, it indicates that the estimated wind resources are not set to decrease in the future.

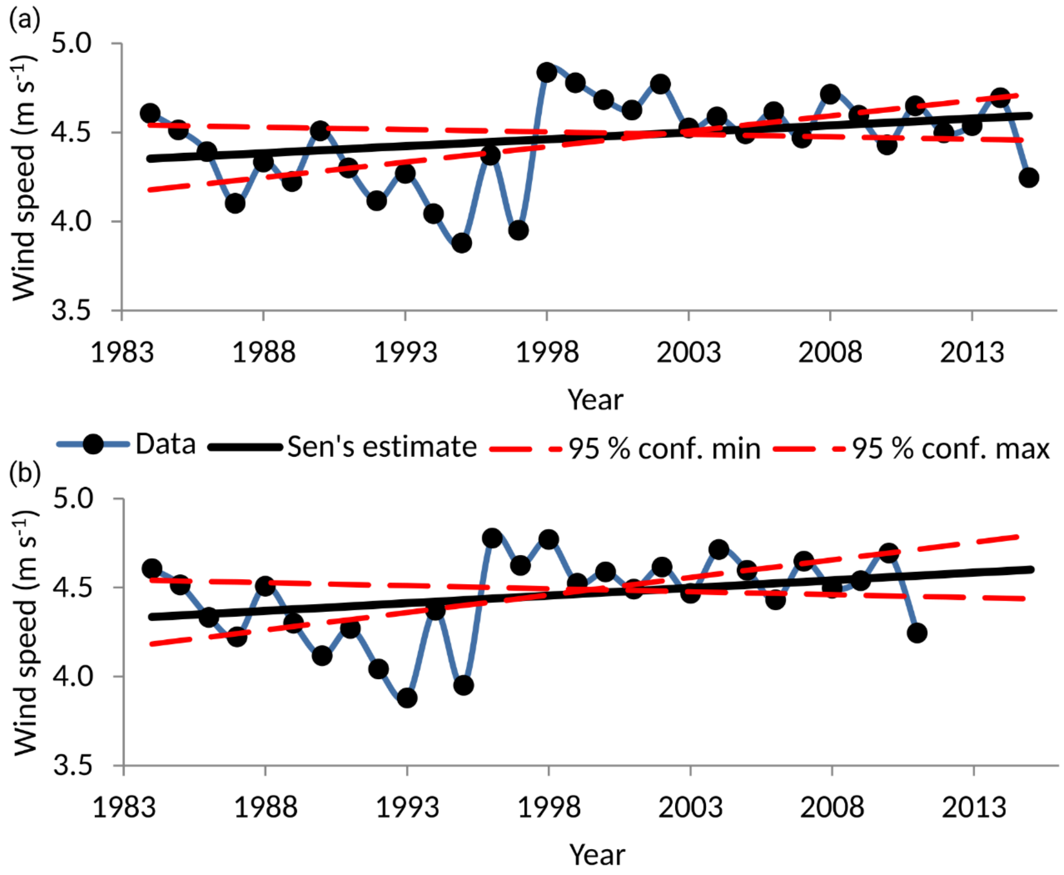

Figure 5-8. Long-term wind speed trends for the period 1984-2015. (a) All years being considered and (b) only years with the data coverage above 85% are considered.

The extreme value analysis is performed on two sets of data: (1) maximum annual 5-second gusts and (2) maximum 2-minute mean wind speeds per annum (Figure 5-9). Note that the maximum 2-minute mean wind speeds are available for each year in the period 1984-2015, whereas the gusts are only available for the time period after 1998 (18 years in total).

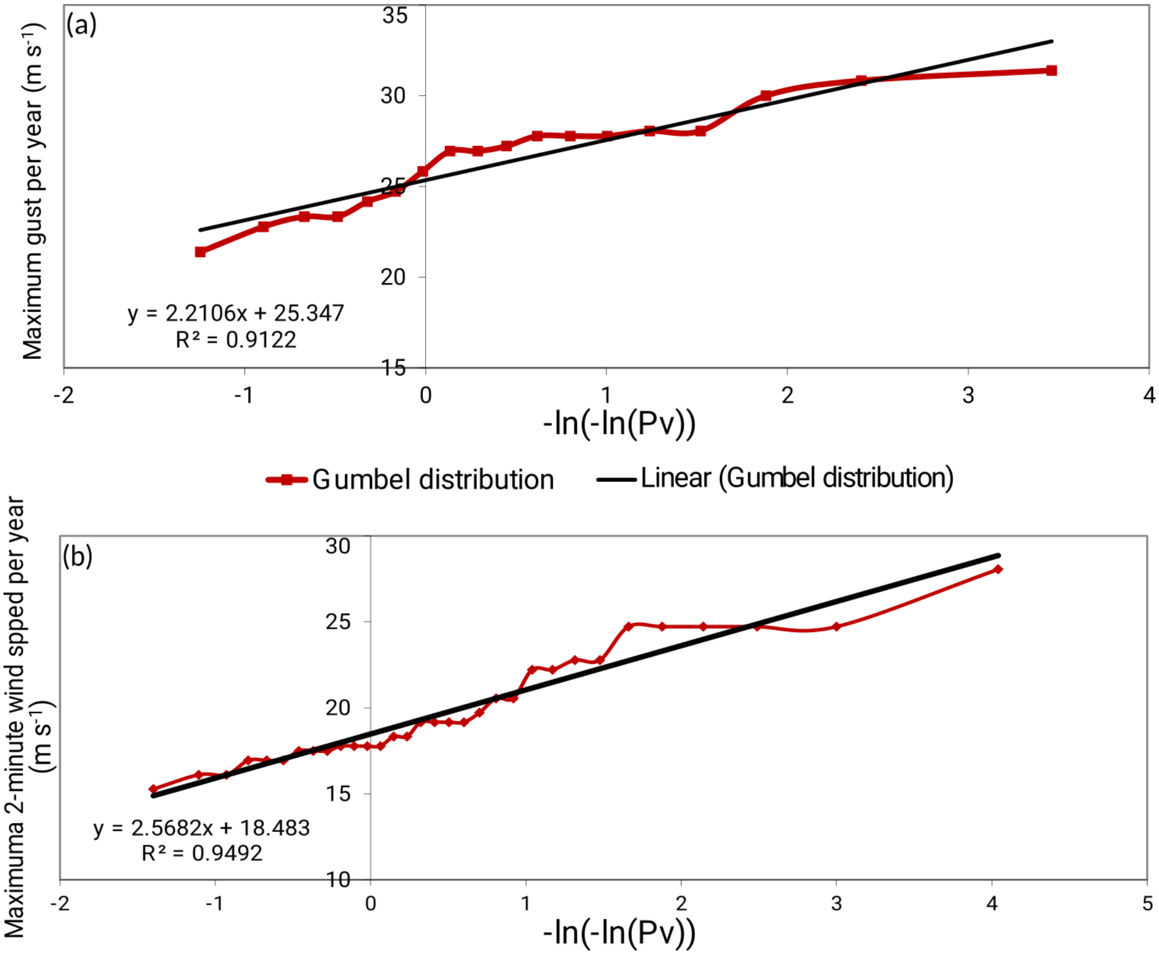

Figure 5-9. Extreme wind speed analysis performed on (a) maximum yearly gusts and (b) maximum 2-minute mean wind speed per year.

The Gumbel distribution represents a good fit of the observed extreme wind speeds. The coefficient of determination (R^2) is above 0.9 in both cases. Note that R^2 represents a measure of how well the linear regression lines: (a) $y = 2.2106x + 25.347$ and (b) $y = 2.5682x + 18.483$ fit the theoretical Gumbel distribution. The distribution parameters are determined through the following expressions: $\mu = -\text{offset} \cdot \sigma$; $\sigma = 1/\text{slope}$, and are equal to: (a) $\mu = -11.466$, $\sigma = 0.452$ and (b) $\mu = -7.197$, $\sigma = 0.389$. Extreme wind speeds for five return periods (i.e. 5, 10, 50, 100 and 500 years) at KP28 are presented in Table 5-6.

Table 5-6. Extreme wind speeds for different return periods.

Wind speed series	Return period (years)				
	5	10	50	100	500
Maximum gust (m s^{-1})	28.66	30.32	33.97	35.52	39.08
Maximum 2-minute mean wind speed (m s^{-1})	22.34	24.26	28.50	30.30	34.44

The ratio between these two series, i.e. maximum gusts and maximum 2-minute mean wind speeds is between 1.2 and 1.7, with the mean value equal to 1.4. Similar relationships have been found elsewhere (Durst 1960). Consequently, the average ratio between the extreme wind speeds for different return periods (listed in Table 5-6) is 1.7.

5.3.2 Wind resource assessment study

The wind atlas contains data for 5 reference roughness lengths (0 m, 0.03 m, 0.05 m, 0.5 m, 0.9 m) and 5 reference heights (10 m, 50 m, 80 m, 100 m, 150 m) above ground level. The regional wind climate is given in Table 5-7.

As expected, wind potential growth is directly proportional to the increase in height above ground and/or to the decrease in terrain roughness. Note that the wind atlas data are site-independent and the wind distributions have been reduced to a set of standard conditions; i.e. 5 standard roughness classes and 5 standard heights above ground level. Typical roughness lengths used in the WAsP wind atlas calculations are 0 m and 0.03 m. The other three roughness lengths (0.05 m, 0.5 m and 0.9 m) are also included in the analysis as these land covers are frequently found in the region (Section 5.2.3). The height of 10 m above ground is always included in the wind atlas calculations, whereas the other four heights are selected in order to have at least three levels in the layer between 80 m and 150 m above ground. This is the typical range for hub height of modern wind turbines.

Table 5-7. Regional wind atlas.

Height (m)	Parameter	Roughness lengths				
		0 m	0.03 m	0.05 m	0.5 m	0.9 m
10	A (m s^{-1})	8.0	5.7	5.4	3.7	3.2
	k	1.99	1.79	1.80	1.81	1.82
	U (m s^{-1})	7.05	5.11	4.84	3.31	2.81
	P (W m^{-2})	390	166	141	45	27
50	A (m s^{-1})	9.3	7.9	7.6	6.0	5.5
	k	2.10	2.08	2.07	2.03	2.01
	U (m s^{-1})	8.26	6.96	6.71	5.33	4.89
	P (W m^{-2})	595	359	324	166	129
80	A (m s^{-1})	9.8	8.7	8.4	6.8	6.3
	k	2.08	2.25	2.25	2.17	2.15
	U (m s^{-1})	8.68	7.70	7.45	6.05	5.61
	P (W m^{-2})	697	454	410	227	182
100	A (m s^{-1})	10.0	9.2	8.9	7.3	6.8
	k	2.06	2.25	2.26	2.25	2.24
	U (m s^{-1})	8.90	8.12	7.85	6.42	5.98
	P (W m^{-2})	757	531	479	263	213
150	A (m s^{-1})	10.5	10.2	9.8	8.1	7.6
	k	2.03	2.22	2.23	2.25	2.26
	U (m s^{-1})	9.33	9.00	8.70	7.18	6.73
	P (W m^{-2})	887	731	660	368	301

The wind resource grids depict the power density above the project site and they are calculated at four different heights above ground (50 m, 80 m, 100 m and 150 m). The grid resolution is 10 m in all cases. The resulting maps are shown in Figure 5-10.

The power density, as expected, increases with height above ground. It is relatively straightforward to determine the areas within the KP site favorable for installing a wind turbine or a couple of wind turbines. Namely, the best wind resource is found in the southwest regions of the site. This hilly area is covered with tall bushes and/or small trees. At 100 m above ground, for example, the power density on the top of the hill in the southwest part of the site is approximately 400 W m^{-2}. Going up to 150 m above the ground, the power density reaches 560 W m^{-2}. Comparing these values with the data presented in the NREL wind resource maps (NREL 2009), it seems that the site falls into “fair” wind resources category.

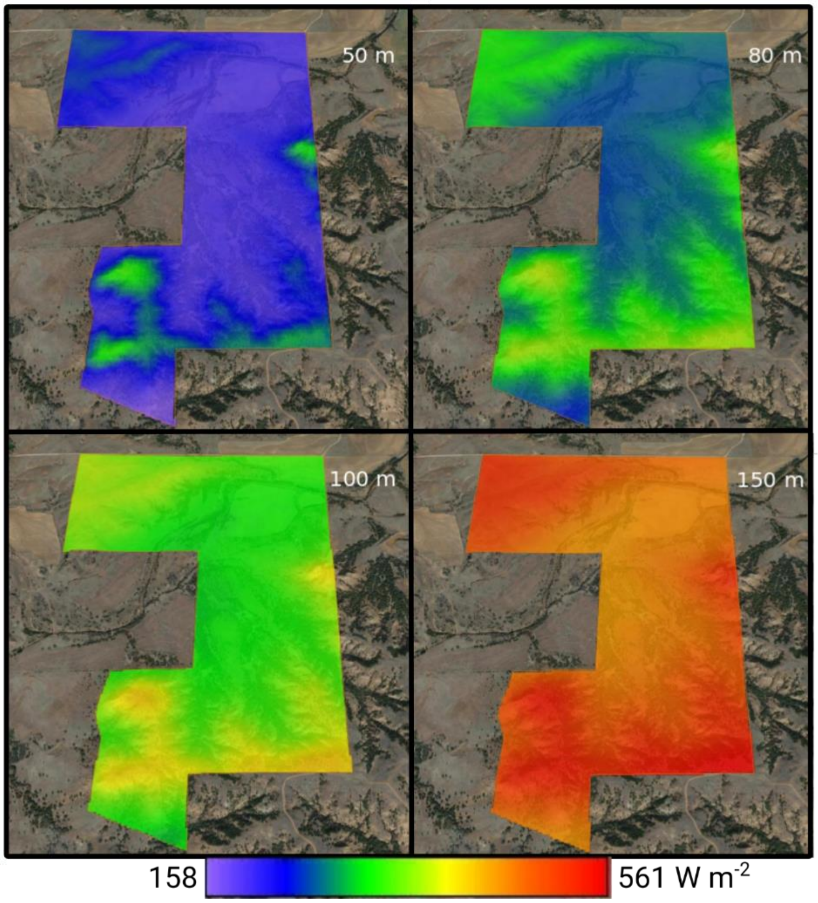

Figure 5-10.Wind resource maps at 50 m, 80 m, 100 m and 150 m above ground showing the power density in W m^{-2}.

Most of the modern wind turbines have hub heights over 80 m tall. For that reason, the analysis of wind resources at 80 m, 100 m and 150 m above ground is more relevant for practical purposes. The wind potential and the size of the project site are suitable for installing two to three units. For instance, one turbine can be installed in the southwest part of the site and the second wind turbine could be located in the southeast part of the site. Both locations have adequate wind potential and are situated at the top of the hills. Equally important, the locations are displaced in the west-east direction (i.e. perpendicular to the prevailing wind directions), thus minimizing the wake interference between the wind turbines.

Good wind potential is also found in the northwest corner of the site. The power density at 100 m above ground in that area reaches 378 W m^{-2}. The hills situated in the south region of the site are characterized by a power density of approximately 420 W m^{-2} at the 100 m level. The difference in wind potential between the hilly south part of the site and the flat northwest corner of the site is approximately 40 W m^{-2}.

Five reference sites are placed across the KP site (Figure 5-11). Reference sites, similar to turbine sites, are used to calculate a predicted wind climate for a particular point, but without calculating the electricity production (power and thrust curves are not needed). Therefore, a reference site can be thought of as a virtual weather station. Reference sites are situated 100 m above ground and their location is shown in Figure 5-11.

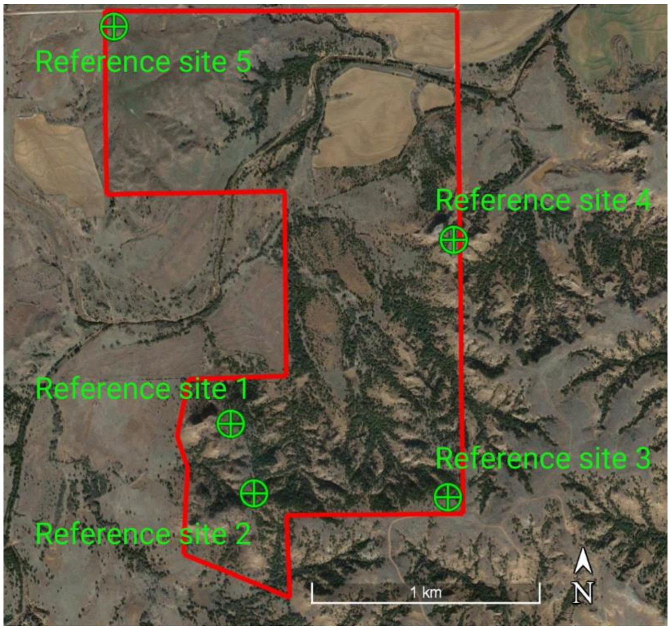

Figure 5-11. Locations of five reference sites placed across the project site.

The first four reference sites are placed in the rugged area of the site covered with tall vegetation (bushes and small trees). Reference site 5 is situated in the northwest corner of the site. These five locations mark potential sites for one or more wind turbines. It can be seen in Table 5-8 that Reference sites 1 and 3 have the best wind potential with the mean annual power density of 423 W m^{-2} and 420 W m^{-2}, respectively, at 100 m above ground. Reference sites 2 and 4 have a similar wind potential of approximately 400 W m^{-2}. Lastly, Reference site 5 is characterized by the lowest wind potential. To be more precise, the mean annual power density at Reference site 5 is 6.25% lower in comparison with Reference sites 2 and 4.

Table 5-8. (Emergent) wind resources at the five reference sites indicated in Figure 5-11.

Reference site number	U (m s^{-1})	P (W m^{-2})
1	7.44	420
2	7.33	401
3	7.48	423
4	7.38	404
5	7.19	377

5.3.2.1Ruggedness Index

WAsP is a linear model that requires smooth terrains with orography slopes of less than approximately 30° (Troen and Petersen 1989, Mortensen et al. 2006). In these situations, the flow is attached to the surface without separating from it. In order to estimate the topographic complexity of the site, Ruggedness Index (RIX) is introduced as the fractional extent of the surrounding terrain which is steeper than a critical slope (Bowen and Mortensen 2004), and therefore susceptible to flow separation. Such flow regime is outside of the WAsP performance envelope. In addition, ΔRIX is defined as the difference in the percentage fractions between the predicted and reference sites (Bowen and Mortensen 2004). For a transition from a smooth site (such as the reference weather station KP28) to a rugged site (such as, to some extent, the KP site), the WAsP predictions will be over-estimated and present a positive error (Bowen and Mortensen 2004). This uncertainty can be partially addressed by having several reference stations around the site and cross-referencing the results between them. However, such measurements are not available as the KP28 weather station in Medicine Lodge is the only source of wind data in that region.

The ruggedness of terrain around the KP28 weather station and the KP site is shown in Figure 5-12.

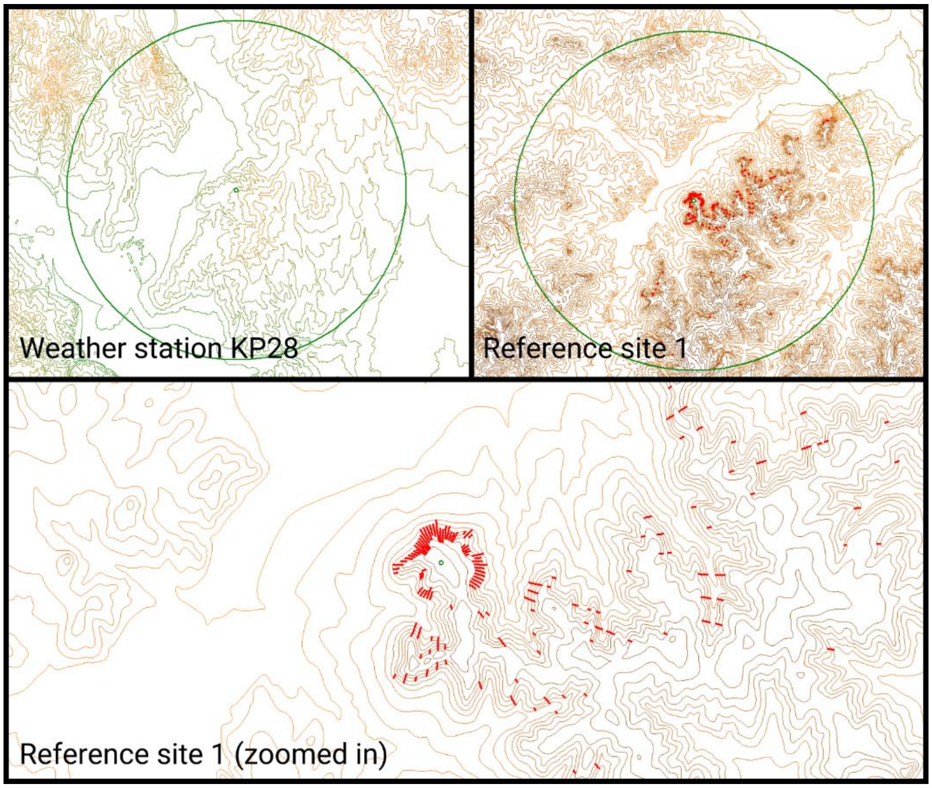

Figure 5-12. The terrain around weather station site and Reference site 1 as seen in the WAsP Map Editor. Terrain steeper than a 30° angle is indicated by the thick red (radial) lines.

The RIX calculations are performed for 12 directional sectors and for the radial distance of 3.5 km around the sites. RIX threshold is set to 0.3 (i.e. 30° slope). It can be seen that the terrain around the KP28 weather station is completely smooth. The terrain around the Reference site 1, on the other hand, is rugged as indicated by the radial red lines. Keeping in mind that ΔRIX is the difference between RIX at predicted site (the KS site) and weather station (KP28), and taking into account that RIX around KP28 is zero, it can be concluded that ΔRIX is equal to RIX around the KP site. Therefore, all ΔRIX values at the project site are positive and consequentially indicate potential over-estimations of WAsP predictions. Figure 5-13 demonstrated the magnitude of ΔRIX at the project site, calculated as the mean of the sector-wise ΔRIX values.

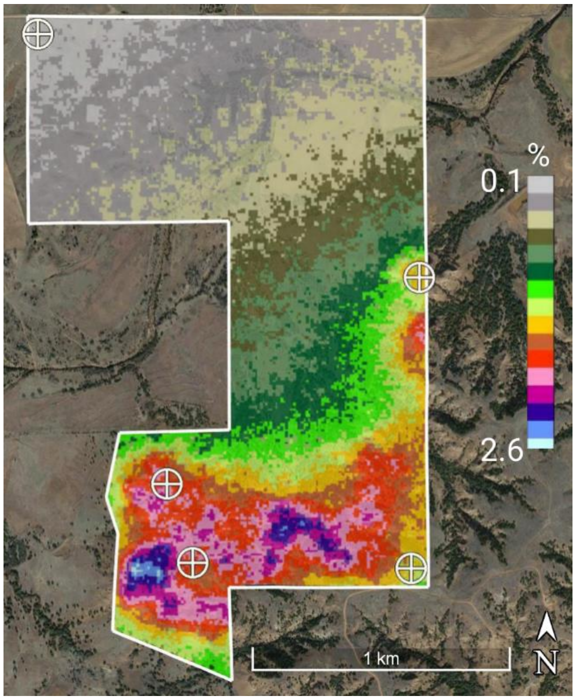

Figure 5-13. ΔRIX values at 100 m above the project site.

ΔRIX at the project site varies between 0.1% in the northwest parts of the site and 2.6% in the hilly south parts of the site. At this point, although the ΔRIX magnitude at the project site is known, it is impossible to quantitatively estimate the uncertainty of WAsP simulations. There are few empirical relationships established between ΔRIX values and the error in predicted wind speeds (Bowen and Mortensen 2004, Mortensen et al. 2006). According to the equation provided in the work of Mortensen and his colleagues (Mortensen et al. 2006), the over-predictions for each of the five Reference sites should be below 0.5 m s^{-1}. However, the reported dependency between ΔRIX and estimation errors is highly empirical and might be limited to only the site in Portugal for which it was originally derived. However, keeping in mind that ΔRIX values at the KP site are small (below 2.5%), it can be argued that WAsP is not largely outside of its performance envelope. Furthermore, Berge et al. (2006) have shown that in some cases WAsP produces more reliable results in complex terrains than some computational fluid dynamics (CFD) models. Similar results showing the increased accuracy of WAsP over CFD have also been reported in a few other studies (Van Luvanee et al. 2009, Periera et al. 2010, Sumner et al. 2010).

5.3.2.2Roughness map uncertainties

Note that evaluation of roughness length values, and consequently creating roughness maps, is subjective and user dependent. For instance, it is easy to distinguish between farmland and forest area or water area, but differentiating between two different types of forest might be challenging. Some of the existing empirical relationships for roughness length estimations are in many circumstances difficult to implement as they require precise knowledge of many input parameters (Raupach 1992, Hryama et al. 1996). Moreover, these methods also possess a certain degree of uncertainty (Conder 1999).

When it comes to the consistency of the roughness lengths in Figure 5-4, the largest source of uncertainty is associated with the roughness length of 0.9 m for the forests areas. For that reason, an uncertainty analysis is carried out in order to estimate what influence changing the roughness length from 0.9 m to 0.5 m would have on the calculated wind potential above the region. The underlying assumption behind this check is that the forest areas in the computational domain might have smaller density and height of trees, as well as smaller leaf density in the crown. A change of roughness length from 0.9 m to 0.5 m is not a negligible modification to the roughness map. The regional wind atlas and wind resources at the five reference sites are estimated using this new roughness map and the results are shown in Table 5-9 and Table 5-10, respectively.

The comparison of values reported in Table 5-9 with the corresponding values given in Table 5-7, verifies that the described change in roughness map values had a small influence on the estimated wind resources in the region. For instance, the mean power density at 100 m above ground for the roughness length of 0.5 m in Table 5-9 is 260 W m^{-2}, while the corresponding value in Table 5-7 is 1.15% higher (263 W m^{-2}). Those discrepancies are negligible.

Table 5-9. Wind atlas generated after changing the roughness length of forest areas from 0.9 m to 0.5 m.

Height (m)	Parameter	Roughness lengths				
		0 m	0.03 m	0.05 m	0.5 m	0.9 m
10	A (m s^{-1})	7.9	5.7	5.4	3.7	3.1
	k	2	1.8	1.8	1.81	1.82
	U (m s^{-1})	7.03	5.09	4.83	3.3	2.8
	P (W m^{-2})	384	164	139	44	27
50	A (m s^{-1})	9.3	7.8	7.6	6	5.5
	k	2.1	2.09	2.08	2.03	2.03
	U (m s^{-1})	8.23	6.94	6.7	5.32	4.88
	P (W m^{-2})	588	355	320	164	127
80	A (m s^{-1})	9.8	8.7	8.4	6.8	6.3
	k	2.08	2.27	2.26	2.18	2.16
	U (m s^{-1})	8.65	7.69	7.43	6.04	5.59
	P (W m^{-2})	689	449	406	224	180
100	A (m s^{-1})	10	9.2	8.8	7.2	6.7
	k	2.07	2.26	2.27	2.27	2.25
	U (m s^{-1})	8.87	8.11	7.84	6.41	5.97
	P (W m^{-2})	748	526	474	260	211
150	A (m s^{-1})	10.5	10.2	9.8	8.1	7.6
	k	2.04	2.23	2.24	2.26	2.27
	U (m s^{-1})	9.31	8.99	8.7	7.17	6.71
	P (W m^{-2})	877	727	656	365	298

Table 5-10. Comparison between the all-sector Emergent mean wind speed and power density values at the five reference sites reported in Table 5-8 against the corresponding values obtained after changing the roughness length of forests from 0.9 m to 0.5 m.

Reference site number	Original values (from Table 5-8)		Altered values	
	U (m s^{-1})	P (W m^{-2})	U (m s^{-1})	P (W m^{-2})
1	7.44	420	7.54	433
2	7.33	401	7.44	414
3	7.48	423	7.58	437
4	7.38	404	7.48	418
5	7.19	377	7.28	387

Table 5-10 shows that changing the roughness length of forests from 0.9 m to 0.5 m does not have a significant influence on the estimated wind potential at the KP site. The overall wind speed increase is 1.36%, which is based on the average value over the five reference sites. Due to the cubic relationship between wind speed and its power, the power density increase is more pronounced (3.15%). The largest increase of wind resources (3.47%) is observed at Reference site 4, while the smallest increase (2.62%) is detected at Reference site 5.

To summarize, changing the roughness length for forest areas from 0.9 m to 0.5 m had a slight influence on the calculated wind potential for the whole region, as well as for the KP site. This result is important as it significantly reduces the uncertainty in estimated wind resources.

5.4 Summary and conclusions

A complete wind climatology and a detailed wind resource assessment study were performed for a modern development, planned to be built in “Tornado Alley”, in South

Central Kansas (named the Kansas Project). The project aims at the highest sustainability and resilience standards. The entire analysis was carried out on wind data obtained from the nearest automated weather station located in the town of Medicine Lodge.

The wind climatology study shows that the mean wind speed at 10 m above ground is 4.45 m s^{-1}. The highest winds occur in January and July, whereas the lowest wind speeds are observed in December and transitional seasons. The two prevailing wind directions at the site are from south and north. These directions are also associated with the strongest winds. The diurnal wind speed cycle shows that the strongest winds blow around 15:00 h, while the weakest winds occur during the night. Statistically insignificant, but nevertheless positive trends of the mean annual wind speeds are found for the period 1984-2015 (0.2 m s^{-1} over the analyzed period). The extreme value analysis is performed on the annual maximum 5-second gusts and annual maximum 2-minute mean wind speeds.

The wind resource assessment analysis performed using WAsP package demonstrates good wind potential at the project site, particularly in the hilly south region of the site. The three tentative locations were identified for installing wind turbines on the site. The estimated mean wind speed at 100 m above ground is above 7 m s^{-1}. The power density at two reference sites exceeds 420 W m^{-2}.

Uncertainties in estimated wind resources caused by the ruggedness of the site were analyzed through the concept of the Ruggedness Index (RIX). Based on the conducted analysis and literature review, it seems that WAsP is marginally outside of its performance envelope. Uncertainties associated with the roughness map were investigated by comparing the wind resources before and after altering the roughness length of forest areas from 0.9 m to 0.5 m. This change has small repercussions to the estimated wind potential at the site.

References

AWEA (2016) U.S. number one in the world in wind energy production. http://www.awea.org/MediaCenter/pressrelease.aspx?ItemNumber=8463. Accessed 10 Aug 2016

Berge E, Gravdahl AR, Schelling J, et al (2006) Wind in complex terrain. A comparison of WAsP and two CFD-models. In: *European Wind Energy Conference (EWEC).* European Wind Energy Association (EWEA), Athens, Greece, pp 1–10

Bowen AJ, Mortensen NG (2004) *WAsP prediction errors due to site orography*. Wind Energy Department, Risø National Laboratory, Roskilde, Denmark

Castro-Santos L, Filgueira-Vizoso A, Carral-Couce L, Formoso JÁF (2016a) Economic feasibility of floating offshore wind farms. *Energy* **112**:868–882. doi: 10.1016/j.energy.2016.06.135

Castro-Santos L, Martins E, Guedes Soares C (2016b) Cost assessment methodology for combined wind and wave floating offshore renewable energy systems. *Renew Energy* **97**:866–880. doi: 10.1016/j.renene.2016.06.016

Conder MR (1999) *Estimation of roughness lengths through gust factor analysis*. Master Thesis, Texas Tech University

Delucchi MA, Jacobson MZ (2011) Providing all global energy with wind, water, and solar power, Part II: Reliability, system and transmission costs, and policies. *Energy Policy* **39**:1170–1190. doi: 10.1016/j.enpol.2010.11.045

Durst C (1960) Wind speeds over short periods of time. *Meteorological Magazine* **89**:181–186.

Elliott D, Holladay C, Barchet W, et al (1986) *Wind Energy Resource Atlas of the United States*. U.S. Department of Energy, Washington, US

EPA (2013) *AERSURFACE User's Guide*. United States Environmental Protection Agency (EPA), Office of Air Quality Planning and Standards Air Quality Assessment Division Air Quality Modeling Group Research Triangle Park, North Carolina

Gringorten II (1963) A plotting rule for extreme probability paper. *Journal of Geophysical Research* **68**:813–814. doi: 10.1029/JZ068i003p00813

GWEC (2016) *Global wind report: Annual market update 2015*. Global Wind Energy Council, Washington D.C, United States

Hangan H (2010) Current and future directions for wind research at Western: a new quantum leap in wind research through the Wind Engineering, Energy and Environment (WindEEE) Dome. *Wind Engineering JAWE* **35**:277–281. doi: 10.5359/jawe.35.277

Homer C, Dewitz J, Yang L, et al (2015) Completion of the 2011 national land cover database for the conterminous United States – representing a decade of land cover change information. *Photogrammetric Engineering* & *Remote Sensing,* **81**:345–354.

Hryama T, Sugita M, Kotoda K (1996) Regional roughness parameters and momentum fluxes over a complex area. *Journal of Applied Meteorology*, **35**:2179–2190. doi: 10.1175/1520-0450(1996)035<2179:RRPAMF>2.0.CO;2

Jacobson MZ, Delucchi MA (2011) Providing all global energy with wind, water, and solar power, Part I: Technologies, energy resources, quantities and areas of infrastructure, and materials. *Energy Policy*, **39**:1154–1169. doi: 10.1016/j.enpol.2010.11.040

Johansson TB, Kelly H, Reddy AKN, Williams RH (1993) Renewable fuels and electricity for a growing world economy: Defining and achieving the potential. *Energy Studies Review*. doi: 10.15173/esr.v4i3.284

Kendall MG (1970) *Rank correlation methods*. Griffin, London

Lopez A, Roberts B, Heimiller D, et al (2012) *U.S. renewable energy technical potentials: A GIS-based analysis*. National Renewable Energy Laboratory, Washington, D.C., United States

Mann HB (1945) Nonparametric tests against trend. *Econometrica*, **13**:245–259. doi: 10.2307/1907187

Mann J, Teilmann J (2013) Environmental impact of wind energy. *Environmental Research Letters*, **8**:35001. doi: 10.1088/1748-9326/8/3/035001

Mortensen NG, Bowen AJ, Ioannis A (2006) Improving WAsP predictions in (too) complex terrain. *European Wind Energy Association (EWEA)*, Athens, Greece, pp 1–9

Mortensen NG, Heathfield DN, Rathmann O, Nielsen M (2014) *Wind Atlas Analysis and Application Program: WAsP 11 Help Facility*. RISØ National Laboratory, Roskilde, Denmark

NCDC (2003) *ASOS 5-Minute Data: Data Documentation*. National Climatic Data Center (ftp://ftp.ncdc.noaa.gov/pub/data/asos-fivemin/td6401b.txt) Accessed: 2016-08-05

NOAA (1998) *Automated Surface Observing System (ASOS): User's Guide*. National Oceanic and Atmospheric Administration (NOAA).

NREL (2009) *NREL: Dynamic Maps, GIS Data, and Analysis Tools - Wind Data*. http://www.nrel.gov/gis/data_wind.html. Accessed 10 Aug 2016

Oh K-Y, Kim J-Y, Lee J-S, Ryu K-W (2012) Wind resource assessment around Korean Peninsula for feasibility study on 100 MW class offshore wind farm. *Renewable Energy*, **42**:217–226. doi: 10.1016/j.renene.2011.08.012

Palutikof JP, Brabson BB, Lister DH, Adcock ST (1999) A review of methods to calculate extreme wind speeds. *Meteorological Applications*, **6**:119–132. doi: 10.1017/S1350482799001103

Periera R, Guedes R, Santos C. (2010) Comparing WAsP and CFD wind resource estimates for the “regular” user. In: *European Wind Energy Conference (EWEC)*. European Wind Energy Association (EWEA), Warsaw, Poland,

Raupach MR (1992) Drag and drag partition on rough surfaces. *Bound-Layer Meteorology*, **60**:375–395. doi: 10.1007/BF00155203

Romanić D, Ćurić M, Jovičić I, Lompar M (2015a) Long-term trends of the “Koshava” wind during the period 1949–2010. *International Journal of Climatology*, **35**:288–302. doi: 10.1002/joc.3981

Romanić D, Rasouli A, Hangan H (2015b) Wind resource assessment in complex urban environment. *Wind Engineering*, **39**:193–212. doi: 10.1260/0309-524X.39.2.193

Romanic D, Rasouli A, Hangan H (2016a) Urban wind resource assessment in changing climate: Case study. *Wind Engineering*, 0309524X16653486. doi: 10.1177/0309524X16653486

Romanic D, Refan M, Wu C-H, Michel G (2016b) Oklahoma tornado risk and variability: A statistical model. *International Journal of Disaster Risk Reduction*, **16**:19–32. doi: 10.1016/j.ijdrr.2016.01.011

Saidur R, Rahim NA, Islam MR, Solangi KH (2011) Environmental impact of wind energy. *Renewable and Sustainable Energy* Reviews, **15**:2423–2430. doi: 10.1016/j.rser.2011.02.024

Sen PK (1968) Estimates of the regression coefficient based on Kendall’s Tau. *Journal of the American Statistical Association*, **63**:1379–1389. doi: 10.2307/2285891

Sharma K, Ahmed MR (2016) Wind energy resource assessment for the Fiji Islands: Kadavu Island and Suva Peninsula. *Renewable Energy*, **89**:168–180. doi: 10.1016/j.renene.2015.12.014

Sumner J, Watters CS, Masson C (2010) CFD in wind energy: The virtual, multiscale wind tunnel. *Energies*, **3**:989–1013. doi: 10.3390/en3050989

Troen I, Petersen EL (1989) *European Wind Atlas*. RISØ National Laboratory, Roskilde, Denmark

Van Luvanee D., Rogers T, Randall G, et al (2009) Comparison of WAsP, MS-Micro/3, CFD, NWP, and analytical methods for estimating site-wide wind speeds. *American Wind Energy Association (AWEA)*, Minneapolis, MN, United States

Watts D, Oses N, Pérez R (2016) Assessment of wind energy potential in Chile: A project-based regional wind supply function approach. *Renewable Energy* **96, Part A**:738–755. doi: 10.1016/j.renene.2016.05.038

Weekes SM, Tomlin AS, Vosper SB, et al (2015) Long-term wind resource assessment for small and medium-scale turbines using operational forecast data and measure–correlate–predict. *Renewable Energy,* **81**:760–769. doi: 10.1016/j.renene.2015.03.066

Welch JB, Venkateswaran A (2009) The dual sustainability of wind energy. *Renewable and Sustainable Energy Reviews*, **13**:1121–1126. doi: 10.1016/j.rser.2008.05.001

Chapter VI

6 Field data analysis and weather scenario of a downburst event in Livorno, Italy on October 1, 2012

6.1 Introduction

The Gulf of Genoa is a well-known cyclogenesis area. Moreover, the Mediterranean basin has the highest frequency of occurrence of cyclones around the globe. Ground-breaking studies on this subject are those by Petterssen (1956) and Klein (1957). These hand-made analysis performed on hemispheric-scale synoptic charts demonstrated that the Mediterranean, and the Western Mediterranean in particular, are areas characterized by a very high cyclonic activity in winter. The studies in the late 1980s (Radinović 1987, Genoveś and Jansà 1989) used the same subjective method for detection of cyclones, but on the mesoscale synoptic charts, and reported that the number of cyclones in the Western Mediterranean is larger than previously documented in the hemispheric studies. Furthermore, Radinović (1987) demonstrated that Mediterranean cyclones are one of the major climate and weather factors in Mediterranean. These findings were later refined using a number of objective methods for cyclone detection and tracking (e.g. Maheras et al. 2001, Flocas et al. 2010, Kouroutzoglou et al. 2011, Romanić et al. 2016a). Although

Mediterranean cyclones should not be confused with extratropical cyclones that form in North Atlantic (Trigo et al. 1999), they are nevertheless associated with a number of severe weather phenomena in the Mediterranean and close-by regions (Lionello et al. 2006).

There is a wide body of literature on the subject of extreme weather events in the Mediterranean basin, as well as on the relationship between severe weather and the Mediterranean cyclones. For example, Jansa et al. (2001) and Maheras and Anagnostopoulou (2003) reported that more than 90% of heavy rains in the Western Mediterranean are associated with the presence of a cyclone, but not necessarily a strong cyclone. A statistical relationship between Mediterranean cyclones and hazardous torrential rains, however, is still unclear (Alpert et al. 2002). On the other hand, a connection between Mediterranean cyclones and local winds in the Mediterranean basin is generally well known. Namely, local winds in Mediterranean, such as Libeccio, Sirocco, Mistral, Tramontana, Bora, Koshava and Etesian (Burlando 2009), are a mutual product of a low-pressure system situated somewhere in Mediterranean and the unique orography of this basin (Campins et al. 1995, Grisogono and Belušić 2009, Romanić et al. 2016a). Other types of severe weather are also present in Mediterranean, such as wind storms (Nissen et al. 2010), storm surges (Lionello 2005) and lightning (Kotroni and Lagouvardos 2016). Lastly, detailed investigations of extreme weather patterns in Mediterranean is of particular importance since this region is identified as one of the two most susceptible regions for the predicted climate changes (Giorgi 2006).

Downbursts, although being an extreme weather phenomena, have not been extensively researched in the Mediterranean region. These weather phenomena are defined as strong downdrafts originating from thunderstorm (cumulonimbus) or other cumuliform clouds (e.g. altostratus or cumulus) (Byers and Braham 1949) which result in vigorous starburst outflows at or near the surface (Fujita 1981). Based on the horizontal scale of diverging winds, downbursts are divided into macrobursts (outburst winds exceeding 4 km in horizontal dimension) and microburst (outburst winds below 4 km in horizontal dimension) (Fujita 1985). Damaging winds in intense microbursts can be as high as 75 m s^{-1} (Fujita 1990), which for example corresponds to EF3 tornados, based on the forensic Enhanced Fujita Scale (EF) for tornadoes (Wind Science and Engineering Centre 2006). Yet another classification of downbursts is as wet or dry depending on whether downburst events are accompanied with precipitation or not, respectively. It has been observed that dry downbursts are typically produced in weak cumulonimbus or altocumulus clouds (Wakimoto 1985) whereas wet downbursts are usually associated with well-developed thunderstorms (Atkins and Wakimoto 1991). Most of downburst-related studies are based on or validated against the meteorological data obtained above the continental parts of the United States (e.g. the above-mentioned pioneering studies performed by Byers, Braham, and Fujita, and many others carried out by Goff 1976, Wakimoto 1985, Hjelmfelt 1988, Holmes et al. 2008, Lombardo et al. 2014, Gunter and Schroeder 2015) or Asia-Pacific (Gomes and Vickery 1976, Sherman 1987, Choi 1999, 2004, Geerts 2001, Rowcroft 2011), while none have used meteorological data in the Mediterranean. Therefore, while greatly contributing to understanding the downburst phenomena, the results presented in these studies may have limited geographical applicability. Namely, it is known in meteorology that the microphysics of cumuliform clouds sometimes significantly vary from one geographical region to another (You et al. 2016). Since downburst are closely coupled with the existence of cumuliform clouds, it is important to understand the geographical precursors for these non-synoptic storm systems through comprehensive research over different areas around the globe. The Mediterranean region, being the “hot-spot” for different types of severe weather, is therefore of particular importance and the present study aims at bringing new insights on downburst meteorological and surface wind aspects related to this region.

A systematic research on downbursts in an area of the Mediterranean region, the Ligurian and Northern Tyrrhenian Sea, has recently began thanks to the creation of an extensive and high quality wind monitoring network (Section 6.2) realized for two European Union (EU) Projects, “Wind and Ports” (WP) (Solari et al. 2012) and “Wind, Ports and Sea” (WPS) (Burlando et al. 2015), which took place in the period between 2009 and 2015. WP has produced, while WPS is still generating a uniquely wide dataset of measurements that represent an unprecedented patrimony to carry out broad band research in manifold scientific fields.

The Wind Engineering and Structural Dynamics (Windyn) research group at the University of Genoa, which realized these two EU Projects and the monitoring network, initially used wind measurements to evaluate wind actions and effects on structures due to thunderstorms. A semi-automatic procedure has been first implemented that separates intense wind events (Gomes and Vickery 1977/1978) into three families (De Gaetano et al. 2014): (1) stationary Gaussian records, basically related to synoptic phenomena; (2) transient non-stationary non-Gaussian records, potentially caused by thunderstorm and convective events; and, (3) intermediate records, endowed with typical stationary non-

Gaussian features. Processing a huge amount of data made necessary the adoption of a separation criterion based on a few synthetic parameters (Riera and Nanni 1989, Twisdale and Vickery 1992, Choi and Tanurdjaja 2002, Kasperski 2002, Cook et al 2003, Duranona et al 2006, Lombardo et al 2009), without carrying out systematic and prohibitive meteorological surveys of the weather scenarios out of which events took place. Thanks to this tool a unique set of transient wind records has been gathered and submitted to statistical evaluations aiming to define the main characteristics of thunderstorms relevant to the wind loading of structures (Solari et al. 2015a). These characteristics have formed the base upon which a novel method to determine the dynamic response of structures to thunderstorm downbursts has been formulated (Solari et al. 2015b, Solari 2016).

Despite its merits, this approach clearly suffers two main shortcomings. The first is the lack of systematic analyses of the meteorological conditions that occur during phenomena classified as thunderstorms without recognizing precisely their actual nature. The second relates to the refined knowledge of the local time structure of the detected phenomena while lacking a description of their space structure. Both these aspects contribute to the relevant gap that still exists between wind engineering and atmospheric sciences (Solari 2014), and the unexplored potential of filling such gap.

The first aspect relates to the different approaches in these two disciplines. In wind engineering, which is mainly oriented to evaluate aerodynamic loads on structures, the data is usually collected and processed in statistical form, focusing on the limited portion of the atmosphere that houses the built environment; thus it does not usually perform a comprehensive study of the larger weather parent phenomena out of which the data results.

Atmospheric sciences, oriented towards the analysis of the genesis, morphology and life-cycle of thunderstorms, concentrates on the larger scales of atmospheric processes, with winds being just one of the variables, and with the surface layer being treated through integral parameters only. As a result, the scales of motion with which the two disciplines are concerned are different and the measurements and characterization methodologies are also different. Wind engineering mainly aims to detect wind speed time-series with a broad energy content, so it uses ultrasonic anemometers with a high frequency rate located at the ground. Atmospheric sciences base their analysis, instead, on a variety of tools (e.g. satellites, Doppler radar, radio-sounding, thunderstorms and lightning detection networks, classic weather stations); while ground surface data is used in prediction models, high resolution wind data at the ground surface are obviously welcome but not indispensable. This near ground data, which is difficult to measure mostly in localized thunderstorm type events, can be rather physically or numerically simulated.

Traditionally downbursts have been physically simulated by creating an impinging jet over the floor of a test chamber (Wood et al. 2001, Chay and Letchford 2002, Letchford and Chay 2002, Mason et al. 2005, Xu and Hangan 2008, Sengupta and Sarkar 2008, McConville et al. 2009) or tentatively by reproducing only the downburst outflow with a wall-jet by modifying the axial flow of a wind tunnel (Lin et al. 2007). In any case these facilities generate small-scale downbursts in which capturing details of the outflows and especially the turbulence structure is almost impossible (Zhang et al 2013). The emergence of new larger and more complex facilities like the Wind Engineering Energy and Environment **(**WindEEE) Dome at the Western University gradually allows the simulation and reproduction of large-scale downburst events (Hangan 2014, Jubayer et al. 2016). It also offers the unique opportunity to clarify the crucial role of scale effects (Xu and Hangan 2008, McConville et al. 2009) through the comparison with the results obtained in other laboratories and ultimately with field data.

Computational Fluid Dynamics (CFD) simulations have also been applied through full-cloud, sub-cloud and impinging wall jet models. The full-cloud model (Orf et al. 2012) offers a comprehensive representation of the whole phenomenon, but fails in allowing a fine resolution close to the ground. Therefore while it is an important tool for atmospheric sciences, at least by now, cannot provide relevant information to wind engineering. Thus wind engineering adopts sub-cloud (Orf and Anderson 1999, Lin et al. 2007, Mason et al. 2010, Vermeire et al. 2011) and impinging jet (Letchford and Chay 2002, Kim and Hangan 2007, Sengupta and Sarkar 2008, Sim et al. 2016) models making recourse to the Reynolds Averaged Navier-Stokes (RANS) and Large Eddy Simulations (LES). However, RANS models suffer from the inherent modelling of Reynolds stresses and their results in terms of turbulence are essentially filtered. LES, on the other hand, simulates a wider range of turbulence scales, but it is numerically very demanding at the encompassing downburst relevant scales. The use of LES in sub-cloud models is highly promising but still far from being well-established.

From a meteorology and weather forecasting perspective, mesoscale numerical models are used to simulate atmospheric processes on scales much larger than the downburst-specific models (Lorente-Plazas et al. 2016). For example, computational domains in the Weather Research and Forecasting (WRF) model might vary from several hundreds of kilometers in longitudinal and latitudinal directions to a large as the whole globe. Under these circumstances, the grid size typically varies between a few hundreds of meters up to about 10 km in horizontal direction and more than 30 vertical levels (Romanić et al. 2016b). If the horizontal grid size is of the order of 2 km or larger, it is common practice to parameterize the whole cumulus convection inside the domain. In these situations, the cumulus convection and thus the downbursts are all sub-grid processes which are not directly resolved during the computations, but rather are indirectly parameterized.

A new approach for coupling an analytical model of downburst winds with a physical simulator capable of reproducing non-synoptic winds has recently been proposed by Romanic et al. (2016c). Firstly, the analytical model is used to reconstruct a downburst event and the main flow parameters are obtained (e.g. jet diameter, maximum radial velocity, the height of the maximum radial velocity and its distance from the jet center). Secondly, these parameters are used to set up the physical simulations of downburst in the WindEEE Dome. Lastly, the scaled model of an urban environment can be placed inside the testing chamber and the downburst effects on the urban environment can be evaluated.

Overall, both physical and numerical simulations of thunderstorms suffer from the difficulty of representing the large complexity and multitude of physical processes at different scales involved in their life cycle. The huge amount of field measurements provided by the WP and WPS wind monitoring network generates a unique opportunity to analyze these events from a multi-scale perspective as well as to provide a database that can serve the calibration of both physical and CFD simulations, clarifying their inherent limits and advancing these tools towards a better representation of reality. This data base can also be used as a basis for storm reconstruction (either numerically or laboratory based) and therefore open new venues in damage and forensic studies of relevance to other sectors such as the insurance industry.

The present work is part of a longer collaboration between Windyn (University of Genoa) and WindEEE (Western University) carried out as an interdisciplinary effort between two groups involving atmospheric scientists and wind engineers, with the objective to conduct a comprehensive analysis of field measurements and weather scenarios related to non-synoptic wind systems in the Mediterranean. In this paper, the downburst event that struck the Livorno coast on October 1, 2012 at about 12:10 UTC (i.e. 1.10 pm local Italian time) is investigated as a test-case.

Firstly, the field measurements provided by the WP and WPS monitoring network are reported in Section 6.2, where Section 6.2.1 analyzes the data in order to investigate the large scale weather precursors related to the downburst event. Section 6.2.2 examines the wind velocity records, decomposes them and describes their main features in the framework of statistical analyses extended to the whole dataset. Then, 6.3 provides a broad investigation of the weather scenario in the following order: Section 6.3.1 illustrates a synoptic analysis with the aim of presenting the meteorological conditions that, at the macro- and meso-scale, determined the onset of the event, whereas Section 6.3.2 shows that the classical measurements available at a smaller scale are useful to demonstrate the convective nature of this phenomenon and, finally, Section 6.3.3 investigates a couple of instability indices associated with this event. The concluding remarks follow in the last section of this chapter, together with some prospects for future research.

6.2 Field measurements

6.2.1 Monitoring network, dataset, and test-case event

WP 2009-2012 and WPS 2013-2015 were two European Projects carried out by Windyn at the University of Genoa in co-operation with the Port Authorities of the main commercial ports in the Ligurian and Northern Tyrrhenian Sea, namely Genoa, Savona, La Spezia, Livorno, and Bastia (Figure 6-1a, magenta squares). These projects handled the wind and wave forecast in port areas through an integrated system made up of an extensive in-situ monitoring network, the numerical simulation of wind and wave fields, the statistical analysis of wind climate, and algorithms for medium- (1-3 days) and short-term (0.5-2 hours) forecasting. The anemometric monitoring network is made up of 28 ultra-sonic anemometers, 3 weather stations (each one including an additional ultra-sonic anemometer, a barometer, a thermometer and a hygrometer), and 3 LiDAR (Light Detection And Ranging) wind profilers. This monitoring network constitutes a unique opportunity to detect high-resolution thunderstorm records, to analyze these on a statistical basis, and to select specific events of particular interest.

De Gaetano et al. (2014) implemented a semi-automated procedure to extract a selective database of strong wind events that could be considered to a reasonable extent thunderstorm-related. Using this procedure Solari et al. (2015a) identified 64 independent thunderstorms based on 9 anemometric datasets between 2011 and 2012. These thunderstorm events were analyzed in order to study their main characteristics relevant to the wind loading of structures. More recently the analysis has been extended to 14 anemometers between 2011and 2015, and over 200 transient non-stationary events that can be considered as independent thunderstorms or strongly convective events have been identified (Zhang et al. 2016). However, so far no single event has been analyzed individually from a meteorological point of view.

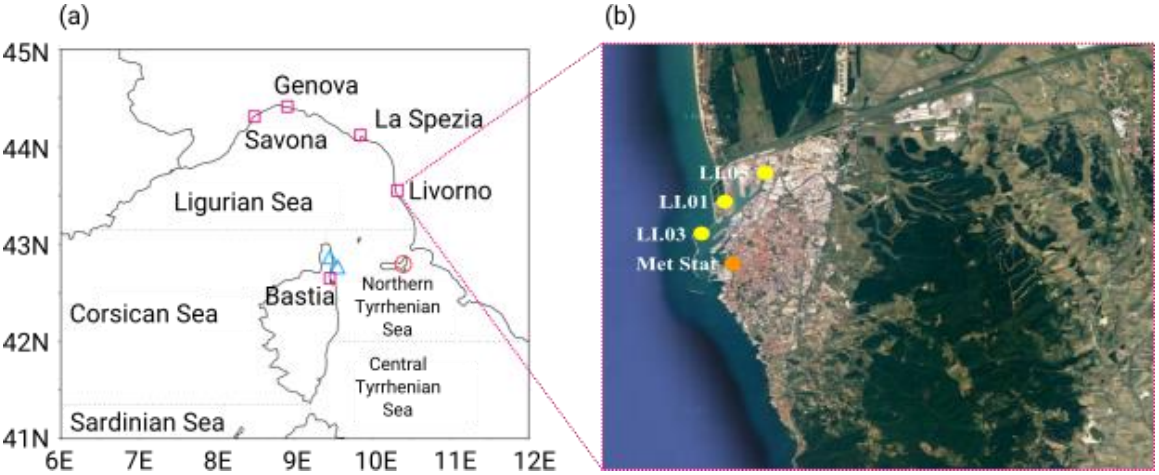

Figure 6-1. (a) Map of the Northern Mediterranean Basin with the international nomenclature of its sub-basins, position where waterspouts occurred on October 1 (blue triangles), location of the meteorological radar in Elba Island (red circle), and position of Livorno City (magenta square). (b) Map of Livorno City with the position of anemometers LI.01, LI.03, LI05 (yellow circles) and the LaMMA meteorological station (orange circle). See Table 6-1 for anemometers' coordinates.

In the present study, one of the events, identified by Solari et al. (2015a) in the area of the Port of Livorno, has been selected for a comprehensive phenomenological investigation. This choice was mainly based on the fact that this is the only monitored area which is not topographically complex. Moreover, an event measured by more than two anemometers at the same time was selected, in order to have information about its evolution in time and space, as well. According to these criteria, the event that occurred on October 1, 2012 was chosen as a test case used to calibrate a general procedure to link field measurements with the parent weather scenario in order to identify any link between transient non-stationary anemometric records and convective phenomena.

The selected event was recorded by three of the five anemometers monitoring the Livorno site (Table 6-1), as two instruments were out of order at that time. All the instruments are three-axial ultra-sonic anemometers with sampling rate 10 Hz, which detect the wind velocity and direction with a precision of 0.01 m s^{-1} and 1°, respectively. The position of the three anemometers, i.e. LI.01, LI.03, and LI.05, which recorded the event of October 1 is shown in Figure 6-1b. Their position was selected in order to register undisturbed wind velocity time histories.

Table 6-1. Full composition of the anemometric monitoring network in the Port of Livorno in 2012. The position of anemometers LI.01, LI.03, and LI.05 is indicated in Figure 6-1b.

Code	Geographical coordinates (λ, ϕ, h) (°E, °N, m ASL)	Position	Height above ground (m)
LI.01	(10.301, 43.570, 20.0)	Tower	20
LI.02	(10.307, 43.583, 20.0)	Tower	20
LI.03	(10.290, 43.558, 20.0)	Tower	20
LI.04	(10.294, 43.541, 20.0)	Tower	20
LI.05	(10.319, 43.580, 75.0)	Building[1]	75

[1] The anemometer is at the top of an antenna mast, 2.5 m above the building roof.

Figure 6-2 shows the time series of the wind speed v and direction α recorded by the anemometers LI.03 (top), LI.01 (centre), and LI.05 (bottom) for the time interval between 11:30 and 12:30 UTC of October 1, 2012. The order (from top to bottom) of the time series has been chosen to follow the chronological occurrence of this meteorological event. The anemometer LI.03, which is the closest to the sea, was the first to measure the wind speed increase that occurred at around 12:09 UTC, as indicated by the vertical dashed line in

Figure 6-2a while anemometers LI.01 and LI.05, which are gradually farther from the coast (see Figure 6-2b), measured the same ramp and peak at about 12:11 (Figure 6-2c) and 12:15 UTC (Figure 6-2e), respectively. The maximum value of the peak slightly decreases from the sea to the inland, i.e. from LI.03 to LI.05. The wind direction, which was approximately from the north until 11:50 UTC, backed 90°, i.e. from west, at the peak occurrence and then veered to the original direction. The entire event lasted about 20-30 minutes.

This description resembles a non-stationary event, like a downdraft-induced gust front, that seems to come from the sea, where it probably originated, and move east or northeastwardly. Besides, a spike stronger than the main peak occurred a few minutes after (in LI.03 and LI.05) or concurrent to the peak itself (in LI.01), which may be interpreted as a small-scale jet-like microburst embedded into the larger scale main downdraft (Fujita 1986, Hjelmfelt 1988). Most likely the spike is not caused by a local random fluctuation of wind speed since it is observed at all three stations and it is associated with an abrupt clockwise change in wind direction, as clearly illustrated in Figure 6-2b and Figure 6-2f. The wind direction shifts between the first peak and the spike are approximately 90º and 130º at LI.03 and LI.05, respectively.

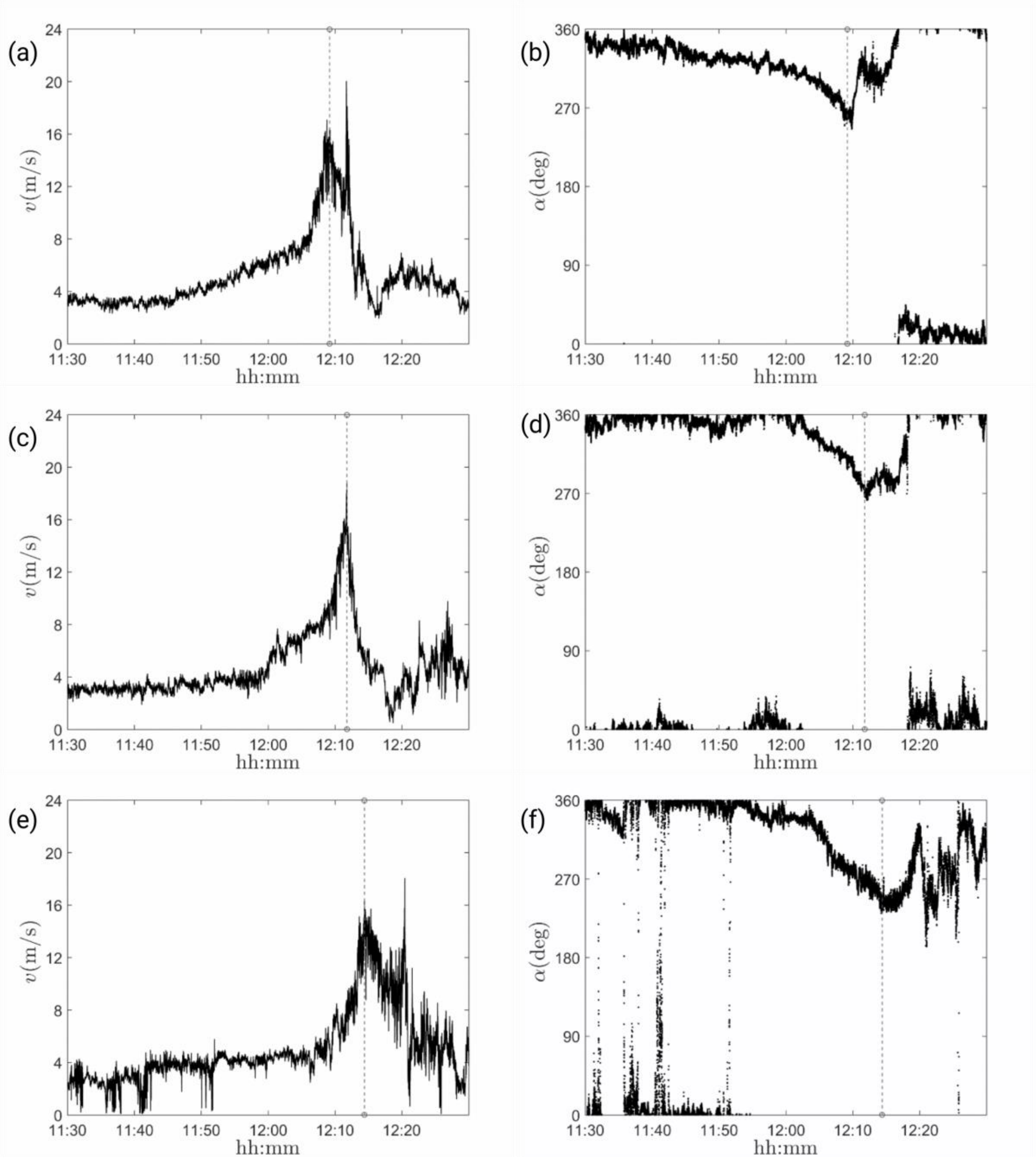

Figure 6-2. Wind speed (left) and direction (right) measured by the anemometers LI.03 (top), LI.01 (center), and LI.05 (bottom) of the Port of Livorno monitoring network from 11:30 to 12:30 UTC on October 1, 2012. Vertical dashed lines show the approximate time of the gust front passage.

While the wind records shown in Figure 6-2 are not overall representative of all situations detected by the WP and WPS monitoring network they provide a basis to analyze the trends of such a non-stationary event. It is important to notice a difference between the records reported in Figure 6-2 and the typical downburst wind time series measured across the United States and elsewhere. The wind records from the United States (Goldman and Sloss 1969, Charba 1974, Wakimoto 1982, Fujita 1985, Gast and Schroeder 2004, Holmes et al. 2008) and Singapore (Choi 2004) seem to have either a constant background wind speed or a sudden drop in wind speed prior the downburst. On the other hand, the wind records in Figure 6-2a and Figure 6-2c are characterized by a steady increase of wind speed before reaching the downburst ramp-up. In these two cases, wind speed increased by approximately 5 m s^{-1} between 11:45 and 12:05 UTC and from 12:00 to 12:10 UTC, respectively. Simultaneously, the wind direction steadily shifted in counterclockwise direction reaching approximately 280º-290º before the ramp-up at both anemometers Figure 6-2b and Figure 6-2d). The anemometer records in Figure 6-2, however, look very similar to the graphs of a weak downburst measured at a suburban area of Brisbane, Australia (Sherman 1987). Sherman noticed that the spike was most pronounced close to the surface and diminished moving upwards. The reported measurements in Figure 6-2 seem to differ from downbursts measured across the continental parts of Europe (Järvi et al. 2007, Pistotnik et al. 2011). The downburst recorded in Southern Finland (Järvi et al. 2007) was characterized by an intense gust front prior to the downburst, but it lacks the secondary peak in two out of three wind speed records. Field measurements from Austria (Pistotnik et al. 2011) show two pronounced peaks in both mean and peak wind speeds, but the wind speed seem to rapidly decrease prior the downburst – a signature that is typical for downbursts observed in the United States, as discussed above.

Wakimoto (1982) analyzed several data records of weak downbursts measured outside of Chicago, United States, using a Doppler radar, radiosondes and a network of surface measurements. He classified the life cycle of a downburst into four stages (formative, early mature, late mature and dissipative) and presented measurements for each of these stages. Applying his conceptual classification to the wind direction in Figure 6-2, it seems that the reported downburst resembles downbursts at stages II and III, which are characterized by sudden shifts in wind directions before, during and after the downbursts as well as wind speeds between 10 and 30 m s^{-1}. However, his analysis also suggests a noticeable decrease in wind speed prior to the arrival of the downburst with the first peak being always the most pronounced (also noticed in a number of other downburst measurements). None of these two features have been observed in the presented case. Instead, these measurements seem to be among the first wind time series of a microburst embedded in a macroburst in the Mediterranean region.

The pronounced spike after the first well-defined peak, such as the ones measured by the LI.03 and LI.05 anemometers, has been numerically simulated by (Orf et al. 2012). Their results, obtained using a non-hydrostatic LES cloud model (Bryan and Fritsch 2002), show a steady increase of wind speed prior to the non-steady and highly fluctuating downburst peaks, similar to anemometer records in Figure 6-2. They reported the existence of a pronounced spike after the first downdraft at a reference point situated on the east flank of the downdraft, whereas the same pattern has not been observed on the west flank of the downdraft. The assumption that LI.03 and LI.05 anemometers were on the opposite sides of the downdraft, however, does not match with the wind directions at these two measuring stations that approximately coincide with each other

6.2.2 Signal analysis

To inspect the characteristics of the wind speed records shown in Figure 6-2, the classical decomposition rule of transient wind velocity signals (Choi and Hidayat 2002, Chen and Letchford 2004, Holmes et al. 2008, Kwon and Kareem 2009, Solari et al. 2015a) is herein applied:

$$v(t) = \bar{v}(t) + v'(t) \tag{6-1}$$

where $t \in [0, \Delta T]$ is the time, ΔT = 1 hour is the period in which the signals are examined, $\bar{v}$ is the slowly-varying mean wind velocity, related to the low frequency content of v, and v' is the residual fluctuation, related to the high frequency content of v.

The slowly-varying mean wind velocity is driven by the large scale flow. It is often modelled as deterministic and is filtered from the initial signal by a moving average process. The residual fluctuation is induced by the small scale turbulence and is usually dealt with as a non-stationary random process defined as:

$$v'(t) = \sigma_v(t)\widetilde{v'}(t) \tag{6-2}$$

where σ_v is the slowly-varying standard deviation of v', and $\widetilde{v'}$ is referred to as the reduced turbulent fluctuation. Chen and Letchford (2004) conceptually related the slowly-varying standard deviation to the medium scales of motion: on one hand, it is a property of the fluctuation at the turbulence scale; on the other hand, it is driven by the mean wind velocity at the large scale and it is thus often modelled as deterministic. This interpretation refers to the process of defining and extracting the slowly varying mean. The reduced turbulent fluctuation is then related to the small scales of turbulence and is until now modelled as a rapidly-varying stationary Gaussian random process with zero mean and unit standard deviation (Chen and Letchford 2004, Holmes et al. 2008, Kwon and Kareem 2009, Solari et al. 2015a).

The extraction of $\overline{v}$ from v and of σ_v from v' is herein carried out by a moving average filter (Choi and Hidayat 2002, Holmes et al 2008) with period T = 30 s (Solari et al 2015a). Other methods are available (McCullough et al 2014). Inserging Eq. (6-2) into Eq. (6-1) yields:

$$v(t) = \bar{v}(t)[1 + I_v(t)\widetilde{v'}(t)] \tag{6-3}$$

where:

$$I_v(t) = \frac{\sigma_v(t)}{\bar{v}(t)} \tag{6-4}$$

is the slowly-varying turbulence intensity. Since it is usually a weakly-dependent function of time, several authors approximate it by its average value over a suitable averaging time period (Chen and Letchford 2004, 2007, Chay et al 2006, Holmes et al 2008). Zhang et al. (2016) pointed out that this approximation is questionable and may give rise to some shortcomings.

Figure 6-3 shows the diagrams of the slowly-varying mean wind velocity $\overline{v}$ (top), the residual fluctuation v' (centre), and the slowly-varying standard deviation σ_v (bottom), as extracted from the LI.03 (a, d, and g), LI.01 (b, e, and h), and LI.05 (c, f, and i) wind speed records shown in Figure 6-2.

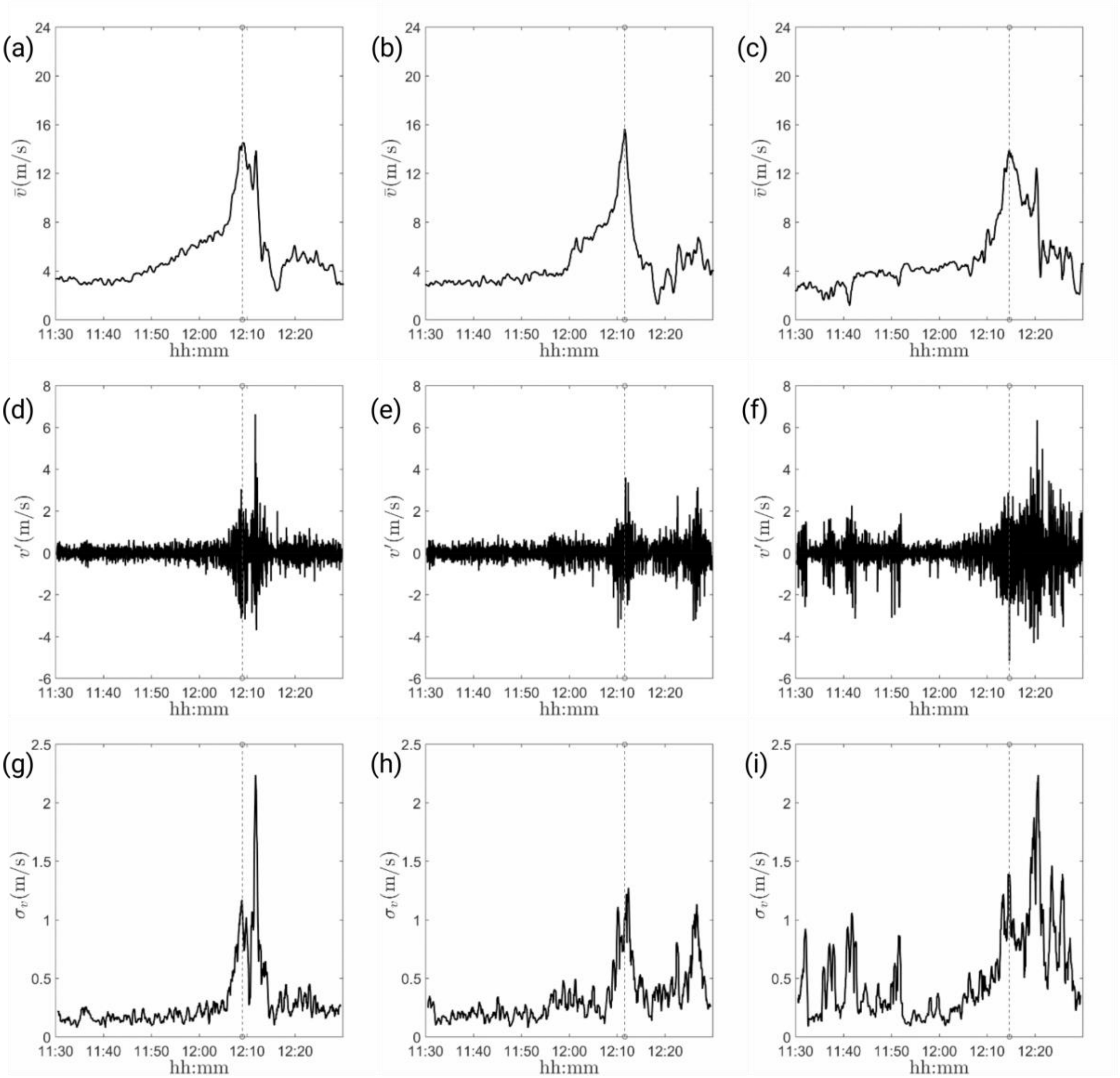

Figure 6-3. Slowly-varying mean wind velocity (top), residual fluctuation (center), and slowly-varying standard deviation (bottom), as extracted from the records detected by the anemometers LI.03 (a, d, and g), LI.01 (b, e, and h), and LI.05 (c, f, and i) of the Port of Livorno monitoring network from 11:30 to 12:30 UTC on October 1, 2012. Vertical dashed lines show the approximate time of the gust front passage.

Figure 6-4 shows the diagrams of the slowly-varying turbulence intensity I_v over ΔT = 1 hour (top) and the 10-min interval centred around the time instant at which $\overline{v}_{max}$ occurs (bottom), as extracted from LI.03 (a, d), LI.01 (b, e), and LI.05 (c, f).

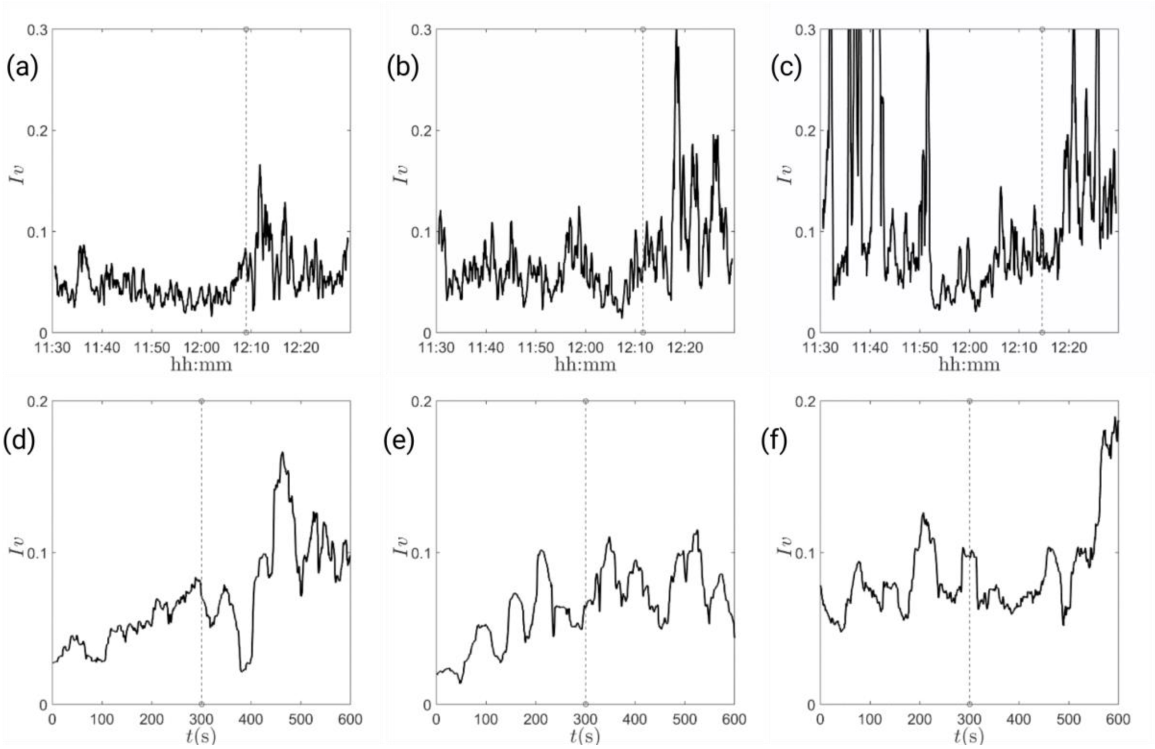

Figure 6-4. Slowly-varying turbulence intensity over ΔT = 1 hour (top) and the 10-min interval centred around the time instant at which $\overline{v}_{max}$ occurs (bottom), as extracted from the records detected by the anemometers LI.03 (a, d), LI.01 (b, e), and LI.05 (c, f) of the Port of Livorno monitoring network from 11:30 to 12:30 UTC on October 1, 2012. Vertical dashed lines show the approximate time of the gust front passage.

Figure 6-5 shows the diagrams of the rapidly-varying reduced turbulent fluctuation $\widetilde{v}'$ (top), $f_{\widetilde{v}'}$ of their histogram compared with a reference Gaussian probability density function (PDF) (thick line) (centre), and of their power spectral density (PSD) $S_{\widetilde{v}'}$ (bottom), n being the frequency, as extracted from LI.03 (a, d and g), LI.01 (b, e and h), and LI.05 (c, f and i).

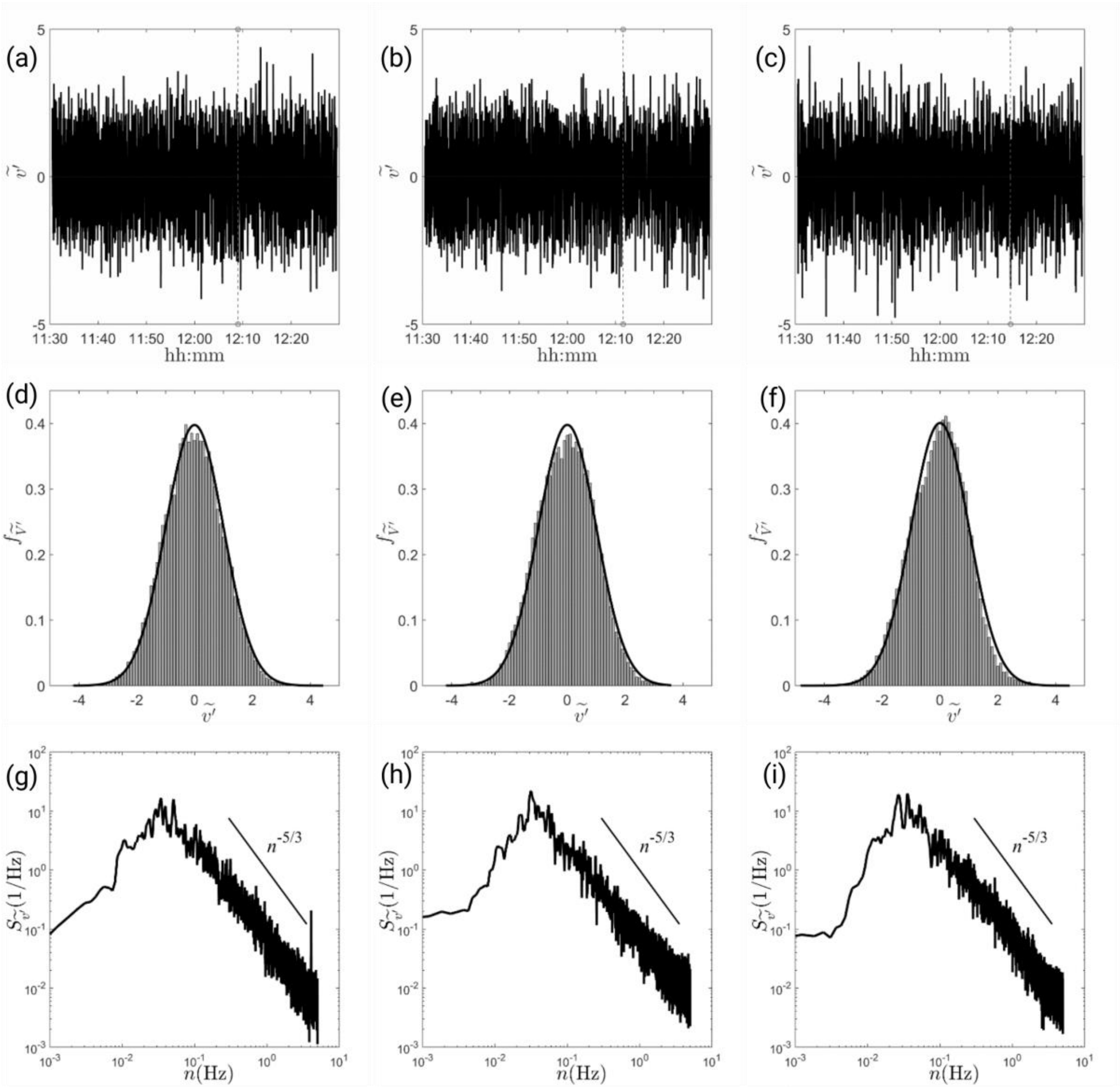

Figure 6-5. Rapidly-varying reduced turbulence fluctuation (top), histogram compared with a reference Gaussian PDF (thick line) (center), and PSD (bottom), as extracted from the records detected by the anemometers LI.03 (a, d, and g), LI.01 (b, e, and h), and LI.05 (c, f, and i) of the Port of Livorno monitoring network from 11:30 to 12:30 UTC on October 1, 2012.

Table 6-2 shows some synthetic parameters of the wind velocity records. In this table, $\hat{v}$, $\bar{v}_{max}$, and $G = \hat{v} / \bar{v}_{max}$ are the 1-s peak wind velocity, the maximum value of the slowly-varying mean wind velocity, and the gust factor associated with the primary peak whereas the values related to the secondary peak, if present, are put in parentheses; $\bar{I}_v(1-\mathrm{hr})$ and $\bar{I}_v(10-\mathrm{min})$ are the average values of I_v over ΔT = 1 hour and the 10-min interval centered around the time instant at which $\bar{v}_{max}$ occurs; μ', σ', γ', κ', and L'_v are, respectively, the mean value, the standard deviation, the skewness, the kurtosis, and the integral length scale of the reduced turbulent fluctuation $\tilde{v}'$.

Table 6-2. Synthetic parameters of the wind velocity records.

Parameter	LI.03	LI.01	LI.05
$\hat{v}$ (m s^{-1})	19.98 (15.81)	18.00	15.45 (17.27)
$\bar{v}_{max}$ (m s^{-1})	14.55 (13.89)	15.66	13.93 (12.46)
G	1.30 (1.14)	1.15	1.11 (1.39)
$\bar{I}_v(1-\mathrm{hr})$	0.052	0.074	0.114
$\bar{I}_v(10-\mathrm{min})$	0.071	0.065	0.083
μ'	-0.003	0.000	0.000
σ'	1.003	1.003	1.000
γ'	-0.032	-0.059	-0.125
κ'	2.914	2.863	3.178
L'_v (m)	26.52	28.88	27.12

The joint analysis of Figure 6-3 to Figure 6-5 and Table 6-2 shows that the slowly-varying mean wind velocity $\bar{v}$ provides a very clear picture of the movement of the gust front from the sea to the inland. It is worth noting that the moving average does not filter out the secondary peak in the LI.03 and LI.05 records, confirming that such peak represents a dominant feature of the large scale flow. As opposed to the typically adopted wind tunnel modelling approaches, it is clear that the residual fluctuation v' shows nonstationary random properties with large intensities and intermittency strongly correlated to the largest values of $\overline{v}$. This trend is confirmed by the slowly-varying standard deviation σ_v, which exhibits very large values corresponding to the secondary peak detected by the LI.03 and LI.05 anemometers. This observation does not alter the fact that this peak is a dominant feature of the large scale flow, but points out that its large intensity is significantly enhanced by strong random fluctuations.

The diagrams of the slowly-varying turbulence intensity I_v and its average values $\overline{I}_v$ over different time intervals confirm that this quantity is not strongly time dependent, unless for the presence of some spurious large values that occur when $\overline{v}$ is very small (Eq. (6-4)), like, for instance, the spike over 0.3 of LI.01 in correspondence of an almost null $\overline{v}$ value. Coherently with Solari et al. (2015a) and Zhang et al. (2016), $\overline{I}_v$ = 0.05-0.12. Note that on the shorter time scales ΔT = 10-min, $\overline{I}_v$ does not show any significant growth from the sea to the inland, whereas $\overline{I}_v$ doubles from LI.03 to LI.05 on the larger time scale ΔT = 1 hour. This provides a partial confirmation that the time evolution of a downburst is so rapid and short that its wind field does not reach an equilibrium condition over the roughness of the terrain, thus turbulence intensity is not much affected by this parameter.

The diagrams of the rapidly-varying reduced turbulent fluctuation $\tilde{v}'$ exhibit the classical random stationary Gaussian features supported by many authors in literature (Chen and Letchford 2004, Holmes et al. 2008, Solari et al. 2015a). The Gaussian property of the three signals overall is confirmed by the good agreement between the histogram of $\tilde{v}'$ and the reference Gaussian PDF with $\mu' = 0$ and $\sigma' = 1$; the partial detachment, observed mostly for the middle and right hand side (RHS) signal correlates with skewness values γ' not exactly equal to 0 and kurtosis values κ' not exactly equal to 3. Also the PSD of $\tilde{v}'$ matches overall the results provided by Solari et al. (2015a). $S_{\tilde{v}'}$ shows a relative maximum around T = 30 s, just the moving average period: on its left the PSD clearly falls down; on its right it decreases with a slope nearly proportional to the curve $n^{-5/3}$ that is typical of the inertial sub-range $S_{\tilde{v}'}$ of synoptic-type winds. The integral length scale of turbulence L'_v has been determined by fitting the experimental PSD by the model proposed by Solari and Piccardo (2001); it is almost invariant from signal to signal and is fully coherent with the data reported by Solari et al. (2015a). Also the gust factor G, between 1.11 and 1.39, is coherent with the data reported by Solari et al. (2015a).

However, take note that mostly for the middle signal but also for the RHS signal these slopes differ from the typical -5/3. This type of departure from the local universal equilibrium has been previously observed in flows that have sharp interfaces and high intermittency (Braza et al. 2006), similar to the downburst event analyzed herein.

6.3 Weather scenario and meteorological precursors

6.3.1 Synoptic dynamics

Figure 6-6 (panels a-b) depicts the synoptic condition over Europe on October 1, 2012, showing the position of cyclones and anticyclones at 00:00 UTC (a) and 12:00 UTC (b). The data are obtained from the National Center for Environmental Prediction (NCEP)

Global Forecast System (GFS) analyses, available on a 0.5º by 0.5º geographical grid and acquired from the National Centers for Environmental Information database.

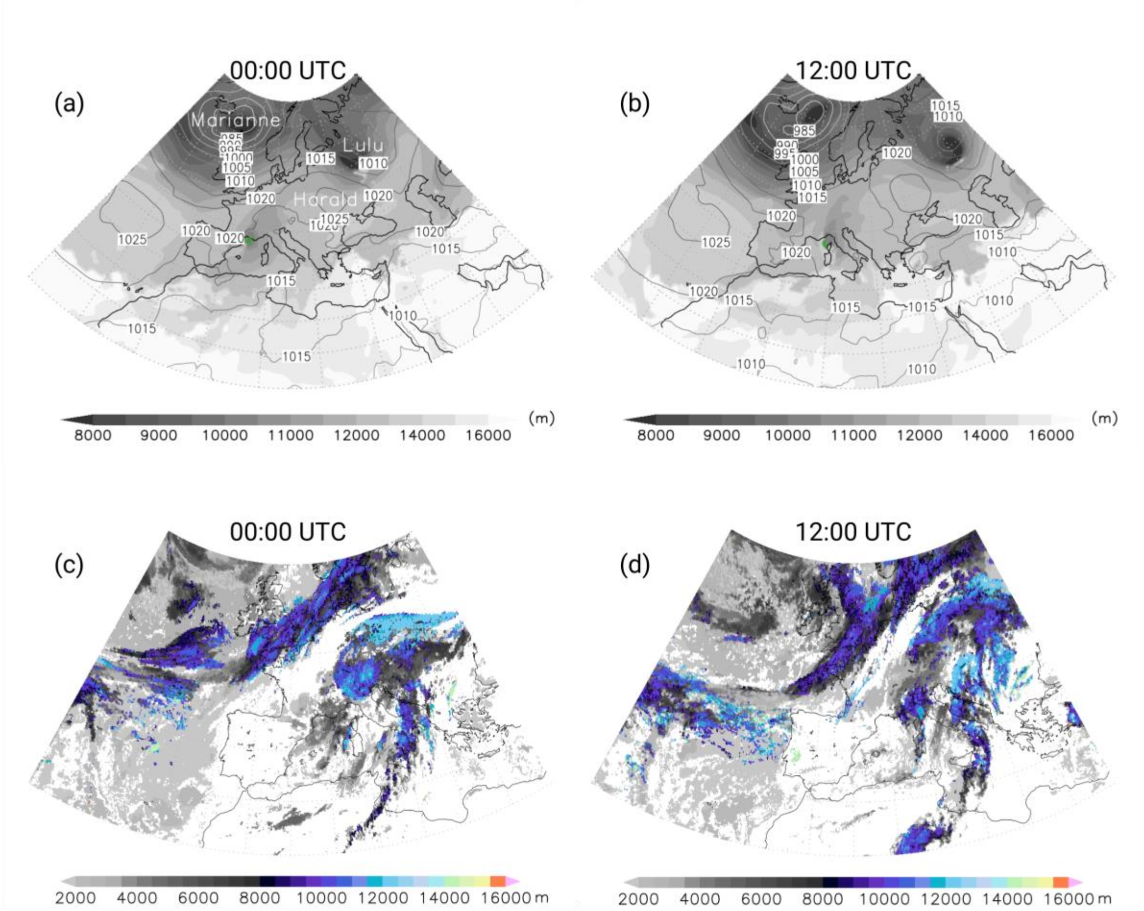

Figure 6-6. Top panels (a-b): mean sea level pressure (contours) and tropopause height (shaded contours) over Europe from GFS analyses (the green contour corresponds to the minimum of the tropopause anomaly cut-off over the western Alps). Bottom panels (c-d): cloud top height from MSG data. Left (right) panels correspond to October 1, at 00:00 (12:00) UTC.

The meteorological situation over Europe was dominated by the presence of the extra-tropical cyclone Marianne (following the names given by the Institute of Meteorology of the Freie Universität Berlin, Germany) southeast of Iceland, with a surface low pressure minimum below 985 hPa and a trough aloft extending southward to the western Alps. To the east, the occluded front of the extra-tropical cyclone Lulu, which was born on September 25 in the Labrador Sea, extended from north-western Russia to the north of the Sea of Azov. Finally, the anticyclone Harald, which was situated over central Europe a few days before, at this point had moved its high-pressure maximum of 1025 hPa over Poland and Ukraine, indicating a blocking situation (Rex 1950).

At 00:00 UTC, the tropopause anomaly cut-off had a relative minimum of 9870 m and it was located in the Northern Mediterranean over the Gulf of Lion (France). The anomaly cut-off moved westward over the Gulf of Genoa at midday. This situation is depicted by the position of the 10000 m height (green contour reported in Figure 6-6 (a-b)). In fact, according to GFS analyses, at 12:00 UTC the tropopause height showed an abrupt discontinuity along a distance of about 100 km, spanning from less than 10 km over the Gulf of Genoa to more than 13 km over the Corsican Sea (i.e. to the west of Corsica, see Figure 6-1a), denoting the existence of a frontal zone beneath.

The distribution of cloud top heights obtained from the cloud analysis performed by Eumetsat (EUMETSAT 2013, Derrien et al. 2013), based on infrared measurements collected by SEVIRI (Spinning Enhanced Visible & Infrared Imager) on board the Meteosat Second Generation (MSG) satellites, also shows the presence of a smaller cyclone in the Eastern Padan Plain at 00:00 UTC (Fig. 6c). The cyclone, which developed on September 29, as a secondary cyclogenesis event in the Gulf of Genoa (Trigo et al. 2002), at 12:00 UTC had moved over the Balkans. Figure 6-6d shows, however, that a meso-scale convective system, which was only in its embryonic stage at 00:00 UTC, developed rapidly over the Gulf of Genoa during the morning. This cloud system is the main contributor responsible for the strong wind event described in Section 6.2.

Both an upper-level trough upstream of the Alps, like the one of cyclone Marianne, and a low-level frontal system impinging on the Alps, as denoted by the tropopause discontinuity mentioned above, are considered indispensable meteorological precursors of lee cyclogenesis. These factors play a fundamental role especially during the rapid trigger phase due to the interaction between frontal zone and mountains (Buzzi and Tibaldi 1978). During this stage, the cyclone deepens while remaining quasi-stationary, the upper-level trough fills north of the Alps and deepens to the south, and the jet stream splits northwest of the Alps into a secondary branch over the Mediterranean, which reconnects to the main branch to the north of the Black sea (Figure 6-7).

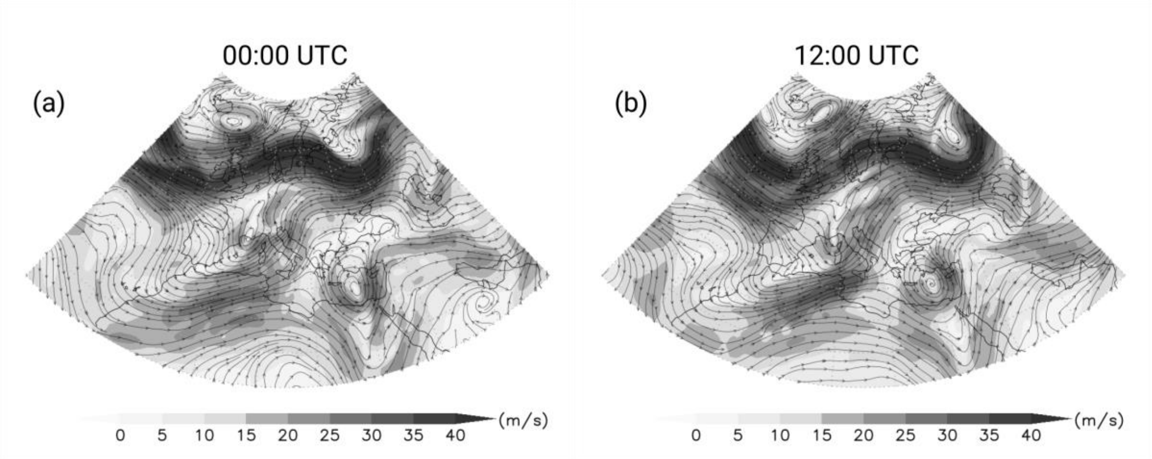

Figure 6-7. Wind speed (shaded contours) and streamlines at 300 hPa. Left (right) panels correspond to October 1, at 00:00 (12:00) UTC, respectively.

Many different and partially concurrent mechanisms have been proposed for lee cyclogenesis during the trigger phase (Buzzi and Tibaldi 1978, McGinley 1982, Mattocks and Bleck 1986, Bluestein 1995, McTaggart-Cowan et al. 2009a, McTaggart-Cowan et al. 2009b). For example, Bluestein (1995) analyzed the role of cyclonic vorticity advection that occurs downstream from the maxima in absolute vorticity aloft, which is typically located along the trough axis. Due to the vorticity advection, a rising motion occurs downstream from the upper-level trough, which contributes to the surface pressure fall, as theoretically demonstrated by Sutcliffe (1947). The field of absolute vorticity at the 300 hPa level over Italy on October 1 at 00:00 UTC and 12:00 UTC is depicted in Figure 6-8a and b, respectively. Only contours higher than 0.00025 s^{-1} are drawn, to indicate the position of the trough (see also Figure 6-6a-b) that moves from upstream the Alps to the lee side where secondary cyclogenesis took place.

According to Bluestein (1995), the rising motions should occur ahead the through, where the cold front occurs as well. Moreover, Mattocks and Bleck (1986) concluded that the rapid intensification of lee cyclones during their trigger phase, which is characterized by strong vertical motions, starts before the cold air reaches the lee side of the Alps, namely in the Gulf of Genoa, where cyclones usually continue growing because of baroclinic instability. These conditions seem to be present on October 1, when relative humidity at 700 hPa (Figure 6-8a-b, shaded contours) took values greater than 99% over the Corsican Sea at 00:00 UTC and over the Ligurian Sea at 12:00 UTC. The spatial distribution of cloud-top heights reported in Figure 6-8c-d, however, shows that early in the morning the vertical extension of the cloud cover is limited to the middle troposphere (grey to black colors over the Corsican Sea in Figure 6-8c). Later at midday, high clouds covered the whole Ligurian Sea and a deep convective system with cloud-top heights above 10000 m formed and extended from the north-east of Corsica to the coast of Tuscany.

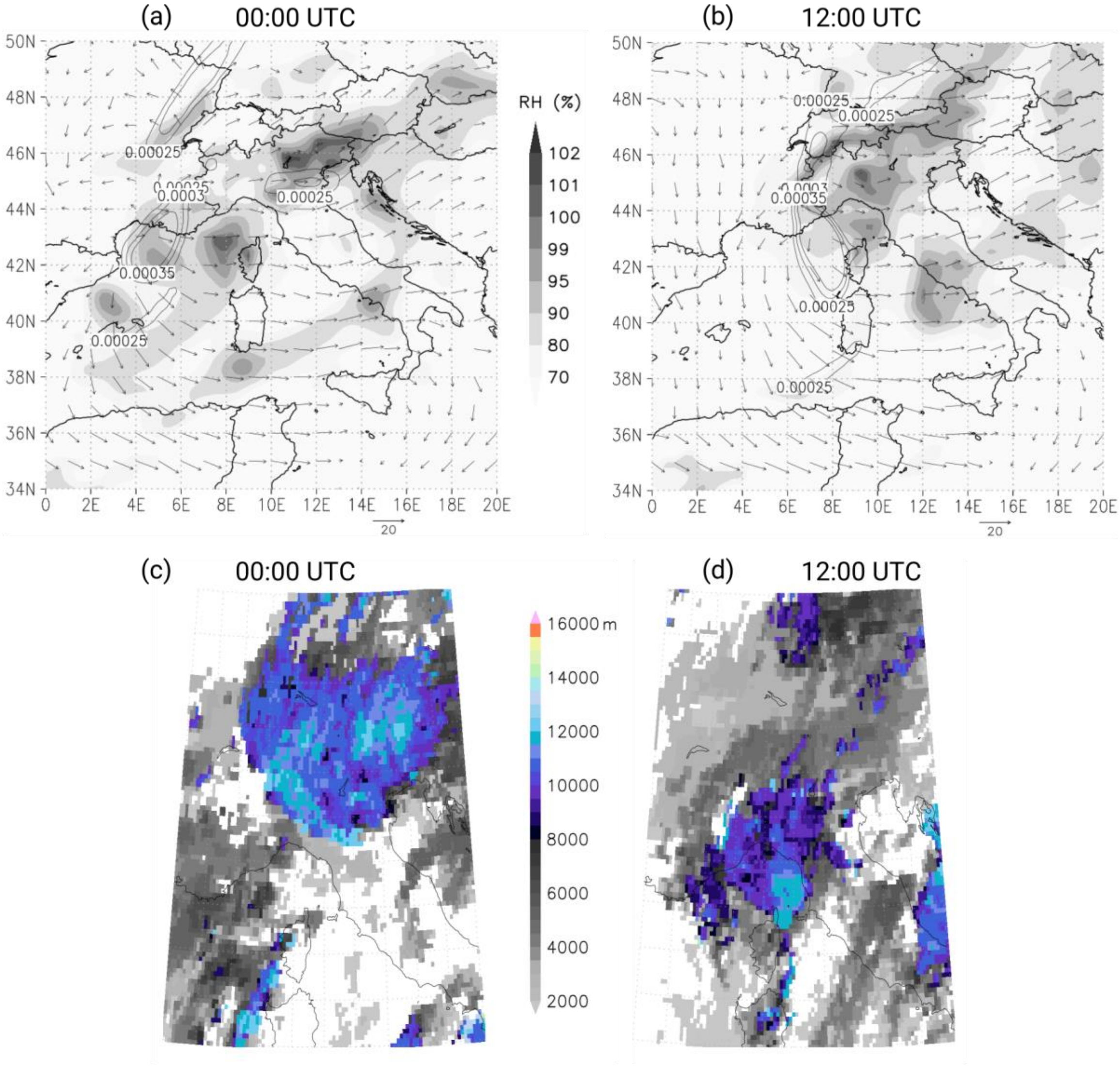

Figure 6-8. Top panels (a-b): relative vorticity (contours) at 300 hPa, relative humidity (shaded contours) at 700 hPa, and mean storm motion (vectors) from GFS analyses. Bottom panels (c-d): cloud top height from MSG data. Left (right) panels correspond to October 1, at 00:00 (12:00) UTC.

Figure 6-8a-b also show the mean storm motion (vectors), which is calculated as an integral measure of the wind velocity variation between 0 and 6000 m above sea level (ASL). This information, which is related to the vertical wind shear, is very useful to predict the spatial evolution of thunderstorms inside complex convective systems. In the present case, the mean storm motion at 12:00 UTC in the eastern Ligurian and Northern Tyrrhenian Sea (Fig. 8b) was almost purely zonal with an average magnitude of about 6 m s^{-1} to the east. This value is the result of the wind field shift from south-southeast in the lower troposphere (at 925 hPa) to southwest aloft (at 400 hPa). Updrafts turn clockwise as they rise and their corresponding gust fronts occur prevailingly to the eastern side of the convective cells, where new updrafts form. The multicell system is driven by the lifting of warm air along the gust front and the system shifts eastward under such wind shear conditions. The storm-relative helicity (SRH), calculated in a layer from 0 to *h*=3000 m ASL, is another important parameter that helps determine the type of thunderstorm to develop. This parameter measures the vertical transfer of energy by the shear of the wind:

$$\mathrm{SRH} = -\int_0^h \boldsymbol{k} \cdot (\boldsymbol{V} - \boldsymbol{C}) \times \frac{d\boldsymbol{V}}{dz}\, dz, \tag{6-5}$$

where $\boldsymbol{V}$ is the environmental wind vector, $\boldsymbol{C}$ is the storm's translation velocity, $\boldsymbol{k}\times d\boldsymbol{V}/dz$ is the horizontal vorticity with $\boldsymbol{k}$ being the unit vector in the vertical (z) direction. This index reached the maximum value of 116 m^2 s^{-2} (not shown) 25 km to the west-southwest of Livorno. According to Rasmussen and Blanchard (1998), who reported a statistical analysis of the values of shear-related parameters for supercells with tornadoes, supercells without tornadoes, and non-supercell thunderstorms, the calculated values of the mean storm motion and storm-relative helicity correspond to non-supercell thunderstorm conditions. It is worth noting, however, that the maximum SRH is above the 75th percentile of the SRH distribution of non-supercell thunderstorms and very close to the median (i.e. 124 m^2 s^{-2}) of the SRH distribution of supercells without tornadoes. Therefore, the possibility of supercell-like thunderstorms off the coast of Livorno cannot be a priori completely excluded. The SRH, however, should always be interpreted with caution since the values above 350 m^2 s^{-2} were observed in intense low-level jets and stable stratification (Romanić et al. 2016b).

In conclusion, it seems reasonable to claim that the strong wind event that occurred on October 1 in Livorno a few minutes after 12:00 UTC was due to the meso-scale convective system described above, which represented the initial evolution of a cyclone in the lee of the Alps during its trigger stage. This cyclone did not grow to a mature extra-tropical-like cyclone afterwards, as it collided with the lee cyclone previously formed that had not moved far eastward due to the presence of the quasi-stationary anticyclone Harald. The two cyclones mixed completely in the evening

6.3.2 Local-scale observations

According to satellite images (not shown), the deep convective system shown in Figure 6-8d started growing to the northeast of Corsica between 09:00 and 10:00 UTC on October 1. As reported in the European Severe Weather Database (Dotzek et al. 2009), operated by the European Severe Storms Laboratory, two waterspouts were observed at 09:00±15 min UTC and 10:00±15 min UTC at Pietracorbara and Santa Maria di Lota (Corsica), respectively. The position of the waterspouts is shown in Figure 6-1a (blue triangles). Later on, the convective system grew as a multicell thunderstorm along a rather straight line developed along the mean storm motion. Figure 6-9 shows the reflectivity measured by the meteorological radar installed in Elba Island (east of Corsica, the position is shown by a red circle in Figure 6-1a), which spans a circular area with radius of about 108 km: panels (a-d) show the time evolution of the convective system from 11:00 UTC to 12:30 UTC with a 30-minute time step.

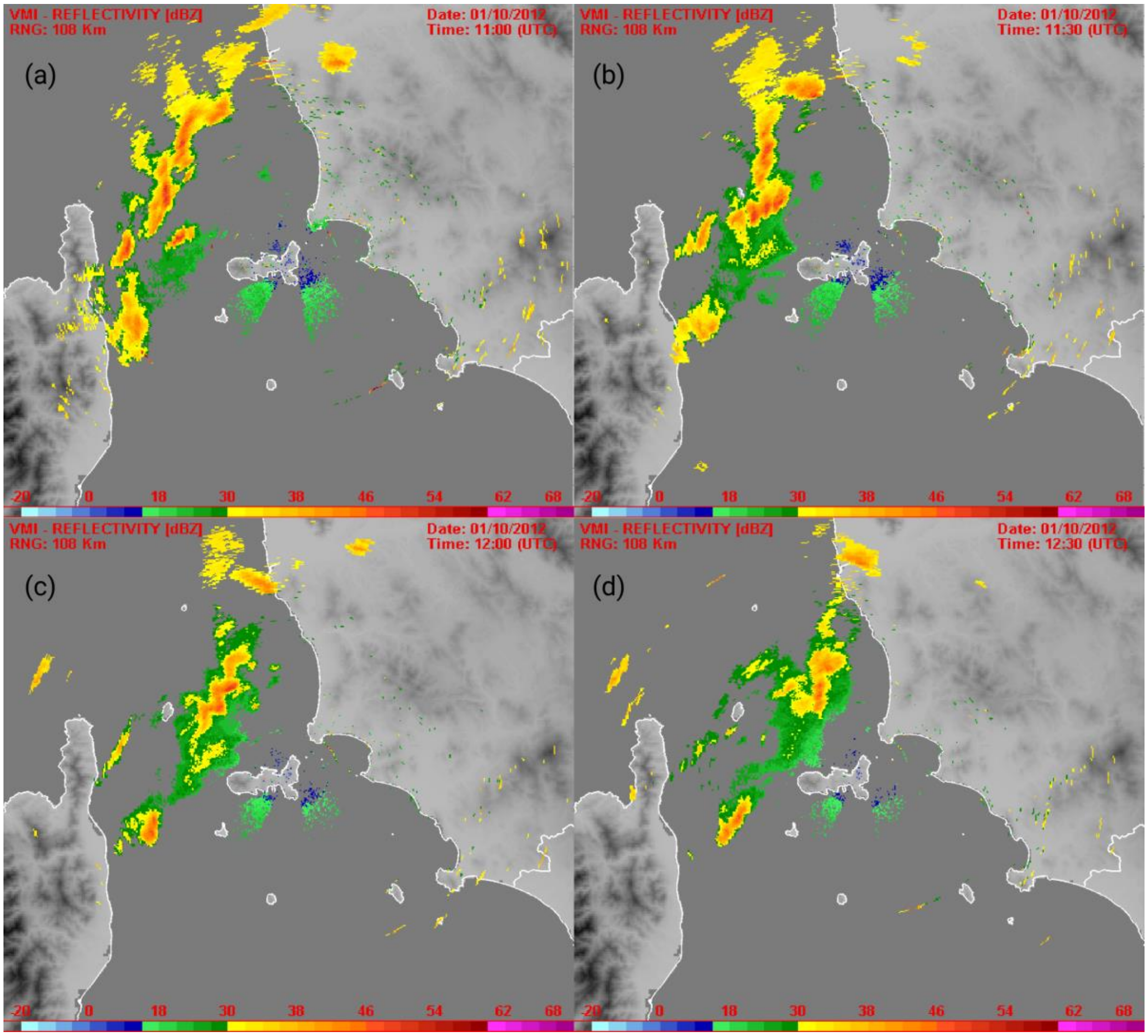

Figure 6-9. Reflectivity (dBz, Vertical Maximum Intensity) measured by the meteorological X-band radar, installed at Cima di Monte (Elba Island) at 480 m ASL, at 11:00 (a), 11:30 (b), 12:00 (c), and 12:30 UTC (d). Courtesy LaMMA Consortium.

At 11:00 UTC, the values of radar reflectivity around 30 dBz show the position of scattered thunderstorms organized along a straight line from Corsica to Tuscany, which slightly shifts to the northeast in the next hour. Such an arrangement of thunderstorm clouds is known as the squall line. This observation seems to be coherent with the mean storm motion obtained from the GFS analyses mentioned in the previous section, as the thunderstorms develop new cells to the right of the mean flow, which is about northward. At 11:30 UTC (Figure 6-9b) a roughly circular blob appears to the west-southwest of Livorno, in the same position where the maximum SRH value was observed. This convective thunderstorm landed at 12:00 UTC in Livorno (Figure 6-9c) and, in the authors' opinion, it is responsible for the strong wind event depicted in Section 6.2. However, an a priori exclusion of a supercell-like thunderstorm is not possible since the radar images show a small hook-shaped appendage to the east. At 12.30 UTC (Figure 6-9d), the convective cell had already moved to the north of Livorno. The recorded wind directions during the downburst event (Figure 6-2 b,d,f) supplemented with the results in Figure 6-9c-d suggest that the downburst was spawned in the north part of the convective system. Interestingly, this region is not characterized with the highest radar reflectivity.

The intense convective activity that occurred over the area from Corsica and Tuscany in the morning of October 1 is confirmed by the great number of lightning strikes registered by the Blitzortung network for lightning and thunderstorms, as reported in Figure 6-10 where panel (a) shows the strike occurrence from 11:00 to 12:30 UTC and panel (b) refers to the period from 12:00 to 12:30 UTC. Lightning strikes were localized in the south part of the convective system, which is the area populated with the deepest (Figure 6-6d and

Figure 6-8d) and most intensive (Figure 6-9c) clouds. Lightning strikes were observed in Livorno during this event.

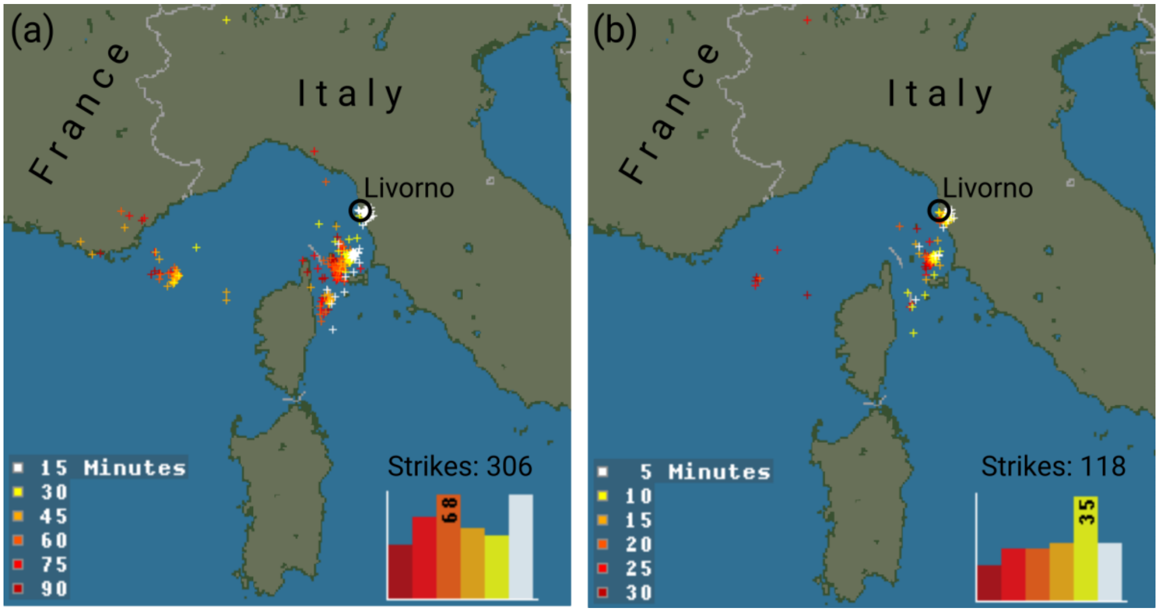

Figure 6-10. Strikes recorded on October 1, from 11:00 to 12:30 UTC (left) and from 12:00 to 12:30 UTC (right), by means of the Blitzortung network for lightning and thunderstorms, retrieved through the online archive. Courtesy Blitzortung.org.

Finally, the weather station located in the city center (see the orange circle in Fig. 1b) and operated by the meteorological office in Tuscany (LaMMA Consortium) measured several important parameters during the thunderstorm with a record sampling of 15 minutes. The records of wind speed and direction, temperature, solar radiation, and precipitation are reported in Figure 6-11. During the whole day, the station measured quite a low mean (i.e. 15 minutes averaged, black line) and maximum (grey line) wind speed and a rather regular prevailing (black line) and gust (grey line) wind direction from the northern sector, as shown in Figure 6-11a and b.

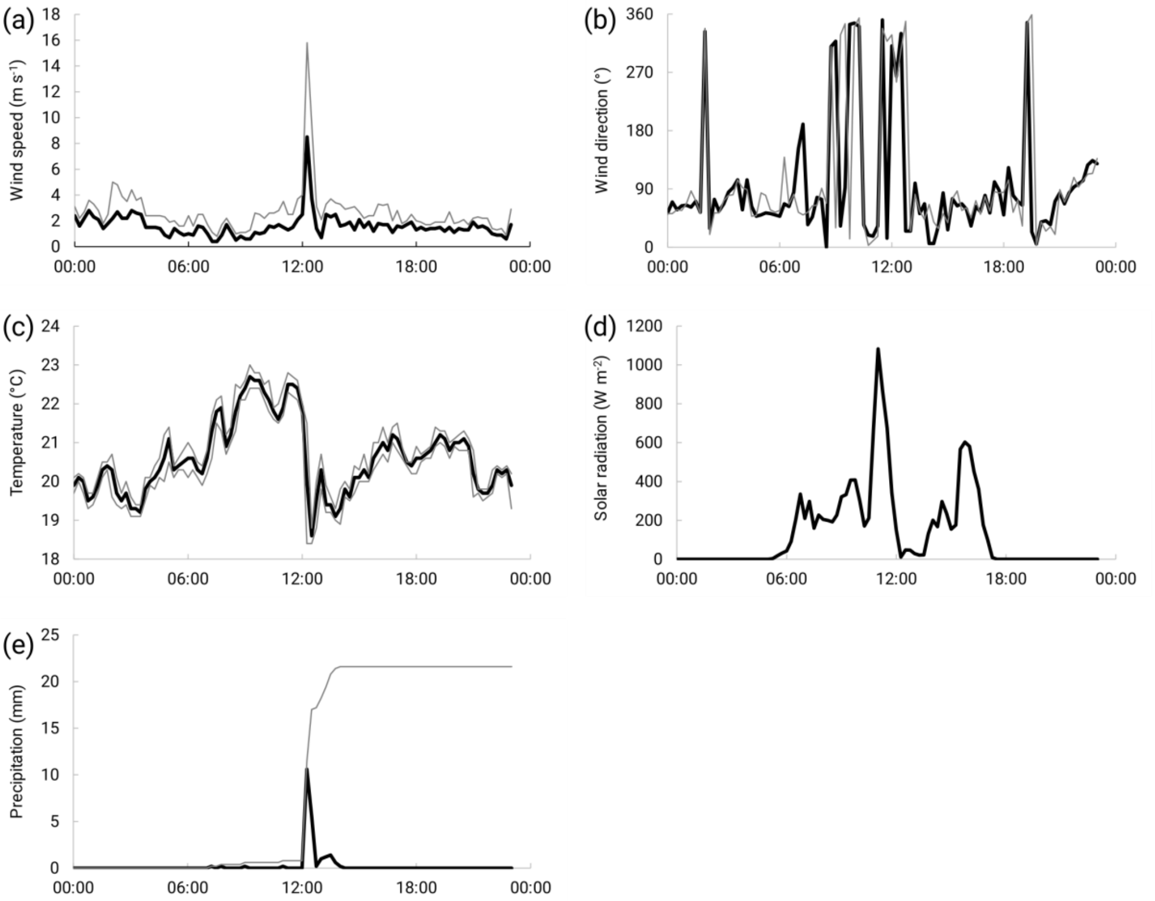

Figure 6-11. Measurements of the LaMMA meteorological station in Livorno: mean (black) and maximum (grey) wind speed in m s^{-1} (a); prevailing (black) and gust (grey) wind direction in degrees (b); temperature (black) and its variability (grey) in Celsius degrees (c); maximum solar radiation (black) in W m^{-2} (d); precipitation (black) and daily cumulated rain (grey) in mm. Data are available every 15 minutes. Courtesy LaMMA Consortium.

As far as the wind velocity is concerned, the only anomaly was registered at 12:15 UTC, when both the mean and maximum wind speeds spiked to 8.5 and 15.8 m s^{-1}, respectively. Around noon, the temperature also decreased for more than 3º from 21.9°C at 12:00 to 18.6°C at 12:30 UTC. At the same time, solar radiation dropped from its daily maximum of 1082 W m^{-2} at 11:00 UTC to 11.2 W m^{-2} at 12:15 UTC, and the rain gauge registered 10.6 mm of precipitation at 12:15 UTC and 5.6 mm at 12:30 UTC. The local observations combined with the anemometer records in Figure 6-2 indicate that the studied downburst should be classified as a wet downburst (Atkins and Wakimoto 1991). The sequence of meteorological events follows the qualitative scheme proposed by Wakimoto (1982). Furthermore, the pronounced decrease in solar radiation indicates the existence of well-developed and deep thunderstorm clouds in the area.

6.3.3 Instability indices

In case of small scale convective phenomena, many instability indices exist that are intended to provide some deterministic or probabilistic information about the occurrence of severe weather conditions, such as the Lifted Index, Showalter Index, Total Totals, K Index, SWEAT, Bulk Richardson number, CAPE, etc. These indices can be used alone or jointly and they can be calculated by means of the thermodynamic diagrams obtained from radiosoundings used for nowcasting or numerical simulations used for weather forecasting purposes. In the present study, we have analyzed two instability indices that can be considered specific of wet downdrafts: the so-called WINDEX, which can be interpreted as a direct measure of downdraft instability, in contrast to the more popular Lifted Index (LI), which is widely used as a measure of updraft instability in weather forecasting.

McCann (1994) developed an empirical index for estimating the potential of a thunderstorm to spawn a downburst. Following the works of Proctor (1988) and Wolfson (1990), he proposed the following expression for the WINDEX (WI):

$$\mathrm{WI} = 5\sqrt{H_M R_Q (\Gamma^2 - 30 + Q_L - 2Q_M)}, \tag{6-6}$$

where H_M is the height of the melting level above ground (in km), $R_Q = \min(Q_L/12\,, 1)$, $Q_L$is the mixing ratio in the first 1 km above the surface, Γ is the temperature lapse rate from the surface to the melting point (in ºC km^{-1}) and Q_M is the mixing ratio at the melting level.

The WINDEX values, calculated at 12 UTC from GFS data over the Ligurian and Northern Tyrrhenian Sea, are shown in Figure 6-12a. Note that, as reported by McCann (1994), the index is missing where the lapse rate is lower than about 5.5 C km^{-1}, which occurs especially over the Alps and the eastern Ligurian Apennines. In Livorno, the WINDEX is between 35 and 40, which is quite similar to the peak velocities (in knots) presented in Figure 6-2. The LI available at 12 UTC from GFS data is shown in Figure 6-12b. Values of this index greater than 2 correspond to no significant convective activity, whereas thunderstorms are possible if some kind of forced lifting occurs in which case the LI ranges from 0 to 2. If, on the other hand, the LI ranges from 0 to -2, thunderstorms are possible due to unforced convection, while thunderstorms are very probable if LI is lower than -2. According to the GFS data, severe thunderstorms were expected to occur over Corsica, the Central Tyrrhenian Sea, the south-western Alps, and the Eastern Padan Plain.

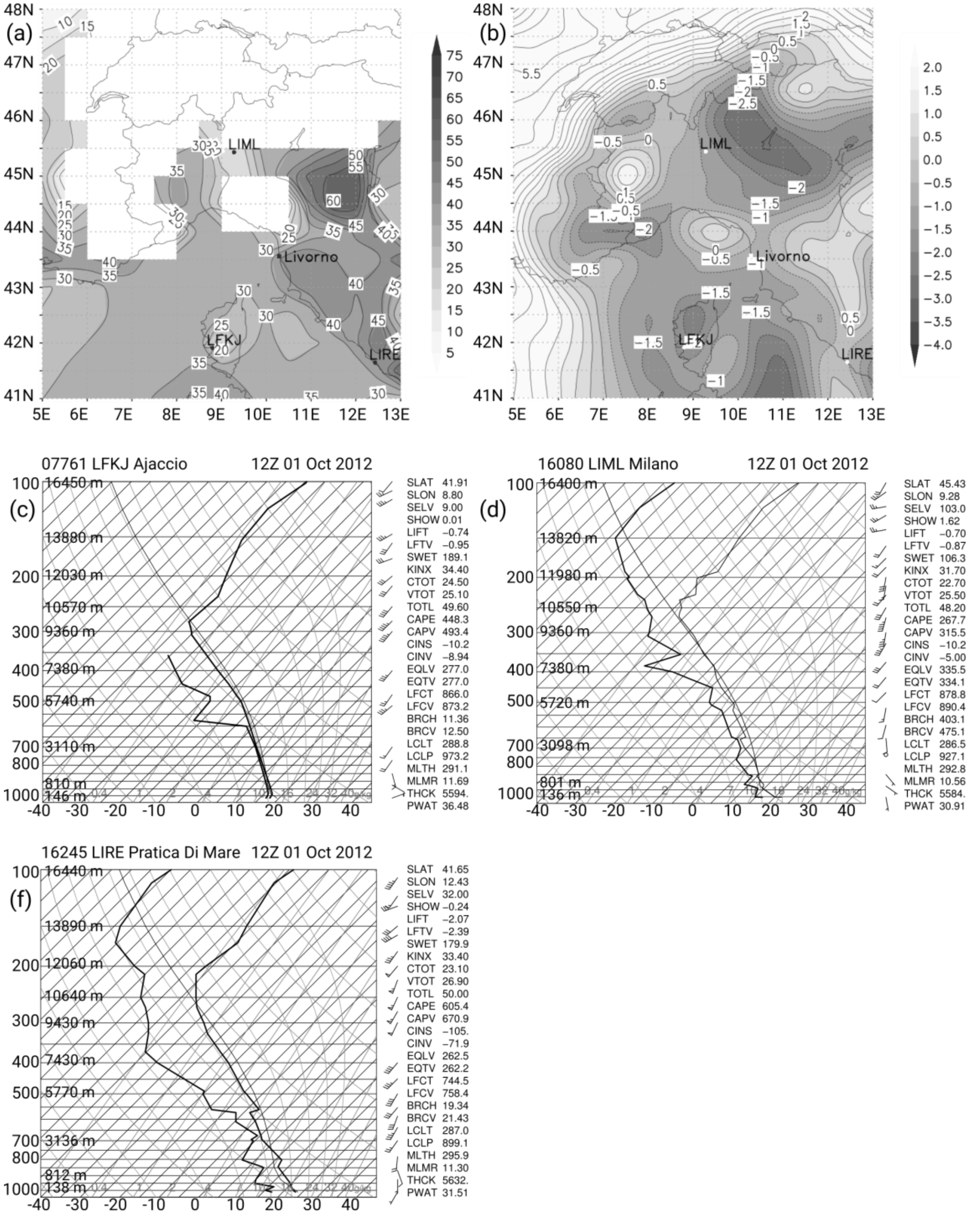

```
SLAT 41.91
SLON 8.80
SELV 9.00
SHOW 0.01
LIFT –0.74
LFTV –0.95
SWET 189.1
KINX 34.40
CTOT 24.50
VTOT 25.10
TOTL 49.60
CAPE 448.3
CAPV 493.4
CINS –10.2
CINV –8.94
EQLV 277.0
EQTV 277.0
LFCT 866.0
LFCV 873.2
BRCH 11.36
BRCV 12.50
LCLT 288.8
LCLP 973.2
MLTH 291.1
MLMR 11.69
THCK 5594.
PWAT 36.48
```

```
SLAT 45.43
SLON 9.28
SELV 103.0
SHOW 1.62
LIFT –0.70
LFTV –0.87
SWET 106.3
KINX 31.70
CTOT 22.70
VTOT 25.50
TOTL 48.20
CAPE 267.7
CAPV 315.5
CINS –10.2
CINV –5.00
EQLV 335.5
EQTV 334.1
LFCT 878.8
LFCV 890.4
BRCH 403.1
BRCV 475.1
LCLT 286.5
LCLP 927.1
MLTH 292.8
MLMR 10.56
THCK 5584.
PWAT 30.91
```

```
SLAT 41.65
SLON 12.43
SELV 32.00
SHOW –0.24
LIFT –2.07
LFTV –2.39
SWET 179.9
KINX 33.40
CTOT 23.10
VTOT 26.90
TOTL 50.00
CAPE 605.4
CAPV 670.9
CINS –105.
CINV –71.9
EQLV 262.5
EQTV 262.2
LFCT 744.5
LFCV 758.4
BRCH 19.34
BRCV 21.43
LCLT 287.0
LCLP 899.1
MLTH 295.9
MLMR 11.30
THCK 5632.
PWAT 31.51
```

Figure 6-12. Top panels: WINDEX (a) and lifted index (b) from GFS analyses. Bottom panels: skewT-logP thermodynamic diagrams at Ajaccio (c), Milan (d), and Rome (e). All panels refers to October 1, at 12:00 UTC. Diagrams courtesy of the University of Wyoming.

The atmospheric soundings for the closest available places around Livorno are obtained for October 1 at 12 UTC. The locations of these three sounding stations are indicated in Figure 6-12a and b and they are: station LFKJ (number 7761, the airport of Ajaccio), station LIML (number 16080, the Milan Linate airport) and station LIRE (number 16245, Pratica di Mare, is an Air Force base close to Rome). The skew$T$-log$P$ thermodynamic diagrams from these stations are reported in Figure 6-12(c-e). The WINDEX evaluated from the corresponding TEMP messages is 39.5 and 33.5 for LIML and LIRE, respectively, whereas it is nil in Ajaccio as the lapse rate there is equal to -5.37°C km^{-1}. The LI based on radiosoundings is -0.74, -0.70, and -2.07 for LFKJ, LIML, and LIRE, respectively.

6.4 Conclusions and some prospects

This study provides a comprehensive description and a detailed interpretation of the field measurements and weather scenario associated with a transient event, preliminarily classified as a thunderstorm downburst, which struck the Livorno coast on October 1, 2012 at about 12:10 UTC (i.e. 1.10 p.m. local Italian time). In the framework of a wide research program dealing with downbursts, this event has been chosen as a test case aiming at establishing a better link between complementary approaches in wind engineering and atmospheric sciences, with the prospect of improving the understanding, characterization and modeling of non-synoptic wind events such as downbursts.

The wind speed records detected by three ultrasonic anemometers of the monitoring network created for the European Projects “Wind and Ports” and “Wind, Port and Sea” have been analyzed and decomposed into component parts to inspect the main features of this event. A statistical analysis for non-stationary wind events has been applied for this case and the resulting components have been discussed both individually and together. Especially the joint analysis of different decomposed signals provides some interesting remarks.

Despite some peculiar aspects of this event, first of all the double peak registered by two of three sensors, its properties match rather closely the basic features of the whole database generated by the monitoring network. In particular the set of the slowly-varying mean wind velocity components provides, in its whole, a clear picture of the movement of the gust front from the sea to the inland; in addition it supports a robust separation between the dominant features of the large scale flow and the random turbulent fluctuations. Despite the residual fluctuation has strongly nonstationary random properties, the set of the diagrams of the slowly-varying turbulence intensity confirms that this quantity is not strongly time dependent; it also provides a partial confirmation that the time evolution of a downburst is so rapid and short that its wind field does not reach an equilibrium condition over the roughness of the terrain, thus turbulence intensity is not much affected by this parameter. The probability density functions of the rapidly-varying reduced turbulent fluctuation exhibit classical Gaussian features as many other authors observed in literature; moreover, its power spectral density tends to decrease in the high frequency range with a slope that is typical of the inertial sub-range of synoptic-type winds.

The analysis of the meteorological conditions concurrent with this event has been carried out by gathering all the meteorological data available in this area, making use of model analyses, standard in-situ measurements (stations and radio-soundings), remote sensing techniques (radar and satellite), proxy data (lightning), and direct observations (from the

European Severe Weather Database). All this information contributed to reconstruct the comprehensive weather scenario that occurred on October 1, 2012, over the City of Livorno, confirming that the strong wind event detected by the high-sampling rate anemometers of the local monitoring network was most probably a wet downburst.

This is an important result as it demonstrates the role of specific synoptic-scale conditions over the western Europe, e.g. the formation of a secondary cyclone in the lee of the Alps, as a necessary meteorological prerequisite and precursor to the occurrence of local-scale convectively-forced strong wind events in the northern Mediterranean Basin. Moreover, the downburst position seems to be detectable, at least in the present case, by some local signals like higher values of storm-relative helicity, as well as using standard storm-specific indexes, like the WINDEX and the Lifted Index.

It is worth noting the interest in bringing together the two different viewpoints provided by wind engineering and atmospheric sciences. In this case, the high-sampling rate wind speed records detected in a typical wind engineering framework have proven to be an excellent tool which can correlate to a meteorological event further investigated through a typical meteorological approach. Several outcomes from the atmospheric science framework evaluations were later refined using the information provided by the local anemometric network and signal analysis.

The present study may therefore form the basis for an extended analysis of non-stationary events in the Mediterranean region using this mixed approach in correlation with the extensive data base gathered by the WP and WPS campaigns.

A first implication of this kind of analysis will be its extension to a selection of the strongest wind events recorded by the anemometric network, aiming to distinguish, on a statistical basis, the events related to convection (wet and dry) with respect to the ones due to a different forcing, like downslope winds in complex topography areas. Subsequently, based upon the identification of a statistically-relevant set of convectively-forced strong wind events, research will be carried out in order to check systematically whether the aforementioned local signals can be considered recurrent footprints of wet and dry downbursts, for forecast purposes.

A second implication of this research program is strengthening the link between field measurements and analytical models, physical and numerical simulations through the systematic statistical analysis of a broad range of transient events for which high quality measurements are made available. Overall this kind of study may greatly contribute to improve the quality of simulation tools, as well as to refine our knowledge of the multi-scale space-time structure of thunderstorm events in general and downbursts in particular.

References

Alpert, P., and Coauthors, 2002: The paradoxical increase of Mediterranean extreme daily rainfall in spite of decrease in total values. *Geophysical Research Letteers*, **29**, 31–1.

Atkins, N. T., and R. M. Wakimoto, 1991: Wet microburst activity over the southeastern United States: Implications for forecasting. *Weather and Forecasting*, **6**, 470–482.

Bluestein, H. B., 1995: *Synoptic-Dynamic Meteorology in Midlatitudes: Volume II: Observations and Theory of Weather Systems*. Oxford University Press, New York, USA, 608 pp.

Braza, M., R. Perrin, and Y. Hoarau, 2006: Turbulence properties in the cylinder wake at high Reynolds numbers. *Journal of Fluids and Structures*, **22**, 757–771, doi:10.1016/j.jfluidstructs.2006.04.021.

Bryan, G. H., and J. M. Fritsch, 2002: A benchmark simulation for moist nonhydrostatic numerical models. *Monthly Weather Review*, **130**, 2917–2928.

Burlando, M., 2009: The synoptic-scale surface wind climate regimes of the Mediterranean Sea according to the cluster analysis of ERA-40 wind fields. *Theoretical and Applied Climatology*, **96**, 69–83

——, P. De Gaetano, M. Pizzo, M. P. Repetto, G. Solari, M. Tizzi and G. Bonino, 2015. The European Project "Wind, Ports and Sea". Proceedings, *14th International Conference on Wind Engineering*, Porto Alegre, Brasil.

Buzzi, A., and S. Tibaldi, 1978: Cyclogenesis in the lee of the Alps: A case study. *Quarterly Journal of the Royal Meteorological Society*, **104**, 271–287.

Byers, H. R., and R. R. Braham, 1949: The thunderstorm: Final report of the Thunderstorm Project. U.S. Government Printing Office, Washington, DC.Campins, J., A. Jansa, B. Benech, E. Koffi, and P. Bessemoulin, 1995: PYREX observation and model diagnosis of the tramontane wind. *Meteorology and Atmospheric Physics*, **56**, 209–228.

Charba, J., 1974: Application of gravity current model to analysis of squall-line gust front. *Monthly Weather Review*, **102**, 140–156.

Chay, M. T., and C. W. Letchford, 2002: Pressure distributions on a cube in a simulated thunderstorm downburst. Part A: stationary downburst observations. *Journal of Wind Engineering and Industrial Aerodynamics*, **90**, 711-732.

——, F. Albermani, and B. Wilson, 2006: Numerical and analytical simulation of downburst wind loads. *Engineering Structures*, **28**, 240-254.

Chen, L., and C. W. Letchford, (2004): A deterministic-stochastic hybrid model of downbursts and its impact on a cantilevered structure. *Engineering Structures*, **26**, 619-629.

——, and C. W. Letchford, 2007: Numerical simulation of extreme winds from thunderstorm downbursts. *Journal of Wind Engineering and Industrial Aerodynamics*, **95**, 977-990.

Choi, E. C. C., 1999: Extreme wind characteristics over Singapore - an area in the equatorial belt. *Journal of Wind Engineering and Industrial Aerodynamics*, **83**, 61-69.

——, 2004: Field measurement and experimental study of wind speed profile during thunderstorms. *Journal of Wind Engineering and Industrial Aerodynamics*, **92**, 275–290.

——, and F. A. Hidayat (2002): Dynamic response of structures to thunderstorm winds, *Progress in Structural Engineering and Materials*, **4**, 408-416.

——, and A. Tanurdjaja, 2002: Extreme wind studies in Singapore. An area with mixed weather system. *Journal of Wind Engineering and Industrial Aerodynamics*, **90**, 1611-1630.

Cook, N. J., R. I. Harris, and R. Whiting, 2003: Extreme wind speeds in mixed climates revisited. *Journal of Wind Engineering and Industrial Aerodynamics*, **91**, 403-422.

De Gaetano, P., M. P. Repetto, T. Repetto, and G. Solari, 2014: Separation and classification of extreme wind events from anemometric records. *Journal of Wind Engineering and Industrial Aerodynamics*, **126**, 132–143.

Derrien, M., H. Le Gléau, and P. Fernandez, 2013: *Algorithm theoretical basis document for "Cloud Products."* Météo France, Toulouse, France.

Dotzek, N., P. Groenemeijer, B. Feuerstein, and A. M. Holzer, 2009: Overview of ESSL's severe convective storms research using the European Severe Weather Database ESWD. *Atmospheric Res.*, **93**, 575–586.

Duranona, V., M. Sterling, and C. J. Baker, 2006: An analysis of extreme non-synoptic winds. *Journal of Wind Engineering and Industrial Aerodynamics*, **95**, 1007-1027.

EUMETSAT, 2013: *MTG-FCI: ATBD for cloud mask and cloud analysis product*. European Organisation for the Exploitation of Meteorological Satellites (EUMETSAT), Darmstadt, Germany.

Flocas, H. A., I. Simmonds, J. Kouroutzoglou, K. Keay, M. Hatzaki, V. Bricolas, and D. Asimakopoulos, 2010: On cyclonic tracks over the Eastern Mediterranean. *Journal of Climate*, **23**, 5243-5257.

Fujita, T. T., 1981: Tornadoes and downbursts in the context of generalized planetary scales. *Journal of Atmospheric Science*, **38**, 1511–1534.

——, 1985: *The downburst: microburst and macroburst*. Satellite and Mesometeorology Research Project, Dept. of the Geophysical Sciences, University of Chicago, Chicago, IL, United States, 136 pp.

——, 1986: *DFW microburst on August 2, 1985*. 1st edition. University of Chicago, 154 pp.

——, 1990: Downburst: meteorological features and wind field characteristics. *Journal of Wind Engineering and Industrial Aerodynamics*, **36**, 75-86.

Gast, K. D., and S. Schroeder, 2004: Extreme wind events observed in the 2002 Thunderstorm Outflow Experiment. *22nd Conference on Severe Local Storms, 11th Conference on Aviation, Range, and Aerospace and the 22nd Conference on Severe Local Storms*, Boston, United States, American Meteorological Society https://ams.confex.com/ams/11aram22sls/webprogram/22SLS.html (Accessed July 30, 2016).

Geerts, B., 2001: Estimating downburst-related maximum surface wind speeds by means of proximity soundings in New South Wales, Australia, *Weather and Forecasting*, American Meteorological Society, **16**, 261-269.

Genoveś, A., and A. Jansà, 1989: *Statistical approach to mesoscale non-alpine West Mediterranean cyclogenesis*. World Meteorological Organization, Geneva, Switzerland.

Giorgi, F., 2006: Climate change hot-spots. *Geophysical Research Letteers*, **33**, L08707.

Goff., R. G., 1976: Vertical structure of thunderstorm outflows. *Monthly Weather Review*, **104**, 1429-1440.

Goldman, J. L., and P. Sloss, 1969: *Structure of the leading edge of thunderstorm cold-air outflow*. http://ntrs.nasa.gov/search.jsp?R=19700042459 (Accessed July 31, 2016).

Gomes, L., and B. J. Vickery, 1976: On thunderstorm wind gusts in Australia. *Civil Engineering Transactions (Institute of Engineers, Australia),* **18**, 33-39.

——, and B. J. Vickery, 1977/1978: Extreme wind speeds in mixed climates. *Journal of Wind Engineering and Industrial Aerodynamics*, **2**, 331-344.

Grisogono, B., and D. Belušić, 2009: A review of recent advances in understanding the meso- and microscale properties of the severe Bora wind. *Tellus A*, **61**, 1–16.

Gunter, W. S., and J. L. Schroeder, 2015: High-resolution full-scale measurements of thunderstorm outflow winds. *Journal of Wind Engineering and Industrial Aerodynamics*, **138**, 13-26.

Hangan, H. 2014: The Wind Engineering Energy and Environment (WindEEE) Dome at Western University, Canada. *Wind Engineering, Japan Association for Wind Engineering,* **39**, 350-351.

Hjelmfelt, M. R., 1988: Structure and life cycle of microburst outflows observed in Colorado. *Journal of Applied Meteorology*, **27**, 900–927.

Holmes, J. D., H. M. Hangan, J. L. Schroeder, C. W. Letchford, and K. D. Orwig, 2008: A forensic study of the Lubbock-Reese downdraft of 2002. *Wind and Structures*, **11**, 137–152.

Jansa, A., A. Genoves, M. A. Picornell, J. Campins, R. Riosalido, and O. Carretero, 2001: Western Mediterranean cyclones and heavy rain. Part 2: Statistical approach. *Meteorological Applications*, **8**, 43–56.

Jubayer C., A. Elatar, H. Hangan, 2016: Pressure distributions on a low-rise building in a laboratory simulated downburst. *8th Int. Colloquium on Bluff Body Aerodynamics and Applications.* Boston, Massachusetts, USA.

Kasperski, M. 2002: A new wind zone map of Germany. *Journal of Wind Engineering and Industrial Aerodynamics*, **90**, 1271-1287.

Kim, J., and H. Hangan, 2007: Numerical simulations of impinging jets with application to downbursts. *Journal of Wind Engineering and Industrial Aerodynamics*, **95**, 279–298.

Klein, W., 1957: *Principal tracks and mean frequencies of cyclones and anticyclones in the Northern Hemisphere*. U.S. Weather Bureau, Washington, DC.

Kotroni, V., and K. Lagouvardos, 2016: Lightning in the Mediterranean and its relation with sea-surface temperature. *Environmental Research Letters*, **11**, 34006.

Kouroutzoglou, J., H. A. Flocas, K. Keay, I. Simmonds, and M. Hatzaki, 2011: Climatological aspects of explosive cyclones in the Mediterranean. *International Journal of Climatology*, **31**, 1785–1802.

Kwon, D. K., and A. Kareem, (2013): Generalized gust-front factor: A computational framework for wind load effects. *Engineering Structures*, **48**, 635-644.

Letchford, C. W., and M. T. Chay, 2002: Pressure distributions on a cube in a simulated thunderstorm downburst. Part B: moving downburst observations. *Journal of Wind Engineering and Industrial Aerodynamics*, **90**, 733–753.

Lin, W. E., L. G. Orf, E. Savory, and C. Novacco, 2007: Proposed large-scale modelling of the transient features of a downburst outflow. *Wind and Structures*, **10**, 315–346.

Lionello, P., 2005: *Flooding and environmental challenges for Venice and its lagoon : State of knowledge*. Cambridge University Press, Cambridge, 59-65 pp.

——, and Coauthors, 2006: Chapter 6 Cyclones in the Mediterranean region: Climatology and effects on the environment. *Developments in Earth and Environmental Sciences*, P.M.-R. and R.B. P. Lionello, Ed., Vol. 4 of *Mediterranean*, Elsevier, 325–372 http://www.sciencedirect.com/science/article/pii/S1571919706800091 (Accessed July 27, 2016).

Lombardo, F. T., J. A. Main, and E. Simiu, 2009: Automated extraction and classification of thunderstorm and non-thunderstorm wind data for extreme-value analysis, *Journal of Wind Engineering and Industrial Aerodynamics*, **97**, 120–131.

——, D. A. Smith, J. L. Schroeder, and K. C. Mehta, 2014: Thunderstorm characteristics of importance to wind engineering. *Journal of Wind Engineering and Industrial Aerodynamics*, **125**, 121–132.

Lorente-Plazas, R., P.A. Jiménez, J. Dudhia, J.P. Montávez, 2016: Evaluating and improving the impact of the atmospheric stability and orography on surface winds in the WRF model. *Monthly Weather Review,***144**, 2685-2693.

Maheras, P., and C. Anagnostopoulou, 2003: Circulation types and their influence on the interannual variability and precipitation changes in Greece. *Mediterranean*

Climate, H.-J. Bolle, Ed., *Regional Climate Studies*, Springer Berlin Heidelberg, 215–239.

——, H. a. Flocas, I. Patrikas, and C. Anagnostopoulou, 2001: A 40 year objective climatology of surface cyclones in the Mediterranean region: spatial and temporal distribution. *International Journal of Climatology,* **21**, 109–130

Mason, M., C. W. Letchford, and D. L. James, 2005: Pulsed jet simulation of a stationary thunderstorm downburst. Part A: Physical structure and flow field characterization, *Journal of Wind Engineering and Industrial Aerodynamics*, **93**, 557-580.

——, G. S. Wood, and D. F. Fletcher, 2010: Numerical investigation of the influence of topography on simulated downburst wind fields. *Journal of Wind Engineering and Industrial Aerodynamics*, **98**, 21–33.

Mattocks, C., and R. Bleck, 1986: Jet Streak Dynamics and Geostrophic Adjustment Processes during the Initial Stages of Lee Cyclogenesis. *Monthly Weather Review*, **114**, 2033–2056.

McCann, D. W., 1994: WINDEX—A new index for forecasting microburst potential. *Weather and Forecasting*, **9**, 532–541.

McConville, A. C., M. Sterling, and C. J. Baker, 2009: The physical simulation of thunderstorm downbursts using an impinging jet, *Wind and Structures*, **12**, 133-149.

McCullough, M., D. K. Kwon, A. Kareem, and L. Wang, 2014: Efficacy of averaging interval for nonstationary winds. *Journal of Engineering Mechanics (ASCE)*, **140**, 1-19.

McGinley, J., 1982: A diagnosis of Alpine lee cyclogenesys. *Monthly Weather Review*, **110**, 1271–1287.

McTaggart-Cowan, R., T. J. Galarneau, L. F. Bosart, and J. A. Milbrandt, 2009a: Development and tropical transition of an Alpine lee cyclone. Part I: Case analysis and evaluation of numerical guidance. *Monthly Weather Review*, **138**, 2281–2307.

——, ——, ——, and ——, 2009b: Development and tropical transition of an Alpine lee cyclone. Part II: Orographic influence on the development pathway. *Monthly Weather Review*, **138**, 2308–2326.

Nissen, K. M., G. C. Leckebusch, J. G. Pinto, D. Renggli, S. Ulbrich, and U. Ulbrich, 2010: Cyclones causing wind storms in the Mediterranean: characteristics, trends and links to large-scale patterns. *Natural Hazards and Earth System Sciences*, **10**, 1379–1391.

Orf, L., E. Kantor, and E. Savory, 2012: Simulation of a downburst-producing thunderstorm using a very high-resolution three-dimensional cloud model. *Journal of Wind Engineering and Industrial Aerodynamics*, **104–106**, 547–557.

——, and J. R. Anderson, 1999: A numerical study of traveling microbursts. *Monthly Weather Review*, **127**, 1244–1258.

Petterssen, S., 1956: *Weather analysis and forecasting. Volume I: motion and motion systems*. 2nd edition. McGraw-Hill, New York, 428 pp.

Pistotnik, G., A. M. Holzer, R. Kaltenböck, S. Tschannett, 2011: An F3 downburst in Austria—A case study with special focus on the importance of real-time site surveys. *Atmospheric Research*, **100**, 565-579.

Proctor, F. H., 1988: Numerical simulations of an isolated microburst. Part II: Sensitivity experiments. *Journal of Atmospheric Science*, **46**, 2143–2165.

Radinović, D., 1987: *Mediterranean cyclones and their influence on the weather and climate*. WMO, Geneva, Switzerland, 131 pp.

Rasmussen, E. N., and D. O. Blanchard, 1998: A baseline climatology of sounding-derived supercell and tornado forecast parameters. *Weather and Forecasting*, **13**, 1148–1164.

Rex, D. F., 1950: Blocking Action in the middle troposphere and its effect upon regional climate. *Tellus*, **2**, 196–211.

Riera, J. D., Nanni, L. F., 1989: Pilot study of extreme wind velocities in a mixed climate considering wind orientation. *Journal of Wind Engineering and Industrial Aerodynamics*, **32**, 11-20.

Romanić, D., M. Ćurić, M. Lompar, and I. Jovičić, 2016a: Contributing factors to Koshava wind characteristics. *International Journal of Climatology*, **36**, 956–973.

——, ——, M. Zarić, M. Lompar, and I. Jovičić, 2016b: Investigation of an extreme Koshava wind episode of 30 January–4 February 2014. *Atmospheric Science Letters*, **17**, 199–206.

——, D. Parvu, and H. Hangan, 2016c: Downburst reconstruction using physical simulation and analytical model with application to urban environments. *Proc.,the First Int. Conf. on Urban Physics (FICUP)*, Quito-Galápagos, Ecuador.

Rowcroft, J., 2011: Vertical wind shear profiles in downburst events and the insufficiency of wind turbine design codes, *Proc., 13th Int. Conf. on Wind Engineering*, Amsterdam, The Netherlands.

Sengupta, A., and P. P. Sarkar, 2008: Experimental measurement and numerical simulation of an impinging jet with application to thunderstorm microburst winds, *Journal of Wind Engineering and Industrial Aerodynamics*, **96**, 345-365.

Sherman, D. J., 1987: The passage of a weak thunderstorn downburst over an instrumented tower. *Monthly Weather Review*, **115**, 1193–1205.

Sim, T. S., M. C. Ong, W. Y. Quek, Z. W. Sum, W. X. Lai, and M. Skote, 2016: A numerical study of microburst-like wind load acting on different block array configurations using an impinging jet model. *Journal of Fluids and Structures*, **61**, 184–204.

Solari, G., 2014: Emerging issues and new frameworks for wind loading on structures in mixed climates. *Wind and Structures*, **19**, 295-320.

——, 2016: Thunderstorm response spectrum technique: theory and applications. *Engineering Structures*, **108**, 28-46.

——, and G. Piccardo, 2001: Probabilistic 3-D turbulence modeling for gust buffeting of structures. *Probabilistic Engineering Mechanics,* **16**, 73-86.

——, M. P. Repetto, M. Burlando, P. De Gaetano, M. Pizzo, M. Tizzi, and M. Parodi, 2012: The wind forecast for safety management of port areas. *Journal of Wind Engineering and Industrial Aerodynamics*, **104–106**, 266–277.

——, M. Burlando, P. De Gaetano, and M. P. Repetto, 2015a: Characteristics of thunderstorms relevant to the wind loading of structures. *Wind and Structures*, **20**, 763–791.

——, P. De Gaetano, and M. P. Repetto, 2015b: Thunderstorm response spectrum: Fundamentals and case study. *Journal of Wind Engineering and Industrial Aerodynamics*, **143**, 62–77.

Sutcliffe, R. C., 1947: A contribution to the problem of development. *Quarterly Journal of the Royal Meteorological Society*, **73**, 370–383.

Trigo, I. F., T. D. Davies, and G. R. Bigg, 1999: Objective climatology of cyclones in the Mediterranean region. *Journal of Climate*, **12**, 1685–1696.

——, G. R. Bigg, and T. D. Davies, 2002: Climatology of cyclogenesis mechanisms in the Mediterranean. *Monthly Weather Review*, **130**, 549–569, doi:10.1175/1520-0493(2002)130<0549:COCMIT>2.0.CO;2.

Twisdale, L. A., and P. J. Vickery, 1992: Research on thunderstorm wind design parameters. *Journal of Wind Engineering and Industrial Aerodynamics*, **41**, 545-556.

Vermeire, B. C., L. G. Orf, and E. Savory, 2011: Improved modeling of downburst outflows for wind engineering applications using a cooling source approach, *Journal of Wind Engineering and Industrial Aerodynamics*, **99**, 801-814.

Wakimoto, R. M., 1982: The life cycle of thunderstorm gust fronts as viewed with Doppler radar and rawinsonde data. *Monthly Weather Review*, **110**, 1060–1082.

——, 1985: Forecasting dry microburst activity over the High Plains. *Monthly Weather Review.*, **113**, 1131–1143.

Wind Science and Engineering Centre, 2006: *A recommendation for an enhanced Fujita scale (EF-Scale)*. Texas Tech University, Lubbock, Texas, http://www.depts.ttu.edu/nwi/Pubs/FScale/EFScale.pdf (Accessed July 2, 2015).

Wolfson, M. M., 1990*: Understanding and predicting microbursts*. Massachusetts Institute of Technology, http://dspace.mit.edu/handle/1721.1/13970 (Accessed July 30, 2016).

Wood, G. S., K. C. S. Kwok, N. A. Motteram, and D. F. Fletcher, 2001: Physical and numerical modelling of thunderstorm downburst, *Journal of Wind Engineering and Industrial Aerodynamics*, **89**, 535-552.

Xu, Z., and H. Hangan, 2008: Scale, boundary and inlet condition effects on impinging jets with application to downburst simulations, *Journal of Wind Engineering and Industrial Aerodynamics*, **96**, 2383-2402.

Xu, Z., H. Hangan, and P. Yu, 2008: Analytical solutions for inviscid Gaussian impinging jets, Journal of Applied Mechanics *ASME*, **75(**2).

You, C.-H., D.-I. Lee, M.-Y. Kang, and H.-J. Kim, 2016: Classification of rain types using drop size distributions and polarimetric radar: Case study of a 2014 flooding event in Korea. *Atmospheric Research*, **181**, 211–219.

Zhang, S., M. Burlando, M. P. Repetto, and G. Solari, 2016: Advances in properties of thunderstorm outflows relevant to the wind loading of structures. *14th International Symposium on Structural Engineering ISSE14*, Beijing, China.

Zhang, Y., H. Hu, and P. P. Sarkar, 2013: Modeling of microburst outflows using impinging jet and cooling source approaches and their comparison. *Engineering Structures*, **56**, 779–793.

Chapter VII

7 Concluding remarks and recommendations

7.1 Summary

Sustainable and resilient developments are among the top priorities of modern society. Moreover, these two fields are highly interdisciplinary and interconnected. A sustainable development should in general be resilient and vice versa. In this document, these two subjects have been analyzed from meteorological and wind engineering points of view. Multiscale wind sustainability and resilience oriented analysis have been performed at various locations around the globe for an urban block located in downtown Toronto (Ontario, Canada), a remote site in the Central South Kansas (United States) and the coastal city of Livorno (Italy).

The main focus of the Toronto case studies was sustainability, particularly assessing the wind resources for the 2015 Pan American Games Athletes' Village (PanAm Village). For the first time, the Canadian Wind Energy Atlas (Environment Canada 2003) has been coupled with a CFD tool in order to estimate available urban wind resources. Using the methodology described in Chapter II, the wind energy atlas was used to provide the inlet conditions for direction-dependent CFD simulations. The employed CFD software were Star-CCM+ (CD-Adapco 2014). The results were used to analyze some of the main features of flows in highly complex urban environment, such as flow channeling, separation, reattachment and wake. Wind energy sustainability analysis of the PanAm Village was conducted using a generic 30 kW wind turbine and estimated energy demands of that block. It was demonstrated that two wind directions (90° and 240°) can supply between 3% and 12% of the total energy demand of PanAm Village.

In the next step (Chapter III), wind climatology of Toronto was computed using the NCEP/NCAR reanalysis 1 data (Kalnay et al. 1996). This freely available dataset covers the whole globe with temporal coverage from 1848 to present. Data are available at three temporal resolutions: 4-times daily, daily and monthly values. The analysis was performed at the sigma-995 level (~41.1 m above ground), which is the level above surface where pressure is 99.5% of the surface pressure. It was shown that the winds coming in from 240°, 270° and 210° had the highest frequency of occurrence. The windiest season is winter with an average wind speed of 5.61 m s^{-1} and the wind power density of 190.7 W m^{-2}. Long-term wind speed and occurrence trends have also been analyzed. The same study also investigated the low-frequency wind spectra and the three pronounced peaks were detected. The periods of these peaks are: (1) 2-4.5 days, (2) 1 year and (3) 11 years.

Combining these results, Chapter IV investigates the long-term stability of urban wind resources in changing climate. That is, a new methodology is developed in order to quantify the impact of the observed long-term wind speed trend on the available wind energy in

PanAm Village. It was shown that the positive trends in wind speed have a negligible implications to the urban wind energy sector.

Chapter V is a comprehensive wind sustainability analysis of a new development that is planned to be built at a remote site located in "Tornado Alley" in Central South Kansas (the Kansas Project). The site is envisioned to be the state-of-the-art when it comes to self-sustainability and resilience to tornadoes and downbursts. The following wind analysis was conducted: (1) wind climatology, (2) extreme wind analysis and (3) wind resource assessment study. Data used in these analysis were obtained from the nearby automated weather station. The anemometric records are 2-minute means, whereas the extreme wind analysis is performed on both 2-minute means and 5-second gusts. Regional wind atlas and wind resource maps are created using the WAsP software package (Troen and Petersen 1989). Uncertainties of these simulations were also addressed.

Meteorological and wind engineering aspects of a downburst event that struck Mediterranean coastal city Livorno on October 1, 2012 are investigated in detail employing both atmospheric science (meteorology) and wind engineering approaches. The downburst winds were measured in the framework of the European project "Wind and Ports" (Solari et al. 2012) and the event is captured by three sonic anemometers. The peak speed measured at 20 m above ground by the anemometer LI.03 was 28.76 m s^{-1}. This peak was a very short gust that was weaker at the location of anemometers LI.01 and LI.05. The wind direction shifts between the first peak and the spike are approximately 90º and 130º at LI.03 and LI.05, respectively. From meteorological point of view, it was demonstrated that the downburst was spawn in cumulonimbus cloud(s) located southwest of Livorno. In turn, these clouds were a result of a mesoscale system, which represented the initial evolution of a cyclone in the lee of the Alps during its trigger stage. From wind engineering point of view, the whole phenomena is analyzed based anemometric records. It has been shown that the event is non-stationary and non-Gaussian, i.e., pronouncedly different than the synoptic wind records.

7.2 Conclusions

The major specific conclusions from this study are listed below.

<u>Urban sustainability and winds:</u>

- The Canadian Wind Energy Atlas can be used together with a CFD to assess the available wind resources in urban environments. The methodology for this coupling is developed in this study and presented step-by-step using as frame the 2015 Pan American Games Athletes' Village (PanAm Village) in downtown Toronto, Ontario, Canada.
- The most frequent wind direction and an intermediate frequent wind direction combined can supply between 3% and 12% of energy demands several building blocks in PanAm Village. The approach is conservative as it only includes the probabilities associated with two wind directions however, the method can be generalized for any number of wind directions.
- The delivered energy is found to be 3 times smaller compared to the maximum extractable wind energy. This discrepancy is due to lack of optimally design wind turbines for urban environments. The nominal speed and power curve of the available wind turbines demonstrate an important gap between the required rated

speed for urban wind energy production and the specifications of the current designs.

- Mean annual wind speed above Toronto is 4.83 m s^{-1} and the mean wind power density is 123.2 W m^{-2} at the sigma-995 level located at 41.1 m above ground. Mean annual winds speed above Toronto have positive and statistically significant trend. In the period 1948-2014, the annual wind speed increased for 0.2 m s^{-1}. This positive trend is statistically significant at the 95% confidence level.
- The strongest positive trends are observed in the fall and winter seasons. The results are in good agreement with the findings of Holt and Wang (2012), but some differences are found with the results published by Wan et al. (2010).
- These positive trends seem to be caused by an uneven temperature increases across Ontario. The differences in temperature increase result in augmentation of the pressure gradients, which in turn would lead to the positive wind speed trends.
- Spectral analysis of Toronto wind speed series in the low-frequency domain reveals three distinguished peaks. The peaks with the period of 2-4.5 days and 1 year are typical. The existence of the peak with the period of 11-years is the striking feature.
- Cross-correlation analysis between smoothed wind speed series and the total monthly number of sunspots indicates that the 11-year peak in wind spectrum might be due to the solar activity that manifest as the famous 11-year solar cycle. The correlation between these two series is 0.82 at zero time lag.

Rural sustainability and winds:

- The mean annual wind speed at the weather station close to the Kansas Project site (South Central Kansas, United States) is 4.16 m s^{-1} with power density of 102 W m^{-2}, both at 10 m above ground. Wind bi-directionality at the site is very pronounced with north and south winds being present in more than 50% of the time in a year. Diurnal wind cycle shows that the strongest winds occur in the afternoon.
- The extreme value analysis shows that the annual maximum 2-minute average wind speed with the return period of 50 years is 28.50 m s^{-1}, whereas the annual maximum 5-second gust is 33.97 m s^{-1} at 10 m above ground.
- Wind resource maps for the Kansas Project site are created for 50, 80, 100 and 150 m levels above ground. Wind power density at 100 m is approximately 400 W m^{-2} at the locations most suitable for installation of wind turbines. At 150 m above ground, wind power density reaches 560 W m^{-2}. The site has "fair" wind resources compared to the rest of Kansas.

Downburst resilience of a coastal city in the Mediterranean:

- The records of a downburst that struck Livorno, Italy, on October 1, 2012, are one of the first anemometric records of a downburst in Mediterranean. Furthermore, this is a unique events as the downburst was approaching the coast coming from the sea which is different from the usual downburst measurements presented in literature corresponding to inland parts in Untied States.
- The anemometric record of this event is characterized by two well-defined humps, which is a typical downburst signature. The striking feature, however, is the

existence of a pronounced spike short after the first peak (hump). Based on literature, it seems that this spike might be a short-lived microburst embedded in the larger downdraft.

- The existence of the gust front that preceded the downburst event is notable. The same pattern is not observed in the downburst records from the United States.
- Satellite observations, numerical simulations and local measurements from nearby weather stations demonstrate the convective nature of the cluster of cumulonimbus clouds that generated the downburst. Local observations of wind, temperature, precipitation and solar radiation from the weather station in Livorno also captured the phenomena. Based on these observations, the downburst is classified as a wet downburst.
- A classical transient wind stochastic decomposition is applied to the Livorno downburst signal. The slowly-varying mean wind velocity provides a very clear picture of the movement of the gust front from the sea to the inland. The slowly-varying turbulence intensity is not strongly time dependent. The rapidly-varying reduced turbulent fluctuation exhibit some classical random stationary Gaussian features but for one of the stations they also show weak non-Gaussian characteristics.
- Power spectral density of rapidly-varying reduced turbulent fluctuation matches overall the results provided earlier in literature. However, one of the stations shows a departure from the typical -5/3 inertial slope which seems to be a particularity of intermittent flow phenomena.

- Anemometric records of the Livorno downburst event can be further used for validation of numerical and analytical models of downbursts.

The more general, i.e., conceptual conclusions that can be drawn from this doctoral dissertation are as follows.

- Wind-related studies are of practical importance for sustainability and resilience of modern developments whether they are situated in urban environments or not.
- Wind sustainability and resilience analysis require a multiscale modelling approach and processing of data from variety of sources.
- There is a large gap between meteorological and wind engineering analysis of non-synoptic wind phenomena.
- The present thesis therefore is an attempt to treat wind phenomena from a multi-scale, interdisciplinary and global perspective.

7.3 Contributions

The unique contributions from this study to the scientific knowledge are the following:

- A new methodology for urban wind modelling that combines Canadian Wind Energy Atlas and a CFD tool. The methodology was for the first time applied to an urban development in Toronto, Ontario, Canada. As most countries (even whole continents) nowadays have wind atlases, the methodology can be applied to any urban (or rural) area.

- For the first time, a potential peak with the period of 11 years is detected in the low-frequency domain of wind spectra obtained from reanalysis data for an urban environment.
- A simple methodology for assessing the influence of changing climate on urban winds is introduced for the first time in literature. The methodology combines wind trend analysis and a CFD tool.
- Combining the results of urban and rural wind resource assessment studies, this study demonstrated the feasibility of rural wind power project and the current unfeasibility of urban wind power projects. The technological issue of decoupling between urban wind turbine power curves and wind speed probability density functions is highlighted as the main cause of inefficiency of urban wind turbines.
- First detailed multiscale meteorological analysis of a downburst event that occurred above water surface and propagated to the shore. The combination of atmospheric science (meteorological) concepts and tools with engineering surface measurements allows for a unique full characterization of such an event.

7.4 Future recommendations

This study opens the perspective of wind studies from both wind sustainability and resilience perspectives. Based on the foregoing findings of the study, the following are recommended for future enhancement in the fields of wind sustainability and resilience.

- Testing the developed methodology for urban wind resource assessment for the whole wind rose and not just two wind direction. This exercise would certainly increase the calculated percentages of delivered vs. needed electricity for urban blocks.

- Urban CFD simulations in this study are done for one average wind inflow condition. This approach might impact results over Weibull distribution in terms of local flow changes with mean inflow speed. Therefore, it would be interesting to investigate how different the results would be if multiple CFD runs are performed at different inflow conditions over several wind speed bins.
- Comparison between calculated urban wind energy resources using the methodology developed in this study and in-situ measurements would be of particular importance for the validation of the proposed method.
- The methodology for urban wind modelling in changing climate needs to be improved taking into account local scale influences as well as changes in urban development over time.
- Coupling between a climate model and CFD could be investigated instead of wind atlas – CFD coupling that was analyzed in this study. This new method of coupling would require a new methodology that would bridge the gap between large scales in climate models and CFD domain(s).
- The existence of 11-year peak in wind spectrum based on the reanalysis dataset should to be confirmed by using real wind measurements. Furthermore, other geographical locations should be considered as well.
- There is no satisfactory theoretical relationship between the 11-year solar activity cycle and earth’s climate. Instead, studies report statistical relationships between these two.

- Governing parameters of the analyzed downburst (e.g. jet diameter, exact location of the touchdown, maximum radial velocity and its location, etc.) should be determined using microscale numerical modelling or analytical models, or both.
- Upon obtaining the downburst parameters, the event can be physically reconstructed in the new generation wind tunnel facility such as the Wind Engineering, Energy and Environment (WindEEE) Dome at Western University. The coupling procedure between analytical models and the WindEEE Dome is described in Romanic and Hangan (2015) and Romanic et al. (2016).

References

CD-Adapco, 2014: *STAR-CCM+ User Guide Version 9.02*. CD-Adapco, Melville, New York, Computer file (Accessed September 23, 2014).

Environment Canada, 2003: *Canadian Wind Energy Atlas [computer file]*. Environment Canada, Gatineau, QC, http://www.windatlas.ca/ (Accessed December 4, 2012).

Holt, E., and J. Wang, 2012: Trends in Wind Speed at Wind Turbine Height of 80 m over the Contiguous United States Using the North American Regional Reanalysis (NARR). *Journal of Applied Meteorology and Climatology*, **51**, 2188–2202, doi:10.1175/JAMC-D-11-0205.1.

Kalnay, E., and Coauthors, 1996: The NCEP/NCAR 40-Year Reanalysis Project. *Bulletin of the American Meteorological Society*, **77**, 437–471, doi:10.1175/1520-0477(1996)077<0437:TNYRP>2.0.CO;2.

Romanic, D., and H. Hangan, 2015: Coupling of numerical weather prediction models and physical simulations for urban wind environment. *9th International Conference on Urban Climate (ICUC9)*, Toulouse, France, Meteo-France, 1–5 https://www.conftool.com/icuc9/index.php?page=browseSessions&form_session=27&presentations=hide (Accessed October 22, 2015).

——, D. Parvu, and H. Hangan, 2016: Downburst Reconstruction using Physical Simulation and Analytical Model with Application to Urban Environments.

Procedings of the First International Conference on Urban Physics (FICUP) First International Conference on Urban Physics (FICUP), Quito – Galápagos, Ecuador, 1–12.

Solari, G., M. P. Repetto, M. Burlando, P. De Gaetano, M. Pizzo, M. Tizzi, and M. Parodi, 2012: The wind forecast for safety management of port areas. *Journal of Wind Engineering and Industrial Aerodynamics*, **104–106**, 266–277, doi:10.1016/j.jweia.2012.03.029.

Troen, I., and E. L. Petersen, 1989: *European Wind Atlas*. RISØ National Laboratory, Roskilde, Denmark, 656 pp.

Wan, H., X. L. Wang, and V. R. Swail, 2010: Homogenization and Trend Analysis of Canadian Near-Surface Wind Speeds. *Journal of Climate*, **23**, 1209–1225, doi:10.1175/2009JCLI3200.1.

Appendices

Appendix A: RANS model – Fundamental equations

Computational fluid dynamics (CFD) analysis in this study are based on Reynolds-Averaged Navier-Stokes (RANS) equations with a steady solver. For an incompressible fluid and neglecting the Coriolis force in all three directions, the continuity equation and the equation of motion are, respectively:

$$\frac{\partial u_i}{\partial x_j} = 0 \tag{A-1}$$

$$\frac{\partial u_i}{\partial t} + u_j \frac{\partial u_i}{\partial x_j} = -\frac{1}{\rho}\frac{\partial p}{\partial x_j} + \frac{\partial}{\partial x_j}\left(\frac{\mu}{\rho}\frac{\partial u_i}{\partial x_j}\right) \tag{A-2}$$

where u_i and u_j are the instantaneous velocity components, ρ is the air density, p is the instantaneous pressure, μ is the dynamic viscosity and t is time. Defining the Reynolds averaging as:

$$u_i(t) = U_i + u_i'(t), \tag{A-3}$$

where

$$U_i = \lim_{\Delta T \to \infty} \int_0^{\Delta T} u_i(t)dt\,. \tag{A-4}$$

Here, U_i is the mean velocity in the averaging period ΔT, and u_i' is the fluctuating component of the instantaneous velocity. It can be seen, for instance, that the main difference between Eq. (A-3) and Eq. (6-1) in Chapter VI (Section 6.2.2) is the time dependency of the mean component. Namely, the wind records of transient phenomena, such as the downbursts, require a mobile mean (i.e. moving average technique) to be extracted, instead of simpler averaging defined by Eq. (A-4). However, the Reynolds decomposition is suitable for analyzing the synoptic winds, especially on an annual basis

(Chapter II through Chapter V). As the mean flow filed is the most important flow pattern to be replicated in these simulations, the steady solver is employed instead of an unsteady solver.

Applying Eq.'s (A-3) and (A-4) to Eq.'s (A-1) and (A-2) and after some mathematical manipulations, it reads:

$$\frac{\partial U_i}{\partial x_j} = 0 \tag{A-5}$$

$$U_j \frac{\partial U_i}{\partial x_j} = -\frac{1}{\rho}\frac{\partial P}{\partial x_j} + \frac{\partial}{\partial x_j}\left(\frac{\mu}{\rho}\frac{\partial U_i}{\partial x_j}\right) + \frac{\partial\left(-\overline{u_i' u_j'}\right)}{\partial x_j} \tag{A-6}$$

The additional term in Eq. (A-6) is known as the Reynolds stress components. For a three dimensional flow, this term is a 3×3 matrix (i.e., additional six terms). Therefore, the system of Eq.'s (A-5) to (A-6) is underdetermined. That is, additional equations need to be introduced in order to model the Reynolds stresses. This procedure is known as the "closure problem". In this study, the turbulence is modelled using the Shear Stress Transport (SST) $k-\omega$ turbulence model. The transport equations in this model are (e.g. Menter 1993):

$$\frac{\partial \rho k}{\partial t} + \frac{\partial}{\partial x_j}\left(\rho U_j k - \left(\mu + \frac{\mu_t}{\sigma_k}\right)\frac{\partial k}{\partial x_j}\right) = T_k - \beta^* \rho \omega k, \tag{A-7}$$

$$\begin{gathered}\frac{\partial \rho \omega}{\partial t} + \frac{\partial}{\partial x_j}\left(\rho U_j \omega - \left(\mu + \frac{\mu_t}{\sigma_\omega}\right)\frac{\partial \omega}{\partial x_j}\right) = \\ \alpha_n \frac{\omega}{k} T_k - \beta_n \rho \omega^2 + 2(1-F_1)\frac{\rho \sigma_{\omega 2}}{\omega}\frac{\partial k}{\partial x_j}\frac{\partial \omega}{\partial x_j}.\end{gathered} \tag{A-8}$$

Where, T_k is the production of turbulent kinetic energy, F_1 is the blending function and μ_t is the eddy viscosity defined as:

$$\mu_t = \rho \frac{k}{\omega}. \tag{A-9}$$

The parameters α_n, β_n, $\sigma_{\omega 2}$, and $\beta^*$are model constants. The wall conditions are (Menter 1993):

$$k_{wall} = 0 \tag{A-10}$$

and

$$\omega_{wall} = 10\frac{6\nu}{\beta_1(\Delta d_1)^2} \tag{A-11}$$

where β_1 is a constant and Δd_1 is the distance to the next point away from the wall. A no-slip wall forces all turbulent quantities, except ω, to collapse to zero.

The main shortcoming associated with the eddy viscosity models is in the background assumption that turbulence is fluid property and not the flow property. The SST model is a combination of the $k - \epsilon$ model in the free stream and the $k - \omega$ model near the walls. These two models are blended through the blending function (F_1). The SST $k - \omega$ does not use wall functions and tends to be most accurate when solving the flow near the wall. The better performances of the SST $k - \omega$ model over the $k - \epsilon$ model in wind engineering applications are demonstrated elsewhere (e.g. Jubayer 2014). Note that equations in this appendix are given in a differential form, whereas the RANS equations in Chapter II are presented in an integral form.

Appendix B: WAsP model – Fundamental equations

The process of estimating regional wind atlas can be mathematically expressed as (e.g. Mortensen et al. 2014, Zhang 2015):

$$\mathrm{W}_A = W_R - ORO_A - ROU_A - OBS_A, \tag{B-1}$$

where W_A is the observed wind at location A, W_R is the general regional wind climate, and ORO_A, ROU_A, OBS_A are the effects of orography, roughness and obstacles at location A, respectively. The wind climate at an arbitrary location B is therefore obtained adding the effects of orography, roughness and obstacle to the general (common) wind climate.

WAsP uses a spectral BZ model (Bessel Expansion on a Zooming Grid) to calculate orographic influences on the flow. The model belongs to the family of the Jackson–Hunt theory (Jackson and Hunt 1975) models. At height z above ground, the relative velocity perturbations are calculated as (Walmsley 1990):

$$\frac{\Delta\boldsymbol{u}(z)}{u_0(z)} = \frac{u_0^2(L)}{u_0^2(\max(z,l))}\nabla\chi. \tag{B-2}$$

Here, u_0 is the upstream wind speed, χ is the velocity potential, which for an inviscid flow in cylindrical coordinates (r,ϕ) is defined as:

$$\chi = \alpha_{na} J_n(ar) e^{in\phi} e^{-az}, \tag{B-3}$$

where J_n is the J-th Bessel function of order n and i indicates the term in the Fourier-Bessel expansion. It can be shown that the solution for velocity perturbation is given by the following expression (Troen 1990):

$$\boldsymbol{u} = \frac{1}{2R}(1,i)\sum_j \alpha_j c_j e^{\left(-c_j\frac{z}{R}\right)}, \tag{B-4}$$

where R is the distance from the point of interest where perturbation is zero (i.e., $\nabla\chi = 0$), c_j is the j-th zero of J_1 and α_j are the arbitrary expansion coefficients. Further in Eq. (B-2), L and l are outer- and inner-layer scales, respectively, expressed as (Troen 1990):

$$L = \frac{R}{c_j}, \tag{B-5}$$

$$\frac{l}{z_0} = \alpha\left(\frac{L}{z_0}\right)^{0.67}. \tag{B-6}$$

The coefficient α is equal to 0.3 and z_0 is the roughness length. In WAsP, the radial spacing is focused near the centre and increases through a geometric progression as (Walmsley 1990): $\Delta r_{k+1} = 1.06\Delta r_k$, where k is the radius number.

The roughness model in WAsP calculates the height of internal boundary layer (h) formed due to the change in roughness from $z_{01}$to z_{02} in the downwind direction as (Troen and Petersen 1989):

$$\frac{h}{z_0'}\ln\left(\frac{h}{z_0'} - 1\right) = 0.9\frac{x}{z_0'} \tag{B-7}$$

where $z_0' = \max(z_{01}, z_{02})$ and x is the distance to the roughness change line.

Lastly, the obstacle model in WAsP is very simple and it is based on the (Troen and Petersen 1989) theory. The velocity deficit $(\tilde{u})$ due to the presence of the obstacle is:

$$\tilde{u} = 9.75\eta(1 - P)e^{-0.67\eta^{1.5}}. \tag{B-8}$$

Here, P is the obstacle's porosity and η is defined as:

$$\eta = \frac{z}{h - d}(K\bar{x})^{-\frac{1}{n+2}} \tag{B-9}$$

where h is the obstacle height, d is the displacement height, $\bar{x} = \frac{x}{h-d}$, and parameters K and n are defined in Troen and Petersen (1989).

Appendix C: Copyright agreements

- Wind resource assessment in complex urban environment:

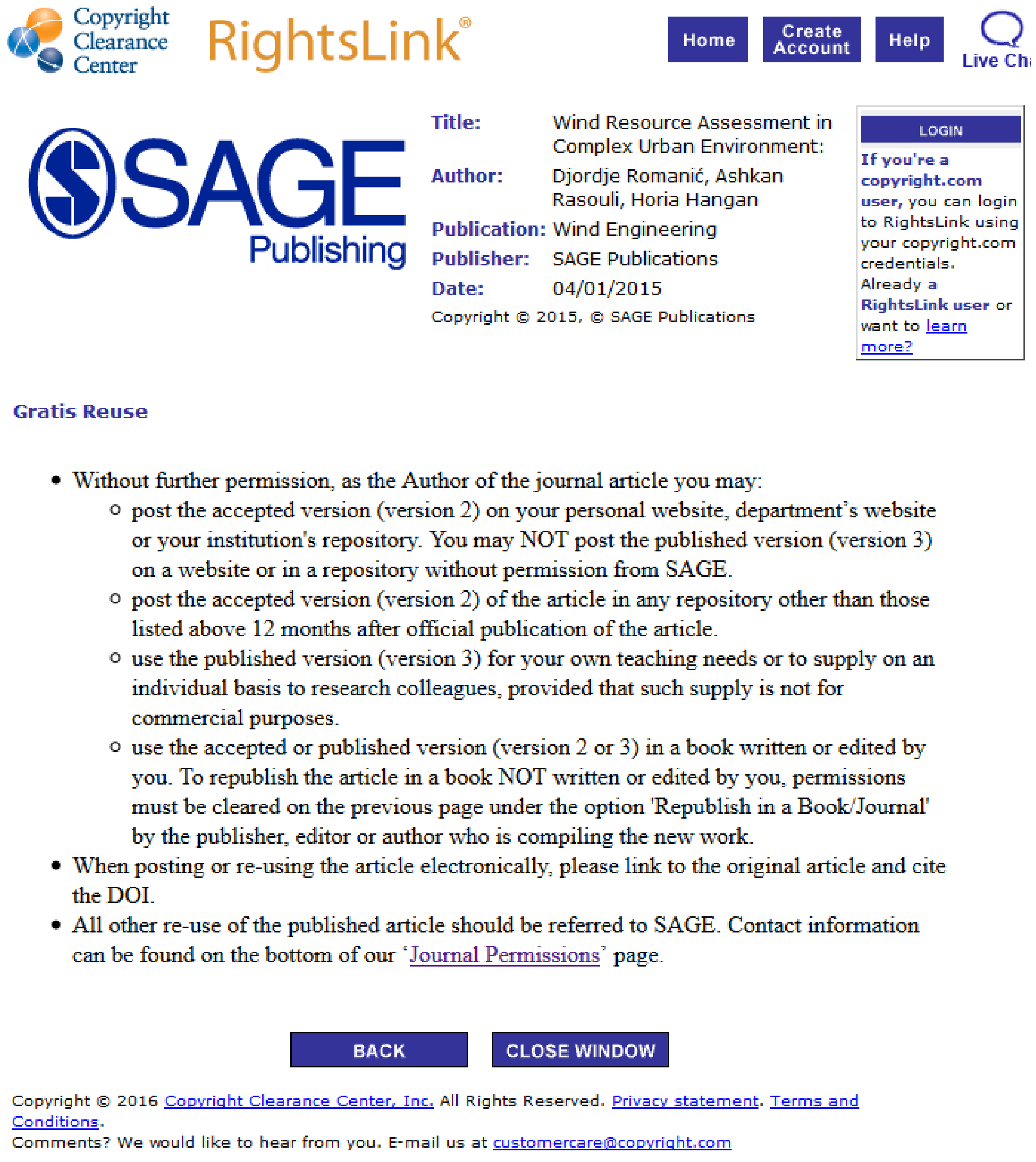

Title: Wind Resource Assessment in Complex Urban Environment:

Author: Djordje Romanić, Ashkan Rasouli, Horia Hangan

Publication: Wind Engineering

Publisher: SAGE Publications

Date: 04/01/2015

Copyright © 2015, © SAGE Publications

If you're a copyright.com user, you can login to RightsLink using your copyright.com credentials. Already **a RightsLink user** or want to learn more?

Gratis Reuse

- Without further permission, as the Author of the journal article you may:
  - post the accepted version (version 2) on your personal website, department's website or your institution's repository. You may NOT post the published version (version 3) on a website or in a repository without permission from SAGE.
  - post the accepted version (version 2) of the article in any repository other than those listed above 12 months after official publication of the article.
  - use the published version (version 3) for your own teaching needs or to supply on an individual basis to research colleagues, provided that such supply is not for commercial purposes.
  - use the accepted or published version (version 2 or 3) in a book written or edited by you. To republish the article in a book NOT written or edited by you, permissions must be cleared on the previous page under the option 'Republish in a Book/Journal' by the publisher, editor or author who is compiling the new work.
- When posting or re-using the article electronically, please link to the original article and cite the DOI.
- All other re-use of the published article should be referred to SAGE. Contact information can be found on the bottom of our 'Journal Permissions' page.

Comments? We would like to hear from you. E-mail us at customercare@copyright.com

- Urban wind resource assessment in changing climate: Case study:

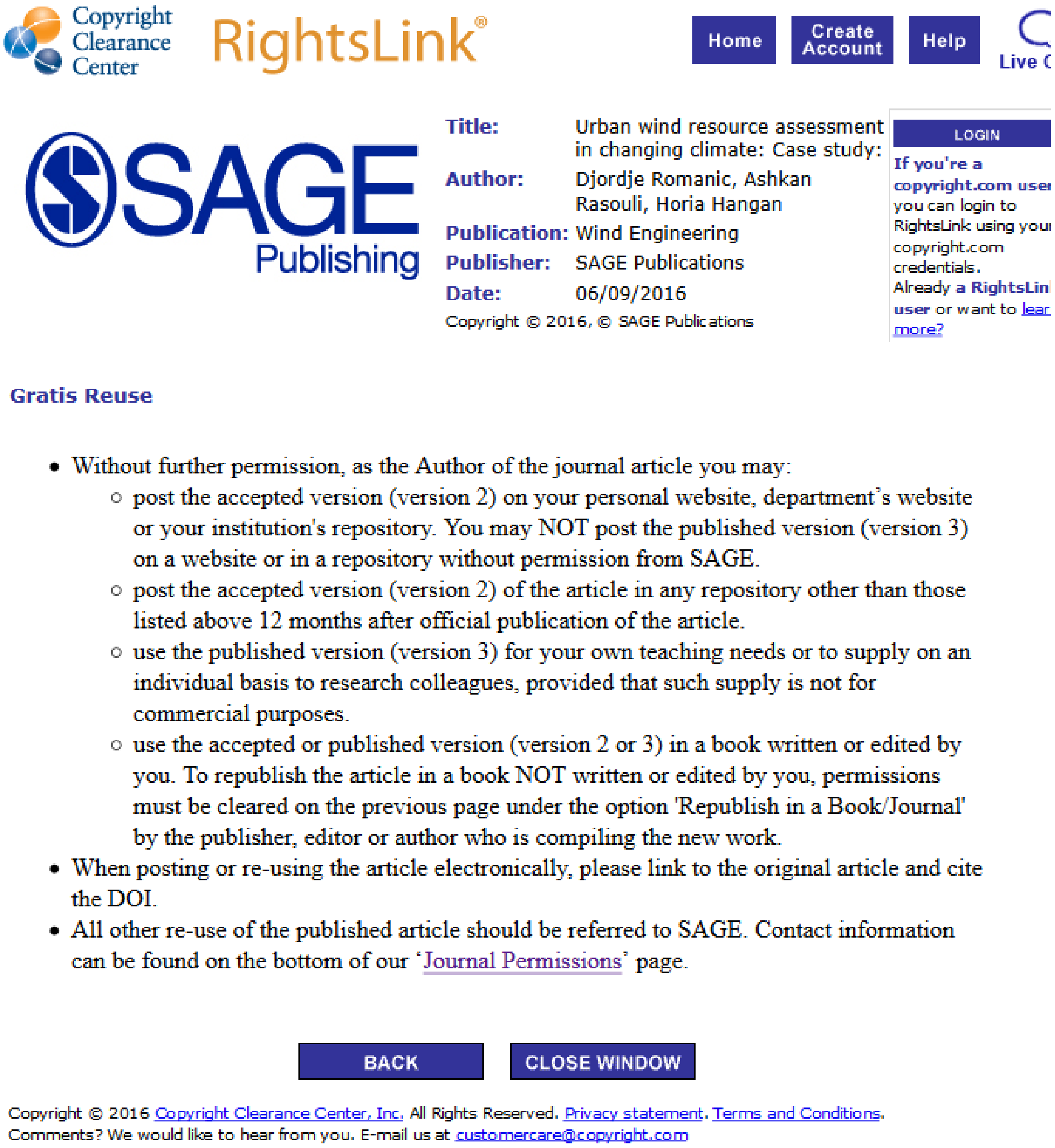

Title: Urban wind resource assessment in changing climate: Case study:

Author: Djordje Romanic, Ashkan Rasouli, Horia Hangan

Publication: Wind Engineering

Publisher: SAGE Publications

Date: 06/09/2016

Copyright © 2016, © SAGE Publications

If you're a copyright.com use you can login to RightsLink using you copyright.com credentials. Already **a RightsLin user** or want to lear more?

Gratis Reuse

- Without further permission, as the Author of the journal article you may:
  - post the accepted version (version 2) on your personal website, department's website or your institution's repository. You may NOT post the published version (version 3) on a website or in a repository without permission from SAGE.
  - post the accepted version (version 2) of the article in any repository other than those listed above 12 months after official publication of the article.
  - use the published version (version 3) for your own teaching needs or to supply on an individual basis to research colleagues, provided that such supply is not for commercial purposes.
  - use the accepted or published version (version 2 or 3) in a book written or edited by you. To republish the article in a book NOT written or edited by you, permissions must be cleared on the previous page under the option 'Republish in a Book/Journal' by the publisher, editor or author who is compiling the new work.
- When posting or re-using the article electronically, please link to the original article and cite the DOI.
- All other re-use of the published article should be referred to SAGE. Contact information can be found on the bottom of our 'Journal Permissions' page.

References

Jackson PS, Hunt JCR (1975) Turbulent wind flow over a low hill. *Quarterly Journal of the Royal Meteorological Society*, **101**:929–955. doi: 10.1002/qj.49710143015

Jubayer C (2014) *Wind and Thermal Effects on Ground Mounted Photovoltaic (PV) Panels*. Electronic Thesis and Dissertation Repository 158. Western University, London, Ontario, Canada

Menter FR (1993) Zonal two equation kappa-omega turbulence models for aerodynamic flows. In: *AIAA Fluid Dynamics Conference*. 6-9 July 1993, Orlando, FL, United States, pp 1–22

Mortensen NG, Heathfield DN, Rathmann O, Nielsen M (2014) *Wind Atlas Analysis and Application Program: WAsP 11 Help Facility*. RISØ National Laboratory, Roskilde, Denmark

Troen I (1990) A high resolution spectral model for flow in complex terrain. In: 9. *Symposium on turbulence and diffusion*. American Meteorological Society, Roskilde, Denmark, pp 417–420

Troen I, Petersen EL (1989) *European Wind Atlas*. RISØ National Laboratory, Roskilde, Denmark

Walmsley JL, Troen I, Lalas DP, Mason PJ (1990) Surface-layer flow in complex terrain: Comparison of models and full-scale observations. *Bound-Layer Meteorology*, **52**:259–281. doi: 10.1007/BF00122090

Zhang MH (2015) *Wind Resource Assessment and Micro-siting: Science and Engineering*, 1 edition. Wiley

Curriculum Vitae

Name:	Djordje Romanic
Post-secondary Education and Degrees:	Western University, London, Ontario, Canada 2012-Present *Doctor of Philosophy,* *Civil and Environmental Engineering*
	University of Belgrade, Belgrade, Serbia 2009-2016 *Doctor of Philosophy,* *Meteorology*
	University of Belgrade, Belgrade, Serbia 2002-2008 *Master of Science, Bachelor of Science,* *Meteorology*
Honors and Awards:	The Ross and Jean Clark Scholarship, 2016
	WISE Competition 1st place award, 2016
	Victor Hangan Global Opportunities Award, 2016

	Student Delegate at the C4 CatIQ Conference Award, 2016
	Alan G. Davenport Memorial Scholarship in Wind Engineering, 2015
	Dr. Robert Addie Graduate Schoolarship in Wind Engineering, 2015
	Graduated with Honors, 2008
	Top 300 Best Students in Serbia, 2007
Related Work Experience:	*Research Assistant*, 2012-2016, Western University
	Teaching Assistant, 2013-2016, Western University
	Meteorologist, 2011-2012, Republic Hydrometeorology Service of Serbia
	Consultant, 2009-2011, South East Europe Consultants Ltd.

Publications:

Journal Articles and Transaction:

1. Romanić D, Ćurić M, Jovičić I, Lompar M (2015) Long-term trends of the “Koshava” wind during the period 1949–2010. Int J Climatol 35:288–302. doi: 10.1002/joc.3981
2. Romanić D, Ćurić M, Lompar M, Jovičić I (2016) Contributing factors to Koshava wind characteristics. Int J Climatol 36:956–973. doi: 10.1002/joc.4397
3. Romanić D, Ćurić M, Zarić M, et al (2016) Investigation of an extreme Koshava wind episode of 30 January–4 February 2014. Atmos Sci Lett 17:199–206. doi: 10.1002/asl.643
4. Romanić D, Hangan H, Ćurić M (2016c) Wind climatology of Toronto based on the NCEP/NCAR reanalysis 1 data set and its potential relation to solar activity. Theor Appl Climatol. In Review
5. Romanic D, Parvu D, Refan M, Hangan H (2016) Wind climatology and wind resource modelling for a modern development situated in “Tornado Alley.” Renewable Energy. In Review
6. Romanic D, Rasouli A, Hangan H (2016) Urban wind resource assessment in changing climate: Case study. Wind Engineering 0309524X16653486. doi: 10.1177/0309524X16653486
7. Romanić D, Rasouli A, Hangan H (2015) Wind resource assessment in complex urban environment. Wind Engineering 39:193–212. doi: 10.1260/0309-524X.39.2.193
8. Romanic D, Refan M, Wu C-H, Michel G (2016) Oklahoma tornado risk and variability: A statistical model. International Journal of Disaster Risk Reduction 16:19–32. doi: 10.1016/j.ijdrr.2016.01.011

9. Burlando M, Romanic D, Solari G, Hangan H, Zhang S (2016) Field data analysis and weather scenario of a downburst event in Livorno, Italy on October 1, 2012. Monthly Weather Review. In Review.

Conference Proceedings:

1. Rasouli A, Romanić D, Hangan H (2014) Wind resource assessment in complex urban environments: case study. In: Offshore Energy & Storage Symposium and Industry Connector Event 2014. Windsor, Ontario, Canada
2. Rasouli A, Romanić D, Hangan H (2014) Sustainable analysis for an urban block: wind energy production. In: 6. International Symposium on Computational Wind Engineering. Metheorological Institute, CEN, Universtiy of Hamburg, Hamburg, Germany, Hamburg, Germany, pp 428–429
3. Romanić Đ, Banjalić M (2010) Modeling method for anemometers installed on roof of weather stations for wind resource assessment. List Saveza energetičara, Zlatibor, Srbija, pp 55–57
4. Romanic D, Hangan H (2015) Coupling of numerical weather prediction models and physical simulations for urban wind environment. Meteo-France, Toulouse, France, pp 1–5
5. Romanić Đ, Jovičić I (2011) Effect of long-term wind speed changes on wind turbine electricity production. In: Energy 2011. Association of Energy Sector Specialists, Kopaonik, Serbia, pp 194–199
6. Romanic D, Parvu D, Hangan H (2016) Fluctuating wind generator: Theoretical concept and model. Gananoque, Ontario, Canada, pp 1–2

7. Romanic D, Parvu D, Hangan H (2016) Downburst Reconstruction using Physical Simulation and Analytical Model with Application to Urban Environments. In: Proceedings of the First International Conference on Urban Physics (FICUP). Quito – Galápagos, Ecuador, pp 1–12
8. Romanic D, Rasouli A, Hangan H (2015) Urban wind resource assessment in changing climate: case study. Montreal, Quebec, Canada, p 1570057493
9. Siddiqui K, Hangan H, Bitsuamlak G, et al (2014) Energy-related research at the WindEEE Research Institute. Ottawa, Ontario, Canada

Technical Reports:

1. Costache A, Refan M, Romanic D (2014) WindEEE Research Institute Annual Report 2013-2014. WindEEE Research Institute, Western University, London, Ontario, Canada
2. Milić-Petrović B, Romanic D (2012) Evaluation of severe weather risks for the city of Novi Sad, Serbia. Republic Hydrometeorological Service of Serbia, Belgrade, Serbia
3. Romanic D (2016) Wind resource assessment study for The Kansas Project. WindEEE Research Institute, Western University, London, Ontario, Canada
4. Romanic D (2016) The Kansas Project: Tornado climatology. WindEEE Research Institute, Western University, London, Ontario, Canada
5. Romanic D (2016) The Kansas Project: Site climatology. WindEEE Research Institute, Western University, London, Ontario, Canada
6. Romanic D (2009) Feasibility study of the Power Tower patent and the small wind turbine concept patent. South East Europe Consultants (S.E.E.C) Ltd., Belgrade, Serbia

7. Romanic D, others (2011) Wind resource assessment - Žabljak, Montenegro. South East Europe Consultants (S.E.E.C) Ltd., Belgrade, Serbia
8. Romanic D, others (2011) Wind resource assessment - measurement. South East Europe Consultants (S.E.E.C) Ltd., Belgrade, Serbia
9. Romanic D, others (2010a) Wind resource assessment - Gacko, Bosnia and Herzegovina. South East Europe Consultants (S.E.E.C) Ltd., Belgrade, Serbia
10. Romanic D, others (2010) Wind resource assessment - Crni Vrh, Serbia. South East Europe Consultants (S.E.E.C) Ltd., Belgrade, Serbia
11. Romanic D, others (2009) Wind resource assessment - Vračev Gaj, Serbia. South East Europe Consultants (S.E.E.C) Ltd., Belgrade, Serbia
12. Romanic D, others (2009) Wind resource assessment - Šušare, Serbia. South East Europe Consultants (S.E.E.C) Ltd., Belgrade, Serbia
13. Romanic D, others (2009) Wind resource assessment - Kruščica, Serbia. South East Europe Consultants (S.E.E.C) Ltd., Belgrade, Serbia
14. Romanic D, others (2009) Wind resource assessment for the „La Piccolina" wind farm and calculation of loads due to wind, snow and ice on a 35kV transsmision power line Zagajica – TS Vršac 1, Serbia. South East Europe Consultants (S.E.E.C) Ltd., Belgrade, Serbia